SHOCK–FITTED NUMERICAL SOLUTIONS OF ONE- AND TWO-DIMENSIONAL DETONATION

A Dissertation

Submitted to the Graduate School
of the University of Notre Dame
in Partial Fulfillment of the Requirements
for the Degree of

Doctor of Philosophy

by

Andrew K. Henrick

Joseph M. Powers, Director

Graduate Program in Aerospace and Mechanical Engineering
Notre Dame, Indiana
April 2008

SHOCK–FITTED NUMERICAL SOLUTIONS OF ONE- AND TWO-DIMENSIONAL DETONATION

Abstract

by

Andrew K. Henrick

One- and two- dimensional detonation problems are solved using a conservative shock-fitting numerical method which is formally fifth order accurate. The shock-fitting technique for a general conservation law is rigorously developed, and a fully transformed time-dependent shock-fitted conservation form is found. A new fifth order weighted essential non-oscillatory scheme is developed. The conservative nature of this scheme robustly captures unanticipated shocks away from the lead detonation wave. The one-dimensional Zel'dovich-von Neumann-Doering pulsating detonation problem is solved at a high order of accuracy, and the results compare favorably with those of linear stability theory. The bifurcation behavior of the system as a function of activation energy is revealed and seen to be reminiscent of that of the logistic map. Two-dimensional detonation solutions are found and agree well with results from linear stability theory. Solutions consisting of a two-dimensional detonation wave propagating in a high explosive material which experiences confinement on two sides are given which converge at high order.

To Notre Dame, to whom I have dedicated everything. May her Father, Son, and Spouse be delighted with me.

CONTENTS

FIGURES

TABLES

ACKNOWLEDGMENTS

I would like to thank Drs. J. M. Powers and T. D. Aslam for teaching, advising, and befriending me throughout my graduate research. I would also like to thank Drs. Samuel Paolucci, Joannes J. Westerink, and Dinshaw S. Balsara for serving on my committee. I would especially like to thank Drs. M. Short and G. J. Sharpe for providing detailed growth rates and frequencies used in comparisons as well as Dr. Hoi D. Ng for useful discussions regarding the path to instability. Drs. Aslan R. Kasimov and D. Scott Stewart shared their numerical solutions for various one-dimensional pulsating detonation cases presented in this dissertation.

I am indebted to the faculty of the University of Notre Dame for more than a decade of formation as a young scholar. I am thankful for the friendship and understanding of many graduate students, especially Dr. Gregory P. Brooks, Dr. Aida Ramos, Mrs. Amanda Stanford, and Dr. John Kamel.

I would like to acknowledge Los Alamos National Laboratory for its generous funding of my work and numerous colleagues whom I count among my friends, especially Drs. John B. Bdzil, Mark Short, Larry G. Hill, Terry R. Salyer, and Scott I. Jackson. I would like to thank the Dinehart family and the Immaculate Heart of Mary parish for caring for me during my stay in Los Alamos and Fr. Terry T. Tompkins for helping to proofread this work.

Most importantly, I thank God and my family for whom I finished this work.

SYMBOLS

Superscripts

$a, \ldots, z$	contravariant index in $\{1, 2, 3\}$
α	contravariant index in $\{0, 1, 2, 3\}$
$*$	dimensionless
$(\ )$	non-tensorial
$\pm$	biased in the $\pm$ coordinate direction

Subscripts

$a, \ldots, z$	covariant index in $\{1, 2, 3\}$
α	covariant index in $\{0, 1, 2, 3\}$
$(\ )$	non-tensorial
$,0$	tensorial partial time derivative
m	material domain

Operators

$\cdot$	tensor product
$a_{(\mathrm{i})}, A(i)$	physical components
$[\![\ ]\!]\,\nu_i$	jump in direction of $\boldsymbol{\nu}$
$\|\ \|$	determinant or largest eigenvalue norm
$\left\{ {}_{j}{}^{i}{}_{k} \right\}$	Christoffel symbol of the second kind
∇	gradient

$\frac{\delta}{\delta t}, \frac{\delta}{\delta \mathtt{t}}$	intrinsic derivative
$\frac{\partial}{\partial y}\Big\vert_z$	partial derivative holding z constant

English Symbols

a_k^j	quadrature weight
$\mathbf{A}, \mathbf{f}, \ldots$	tuple or tensor of arbitrary dimension
$\mathtt{A}, \boldsymbol{\mathtt{f}}, \ldots$	Cartesian representation of a tensor
b_j	quadrature weight
$\boldsymbol{B}$	volumetric source
c	sound speed
c_j	time coefficients
c_p, c_v	specific heats
dS	Cartesian differential surface element
dV	scalar product of differentials
$d\mathbb{V}$	differential volume element
$\boldsymbol{D}$	shock velocity
D_n	shock speed in the direction of the shock gradient
D_o	phase speed
$\boldsymbol{e}$	normalized basis vector
e	internal energy
E	activation energy or total energy
$\mathcal{F}$	WENO5M interpolating function
$\boldsymbol{F}$	conserved quantity
$\boldsymbol{f}^i$	outer-flux
g_k	WENO5M mapping function
$\mathcal{g}$	metric tensor determinant

$\mathcal{g}^{ij}$	metric tensor
$\mathcal{g}_{ij}$	conjugate metric tensor
$\boldsymbol{\mathcal{g}}_{(i)}$	contravariant basis vector $\frac{\partial \boldsymbol{\mathcal{y}}}{\partial x^i}$
$\boldsymbol{\mathcal{g}}^{(i)}$	covariant basis vector $\frac{\partial x^i}{\partial \boldsymbol{\mathcal{y}}}$
h	numerical flux function or enthalpy
h_f^0	heat of formation
$h[f]_i$	numerical flux functional of f at x_i
$\hat{h}(x), \hat{h}[f]_i$	numerical approximations to $h(x)$ and $h[f]_i$
H	Hamiltonian function
$\hat{H}$	numerical Hamiltonian function
$\mathbf{I}$	identity matrix
J	Jacobian
M	molecular weight or Mach number
n	pressure dependence or geometric factor
$\mathbf{n}$	unit normal vector
p	pressure
q_k	WENO5 component stencils
Q	heat release due to reaction
r	axisymmetric coordinate
$\mathbf{R}$	transformation matrix
s	specific entropy
S	control surface or entropy
$t, \mathcal{t}$	time coordinate
T	temperature
$\boldsymbol{\mathcal{T}}$	surface source

$\{u, v\}$	Cartesian velocity components
$U^{(i)}$	grid velocity for time-dependent coordinate
v	specific volume
$\mathbf{v}$	velocity vector
V	Cartesian volume
V	control volume
$\mathbf{w}$	volumetric velocity
$\{x^i, t\}$	general curvilinear coordinates
$\{x, y, t\}$	Cartesian lab frame
x_l, x_r	left and right material boundaries
$\{\mathit{Y}^i, \mathit{t}\}$	Cartesian frame
$Y_{(i)}$	mass fraction of the i^{th} species

Greek Symbols

α	partial WENO5 weight or curvilinear shock angle
α_j	local maximum wave speed
β	indicator of smoothness
γ	adiabatic gamma or control surface
δ	shock deflection angle
ϵ	small parameter
ϵ_{ijk}	Levi-Civita symbol
ε_{ijk}	alternating tensor
λ	progress variable
$\mathbf{\Lambda}$	diagonal matrix of eigenvalues
ν	depletion rate
$\boldsymbol{\nu}$	shock normal

$\{\xi, \eta, \tau\}$	shock-attached frame
ρ	density
σ	control surface or thermicity
Σ	shock locus
ϕ	shock angle
ω	WENO scheme weights
$\dot{\omega}$	rate of species production

CHAPTER 1

INTRODUCTION

The problem of solving a hyperbolic system of partial differential equations involving a discontinuity has a rich history. Analytically, the discontinuity can be effectively removed from the domain by tracking its motion explicitly and solving the resulting Stefan problem [2, 3] explicitly using a similarity variable. Such solutions are only possible under restrictive conditions including one-dimensionality. For more complicated problems, numerical methods are needed.

For cases in which the discontinuity has an unknown shape and speed, a number of numerical solution techniques have been developed. The most common are classified as shock capturing methods [4] where the term shock is synonymous with discontinuity. Such methods use the same scheme to generate solutions in both smooth regions of the flow and in the neighborhood of the shock. Taylor series expansion of the associated finite difference approximations reveals the presence of an artificial viscous term [5, 6]. This numerical artifact, also known as numerical viscosity, allows these schemes to maintain stability in regions where the flow experiences high gradients. Because no special techniques are employed at the shock, these methods have a distinct advantage in situations where shocks can unexpectedly evolve. Unfortunately, numerical viscosity also acts to smear the solution and reduces the convergence properties of these schemes to first order at best.

Another popular technique used to solve problems involving discontinuities is shock tracking. Such a method uses explicit equations to describe the shock surface and its evolution. The phase field method [7] is a contemporary example of this type of technique. In general, however, the tracked shock will propagate to positions between nodes or cell interfaces. Thus, for methods using a fixed grid, interpolation is required to specify the position of the evolving shock causing a loss in accuracy.

Numerical approximations generated by these methods not only suffer from a loss of resolution at shocks, but straightforward attempts to recover this loss by using higher order spatial discretizations result in spurious oscillations in the neighborhood of the shock which will propagate throughout the domain. For scalar equations when first order convergence is sufficient, such oscillations can be forcibly removed by requiring that the scheme be Total Variation Diminishing (TVD), where the total variation is a measure of a solution's oscillation over the domain of interest. This can be accomplished by implementing a slope-limiting method in conjunction with a modified Courant-Friedrichs-Lewy (CFL) restriction [5].

Another recently developed numerical scheme for solving this type of problem is the ghost fluid method [8–10]. This method uses a level set to determine the shock location, although the shock is not tracked in the traditional sense. This method also depends on continuity and differentiability of the solution. For systems of equations, finding a governing set of equations which satisfies these conditions and incorporates the shock motion is difficult.

All of these methods suffer from numerical difficulties which highlight the fact that the governing partial differential equations do not hold at a discontinuity.

Thus, approximation of spatial derivatives by discretization across a discontinuity is the critical issue. An attractive alternative which avoids this issue for problems involving the evolution of a single discontinuity is shock-fitting.

In a shock-fitting method [11–15], a time-dependent change of coordinates embeds the shock position along a coordinate line in the computational domain. Once again, the problem is crisply divided into two regions over which the solution is smooth. In general, the transformed equations contain geometric source terms which are functions of the coordinate motion; a more nuanced partial transformation avoids introducing such source terms. The shock velocity is governed by a balance of fluxes across the discontinuity which takes the form of a system of algebraic constraints, yielding a differential algebraic system. Differentiation of one or more of these constraints recovers a simple system of partial differential equations. The potential for a high order scheme is recovered.

The thrust of the work presented here is a continuation of research on one- and two-dimensional detonation waves using shock-fitting techniques. The model problem for this work is shown in Fig. 1.1 and is known as the sandwich test, which qualitatively describes the geometry involved. The explosive is divided into two domains by a single shock which passes through a High Explosive (HE) material which is confined on both sides by an inert material. As the detonation wave passes through the quiescent explosive, a chemical reaction initiates. The immediate increase in pressure deflects the surrounding confiner. The reaction eventually goes to completion at or behind the sonic locus. The sonic locus consists of points at which the material velocity of the explosive with respect to the shock front is equal to that of the material's sound speed. Such a locus of points represents a mild singularity in the steady flow field.

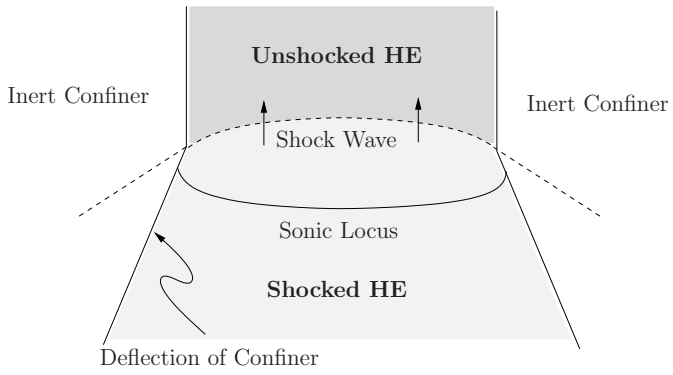

Figure 1.1. Model problem.

The salient features illustrated in Fig. 1.1 which are the focus of this work are the steady state curvature of the shock and sonic locus at their respective intersections with the HE–confiner material interface. This two-dimensional effect is due to radial flow near this interface. Current experimental research [16] shows some disagreement with current numerical and perturbation predictions. In order to resolve this behavior in a practical way, it is necessary to use a high order method which will fit the shock accurately without using a prohibitively dense computational grid. This is the object of this research.

The organization of the dissertation is divided into two main parts: Chapters 2 through 5 rigorously develop the theory necessary to implement shock-fitting, and Chapter 6 through 9 give the numerical techniques and results found by using the shock-fitting theory. Chapter 2 gives the necessary background for studying detonation problems as well as a summary of the tensor notation used throughout the dissertation. Chapter 3 develops the Reynolds' transport theorem in full tensorial form for discontinuous fields described according to time-dependent coordinates. Chapter 4 covers fundamental concepts of conservation including general

jump conditions and conservation form. Chapter 5 develops the shock-fitting technique in a geometric context. Chapter 6 gives the numerical techniques used with an emphasis on conservative numerical methods. Chapter 8 give gaseous one-dimensional detonation results. Chapter 9 gives the corresponding results for two-dimensional detonation culminating in solutions for the condensed phase model problem.

Appendices have been prepared on subjects which are of primary importance to understanding the fundamentals of detonation modeling with conservative numerical methods. Appendices A and B give background on the numerical flux function and two-dimensional metrics. Appendix C gives the Euler equations with reaction in general coordinates as well the conservative and non-conservative one dimensional forms. Appendix D develops the caloric equation of state for an ideal gas mixture which is assumed to describe the constitutive behavior of the HE. Appendix E examines the thermicity coefficient as a measure of the internal energies dependence on reaction. A characteristic analysis of the one-dimensional Euler equations with reaction is performed in Appendix F. From this analysis, the Rankine–Hugoniot jump conditions are developed in Appendix G. As a subset of these jump conditions, the shock polar equations are also developed and the strong shock limit is given in Appendix G.7. Finally, the propagation of a steady, one-dimensional detonation wave through a calorically perfect material governed by the Euler equations in the presence of a single irreversible exothermic reaction is given in Appendix H. This is known as the Zel'dovich-von Neumann-Doering (ZND) problem.

CHAPTER 2

BACKGROUND

In order to acquire a better understanding of the work presented, some background in the field of detonation is necessary. The main purpose of this chapter is to provide a résumé of the requisite information from this field. First, the two-dimensional Euler equations governing the model problem are presented. Next, a description of the relevant HE materials and the pertinent chemistry is given. Some essential characteristics of the ZND solution are then given to introduce the basic elements of detonation dynamics. This is followed by a discussion of two-dimensional detonation. Of particular interest are edge effects and their influence as a perturbation on the one-dimensional solution. The state-of-the art asymptotic and empirical results are presented.

Lastly, much of the theoretical development presented relies heavily on tensor notation. Briefly, standard curvilinear representations of tensors are reviewed and the notation adopted is given. This is then extended to tensor representation according to time-dependent coordinates in preparation for development of the shock-fitting formulation of Eqs. (2.1). While it may at first appear verbose to couch the shock-fitting development in terms of contra-covariant components, such notation makes explicit the precise form of the transformed equations in coordinates which are intrinsic to coordinates of choice. The general nature of the

development allows for direct application to complicated, time-dependent geometries.

2.1 Governing equations

The governing equations of the detonation model problem are the two-dimensional Euler equations with reaction. In conservation form, these are given by

$$\frac{\partial \rho}{\partial t} + \frac{\partial}{\partial x}(\rho u) + \frac{\partial}{\partial y}(\rho v) = 0, \tag{2.1a}$$

$$\frac{\partial}{\partial t}(\rho u) + \frac{\partial}{\partial x}(\rho u^2 + p) + \frac{\partial}{\partial y}(\rho uv + p) = 0, \tag{2.1b}$$

$$\frac{\partial}{\partial t}(\rho v) + \frac{\partial}{\partial x}(\rho vu + p) + \frac{\partial}{\partial y}(\rho v^2 + p) = 0, \tag{2.1c}$$

$$\begin{aligned} \frac{\partial}{\partial t}\left(\rho\left(e + \frac{1}{2}(u^2+v^2)\right)\right) + \frac{\partial}{\partial x}\left(\rho u\left(e + \frac{1}{2}(u^2+v^2) + \frac{p}{\rho}\right)\right) + \\ \frac{\partial}{\partial y}\left(\rho v\left(e + \frac{1}{2}(u^2+v^2) + \frac{p}{\rho}\right)\right) = 0, \end{aligned} \tag{2.1d}$$

$$\frac{\partial}{\partial t}(\rho Y_{(i)}) + \frac{\partial}{\partial x}\left(\rho Y_{(i)} u\right) + \frac{\partial}{\partial y}\left(\rho Y_{(i)} v\right) = M_{(i)}\dot{\omega}_{(i)}, \tag{2.1e}$$

where x and y are Cartesian coordinates, u and v are the respective velocities in each direction, e is the internal energy, ρ is the density, p is the pressure, and $Y_{(i)}$, $M_{(i)}$ and $\dot{\omega}_{(i)}$ are the mass fraction, the molecular mass, and the rate of species production for the i^{th} species. These equations are hyperbolic and may admit shock solutions.

In order to acquire a better understanding of the work presented, some background in the field of detonation is necessary. The purpose of this section is to provide a résumé of the requisite information from this field. First, a description of the relevant HE materials and the pertinent chemistry is given. Next, some

essential characteristics of the ZND solution will be covered as an introduction to the basic elements of detonation dynamics. This is followed by a discussion of two-dimensional detonation. Of particular interest are edge effects and their influence as a perturbation on the one-dimensional solution. The state-of-the art asymptotic and empirical results are presented.

Lastly, much of the theoretical development presented relies heavily on tensor notation. Briefly, standard curvilinear representations of tensors are reviewed and the notation adopted is given. This is then extended to tensor representation according to time-dependent coordinates in preparation for development of the shock-fitting formulation of Eqs. (2.1). While it may at first appear verbose to couch the shock-fitting development in terms of contra-covariant components, such notation makes explicit the precise form of the transformed equations in coordinates which are intrinsic to coordinates of choice. The general nature of the development allows for direct application to complicated, time-dependent geometries.

2.2 High explosive materials

A detonation is defined here as shock induced combustion process in which some or all of the energy required to support the shock is provided by exothermic energy release. A high explosive material is one with the physical capacity to detonate; most HE materials are solids. In order to clarify the relevant characteristics of a material which make it a high explosive, it is helpful to contrast detonations with inert physical explosions and with other combustion processes.

First, not all physical explosions are detonations. For example, a pressurized vessel filled with water can by made to explode by heating. In such mechanical

explosions, the energy required to rupture the confining vessel is wholly supplied from outside the system, and the material, in this case H_2O, remains chemically unaltered. A detonation, however, relies on the rapid release of internally stored chemical energy to generate the same effect.

In such exothermic oxidation-reduction reactions, some of the chemical bond energy in the fuel and oxidizer reactants is liberated as products are formed. Such a reaction occurs at an appreciable rate when the temperature threshold of the material is crossed, initiating significant conversion of chemical energy to thermal energy in a small layer of the bulk material known as the reaction zone. In a combustion process, the propagation of this reaction zone through the bulk of the material is self sustaining.

Second, not all combustion processes are detonations. The physical mechanism by which the required temperature is achieved differentiates detonation from other types of burning. Deflagration is a combustion process in which the reaction propagates through the fuel due to diffusion of heat from a flame front. A candle flame is a typical example of this type of combustion. Detonation, on the other hand, depends on a shock wave to raise the material to an elevated temperature which induces fast reaction and is exceedingly violent and fast: "the reaction is so rapid that the expansion, spreading in a wave propagating at the local speed of sound, is not fast enough to reduce the pressure appreciably, and the reaction is inertially confined by the explosive mass [17, pg. 1]."

Most HE compounds differ from other combustible materials in that both the oxidizer and fuel coexist in the same molecule. The initiating shock wave imparts enough energy to break the molecular bonds between the fuel and oxidizer radicals. Thus, mixing of fuel and oxidizer to achieve an appropriate oxygen balance is

instantaneous, allowing the reaction to occur fast enough to support the shock wave. The temporal analogue of the eigenvalue analysis performed in Ref. [18] reveals that the fastest time scales present in current state-of-the-art reaction kinetics schemes for HE materials are on the order of 10^{-11} seconds; slower time scales on the order of 10^{-4} seconds are also present.

Molecular diagrams of the HE materials considered are shown in Fig. 2.1. Trinitrotoluene (TNT) and triaminotrinitrobenzene (TATB) are known as nitroarenes due to the $C - NO_2$ bonds around the exterior of the central ring. Cyclotrimethylenetrinitramine (RDX) and Cyclotrimethylenetrinitramine (HMX) are nitramine compounds characterized by the exterior $N - NO_2$ bonds. The performance of these HE compounds is characterized by a number of chemical, physical, and explosive properties including the detonation velocity, the packing density, detonation pressure, and the heat of decomposition. These values for the selected materials can be found in [17, pp. 34-35] and are given in Table 2.1.

Depending on the properties of a particular HE, a number of manufacturing techniques are available to form explosive charges of the desired size and shape. TNT, with a melting point of 81^oC, is often heated and then pressed or casted into the desired shape. TATB, RDX, and HMX have considerably higher melting points: 448^oC, 204^oC, 285^oC, respectively. These materials are usually mixed with a wax or polymeric binder to create a more pliant material before machining. Composition A (Comp A) is one such mixture composed of RDX and wax. Another such material is Composition B (Comp B), a castable composite HE consisting of RDX, TNT, and wax. Plastic-Bonded eXplosives (PBX) are another commonly used class of composites consisting of RDX or HMX and a polymer binder such as KelF 800 (polychlorotrifluroethylene).

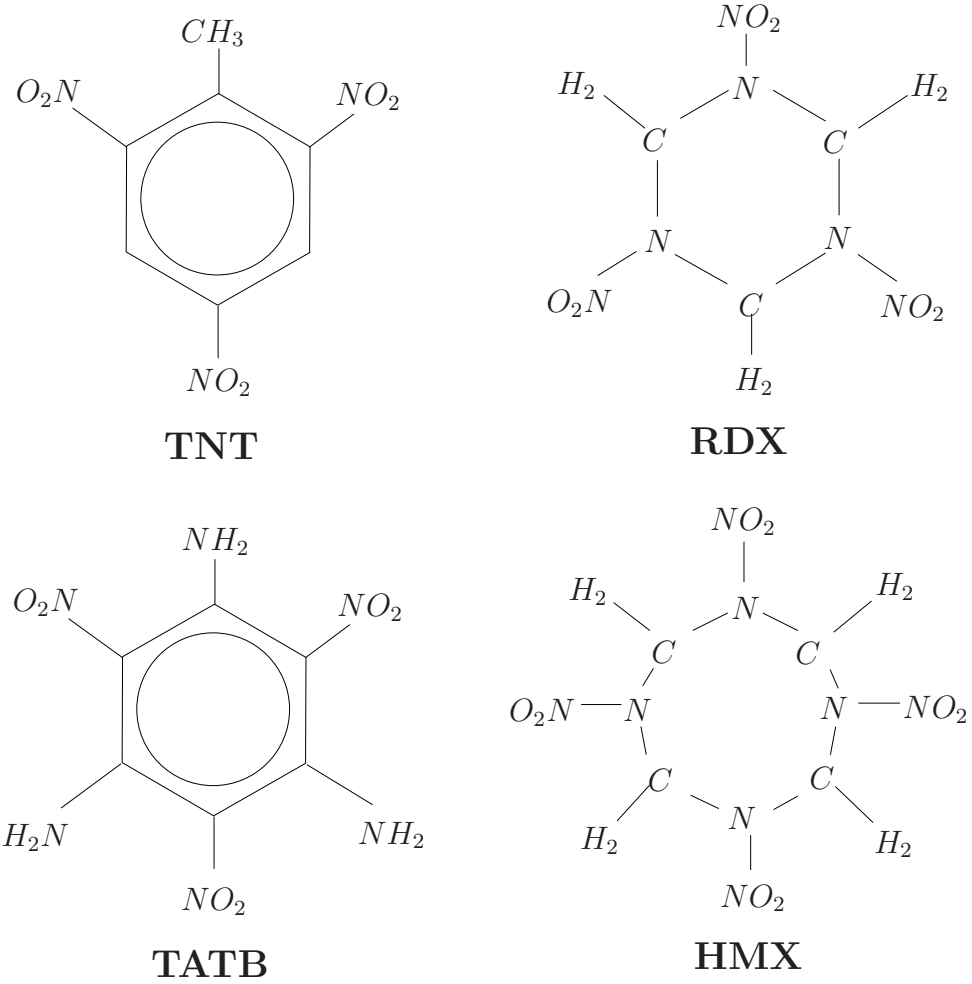

Figure 2.1. HE molecules.

TABLE 2.1

HE MATERIAL PROPERTIES

	Detonation velocity (m/s)	Density (g/cm^3)	Detonation pressure (GPa)	Heat of Decomposition (cal/g)
TNT	7045	1.62	18.9	300
TATB	7660	1.847	25.9	600
RDX	8639	1.767	33.79	500
HMX	9110	1.89	39.5	500

2.3 One-dimensional detonation

Theoretical study of detonation became feasible with the advent of the ZND structure solution in the early 1940's. The classic approach to this problem is outlined by Fickett and Davis [19]. The ZND model postulates that the physical mechanisms dominating a detonation are pressure-driven waves and reaction; body forces, radiation, heat conduction, viscosity, and species diffusion may by neglected. Thus, the one-dimensional Euler equations with reaction are chosen to simplify the mathematics while still allowing shocks to propagate through the material. This model also assumes the HE material to be composed of a calorically perfect ideal gas mixture. Initially, the HE consists entirely of a single reactant species which undergoes a unimolecular reaction initiated by a shock wave to yield a single product species.

With these assumptions, solutions to the ZND problem give the most basic structure expected in a one-dimensional reaction zone; other classes of behavior

observable by addition of mass diffusion or of chemical species are omitted.

At the shock surface, there is an immediate jump in pressure, density, velocity, and temperature. Reaction initiates suddenly at the shock giving a discontinuity in derivative of the reaction rate; there is no jump in the species mass fractions across the shock. After a brief induction time, the reaction rate experiences an sharp spike causing a large release of thermal energy. This is accompanied by a decrease in kinetic energy, pressure, and density. Reaction finally terminates at a sonic point where the wave frame material velocity is equal to the local frozen sound speed.

A study of the forward characteristics reveals that the reaction supplies energy to the shock front so as to continue propagation of the shock wave into the unreacted HE. In particular, a unique solution is found to describe a self-propagating detonation wave which requires no external support. This solution is of primary importance and is known in the literature as the Chapman–Jouguet (CJ) solution. The associated detonation speed, denoted as D_{cj}, is the characteristic by which most HE materials are classified (see Table 2.1).

Other important characteristics exhibited by the ZND solution are given in Appendix H. First, the detonation velocity is seen to depend on the initial density of the unreacted HE; this behavior is shown for a calorically perfect ideal gas in Appendix H. Second, as the amount of chemical energy between products and reactants increase, D_{cj} also increases. Furthermore, the detonation velocity, as well as the solutions attainable in the $(1/\rho, p)$ phase space, are independent of the reaction rate law.

Because the two-dimensional model problem behaves as a quasi–one-dimensional steady detonation wave subject to edge effects, many of these results provide an

intuitive understanding of the expected two–dimensional behavior. In fact, the observed one-dimensional solution structure would be exhibited by the proposed model problem if the HE layer width were infinite.

2.4 Two-dimensional detonation

2.4.1 Diameter effect

Empirical data compiled in Ref. [19] qualitatively confirm much of the theoretical results gathered from simple ZND analysis. In particular, the detonation velocity observed depends on initial explosive density and the amount of energy release. Empirically, D_{cj} is seen to increase linearly with the initial density for solid HE material [17]; unfortunately, this trend is incorrectly predicted by the classic ZND solution due to its use of a calorically perfect ideal gas equation of state. The steady detonation speed is seen to be independent of the reaction rate in the limit of an infinite medium. Furthermore, there is a additional dependency on shock wave curvature and on the type of confinement used [20, 21].

Because the geometry of the proposed problem involves interfaces between layers of high explosive and confiner, it is necessary to develop an understanding of how the shock behaves across these interfaces. As a first approximation of this behavior, it is useful to consider the motion of a detonation wave in an HE layer which experiences weak confinement on two sides, as seen in Fig. 1.1. Of particular interest is the detonation speed as a function of the HE layer width.

This behavior is described by Campbell and Engelke [22] who measured steady detonation speeds in rate sticks of different diameters for a variety of high explosives. Curve fitting reveals that a non-dimensional detonation speed is inversely

proportional to the radius and is given by

$$\frac{D}{D_{cj}} = 1 - \frac{A}{r - r_c}, \tag{2.2}$$

where D is the steady detonation speed, r is the stick radius, r_c is a critical radius length scale, and A is a length parameter. Some selected examples are shown in Fig. 2.2.

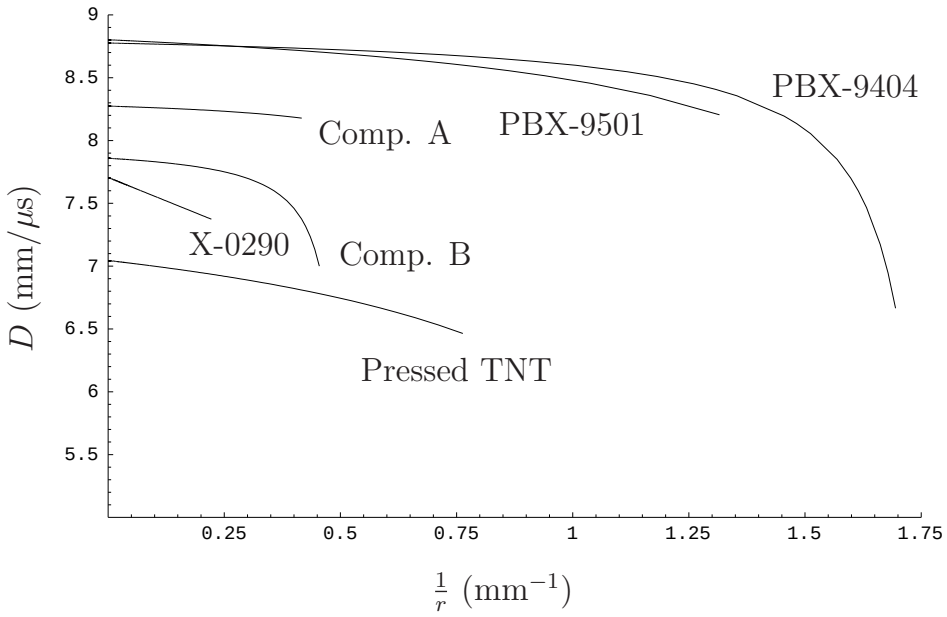

Figure 2.2. Illustration of the diameter effect for weakly confined rate sticks.

The samples of Comp A tested consisted of 92% RDX and 8% wax by weight. The Comp B samples were 36% TNT, 63% RDX, and 1% wax. The PBX-9501

samples were 95% HMX and 5% polymer. The PBX-9404 samples consisted of 94% HMX and 6% polymer. The X-0290 samples consisted of 95% TATB and 5% KelF 800 [22, pg. 647].

These results illustrate the loss of detonation speed due to the presence of edges. More precisely, as the radius decreases, the losses due to axial flow divergence increase. This is due to a non-traditional boundary layer effect at the rate stick's edge which allows for radial flow. As the distance between edges across a diameter of the rate stick decreases, this boundary layer affects a larger fractionof the flow causing appreciable decreases in the detonation velocity until a failure radius is reached. This phenomenon is know as the diameter effect.

Much can be learned from examination of Fig. 2.2. First, the slope of each curve near the limit of infinite diameter gives a measure of the reaction zone thickness. An infinitely thin reaction zone would experience no change in shock speed as the radius becomes finite. As the thickness of the reaction zone increases, edge effects will be more pronounced and cause a steeper negative slope in the neighborhood of an infinite diameter. Furthermore, the total loss in detonation velocity as measured between an infinite radius and the failure radius is known as the "velocity deficit" and is a measure of the sensitivity of the reaction rate to the local state. Thus, contrary to the ZND analysis, two-dimensional edge effects appear to introduce a rate law dependency on the detonation velocity.

Of particular interest is the behavior of X-0290. This explosive exhibits characteristics similar to PBX-9502 which is the explosive of interest. Notice an almost linear relationship between the detonation velocity and the reciprocal of the radius. This behavior continues until the critical radius is reached and detonation can no longer be sustained. Thus, it is reasonable to assume that the reaction

zone thickness is almost independent of the edge effects.

2.4.2 Asymptotic results

The first rigorous theoretical explanation of edge effects was given by Wood and Kirkwood [23]. By assuming that the radius of curvature describing the shock front is large in comparison with the reaction zone length, they determined that the non-dimensional detonation velocity was given by

$$\frac{D}{D_{cj}} = 1 - \beta \frac{z^*}{\hat{S}} + O\left(\left(\frac{z^*}{\hat{S}}\right)^2\right), \tag{2.3}$$

where z^* is the reaction zone length, $\hat{S}$ is the central radius of curvature of the shock, and β is a constant. Comparison of Eqs. (2.2) and (2.3) suggests that the ratio of the shock's radius of curvature to the reaction zone length is proportionate to the HE layer width.

A detailed development and correction to this theoretical explanation of the diameter effect was made by Bdzil [20]. The governing partial differential equations are derived by assuming that the two-dimensional Euler equations with reaction describe the dominate physics in the flow. A rate law is proposed which is a function of the thermodynamic state and the non-dimensional shock speed. The fluid is considered to be polytropic. The resulting analysis reveals a mixed hyperbolic/elliptic problem which is solved according to boundary conditions which model confinement on two opposing sides of the domain.

Through a perturbation expansion which includes non-linear terms, Bdzil shows that the non-dimensional detonation velocity in a dense high explosive is

actually described by

$$\frac{D}{D_{cj}} \propto \frac{1}{r^2}$$

and that Eq. (2.3) is the result of a linearized approximation in the velocity deficit limit. Furthermore, for the case of heavy confinement where the small shock slope approximation is valid, the solution is given by a small correction to the ZND structure solution.

A good mathematical description of such near-Chapman-Jouguet solutions is given by Stewart [24]. By formulation of the governing Euler equations with reaction in Bertrand (shock-attached) coordinates and again assuming that the small shock slope approximation holds, a relationship between the non-dimensional shock speed and the radius of curvature is found. This is known in the literature as the D_n - κ relation and is given by

$$\frac{D_n}{D_{cj}} = 1 - \frac{\alpha(\kappa)}{D_{cj}},$$

where κ is the shock curvature and α is a function parametrized by the material properties of the explosive.

These asymptotic methods reveal a rate law dependence on the detonation velocity at steady state. This agrees with the experimentally observed diameter effect.

2.4.3 Shock polar results

The behavior of the shock at the confiner-HE interface is modeled using shock polar analysis and is discussed by Aslam *et al.* [16, 25]. This analysis is used to provide boundary conditions for certain asymptotic solutions as well as solutions

for comparison with numerical and experimental results. An introduction to the topic can be found in [26]. Shock polar analysis examines the streamline deflection caused by the introduction of an oblique shock wave into the flow. A thorough development of the shock polar equations can be found in Appendix G.7.

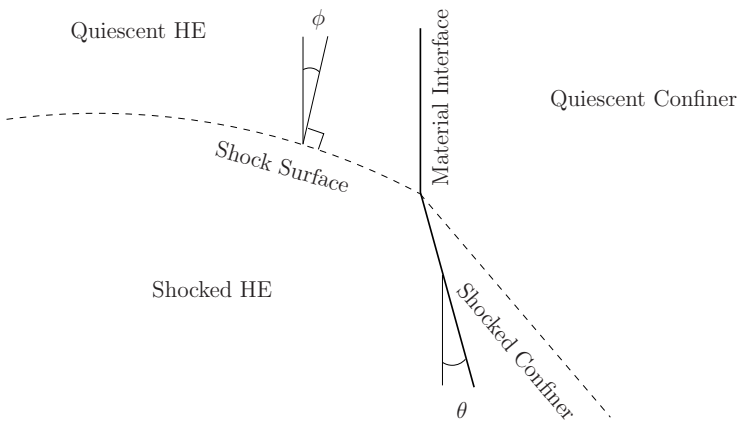

Figure 2.3. Shock polar analysis schematic.

Essentially, the shock polar equations are the Rankine–Hugoniot jump conditions across an oblique shock. A schematic of the shock polar as it applies to geometry encountered at the material interface is shown in Fig. 2.3. The shock deflection angle is ϕ and the streamline deflection angle is θ. Note that in the case of steady flow, the material interface is a streamline along which the deflection is the same for both the inert confiner and the HE. Furthermore, the pressures in both media must match since the material interface is a contact discontinuity. Thus, an overlaying of the shock polars for both the inert and HE materials in the

case of strong confinement will match at a single point giving the streamline deflection, the shock deflection, and the pressure at the intersection of the material interface and the shock locus.

2.4.4 Experimental results

The current state-of-the-art experimental data is the result of ongoing research at Los Alamos National Laboratory. In Ref. [16], Aslam *et al.* compare experimental results to those expected from perturbation theory. Unfortunately, this comparison highlights an unacceptable disagreement between theory and experiment in the behavior predicted near the shock. Fig. 2.4 is a reproduction of Figure 6 from Ref. [16] and gives some qualitative understanding of the results to date.

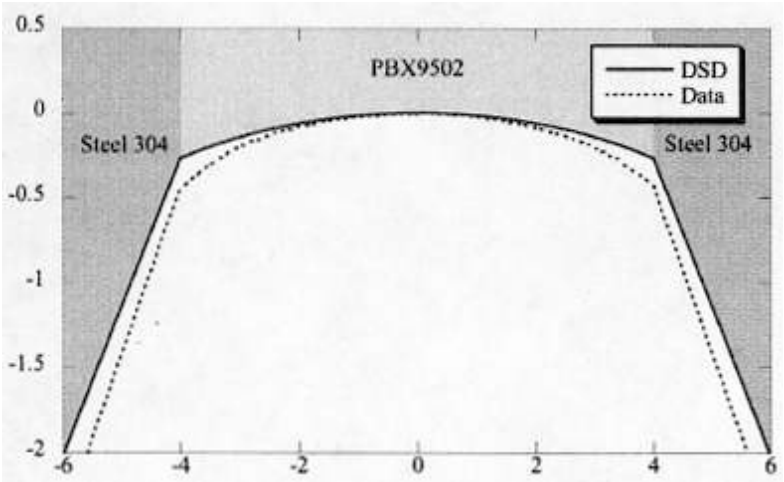

Figure 2.4. DSD and empirical results for a typical sandwich test experiment.

Of particular interest is the region surrounding the intersection of the shock locus and the material interface. Boundary conditions for the DSD theory results are obtained from shock polar analysis. The illustrated discrepancy is characteristic of the results to date and is a serious impediment to correctly predicting the behavior of such detonation phenomena with the accuracy required for many applications. Thus a numerical solution is sought which can accurately predict the observed behavior.

2.5 Standard tensors

A tensor is a single mathematical entity describing a physical property which may have different representations depending on the coordinates chosen. An excellent introduction to standard curvilinear tensors is given by Aris [27]. His adaptation of Einstein notation has been employed as much as possible with some necessary additions. Only transformations which are differentiable, with continuous second partial derivatives, invertible, and single valued are considered in this work [28, pg. 206].

Tensor notation unites the different representations of a tensor through one universal transformation rule:

$$A^i_j = \frac{\partial \bar{x}^i}{\partial x^m} \frac{\partial x^n}{\partial \bar{x}^j} A^m_n, \tag{2.4}$$

where A^i_j is representation of a tensor $\mathbf{A}$ in the x^i coordinates and $\bar{A}^i_j$ is its representation in the $\bar{x}^i$ coordinates. Superscripts denote contravariant indices, and subscripts denote covariant indices [27]. If each of the indices of a quantity transform according to Eq. (2.4), then that quantity is defined to be a tensor.

Because the laws of fluid mechanics are mathematically formulated in Carte-

sian coordinates, such a representation is the most fundamental for tensor calculus. For this reason, the Cartesian representation of a tensor is denoted by a special script. For example,

$$\mathcal{A}^i = \frac{\partial y^i}{\partial x^j} A^j,$$

where $\mathcal{A}^i$ is the Cartesian representation of the tensor $\mathbf{A}$. For consistency, the Cartesian coordinates are given in the same script: $\mathcal{y}^i$.

In general, bold script denotes a hidden dimensionality to the quantity:

$$A^{\cdots i}_{\cdots} = \boldsymbol{\mathcal{A}}^i,$$

where $\mathbf{A}$ is of arbitrary order and the index i has been explicitly denoted. In general, neither all nor part of a quantity denoted in boldface need be tensorial; explicit non-tensorial indices are surrounded in parentheses. In general, the tensorial character of boldface quantity is known from the context. For cases when $\mathbf{A}$ is a tensor, the transformation tensor $\mathbf{R}$ is defined such that

$$\boldsymbol{\mathcal{A}} = \mathbf{A} \cdot \mathbf{R}, \tag{2.5}$$

where $\cdot$ denotes the appropriate tensor product.

One should note that although a position vector is not a curvilinear tensor, indices on coordinates are not surrounded in parentheses for brevity. The contravariant and covariant basis vectors are denoted

$$\boldsymbol{\mathcal{g}}_{(i)} = \frac{\partial \boldsymbol{\mathcal{y}}}{\partial x^i} \qquad \text{and} \qquad \boldsymbol{\mathcal{g}}^{(i)} = \frac{\partial x^i}{\partial \boldsymbol{\mathcal{y}}}, \tag{2.6}$$

where $\boldsymbol{\mathcal{y}}$ is the Cartesian position vector. Equation (2.6) define the contravariant

and covariant bases to be reciprocal such that $\boldsymbol{g}^{(i)} \cdot \boldsymbol{g}_{(j)} = \delta^i_j$. The dot product of a basis vector and its reciprocal can be written as

$$\boldsymbol{g}^{(i)} \cdot \boldsymbol{g}_{(i)} = \left|\boldsymbol{g}^{(i)}\right| \left|\boldsymbol{g}_{(i)}\right| \cos\alpha = 1, \qquad \text{(no sum on } i\text{)} \tag{2.7}$$

indices where α is the angle between the basis vector and its reciprocal. The metric tensor and its conjugate are given as

$$g_{ij} = \frac{\partial \boldsymbol{y}}{\partial x^i} \cdot \frac{\partial \boldsymbol{y}}{\partial x^j}, \tag{2.8a}$$

$$g^{ij} = \frac{\partial x^i}{\partial \boldsymbol{y}} \cdot \frac{\partial x^j}{\partial \boldsymbol{y}}. \tag{2.8b}$$

The determinant of the metric tensor is denoted g such that $\sqrt{g} = \left|\frac{\partial \boldsymbol{y}}{\partial \mathbf{x}}\right|$ is the Jacobian of the transformation.

The corresponding normalized bases, $\boldsymbol{e}^{(i)} = \frac{\boldsymbol{g}^{(i)}}{\left|\boldsymbol{g}^{(i)}\right|}$, are known as "physical bases" and may be written

$$\boldsymbol{e}_{(i)} = \frac{\boldsymbol{g}_{(i)}}{\left|\boldsymbol{g}_{(i)}\right|} \qquad \text{or} \qquad \boldsymbol{e}_{(i)} = \frac{\frac{\partial \boldsymbol{y}}{\partial x^i}}{\sqrt{g_{ii}}}, \tag{2.9a}$$

$$\boldsymbol{e}^{(i)} = \frac{\boldsymbol{g}^{(i)}}{\left|\boldsymbol{g}^{(i)}\right|} \qquad \text{or} \qquad \boldsymbol{e}^{(i)} = \frac{\frac{\partial x^i}{\partial \boldsymbol{y}}}{\sqrt{g^{ii}}}. \tag{2.9b}$$

The corresponding "physical components" of a first order tensor are denoted by a parenthetical non-scripted index:

$$\boldsymbol{a} = a_{(\mathrm{i})}\ \boldsymbol{e}_{(i)} = {}_{(\mathrm{i})}a\ , \qquad \text{(sum on } i\text{)} \tag{2.9c}$$

$$\boldsymbol{A} = A(i)\ \boldsymbol{e}^{(i)} = (i)A\ \boldsymbol{e}^{(i)}. \qquad \text{(sum on } i\text{)} \tag{2.9d}$$

Most operations on or between tensors yield a new tensor expression; this, how-

ever, is not true for differentiation due to the variation of Jacobian matrix over space. To restore its tensorial character, tensor calculus defines tensorial derivatives such that in Cartesian coordinates one is computing standard derivatives [28, pp. 212-213]. Thus, a mathematical expression involving tensor quantities and partial derivatives will only yield a tensorial expression if the coordinates are taken to be Cartesian. In such an expression, one may employ tensor notion directly.

The covariant derivative reduces to a simple partial derivative in Cartesian coordinates and is defined for a first order contravariant tensor as

$$A^i_{,j} = \frac{\partial A^i}{\partial x^j} + A^k \left\{ {}_k{}^i{}_j \right\}, \tag{2.10}$$

where

$$\left\{ {}_j{}^i{}_k \right\} = \frac{\partial^2 Y^n}{\partial x^j \partial x^k} \frac{\partial x^i}{\partial Y^n} \tag{2.11}$$

are Christoffel symbols of the second kind [27, pg. 166]. The additional covariant index arising from the partial derivative is indicated by a comma subscript. A generalization of covariant differentiation for higher order mixed tensors is given by Aris [27, pg. 168].

Two different tensorial time derivatives are important for standard tensor formulations, neither of which increase a tensor's order. The first is $\frac{\partial}{\partial t}$, which is simply the partial derivative with respect to time keeping the Cartesian spatial coordinates constant. The second is the intrinsic derivative, denoted $\frac{\delta}{\delta t}$, which gives the total change of a tensor along a path parametrized by t. It is identical

to $\frac{d}{dt}$ in Cartesian coordinates. For a first order contravariant tensor,

$$\frac{\delta A^k}{\delta t} = \frac{\partial A^k}{\partial t} + A^k_{,j}\frac{dx^j}{dt}. \tag{2.12}$$

Only in the case that t is parametrized to follow a material particle does Eq. (2.12) give the material derivative.

2.6 Tensors in time-dependent coordinates

Consider a general transformation between Cartesian coordinates $\{y^i, \tau\}$ and time-dependent curvilinear coordinates $\{x^i, t\}$ such that

$$y^i = y^i(x^i, t) \qquad \text{and} \qquad \tau = t \tag{2.13a}$$

$$x^i = x^i(y^i, \tau) \qquad \text{and} \qquad t = \tau. \tag{2.13b}$$

As in Section 2.5, only transformations which are differentiable, with continuous second partial derivatives, invertible, and single valued are considered in this work [27, pg. 77]. Note also that the time coordinate is defined to be independent of space.

Practically, tensors represented according to Eqs. (2.13) still transform in space according to the normal transformation rule; however, that transformation rule is now a function of time:

$$A^i = \underbrace{\frac{\partial y^i}{\partial x^j}}_{=f(\tau)} A^j.$$

The metric tensor and its determinant are now also functions of time. Furthermore, since time coordinates are independent of the spatial coordinates from Eq. (2.13), covariant differentiation with respect to spatial coordinates is un-

changed from that for standard tensors.

2.6.1 Grid kinematics

Consider the transformation of the time derivative

$$\frac{\partial}{\partial t} = \frac{\partial}{\partial \tau} + \frac{\partial}{\partial Y^j}\frac{\partial Y^j}{\partial t}. \tag{2.14}$$

Application of Eq. (2.14) to x^i gives

$$\underbrace{\frac{\partial x^i}{\partial t}}_{=0} = \frac{\partial x^i}{\partial \tau} + \frac{\partial x^i}{\partial Y^j}\frac{\partial Y^j}{\partial t}, \tag{2.15}$$

since the $\{x^i, t\}$ are independent. Since $\frac{\partial}{\partial t}$ is the derivative with respect to time keeping the shock coordinates constant, $\frac{\partial Y^i}{\partial t}$ gives the motion of the moving coordinates in the Cartesian frame. Conversely, $\frac{\partial x^i}{\partial \tau}$ gives the motion of the Cartesian coordinates relative to the shock-attached frame.

This relative "velocity" of the coordinates themselves is denoted [29]

$$U^{(i)} = \frac{\partial Y^i}{\partial t} \tag{2.16a}$$

and

$$U^{(i)} = -\frac{\partial x^i}{\partial \tau}, \tag{2.16b}$$

where the negative sign is necessary to account for the coordinate motion relative to the curvilinear frame being in the opposite direction. Equation (2.15) can now

be rearranged as a transformation rule:

$$-\frac{\partial x^i}{\partial t} = \frac{\partial x^i}{\partial Y^j}\frac{\partial Y^j}{\partial t} \qquad \text{or} \tag{2.17a}$$

$$U^{(i)} = \frac{\partial x^i}{\partial Y^j} U^{(j)}, \tag{2.17b}$$

relating $\mathbf{U}$ in the Cartesian and shock-attached coordinates. Although Eq. (2.17b) appears to identify $\mathbf{U}$ as a curvilinear tensor, it is not. Rather, the grid velocity is only an artifact of the coordinates chosen, and $\bar{U}^{(i)} \neq \frac{\partial \bar{x}^i}{\partial x^j} U^{(j)}$ in general. Only in the case of transforming between the Cartesian and curvilinear coordinates may the index be treated as tensorial, obeying Eq. (2.17b). Therefore, the indices in Eq. (2.17b) are enclosed in parentheses to denote their non-tensorial character.

Equation (2.17b) can also be written using Eqs. (2.6) and (2.9) as

$$U^{(i)} = \boldsymbol{g}^{(i)} \cdot \boldsymbol{U}, \tag{2.18a}$$

$$= \left|\boldsymbol{g}^{(i)}\right| \boldsymbol{e}^{(i)} \cdot \boldsymbol{U} \qquad \text{(no sum on } i\text{)}, \tag{2.18b}$$

$$x = \sqrt{g^{ii}}\, \boldsymbol{e}^{(i)} \cdot \boldsymbol{U}. \tag{2.18c}$$

With Eq. (2.7), Eq. (2.18b) can then be rewritten as

$$\begin{aligned} U^{(i)} &= \frac{1}{\left|\boldsymbol{g}_{(i)}\right| \cos\alpha} \boldsymbol{e}^{(i)} \cdot \boldsymbol{U}, \qquad \text{(no sum on } i\text{)} \\ &= \frac{1}{\sqrt{g_{ii}} \cos\alpha} \boldsymbol{e}^{(i)} \cdot \boldsymbol{U}, \end{aligned}$$

or

$$U(i) = \frac{1}{\cos\alpha} \boldsymbol{e}^{(i)} \cdot \boldsymbol{U}, \tag{2.19}$$

where $U(i)$ are the physical components of $\mathbf{U}$ in the x^i system. Note that the potential non-orthogonality of the shock-attached basis is taken into account by the effect of α in Eq. (2.19).

2.6.2 The total time derivative and velocities

As mentioned in Section 2.5, it is necessary to consider a specific parametrization in order to calculate a total time derivative (*cf.* Eq. (2.12)). In other words, the operator $\frac{d}{dt}$ is not well defined until the path $x^i(t)$ along which it is being computed is given explicitly. In order to make such a parametrization explicit for the entire coordinate field, it is expedient to define it according to yet another coordinate transformation.

Consider a transformation of the form

$$x^i = x^i(\bar{x}^j, \bar{t}) \qquad \text{and} \qquad t = \bar{t}, \tag{2.20}$$

subject to the restriction of a non-vanishing Jacobian [27, pg. 77], the transformation is restricted to have a non-vanishing Jacobian Such a transformation is practically chosen so that each equation

$$\bar{\mathbf{x}} \equiv \text{constant}$$

picks out a moving particle of interest (*e.g.* a material or shock surface particle). Thus, holding $\mathbf{x}$ constant in Eq. (2.20) gives $x^i = x^i(\bar{t}) = x^i(t)$, which is the desired parametrized path in the x^i coordinates of the selected particle. Thus, the single system of Eqs. (2.20) provides the desired parametrization for the entire domain.

The operator $\frac{d}{dt}$ can now be defined as $\frac{d}{dt} \equiv \frac{\partial}{\partial \bar{t}}$, which is simply partial differentiation holding $\bar{x}^k$ constant. In Cartesian coordinates, the chain rule gives

$$\frac{d}{dt} \equiv \frac{\partial}{\partial \bar{t}} = \frac{\partial}{\partial t} + \frac{\partial Y^k}{\partial \bar{t}} \frac{\partial}{\partial Y^k} \tag{2.21a}$$

$$= \frac{\partial}{\partial t} + \frac{dY^k}{dt} \frac{\partial}{\partial Y^k}. \tag{2.21b}$$

For the general time dependent coordinates Eq. (2.13), the same operator is written

$$\frac{d}{dt} \equiv \frac{\partial}{\partial \bar{t}} = \frac{\partial}{\partial t} + \frac{\partial x^k}{\partial \bar{t}} \frac{\partial}{\partial x^k} \tag{2.22a}$$

$$= \frac{\partial}{\partial t} + \frac{dx^k}{dt} \frac{\partial}{\partial x^k}. \tag{2.22b}$$

Just as in the analysis of standard tensors, the presence of the partial derivatives with respect to space is enough to render the $\frac{d}{dt}$ operator to be non-tensorial.

While Eqs. (2.21b) and (2.22b) mathematically define the total derivative operator, its physical meaning remains unrestricted. Only after Eqs. (2.20) have been defined in a physical manner can a physical interpretation of the total derivative operator be given. Practically, the system Eqs. (2.20) is defined in terms of a desired control volume whose boundaries have a particular physical meaning: usually a material or shock surface. For this reason, the transformation Eqs. (2.20) is termed "volumetric" where the convention is adopted that such coordinates are always denoted by a bar.

Applying Eq. (2.21b) to a general set of curvilinear coordinates gives the vol-

umetric velocity

$$\begin{aligned}\frac{dx^i}{dt} &= \frac{\partial x^i}{\partial t} + \frac{\partial x^i}{\partial Y^j}\frac{dY^j}{dt}, \\ &= -U^{(i)} + \frac{\partial x^i}{\partial Y^j} w^j, \qquad (2.23a) \\ &= -U^{(i)} + w^i, \qquad (2.23b)\end{aligned}$$

where

$$w^i = \frac{\partial x^i}{\partial Y^j} w^j \qquad (2.23c)$$

is the velocity as measured in the Cartesian coordinates. In general, velocities measured in arbitrary moving coordinates do not transform according to the transformation rule and are not tensors; however, Eq. (2.23c) shows that the Cartesian velocity does remain a tensor.

Since velocities are measured with respect to Cartesian coordinates, their representation in the curvilinear frame is offset by the grid motion. Setting $\bar{x}^i$ to denote a material particle and

2.6.3 Tensorial time differentiation

As with the velocity field, certain quantities are no longer related to their Cartesian counterparts by the tensor transformation rule due to the time-variation of the spatial coordinates. Notably this is the case for derivatives with respect to

time. Consider

$$\begin{aligned}\frac{\partial A^i}{\partial \tau} &= \frac{\partial}{\partial \tau}\left(A^j \frac{\partial Y^i}{\partial x^j}\right) \\ &= \frac{\partial A^j}{\partial \tau}\frac{\partial Y^i}{\partial x^j} + A^j \frac{\partial}{\partial \tau}\left(\frac{\partial Y^i}{\partial x^j}\right),\end{aligned}$$

where $\frac{\partial}{\partial \tau} = \frac{\partial}{\partial t} + \frac{\partial}{\partial x^k}\frac{\partial x^k}{\partial \tau}$ gives

$$\begin{aligned}&= \left(\frac{\partial A^j}{\partial t} + \frac{\partial A^j}{\partial x^k}\frac{\partial x^k}{\partial \tau}\right)\frac{\partial Y^i}{\partial x^j} + A^j\left(\frac{\partial}{\partial t}\left(\frac{\partial Y^i}{\partial x^j}\right) + \frac{\partial}{\partial x^k}\left(\frac{\partial Y^i}{\partial x^j}\right)\frac{\partial x^k}{\partial \tau}\right) \\ &= \left(\frac{\partial A^j}{\partial t} + \frac{\partial A^j}{\partial x^k}\frac{\partial x^k}{\partial \tau} + A^n\frac{\partial x^j}{\partial Y^m}\left(\frac{\partial}{\partial t}\left(\frac{\partial Y^m}{\partial x^n}\right) + \frac{\partial}{\partial x^k}\left(\frac{\partial Y^m}{\partial x^n}\right)\frac{\partial x^k}{\partial \tau}\right)\right)\frac{\partial Y^i}{\partial x^j} \\ &= \left(\frac{\partial A^j}{\partial t} + A^n\frac{\partial^2 Y^m}{\partial x^n \partial t}\frac{\partial x^j}{\partial Y^m} + \left(\frac{\partial A^j}{\partial x^k} + A^n\frac{\partial^2 Y^m}{\partial x^n \partial x^k}\frac{\partial x^j}{\partial Y^m}\right)\frac{\partial x^k}{\partial \tau}\right)\frac{\partial Y^i}{\partial x^j}, \qquad (2.24)\end{aligned}$$

changing dummy indices as needed. Therefore, due to the time variation of the coordinates, an additional Christoffel symbol appears in Eq. (2.24) which is not present in the tensorial spatial derivatives. Allowing the the time coordinate to be denoted with an "0" index, it may be written as

$$\left\{ {}_n{}^j{}_0 \right\} = \frac{\partial^2 Y^m}{\partial x^n \partial x^0}\frac{\partial x^j}{\partial Y^m}. \qquad (2.25)$$

The temporal Christoffel symbol, Eq. (2.25), can be written in terms of the relative grid velocity given by Eqs. (2.16). Since $\frac{\partial y^i}{\partial x^0} = U^{(i)} = \frac{\partial y^i}{\partial x^k}U^{(k)}$, one may

write

$$\begin{aligned}
\left\{ {}_{n}{}^{j}{}_{0} \right\} &= \frac{\partial^2 Y^i}{\partial x^n \partial x^0} \frac{\partial x^j}{\partial Y^i} \\
&= \frac{\partial}{\partial x^n} \left(\frac{\partial Y^i}{\partial x^k} U^{(k)} \right) \frac{\partial x^j}{\partial Y^i} \\
&= \left(\frac{\partial Y^i}{\partial x^k} \frac{\partial}{\partial x^n} \left(U^{(k)} \right) + \frac{\partial^2 Y^i}{\partial x^n \partial x^k} U^{(k)} \right) \frac{\partial x^j}{\partial Y^i} \\
&= \frac{\partial}{\partial x^n} \left(U^{(j)} \right) + \frac{\partial^2 Y^i}{\partial x^n \partial x^k} \frac{\partial x^j}{\partial Y^i} U^{(k)} \\
&= U^{(j)}_{,n}. \qquad (2.26)
\end{aligned}$$

Substantially the same intuitive notation is used in Ref. [29].

In order to incorporate the extra terms of Eq. (2.24) into the tensor notation, one often uses 4-component vectors; however, a separate approach which keeps temporal differentiation distinct from spatial is also possible. Consider Eq. (2.24) *defining* the operator $A^i_{,0}$ as

$$A^j_{,0} = \frac{\partial A^j}{\partial x^0} + A^n \left\{ {}_{n}{}^{j}{}_{0} \right\} + A^j_{,k} \frac{\partial x^k}{\partial Y^0}, \qquad (2.27)$$

or using Eq. (2.26)

$$= \frac{\partial A^j}{\partial x^0} + A^n U^{(j)}_{,n} - A^j_{,k} U^{(k)}, \qquad (2.28)$$

where a subscript ", 0" is a separate tensorial operator for time differentiation of a contravariant vector. Equation (2.24) then becomes

$$\frac{\partial \mathbb{A}^j}{\partial t} = \mathbb{A}^i_{,0} = \frac{\partial Y^i}{\partial x^j} A^j_{,0} \qquad (2.29)$$

and is thus behaves like a tensor such that the fixed 0 index does not increase the order of the tensor.

The intrinsic derivative, given by Eq. (2.12) for standard tensors, can be written for time-dependent tensors. Again, it is defined to reduce to the total derivative in Cartesian coordinates:

$$\frac{\delta A^i}{\delta t} \equiv \frac{dA^i}{dt} = \frac{\partial A^i}{\partial t} + \frac{\partial A^i}{\partial y^j} w^j \tag{2.30}$$

$$\equiv \frac{\partial y^i}{\partial x^j} \frac{\delta A^j}{\delta t}. \tag{2.31}$$

With the volumetric velocities and the tensorial time derivative defined according to Eqs. (2.23) and (2.29), the intrinsic derivative is simply

$$\frac{\delta A^i}{\delta t} = A^i_{,0} + A^i_{,j} w^j. \tag{2.32}$$

Although Eq. (2.32) is fully tensorial, it is not yet well defined until the volumetric coordinates are specified.

CHAPTER 3

REYNOLDS' TRANSPORT THEOREM

The Reynolds' transport theorem refers to a purely mathematical expression describing the time rate of change of an integral over a time-dependent domain. By rooting this expression in the Cartesian coordinate system, a tensor equation results which has a very intuitive physical interpretation. Tensorially, this theorem results in an expression for the time rate of change of the integral of a tensor quantity enclosed within an arbitrary moving volume. Such a volume has its own velocity, independent of the tensor field it encloses, and may deform, changing its size and shape, as it evolves in time. Essentially, a simplified expression for

$$\frac{d}{dt}\int_{V(t)} \boldsymbol{A}\, dV \tag{3.1}$$

is sought, in which the differential and integral operators are interchanged. In Eq. (3.1), $\boldsymbol{A}$ and V denote a tensor of arbitrary order and the volume, respectively.

Reynolds' transport theorem is developed in a number of stages. First, the concept of volume is compared and contrasted with the simple scalar product of coordinate differentials. The special roles and relationship between the metric tensor and Jacobian are developed; the partial derivatives of the Jacobian are considered. Next, Leibniz's rule is given. This is followed by the derivation of Reynolds' transport theorem for a number of cases: the mathematical form, the

standard tensor form for fixed curvilinear coordinates, and finally the tensor form for time-dependent curvilinear coordinates. Both tensor forms are verified for first order contravariant tensor fields. Lastly, Reynolds' transport theorem is extended to include discontinuous tensor fields.

3.1 Volume as a scalar tensor

Before developing Reynolds' transport theorem, an understanding of volume and the corresponding notation should be clarified. Volume is a scalar tensor quantity; *volume is an invariant quantity.* This is a consequence of defining tensorial operations such that lengths and angles are invariants: their values being the same as those computed in Cartesian coordinates. Regardless of the curvilinear coordinate system chosen, the length of a vector and the angle between vectors does not change.

Unfortunately traditional modes of expression do not accurately express this fact. By speaking of transforming volumes from one coordinate system to another, the issue is obscured, and the notation reflects this: $dV \rightarrow dV$ where the two are not equal.

To illustrate this point, a differential volume is computed in a tensorial manner. Such a differential volume element can be thought of as the scalar triple product of three linearly independent differential vectors. If these differential vectors are chosen to be co-linear with the contravariant basis, then

$$d_{Y(i)} = \frac{\partial \boldsymbol{y}}{\partial x^i}\, dx^i,$$

where y^i denote Cartesian coordinates and x^i denote an arbitrary curvilinear coordinate system.

Forming the triple product gives the tensorial expression

$$\begin{aligned} dV &= d\boldsymbol{y}_{(1)} \cdot d\boldsymbol{y}_{(2)} \times d\boldsymbol{y}_{(3)} \\ &= \varepsilon_{ijk}\ d\boldsymbol{y}^i_{(1)} d\boldsymbol{y}^j_{(2)} d\boldsymbol{y}^k_{(3)}, \end{aligned} \tag{3.2}$$

where the alternating tensor ε_{ijk} is equivalent to the Levi-Civita symbol ϵ_{ijk} for Cartesian vectors:

$$\epsilon_{ijk} = \begin{cases} 0 & \text{for } i = j,\ j = k, \text{ or } k = 1, \\ +1 & \text{for } \{i, j, k\} \text{ cyclic}, \\ -1 & \text{for } \{i, j, k\} \text{ anti-cyclic}. \end{cases} \tag{3.3}$$

Substituting the definition of each differential vector gives

$$\begin{aligned} dV &= \epsilon_{ijk}\ \frac{\partial y^i}{\partial x^1} dx^1 \frac{\partial y^j}{\partial x^2} dx^2 \frac{\partial y^k}{\partial x^3} dx^3 \\ &= \epsilon_{ijk}\ \frac{\partial y^i}{\partial x^1} \frac{\partial y^j}{\partial x^2} \frac{\partial y^k}{\partial x^3} dx^1 dx^2 dx^3, \end{aligned}$$

where $\epsilon_{ijk}\ \frac{\partial y^i}{\partial x^1} \frac{\partial y^j}{\partial x^2} \frac{\partial y^k}{\partial x^3} = \left|\frac{\partial \boldsymbol{y}}{\partial \mathbf{x}}\right|$ by definition. Furthermore, $g = \left|\frac{\partial \boldsymbol{y}}{\partial \mathbf{x}}\right|^2$ is simply the determinant of the metric tensor for the x^i coordinates. Thus

$$dV = \sqrt{g}\, dx^1 dx^2 dx^3 \tag{3.4}$$

$$= \sqrt{g}\, dV, \tag{3.5}$$

where dV is the transformed differential "volume." Thus, such differential "volumes," $dV = dx^1 dx^2 dx^3$, are more appropriately called simple scalar products of differentials. Fortunately, dV is exactly the differential required to compute integrals in the curvilinear coordinate system.

Furthermore, the correct expression for dV in a curvilinear coordinate system involves the metric tensor determinant only. Even if dV is initially represented in the arbitrary coordinate system, $\bar{x}^i$, the Jacobian of interest for representing dV in $\hat{x}^i$ coordinates is $\sqrt{\hat{g}} = \left|\frac{\partial_V}{\partial \hat{x}}\right|$ and does not depend on the $\bar{x}^i$ coordinates. Forming dV from a scalar triple product in the $\bar{x}^i$ coordinates, as before, gives

$$\begin{aligned} dV &= \varepsilon_{ijk}\, d\bar{x}^i_{(1)} d\bar{x}^j_{(2)} d\bar{x}^k_{(3)} \\ &= \sqrt{\bar{g}}\, \epsilon_{ijk}\, \frac{\partial \bar{x}^i}{\partial \hat{x}^1} \frac{\partial \bar{x}^j}{\partial \hat{x}^2} \frac{\partial \bar{x}^k}{\partial \hat{x}^3} d\hat{x}^1 d\hat{x}^2 d\hat{x}^3 \\ &= \left|\frac{\partial \boldsymbol{y}}{\partial \bar{\mathbf{x}}}\right| \left|\frac{\partial \bar{\mathbf{x}}}{\partial \hat{\mathbf{x}}}\right| d\hat{x}^1 d\hat{x}^2 d\hat{x}^3 \\ &= \sqrt{\hat{g}}\, d\hat{V}. \end{aligned} \tag{3.6}$$

The ratio of the simple scalar product of differentials in two curvilinear coordinate systems is given by dividing Eqs. (3.5) and (3.6):

$$\begin{aligned} \frac{dV}{d\hat{V}} &= \frac{\sqrt{\hat{g}}}{\sqrt{g}} \\ &= \left|\frac{\partial \boldsymbol{y}}{\partial \hat{\mathbf{x}}}\right| \left|\frac{\partial \mathbf{x}}{\partial \boldsymbol{y}}\right| \\ &= \left|\frac{\partial \mathbf{x}}{\partial \hat{\mathbf{x}}}\right|. \end{aligned}$$

It is in this respect that the ratio of "volumes" between x^i and $\hat{x}^i$ coordinate systems is given by the Jacobian of the transformation:

$$J = \frac{dx^1 dx^2 dx^3}{d\hat{x}^1 d\hat{x}^2 d\hat{x}^3}.$$

In order to remain consistent with the work of others, the traditional notation is employed here with the caveat that the actual (Cartesian) volume is denoted as

V and general triple scalar products of coordinates as dV decorated to match the respective coordinates: $dV = dx^1 dx^2 dx^3$, $d\bar{V} = d\bar{x}^1 d\bar{x}^2 d\bar{x}^3$, $d\hat{V} = d\hat{x}^1 d\hat{x}^2 d\hat{x}^3$, etc.

3.2 Derivatives of the Jacobian

It is also useful to formulate the partial derivatives of the Jacobian.

$$\frac{\partial}{\partial \bar{x}^\alpha}(J) = \frac{\partial}{\partial \bar{x}^\alpha}\left|\frac{\partial \mathbf{x}}{\partial \bar{\mathbf{x}}}\right| \tag{3.7a}$$

$$= \frac{\partial}{\partial \bar{x}^\alpha}\left(\epsilon_{ijk}\,\frac{\partial x^i}{\partial \bar{x}^1}\frac{\partial x^j}{\partial \bar{x}^2}\frac{\partial x^k}{\partial \bar{x}^3}\right) \tag{3.7b}$$

$$= \frac{\partial}{\partial \bar{x}^\alpha}\left(\epsilon^{ijk}\,\frac{\partial x^1}{\partial \bar{x}^i}\frac{\partial x^2}{\partial \bar{x}^j}\frac{\partial x^3}{\partial \bar{x}^k}\right), \tag{3.7c}$$

where Greek indices can have values $\{0, 1, 2, 3\}$ allowing the time-like coordinate in the $\bar{x}^\alpha$ system to be denote $\bar{x}^0$. Latin indices will again only cycle through $\{1, 2, 3\}$. The equivalence of Eqs. (3.7b) and (3.7c) can be verified by writing out the components inside the parentheses of each equation. Note that, in general, Eqs. (3.7) are not tensorial due to the presence of the Levi-Civita symbol ϵ^{ijk} which is only an absolute tensor in Cartesian coordinates.

Using the product rule,

$$\frac{\partial}{\partial \bar{x}^\alpha}(J) = \epsilon^{ijk}\,\frac{\partial}{\partial \bar{x}^i}\left(\frac{\partial x^1}{\partial \bar{x}^\alpha}\right)\frac{\partial x^2}{\partial \bar{x}^j}\frac{\partial x^3}{\partial \bar{x}^k} + \epsilon^{ijk}\,\frac{\partial x^1}{\partial \bar{x}^i}\frac{\partial}{\partial \bar{x}^j}\left(\frac{\partial x^2}{\partial \bar{x}^\alpha}\right)\frac{\partial x^3}{\partial \bar{x}^k} + \epsilon^{ijk}\,\frac{\partial x^1}{\partial \bar{x}^i}\frac{\partial x^2}{\partial \bar{x}^j}\frac{\partial}{\partial \bar{x}^k}\left(\frac{\partial x^3}{\partial \bar{x}^\alpha}\right),$$

since partials of independent coordinates commute. Writing out the first of these

terms gives

$$\epsilon^{ijk}\,\frac{\partial}{\partial\bar{x}^i}\left(\frac{\partial x^1}{\partial\bar{x}^\alpha}\right)\frac{\partial x^2}{\partial\bar{x}^j}\frac{\partial x^3}{\partial\bar{x}^k} = \begin{vmatrix} \frac{\partial}{\partial\bar{x}^1}\left(\frac{\partial x^1}{\partial\bar{x}^\alpha}\right) & \frac{\partial}{\partial\bar{x}^2}\left(\frac{\partial x^1}{\partial\bar{x}^\alpha}\right) & \frac{\partial}{\partial\bar{x}^3}\left(\frac{\partial x^1}{\partial\bar{x}^\alpha}\right) \\ \frac{\partial x^2}{\partial\bar{x}^1} & \frac{\partial x^2}{\partial\bar{x}^2} & \frac{\partial x^2}{\partial\bar{x}^3} \\ \frac{\partial x^3}{\partial\bar{x}^1} & \frac{\partial x^3}{\partial\bar{x}^2} & \frac{\partial x^3}{\partial\bar{x}^3} \end{vmatrix}$$

$$= \begin{vmatrix} \frac{\partial x^k}{\partial\bar{x}^1}\frac{\partial}{\partial x^k}\left(\frac{\partial x^1}{\partial\bar{x}^\alpha}\right) & \frac{\partial x^k}{\partial\bar{x}^2}\frac{\partial}{\partial x^k}\left(\frac{\partial x^1}{\partial\bar{x}^\alpha}\right) & \frac{\partial x^k}{\partial\bar{x}^3}\frac{\partial}{\partial x^k}\left(\frac{\partial x^1}{\partial\bar{x}^\alpha}\right) \\ \frac{\partial x^2}{\partial\bar{x}^1} & \frac{\partial x^2}{\partial\bar{x}^2} & \frac{\partial x^2}{\partial\bar{x}^3} \\ \frac{\partial x^3}{\partial\bar{x}^1} & \frac{\partial x^3}{\partial\bar{x}^2} & \frac{\partial x^3}{\partial\bar{x}^3} \end{vmatrix},$$

$$= \frac{\partial}{\partial x^k}\left(\frac{\partial x^1}{\partial\bar{x}^\alpha}\right)\begin{vmatrix} \frac{\partial x^k}{\partial\bar{x}^1} & \frac{\partial x^k}{\partial\bar{x}^2} & \frac{\partial x^k}{\partial\bar{x}^3} \\ \frac{\partial x^2}{\partial\bar{x}^1} & \frac{\partial x^2}{\partial\bar{x}^2} & \frac{\partial x^2}{\partial\bar{x}^3} \\ \frac{\partial x^3}{\partial\bar{x}^1} & \frac{\partial x^3}{\partial\bar{x}^2} & \frac{\partial x^3}{\partial\bar{x}^3} \end{vmatrix}$$

$$= \frac{\partial}{\partial x^1}\left(\frac{\partial x^1}{\partial\bar{x}^\alpha}\right)J$$

where only the $k = 1$ term has survived since for $k = 2$ or 3, the last determinant shown has a row repeated and thus is 0 [27, pg. 84]. Expansion of the other two terms in Eq. (3.8) in a similar manner leads to

$$\frac{\partial}{\partial\bar{x}^\alpha}(J) = \frac{\partial}{\partial x^k}\left(\frac{\partial x^k}{\partial\bar{x}^\alpha}\right)J, \tag{3.8}$$

which is valid for $\alpha \in 0, 1, 2, 3$. Similarly, let $J_x = \frac{1}{J} = \left|\frac{\partial\bar{\mathbf{x}}}{\partial\mathbf{x}}\right|$. Then

$$\frac{\partial}{\partial\bar{x}^\alpha}\left(J_x^{-1}\right) = \frac{\partial}{\partial x^k}\left(\frac{\partial x^k}{\partial\bar{x}^\alpha}\right)J_x^{-1}$$

or

$$\frac{\partial}{\partial\bar{x}^\alpha}(J_x) = -\frac{\partial}{\partial x^k}\left(\frac{\partial x^k}{\partial\bar{x}^\alpha}\right)J_x. \tag{3.9}$$

3.3 Leibniz's rule

Because the domain of integration in Eq. (3.1) changes with time, differentiation and integration do not commute in a simple fashion. Instead, consider first a simple triple integral of a function ψ over a fixed domain with respect to t. In this case, differentiation and integration commute according to

$$\frac{d}{dt}\int_{\bar{V}} \psi(\bar{x}^i, t)\ d\bar{V} = \int_{\bar{V}} \frac{\partial \psi}{\partial t}(\bar{x}^i, t)\ d\bar{V} \tag{3.10}$$

since all the coordinates ($\bar{x}^i$ and t) are independent of each other. This is known as Leibniz's rule and is a purely mathematical result.

Following Kaplan [28], Eq. (3.10) is proven by first letting $h(t) = \int_{\bar{V}} \frac{\partial \psi}{\partial t}\ d\bar{V}$. Now

$$\begin{aligned}
\textstyle\int_{t_0}^{t} h(\hat{t})\ d\hat{t} &= \textstyle\int_{t_0}^{t} \int_{\bar{V}} \frac{\partial \psi}{\partial t}(\bar{x}^i, \hat{t})\ d\bar{V}\ d\hat{t} \\
&= \textstyle\int_{\bar{V}} \int_{t_0}^{t} \frac{\partial \psi}{\partial t}(\bar{x}^i, \hat{t})\ d\hat{t}\ d\bar{V} \\
&= \textstyle\int_{\bar{V}} \{\psi(\bar{x}^i, t) - \psi(\bar{x}^i, t_0)\}\ d\bar{V} \\
&= \underbrace{\int_{\bar{V}} \psi(\bar{x}^i, t)\ d\bar{V}}_{\text{a function of } t} - \underbrace{\int_{\bar{V}} \psi(\bar{x}^i, t_0)\ d\bar{V}}_{\text{a constant}}
\end{aligned}$$

Differentiating this expression gives

$$\frac{d}{dt}\int_{t_0}^{t} h(\hat{t})\ d\hat{t} = \frac{d}{dt}\int_{\bar{V}} \psi(\bar{x}^i, t)\ d\bar{V} - \underbrace{\frac{d}{dt}\int_{\bar{V}} \psi(\bar{x}^i, t_0)\ d\bar{V}}_{=0}.$$

Thus, using the fundamental theorem of calculus

$$\begin{aligned}
h(t) &= \textstyle\frac{d}{dt}\int_{\bar{V}} \psi(\bar{x}^i, t)\ d\bar{V} \\
&= \textstyle\int_{\bar{V}} \frac{\partial \psi}{\partial t}\ d\bar{V}.
\end{aligned}$$

Having verified Eq. (3.10), all the requisite equations have been given which are needed to develop Reynolds' transport theorem.

3.4 Derivation of Reynolds' transport theorem

The theorem will be derived in three parts. First, a mathematical expression interchanging differentiation and integration over a time-dependent volume is developed without attaching any tensorial meaning to the result. Next, the standard tensorial form is given and verified for a first order contravariant conserved quantity. Lastly, the form employing tensor notation with respect to time-dependent coordinates is given and verified for a first order contravariant conserved quantity. This incremental development precisely delineates the tensorial character typically attributed to Reynolds' transport theorem, a character which is normally simply asserted due to its ambiguity in less rigorous developments.

3.4.1 Mathematical form

Consider an arbitrary n-tuple $\mathbf{A}(x^i, t)$ of arbitrary dimension where each component is a function of the independent variables x^i and t where $i = \{1, 2, 3\}$. The expression of interest is

$$\frac{d}{dt} \int_{V(t)} \mathbf{A}(x^i, t) \, dV. \tag{3.11}$$

To interchange differentiation and integration in Eq. (3.11), $V(t)$ and dV are first transformed to a system where the domain of integration is fixed (*i.e.* independent of time).

According to the nomenclature of Section 2.6.2, such a system is termed "vol-

umetric" and denoted by $\{\bar{x}^i, \bar{t}\}$. This particular volumetric system is defined such that the constant domain of integration corresponding to $V(t)$ is $\bar{V}$. Such a transformation could be envisioned as a one-time labeling of each point such that each moving point of $V(t)$ is smoothly mapped to a fixed point in $\bar{x}$ space. Again, the volumetric system is chosen to be of the form

$$\bar{x}^i = \bar{x}^i(x^j, t) \qquad \text{and} \qquad \bar{t} = t$$

and subject to the same constraints enumerated in Section 2.6.2.

This is followed by application of Leibniz's rule where each component of Eq. (3.11) is considered independently:

$$\begin{aligned} \frac{d}{dt}\int_{V(t)} \mathbf{A}(x^i, t)\, dV &= \frac{d}{d\bar{t}}\int_{\bar{V}} \mathbf{A}(\bar{x}^i, \bar{t})\; J\; d\bar{V} \\ &= \int_{\bar{V}} \left(\frac{\partial \mathbf{A}(\bar{x}^i, \bar{t})}{\partial \bar{t}} J + \mathbf{A}(\bar{x}^i, \bar{t}) \frac{\partial J}{\partial \bar{t}} \right) d\bar{V}. \end{aligned} \tag{3.12}$$

Using Eq. (3.8) with $\frac{\partial}{\partial \bar{x}^\alpha} = \frac{\partial}{\partial \bar{t}}$ gives

$$\frac{\partial J}{\partial \bar{t}} = \frac{\partial}{\partial x^k}\left(\frac{\partial x^k}{\partial \bar{t}}\right) J.$$

Now $\left.\frac{\partial x^i}{\partial \bar{t}}\right|_{\bar{x}}$ is just the time rate of change, measured according the original x^i coordinates, of a point in the transformed domain. Note that this quantity is *independent of* $\mathbf{A}$. The operator $\frac{d}{dt}$ is defined in Eq. (2.22b) as

$$\frac{d}{dt} = \frac{\partial}{\partial \bar{t}} = \frac{\partial}{\partial t} + \frac{\partial x^k}{\partial \bar{t}} \frac{\partial}{\partial x^k} \tag{3.13a}$$

$$= \frac{\partial}{\partial t} + \frac{dx^k}{dt} \frac{\partial}{\partial x^k}, \tag{3.13b}$$

representing differentiation holding $\bar{x}^k$ constant such that $\frac{dx^i}{dt} \equiv \frac{\partial x^i}{\partial \bar{t}}$.

Substitution into Eq. (3.12) yields

$$\begin{aligned}
\frac{d}{dt}\int\limits_{V(t)} \mathbf{A}(x^i,t)\, dV &= \int\limits_{\bar{V}} \left(\frac{\partial \mathbf{A}(\bar{x}^i,\bar{t})}{\partial \bar{t}} J + \mathbf{A}(\bar{x}^i,\bar{t}) \frac{\partial}{\partial x^k}\left(\frac{\partial x^k}{\partial \bar{t}}\right) J \right) d\bar{V} \\
&= \int\limits_{\bar{V}} \left(\frac{\partial \mathbf{A}(\bar{x}^i,\bar{t})}{\partial \bar{t}} + \mathbf{A}(\bar{x}^i,t) \frac{\partial}{\partial x^k}\left(\frac{\partial x^k}{\partial \bar{t}}\right) \right) J\, d\bar{V} \\
&= \int\limits_{V(t)} \left(\frac{d\mathbf{A}(x^i,t)}{dt} + \mathbf{A}(x^i,t) \frac{\partial}{\partial x^k}\left(\frac{dx^k}{dt}\right) \right) dV.
\end{aligned}$$

Thus the Reynolds' transport theorem is simply

$$\frac{d}{dt}\int\limits_{V(t)} \mathbf{A}(x^i,t)\, dV = \int\limits_{V(t)} \left(\frac{d\mathbf{A}(x^i,t)}{dt} + \mathbf{A}(x^i,t) \frac{\partial}{\partial x^k}\left(\frac{dx^k}{dt}\right) \right) dV. \tag{3.14}$$

By expanding the total time derivative using Eq. (3.13b) and employing the divergence theorem, one may also write

$$\frac{d}{dt}\int\limits_{V(t)} \mathbf{A}(x^i,t)\, dV = \int\limits_{V(t)} \left(\frac{\partial \mathbf{A}(x^i,t)}{\partial t} + \frac{\partial}{\partial x^k}\left(\mathbf{A}(x^i,t)\frac{dx^k}{dt}\right) \right) dV \tag{3.15a}$$

$$= \int\limits_{V(t)} \frac{\partial \mathbf{A}(x^i,t)}{\partial t} dV + \int\limits_{S(t)} \mathbf{A}(x^i,t)\frac{dx^k}{dt} n_k dS, \tag{3.15b}$$

where $S(t)$ is the bounding surface of $V(t)$ and n_k is the outward unit normal of $S(t)$.

3.4.2 Standard tensor form

Accordingly, Eqs. (3.14) and (3.15b) are satisfied when Cartesian representations of the underlying tensors are used:

$$\frac{d}{dt}\int\limits_{V(t)} \boldsymbol{\mathcal{A}}\, dV = \int\limits_{V(t)} \left(\frac{\delta \boldsymbol{\mathcal{A}}}{\delta t} + \boldsymbol{\mathcal{A}} w^k_{,k}\right) dV \tag{3.16a}$$

$$= \int\limits_{V(t)} \frac{\partial \boldsymbol{\mathcal{A}}}{\partial t} dV + \int\limits_{S(t)} \boldsymbol{\mathcal{A}} w^k n_k dS, \tag{3.16b}$$

where the Cartesian representation of a tensor is identified by a scripted font, $\boldsymbol{\mathcal{A}}$ is an arbitrary tensor of any order, n_k denotes the normal to the surface S, $\frac{\delta}{\delta t}$ is the intrinsic derivative, and $w^i = \frac{\partial y^i}{\partial t}\Big|_{\bar{x}}$ is the time rate of change of the position of a volumetric coordinate.

Equations (3.16) are, in some sense, themselves *Cartesian tensor equations*; although, the tensors involved are associated with volumes and surfaces instead of a point. This interpretation is possible because the transformation tensor for Cartesian tensors are constant across the entire volume and so can be brought outside of the integration operators. For curvilinear coordinates, however, the coordinate lines change direction across the volume. In other words, throughout the volume $V(t)$, the transformation tensor (*e.g.* $\frac{\partial y^i}{\partial x^j}$) is not constant and, while the integrands are tensors, the integrated quantities are not (*i.e.* they do not transform according to the tensor transformation rule.) Thus, Eqs. (3.16) are not curvilinear tensor equations.

In order to satisfy Eqs. (3.16), one requires that all integrals are done with respect to Cartesian coordinates, the integrands always reducing to the Cartesian tensorial representation. Recalling $\mathbf{R}$ from Eq. (2.5), the theorem for curvilinear

tensors takes the form

$$\frac{d}{dt}\int\limits_{V(t)} \mathbf{A}\ \cdot \mathbf{R}\ dV = \int\limits_{V(t)} \left(\frac{\delta \mathbf{A}}{\delta t} + \mathbf{A} w^k_{,k}\right) \cdot \mathbf{R}\ dV \tag{3.17a}$$

$$= \int\limits_{V(t)} \frac{\partial \mathbf{A}}{\partial t} \cdot \mathbf{R}\ dV + \int\limits_{S(t)} \left(\mathbf{A} w^k n_k\right) \cdot \mathbf{R} dS, \tag{3.17b}$$

where $w^k = \left.\frac{\partial x^k}{\partial t}\right|_{\bar{x}} = \frac{\partial x^k}{\partial Y^i} w^i$ is the volumetric velocity. Note that a contracted zeroth order tensor is invariant (*e.g.* $w^k n_k$). Equation (3.17) is the most general tensorial form of the Reynolds transport theorem.

3.4.3 Verification for first order tensors

In order to verify Eqs. (3.17), consider directly using the mathematical form of the Reynolds transport theorem on the left hand side of Eqs. (3.17) written for a vector. Applying Eq. (3.14) to $\frac{d}{dt}\int_{V(t)} \mathbf{A}(x^i, t) \cdot \mathbf{R}\ dV$ with $\mathbf{A} \equiv A^k$ gives

$$\frac{d}{dt}\int\limits_{V(t)} A^k \frac{\partial Y^i}{\partial x^k}\sqrt{g} dV = \int\limits_{V(t)} \left(\frac{d}{dt}\left(A^k \frac{\partial Y^i}{\partial x^k}\sqrt{g}\right) + A^k \frac{\partial Y^i}{\partial x^k}\sqrt{g}\frac{dw^l}{dx^l}\right) dV, \tag{3.18}$$

where $\mathbf{R} \equiv \frac{\partial y^i}{\partial x^k}$ to match the order of $\mathbf{A}$. Expanding Eq. (3.18) gives

$$\begin{aligned}
\frac{d}{dt}\int_{V(t)} A^k \frac{\partial y^i}{\partial x^k}\sqrt{g}dV &= \int_{V(t)} \left(\frac{\partial}{\partial t}\left(A^k \frac{\partial y^i}{\partial x^k}\sqrt{g}\right) + \frac{\partial}{\partial x^j}\left(A^k \frac{\partial y^i}{\partial x^k}\sqrt{g}\right) w^j \right. \\
&\qquad \left. + A^k \frac{\partial y^i}{\partial x^k}\sqrt{g}\frac{\partial w^l}{\partial x^l}\right) dV \\
&= \int_{V(t)} \left(\sqrt{g}\frac{\partial y^i}{\partial x^k}\left(\frac{\partial A^k}{\partial t} + w^j \frac{\partial A^k}{\partial x^j}\right) \right. \\
&\qquad \left. + A^k \left(w^j \frac{\partial}{\partial x^j}\left(\sqrt{g}\frac{\partial y^i}{\partial x^k}\right) + \frac{\partial y^i}{\partial x^k}\sqrt{g}\frac{\partial w^l}{\partial x^l}\right)\right) dV \\
&= \int_{V(t)} \left(\sqrt{g}\frac{\partial y^i}{\partial x^k}\left(\frac{\partial A^k}{\partial t} + w^j \frac{\partial A^k}{\partial x^j} + w^j \frac{\partial^2 y^l}{\partial x^j \partial x^n} A^n \frac{\partial x^k}{\partial y^l}\right) \right. \\
&\qquad \left. + A^k \left(w^j \frac{\partial y^i}{\partial x^k}\frac{\partial}{\partial x^j}\left(\sqrt{g}\right) + \frac{\partial y^i}{\partial x^k}\sqrt{g}\frac{\partial w^l}{\partial x^l}\right)\right) dV, \qquad (3.19)
\end{aligned}$$

where $\frac{\partial^2 y^l}{\partial x^j \partial x^n}\frac{\partial x^k}{\partial y^l} = \left\{ {}_j{}^k{}_n \right\}$ is a Christoffel symbol of the second kind. Equation (3.19) becomes.

$$\begin{aligned}
\frac{d}{dt}\int_{V(t)} A^k \frac{\partial y^i}{\partial x^k}\sqrt{g}dV &= \int_{V(t)} \left(\sqrt{g}\frac{\partial y^i}{\partial x^k}\left(\frac{\partial A^k}{\partial t} + w^j \left(\frac{\partial A^k}{\partial x^j} + \left\{ {}_j{}^k{}_n \right\} A^n \right)\right) \right. \\
&\qquad \left. + A^k \frac{\partial y^i}{\partial x^k}\frac{\partial}{\partial x^j}\left(\sqrt{g}w^j\right)\right) dV \\
&= \int_{V(t)} \left(\sqrt{g}\frac{\partial y^i}{\partial x^k}\left(\frac{\partial A^k}{\partial t} + w^j A^k_{,j} + A^k \frac{1}{\sqrt{g}}\frac{\partial}{\partial x^j}\left(\sqrt{g}w^j\right)\right)\right) dV \\
&= \int_{V(t)} \left(\frac{\delta A^k}{\delta t} + A^k w^j_{,j}\right)\frac{\partial y^i}{\partial x^k}\sqrt{g}dV, \qquad (3.20)
\end{aligned}$$

where

$$\frac{1}{\sqrt{g}}\frac{\partial}{\partial x^l}\left(\sqrt{g}w^l\right) = w^l_{,l} \tag{3.21}$$

has been employed to write the last term in terms of the tensorial divergence and the intrinsic derivative. Noting $dV = \sqrt{g}dV$, Eq. (3.20) can be re-written in its final form as

$$\frac{d}{dt}\int\limits_{V(t)} A^k \frac{\partial y^i}{\partial x^k} dV = \int\limits_{V(t)} \left(\frac{\delta A^k}{\delta t} + F^k w^j_{,j}\right)\frac{\partial y^i}{\partial x^k} dV. \tag{3.22}$$

Equations (3.17a) and (3.22) are identical where the careful incorporation of tensor notation into Eq. (3.22) reveals the connection between a tensorial interpretation of Reynolds' transport theorem and integration over Cartesian volumes.

Substituting for the intrinsic derivative in Eq. (3.22) from Eq. (2.12) and re-arrangement gives

$$\frac{d}{dt}\int\limits_{V(t)} A^k \frac{\partial y^i}{\partial x^k} dV = \int\limits_{V(t)} \left(\frac{\partial A^k}{\partial t} + \left(A^k w^j\right)_{,j}\right)\frac{\partial y^i}{\partial x^k} dV \tag{3.23a}$$

$$= \int\limits_{V(t)} \frac{\partial A^k}{\partial t}\frac{\partial y^i}{\partial x^k} dV + \int\limits_{S(t)} A^k \frac{\partial y^i}{\partial x^k} w^j n_j dV, \tag{3.23b}$$

where the divergence theorem has been used to form Eq. (3.23b).

3.5 Extension to time-dependent coordinates

Section 2.5 develops Reynolds' transport theorem for tensors represented according to spatial coordinates which are independent of time. Now the case of tensors described according to time-dependent coordinates is considered, where

again tensorial differentiation is defined such that it is identical to partial differentiation in Cartesian coordinates.

Before continuing, however, one should note that this is not the first time that such a time-dependent coordinate system has been utilized. In fact, the mathematical form of Reynolds' transport theorem, Eq. (3.14), was derived by utilizing just such a moving coordinate system, $\{\bar{x}, \bar{t}\}$, which deformed according to the motion of $V(t)$. In fact, Eq. (3.14) was derived as a purely mathematical expression without respect to any tensorial interpretation that could be given to A. Thus, this mathematical form must remain valid for the expressions derived for time-dependent tensorial representations.

3.5.1 Tensorial form

Since the mathematical expression in Cartesian coordinates of both differentiation and the volumetric velocity are identical to the tensorial representation of these quantities, tensor notation can again be employed directly in such an expression. Thus the tensorial representation is identical to Eqs. (3.16):

$$\begin{aligned}\frac{d}{dt}\int_{V(t)} \mathbf{A}\, dV &= \int_{V(t)} \left(\frac{\delta \mathbf{A}}{\delta t} + \mathbf{A} w^k_{,k}\right) dV, \\ &= \int_{V(t)} \mathbf{A}_{,0} dV + \int_{S(t)} \mathbf{A} w^k n_k dS,\end{aligned}$$

except the the time derivative in now written in time-dependent tensorial form.

Since any other such integral expression involving tensorial notation must satisfy Eqs. (3.16), the curvilinear representation of these tensors are incorporated into Eqs. (3.16) by ensuring that the integrands again reduce to the Cartesian

representation:

$$\frac{d}{dt}\int\limits_{V(t)} \mathbf{A}\cdot\mathbf{R}\; dV = \int\limits_{V(t)} \left(\frac{\delta \mathbf{A}}{\delta t} + \mathbf{A}w^k_{,k}\right)\cdot\mathbf{R}\; dV, \tag{3.24a}$$

$$= \int\limits_{V(t)} \mathbf{A}_{,0}\cdot\mathbf{R}\; dV + \int\limits_{S(t)} \left(\mathbf{A}w^k n_k\right)\cdot\mathbf{R} dS. \tag{3.24b}$$

With exception of the first term in Eq. (3.24b), Eqs. (3.24) are again identical to Eqs. (3.17).

3.5.2 Verification for first order tensors

As in Section 3.4.3, verification of Eqs. (3.24) for time-dependent vector representations follows from expanding the left hand side of Eq. (3.24a) using the mathematical form of the Reynolds' transport theorem. The mathematical form given by Eq. (3.14), after substituting for the volumetric velocity from Eq. (2.23b), becomes

$$\frac{d}{dt}\int\limits_{V(t)} \mathbf{A}(x^i,t)\; dV = \int\limits_{V(t)} \left(\frac{d\mathbf{A}(x^i,t)}{dt} + \mathbf{A}(x^i,t)\frac{\partial}{\partial x^k}\left(w^k - U^{(k)}\right)\right) dV, \tag{3.25}$$

where

$$\frac{d}{dt} = \frac{\partial}{\partial t} + \frac{dy^i}{dt}\frac{\partial}{\partial y^i} = \frac{\partial}{\partial t} + w^i\frac{\partial}{\partial y^i} \tag{3.26a}$$

$$= \frac{\partial}{\partial t} + \frac{dx^i}{dt}\frac{\partial}{\partial x^i} = \frac{\partial}{\partial t} + \left(w^i - U^{(i)}\right)\frac{\partial}{\partial x^i}. \tag{3.26b}$$

Setting $\mathbf{A} \equiv A^k \frac{\partial y^i}{\partial x^k}\sqrt{g}$ where $k \in \{1,2,3\}$, Eq. (3.25) becomes

$$\begin{aligned}\frac{d}{dt}\int\limits_{V(t)} A^k \frac{\partial y^i}{\partial x^k}\sqrt{g}\, dV &= \int\limits_{V(t)} \left(\frac{d}{dt}\left(A^k \frac{\partial y^i}{\partial x^k}\sqrt{g}\right)\right. \\ &\qquad \left. + A^k \frac{\partial y^i}{\partial x^k}\sqrt{g}\frac{\partial}{\partial x^j}\left(w^j - U^{(j)}\right)\right) dV \qquad (3.27) \\ &= \int\limits_{V(t)} \left(\frac{\partial y^i}{\partial x^k}\sqrt{g}\frac{dA^k}{dt} + A^k\sqrt{g}\frac{d}{dt}\left(\frac{\partial y^i}{\partial x^k}\right)\right. \\ &\qquad + A^k \frac{\partial y^i}{\partial x^k}\frac{d\sqrt{g}}{dt} \\ &\qquad \left. + A^k \frac{\partial y^i}{\partial x^k}\sqrt{g}\frac{\partial}{\partial x^j}\left(w^j - U^{(j)}\right)\right) dV. \qquad (3.28)\end{aligned}$$

where the left hand side of Eq. (3.27) is identical to that of Eq. (3.17a). For brevity in the subsequent analysis, the more compact form $\frac{d}{dt}\int_{V(t)} A^i dV$ will be used in place of the expanded left hand side of Eq. (3.28).

Using the definition of the $\frac{d}{dt}$ operator given in Eq. (3.26), the term $\frac{d}{dt}\left(\frac{\partial y^i}{\partial x^k}\right)$ becomes

$$\begin{aligned}\frac{d}{dt}\left(\frac{\partial y^i}{\partial x^k}\right) &= \frac{\partial}{\partial t}\left(\frac{\partial y^i}{\partial x^k}\right) + (w^l - U^{(l)})\frac{\partial}{\partial x^l}\left(\frac{\partial y^i}{\partial x^k}\right) \\ &= \frac{\partial U^{(i)}}{\partial x^k} + (w^l - U^{(l)})\frac{\partial^2 y^i}{\partial x^l \partial x^k} \\ &= \frac{\partial y^l}{\partial x^k} U^{(i)}_{,l} + (w^l - U^{(l)})\frac{\partial^2 y^i}{\partial x^l \partial x^k} \\ &= \frac{\partial y^i}{\partial x^m} U^{(m)}_{,k} + (w^l - U^{(l)})\frac{\partial^2 y^i}{\partial x^l \partial x^k}, \qquad (3.29)\end{aligned}$$

since $U^{(m)}_{,k} = \frac{\partial x^m}{\partial y^i}\frac{\partial y^l}{\partial x^k}U^{(i)}_{,l}$. The term $\frac{d\sqrt{g}}{dt}$ becomes

$$\frac{d\sqrt{g}}{dt} = \frac{\partial\sqrt{g}}{\partial t} + (w^j - U^{(j)})\frac{\partial\sqrt{g}}{\partial x^j}; \qquad (3.30)$$

using Eq. (3.8) with $J = \sqrt{g} = \left|\frac{\partial Y}{\partial x}\right|$ gives

$$\begin{aligned}\frac{\partial \sqrt{g}}{\partial t} &= \sqrt{g}\frac{\partial}{\partial Y^j}\left(\frac{\partial Y^j}{\partial t}\right) \\ &= \sqrt{g}U^{(j)}_{,j}. \end{aligned} \tag{3.31}$$

Since $U^{(j)}_{,j} \equiv U^{(j)}_{,j}$, Eq. (3.30) becomes

$$= \sqrt{g}U^{(j)}_{,j} + (w^j - U^{(j)})\frac{\partial \sqrt{g}}{\partial x^j}. \tag{3.32}$$

Substituting Eqs. (3.29) and (3.32) into Eq. (3.28) gives

$$\begin{aligned}\frac{d}{dt}\int_{V(t)} A^i dV = \int_{V(t)} \Bigg(&\frac{\partial Y^i}{\partial x^k}\sqrt{g}\frac{dA^k}{dt} \\ &+ A^k\sqrt{g}\left(\frac{\partial Y^i}{\partial x^m}U^{(m)}_{,k} + (w^l - U^{(l)})\frac{\partial^2 Y^i}{\partial x^l \partial x^k}\right) \\ &+ A^k\frac{\partial Y^i}{\partial x^k}\left(\sqrt{g}U^{(j)}_{,j} + (w^j - U^{(j)})\frac{\partial \sqrt{g}}{\partial x^j}\right) \\ &+ A^k\frac{\partial Y^i}{\partial x^k}\sqrt{g}\frac{\partial}{\partial x^j}\left(w^j - U^{(j)}\right)\Bigg) dV,\end{aligned}$$

or

$$\begin{aligned}\frac{d}{dt}\int_{V(t)} A^i dV = \int_{V(t)} \sqrt{g}\frac{\partial Y^i}{\partial x^k}\Bigg(&\frac{dA^k}{dt} + \\ &A^n\left(U^{(k)}_{,n} + (w^l - U^{(l)})\frac{\partial x^k}{\partial Y^m}\frac{\partial^2 Y^m}{\partial x^l \partial x^n}\right)\Bigg) \\ &+ A^k\frac{\partial Y^i}{\partial x^k}\sqrt{g}\left(U^{(j)}_{,j} + \frac{1}{\sqrt{g}}\frac{\partial}{\partial x^j}\left(\sqrt{g}(w^j - U^{(j)})\right)\right)\Bigg) dV,\end{aligned} \tag{3.33}$$

where dummy indices have been changed as needed. Note that

$\frac{1}{\sqrt{g}}\frac{\partial}{\partial x^j}\left(\sqrt{g}(w^j - U^{(j)})\right) = (w^j - U^{(j)})_{,j}$ is the divergence of the volumetric velocity relative to the curvilinear frame. Cancellation in the last term of Eq. (3.33) gives

$$\begin{aligned}\frac{d}{dt}\int\limits_{V(t)} A^i dV &= \int\limits_{V(t)}\left(\frac{dA^k}{dt} + A^n U^{(k)}_{,n}\right.\\ &\qquad \left. + (w^l - U^{(l)})\left\{ {}_l{}^k{}_n \right\}A^n + A^k w^j_{,j}\right)\frac{\partial Y^i}{\partial x^k}\sqrt{g}dV\\ &= \int\limits_{V(t)}\left(\frac{\delta A^k}{\delta t} + A^k w^j_{,j}\right)\frac{\partial Y^i}{\partial x^k}\sqrt{g}dV,\end{aligned}$$

or

$$\frac{d}{dt}\int\limits_{V(t)} A^k \frac{\partial Y^i}{\partial x^k}dV = \int\limits_{V(t)}\left(\frac{\delta A^k}{\delta t} + A^k w^j_{,j}\right)\frac{\partial Y^i}{\partial x^k}dV, \tag{3.34}$$

where

$$\begin{aligned}\frac{\delta A^k}{\delta t} &= \frac{dA^k}{dt} + A^n U^{(k)}_{,n} + (w^l - U^{(l)})\left\{ {}_l{}^k{}_n \right\}A^n\\ &= \frac{\partial A^k}{\partial t} + (w^l - U^{(l)})\frac{\partial A^k}{\partial x^l} + A^n U^{(k)}_{,n} + (w^l - U^{(l)})\left\{ {}_l{}^k{}_n \right\}A^n\\ &= \frac{\partial A^k}{\partial t} + (w^l - U^{(l)})A^k_{,l} + A^n U^{(k)}_{,n}\\ &= A^k_{,0} + A^k_{,l} w^l\end{aligned}$$

is the intrinsic derivative, Eq. (2.32), for time-dependent first order tensors. Equation (3.34) is the most compact form of the Reynolds' transport theorem for time-dependent tensors and is identical to Eq. (3.22), with the caveat that the intrinsic derivative now contains additional terms due to the relative motion of the coordinates (*cf.* Eqs. (2.16)).

3.6 Extension to discontinuous flows

Thus far, it has been tacitly assumed that the considered fields have been continuous and differentiable over the domain of interest. In this section, this requirement is relaxed, allowing a surface discontinuity in the field. The resulting form of the Reynolds' transport theorem is especially useful in the consideration of shock waves.

Consider a domain $V(t)$ shown in Fig. 3.1 with bounding surface $S(t)$. This domain is intersected by an internal surface $\Sigma(t)$. Now $\Sigma(t)$ moves with an arbitrary

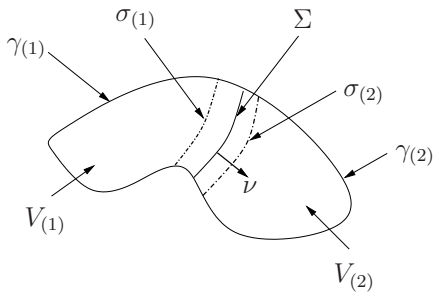

Figure 3.1. Schematic of discontinuity in the bulk of a continuum.

velocity D^i across which an n-tuple $\mathbf{A}(x^i, t)$ suffers a discontinuity, $\mathbf{A}_{(1)}$ and $\mathbf{A}_{(2)}$ being its values on either side.

In order to remove the discontinuity [30], consider two domains $V_{(1)}(t)$ and $V_{(2)}(t)$ on either side of the discontinuity with bounding surface $\sigma_{(i)}(t) \cup \gamma_{(i)}(t)$. Let ν_i be the normal to $\Sigma(t)$ in the direction from $V_{(1)}(t)$ to $V_{(2)}(t)$. Define $\gamma_{(i)}(t)$ to be coincident with the boundary of $V(t)$, and define $\sigma_{(i)}(t)$ to have the same

shape and velocity as $\Sigma(t)$, as seen in Figure 3.1. In the limit as $\sigma_{(i)}(t)$ approaches $\Sigma(t)$, the entire domain $V(t)$ is covered in a piecewise integral sense.

Each of the control volumes, $V_{(i)}$, defines a different volumetric system. The surfaces $\gamma_{(i)}$ are material surfaces, while the surfaces $\sigma_{(i)}$ follow the shock. Thus, the total derivatives according to each are different (*cf* Section 2.6.2). As before, total time derivatives following material surfaces will be denoted $\frac{d}{dt}$; however, the total time differentiation following the shock will be denoted $\frac{d}{dt}|_{\Sigma}$.

Furthermore, as with the volumetric velocity introduced in Eqs. (2.23), $\mathcal{D}^i$ does not transform as a tensor; rather, it is offset by the grid "velocity." Thus,

$$\left.\frac{dx^i}{dt}\right|_{\Sigma} = \frac{\partial x^i}{\partial t} + \frac{\partial x^i}{\partial y^j}\left.\frac{dy^j}{dt}\right|_{\Sigma}, \tag{3.35a}$$

$$\left.\frac{dx^i}{dt}\right|_{\Sigma} = -U^{(i)} + \frac{\partial x^i}{\partial y^j}\mathcal{D}^j. \tag{3.35b}$$

As with Eq. (2.23c), the curvilinear representation of the Cartesian velocity is

$$D^j = \frac{\partial x^j}{\partial y^i}\mathcal{D}^i. \tag{3.35c}$$

In order to extend Reynolds' transport theorem to discontinuous fields, it is expedient and illustrative to first consider the divergence of $\mathbf{A}(x^i, t)$ across the aforementioned domain. Then the mathematical and tensorial forms of the theorem are considered directly.

3.6.1 The divergence theorem across a shock

The classic divergence theorem can not be used since $S(t) - \Sigma(t)$ is not a closed surface and $S(t)$ contains a discontinuity. Over each domain, however, $V_{(i)}(t)$, the

divergence theorem does hold. Thus,

$$\int\limits_{V_{(1)}(t)} \frac{\partial \mathbf{A}^i}{\partial x^i}\, dV = \int\limits_{\gamma_{(1)}(t)} \mathbf{A}^i n_i\, dS + \int\limits_{\sigma_{(1)}(t)} \mathbf{A}^i \nu_i\, dS \tag{3.36a}$$

and

$$\int\limits_{V_{(2)}(t)} \frac{\partial \mathbf{A}^i}{\partial x^i}\, dV = \int\limits_{\gamma_{(2)}(t)} \mathbf{A}^i n_i\, dS - \int\limits_{\sigma_{(2)}(t)} \mathbf{A}^i \nu_i\, dS \tag{3.36b}$$

where the outward flux through $\sigma_{(2)}(t)$ is in the $-\nu_i$ direction and the index on $\mathbf{A}$ has no tensorial connotation.

Since each of the domains in Eqs. (3.36) can be represented as a set of points, set notation may be employed to succinctly describe composite domains: $V(t) - \Sigma(t) \equiv V(t) - V(t) \cap \Sigma(t)$, and $S(t) - \Sigma(t) \equiv S(t) - S(t) \cap \Sigma(t)$. Thus, addition of Eqs. (3.36) and taking the limit as $\sigma_{(i)}(t)$ approaches $\Sigma(t)$ gives

$$\int\limits_{V(t)-\Sigma(t)} \frac{\partial \mathbf{A}^i}{\partial x^i}\, dV = \int\limits_{S(t)-\Sigma(t)} \mathbf{A}^i n_i\, dS + \int\limits_{\Sigma(t)} [\![\mathbf{A}^i]\!]\, \nu_i\, dS$$

or equivalently

$$\int\limits_{S(t)-\Sigma(t)} \mathbf{A}^i n_i\, dS = \int\limits_{V(t)-\Sigma(t)} \frac{\partial \mathbf{A}^i}{\partial x^i}\, dV - \int\limits_{\Sigma(t)} [\![\mathbf{A}^i]\!]\, \nu_i\, dS. \tag{3.37}$$

Integrating over the domain Σ is always taken in a limiting sense; double brackets denote the jump across the discontinuity of the enclosed quantity in the direction of $\boldsymbol{\nu}$: *e.g.* if $\boldsymbol{\nu}$ points in the direction of a jump in $\mathbf{A}$ from $\mathbf{A}_{(1)}$ to $\mathbf{A}_{(2)}$, then $[\![\mathbf{A}]\!] = \mathbf{A}_{(1)} - \mathbf{A}_{(2)}$. With this definition of the jump operator, the orientation of

$\boldsymbol{\nu}$ becomes arbitrary since the contraction is invariant:

$$[\![\mathbf{A}^i]\!]\,\nu_i = (\mathbf{A}^i_{(1)} - \mathbf{A}^i_{(2)})\nu_i = (\mathbf{A}^i_{(2)} - \mathbf{A}^i_{(1)})(-\nu_i). \tag{3.38}$$

Equation (3.40) gives an expression for the flux of an arbitrary tensor field out through the bounding surface of a domain which is intersected by a surface discontinuity.

Since the mathematical and Cartesian representation of tensor components and operators are identical, Eq. (3.37) is the Cartesian tensorial form where index notation can replace the mathematical operators:

$$\int_{S(t)-\Sigma(t)} \boldsymbol{A}^i n_i \; dS = \int_{V(t)-\Sigma(t)} \boldsymbol{A}^i_{,i} \; dV - \int_{\Sigma(t)} [\![\boldsymbol{A}^i]\!]\, \boldsymbol{\nu}_i \; dS, \tag{3.39}$$

where the i^{th} component is now explicitly specified as that on which the divergence and dot product operate. Writing the integrands of Eq. (3.39) according their representation in general coordinates gives

$$\int_{S(t)-\Sigma(t)} \left(\mathbf{A}^i n_i\right) \cdot \mathbf{R} \; dS = \int_{V(t)-\Sigma(t)} \mathbf{A}^i_{,i} \cdot \mathbf{R} \; dV - \int_{\Sigma(t)} \left([\![\mathbf{A}^i]\!]\, \nu_i\right) \cdot \mathbf{R} \; dS. \tag{3.40}$$

3.6.2 Mathematical form

The introduction of the discontinuity renders the mathematical Reynolds' transport theorem, given by Eq. (3.14), invalid; thus, again consider the two domains $V_{(1)}(t)$ and $V_{(2)}(t)$. Over each domain $V_{(i)}(t)$, the Reynolds' transport theorem is valid, as the discontinuity has been effectively removed. Using Eq. (3.15b)

over $V_{(1)}(t)$ and $V_{(2)}(t)$ gives

$$\frac{d}{dt}\int\limits_{V_{(1)}(t)} \mathbf{A}(x^i,t)\ dV = \int\limits_{V_{(1)}(t)} \frac{\partial}{\partial t}\left(\mathbf{A}(x^i,t)\right)\ dV + \int\limits_{\gamma_{(1)}(t)} \mathbf{A}(x^i,t)\frac{dx^k}{dt}n_k\ dS + \int\limits_{\sigma_{(1)}(t)} \mathbf{A}_{(1)}\ \frac{dx^k}{dt}\bigg|_{\Sigma}\nu_k\ dS,$$

$$\frac{d}{dt}\int\limits_{V_{(2)}(t)} \mathbf{A}(x^i,t)\ dV = \int\limits_{V_{(2)}(t)} \frac{\partial}{\partial t}\left(\mathbf{A}(x^i,t)\right)\ dV + \int\limits_{\gamma_{(2)}(t)} \mathbf{A}(x^i,t)\frac{dx^k}{dt}n_k\ dS - \int\limits_{\sigma_{(2)}(t)} \mathbf{A}_{(2)}\ \frac{dx^k}{dt}\bigg|_{\Sigma}\nu_k\ dS,$$

where the outward flux through $\sigma_{(2)}(t)$ is in the $-\nu_k$ direction. Again a piecewise expression over then entire domain $V(t)$ is found by summing and allowing $\sigma_{(i)}(t)$ to approach $\Sigma(t)$ to give

$$\frac{d}{dt}\int\limits_{V(t)-\Sigma(t)} \mathbf{A}(x^i,t)\ dV = \int\limits_{V(t)-\Sigma(t)} \frac{\partial}{\partial t}\left(\mathbf{A}(x^i,t)\right)\ dV + \int\limits_{S(t)-\Sigma(t)} \mathbf{A}(x^i,t)\frac{dx^k}{dt}n_k\ dS + \int\limits_{\Sigma(t)} \left[\!\left[\mathbf{A}(x^i,t)\right]\!\right]\ \frac{dx^k}{dt}\bigg|_{\Sigma}\nu_k\ dS. \quad (3.41)$$

Setting $\mathbf{A}$ in Eq. (3.37) to $\mathbf{A}(x^i,t)\frac{dx^k}{dt}$ yields

$$\int\limits_{S(t)-\Sigma(t)} \mathbf{A}(x^i,t)\frac{dx^k}{dt}n_k\ dS = \int\limits_{V(t)-\Sigma(t)} \frac{\partial}{\partial x^k}\left(\mathbf{A}(x^i,t)\frac{dx^k}{dt}\right)\ dV - \int\limits_{\Sigma(t)} \left[\!\left[\mathbf{A}(x^i,t)\right]\!\right]\frac{dx^k}{dt}\nu_k\ dS.$$

Substituting into Eq. (3.41) gives

$$\frac{d}{dt}\int\limits_{V(t)-\Sigma(t)} \mathbf{A}(x^i,t)\; dV = \int\limits_{V(t)-\Sigma(t)} \left(\frac{\partial}{\partial t}\left(\mathbf{A}(x^i,t)\right) + \frac{\partial}{\partial x^i}\left(\mathbf{A}(x^i,t)\frac{dx^k}{dt}\right)\right)\; dV + \int\limits_{\Sigma(t)} \left(\left[\!\left[\mathbf{A}(x^i,t)\left(\left.\frac{dx^k}{dt}\right|_{\Sigma} - \frac{dx^k}{dt}\right)\right]\!\right]\right)\nu_k\; dS, \quad (3.42)$$

since $[\![\mathbf{A}]\!]\left.\frac{dx^k}{dt}\right|_{\Sigma} - \left[\!\left[\mathbf{A}\frac{dx^k}{dt}\right]\!\right] = \left[\!\left[\mathbf{A}(\left.\frac{dx^k}{dt}\right|_{\Sigma} - \frac{dx^k}{dt})\right]\!\right]$. This is the final mathematical form of the Reynolds' transport theorem over a domain containing a discontinuity.

3.6.3 Tensorial form

As in Sections 2.5 and 3.5, the mathematical and Cartesian representation of tensor components and operators are identical. Thus the Cartesian tensor representation of Eq. (3.42) is simply

$$\frac{d}{dt}\int\limits_{V(t)-\Sigma(t)} \boldsymbol{A}\; dV = \int\limits_{V(t)-\Sigma(t)} \left(\boldsymbol{A}_{,0} + \left(\boldsymbol{A}w^k\right)_{,i}\right)\; dV + \int\limits_{\Sigma(t)} \left([\![\boldsymbol{A}(D^k - w^k]\!]\right)\boldsymbol{\nu}_k\; dS, \quad (3.43)$$

where $\left.\frac{dy^k}{dt}\right|_{\Sigma} = D^k$ is the tensorial velocity of the shock (*cf.* Eqs. (3.35)).

Writing Eq. (3.43) in general curvilinear representation of the tensors is then

$$\frac{d}{dt}\int\limits_{V(t)-\Sigma(t)} \mathbf{A}(x^i,t)\cdot\mathbf{R}\; dV = \int\limits_{V(t)-\Sigma(t)} \left(\mathbf{A}(x^i,t)_{,0} + \left(\mathbf{A}(x^i,t)w^k\right)_{,i}\right)\cdot\mathbf{R}\; dV + \int\limits_{\Sigma(t)} \left([\![\mathbf{A}(x^i,t)(D^k - w^k]\!]\right)\nu_k\mathbf{R}\; dS. \quad (3.44)$$

Equation (3.44) is the final and most general tensorial form developed in the chapter.

Examination of Eq. (3.42) reveals that the instantaneous change inside the domain is no longer due solely to a flux through the outer boundary $V(t) - \Sigma(t)$. Change is also due to the radical jump which $\mathbf{A}(x^i, t)$ undergoes as the discontinuity moves cross the domain. The last term in Eq. (3.42) reveals a type of line source or sink along $\Sigma(t)$ which results from the discontinuity.

CHAPTER 4

CONSERVATION LAWS

Conservation laws are mathematical expressions, either integral or differential, which describe the unchanging nature of a particular quantity throughout a time-evolutionary process. Such laws originate in physical principles observed in various milieu such as traffic flow or economics. In common parlance however, the term has been broadened to include processes where the "conserved" quantity itself also evolves and is truly constant only in particular limits. Here the emphasis rests upon the principles observed in fluid flow involving shock propagation where this more liberal definition is used. It may in fact be more appropriate to consider the laws described in this chapter as "balance laws," but we retain the more common language. General conservation laws commensurate with Eqs. (2.1) are considered using discontinuous tensor fields represented according to curvilinear, time-dependent coordinates.

Using the Reynolds' transport theorem, the fundamental integral form of the tensorial conservation law is expressed. A limiting process is then used to demonstrate required balance of the net flux across the shock by the shock motion itself. The resulting tensorial differential expression is generalized, giving the conservative form of a generic system of PDE's; this conservative nature is precisely articulated. Expanding the tensorial form for the case of time dependent coordinates yielding terms which can be incorporated such that the generic conservative

form is again recovered. Lastly, a much simpler non-tensorial formulation is given which is later employed in the numerical development.

4.1 Integral conservation laws

A material volume is one which encloses the same material for all time. Such a control volume is assumed to exist under the continuum hypothesis and is simply advected with the rest of the flow. Since material volumes contain the same material for all time, Newton's laws of motion and the laws of thermodynamics may be applied to the enclosed systems resulting in a series of conservation laws. Such conservation laws take the primitive form

$$\frac{d}{dt}\int_{V_m(t)} \boldsymbol{F}\, dV = \int_{V_m(t)} \boldsymbol{B}\, dV + \int_{S_m(t)} \boldsymbol{T}^i n_i\, dS, \tag{4.1}$$

where the total change in a conserved quantity ($\boldsymbol{F}$) inside a material volume is due to the net volumetric ($\boldsymbol{B}$) and surface ($\boldsymbol{T}$) sources. Material volumes and surfaces are denoted using a subscript m.

In the case that $V_m(t)$ is intersected by a surface discontinuity, the integral over $V_m(t)$ is defined in a piecewise continuous sense; thus the operators $\int_{V_m(t)} dV$ and $\int_{V_m(t)-\Sigma(t)} dV$ are equivalent. Therefore, Eq. (4.1) may be written in general curvilinear coordinates as

$$\underbrace{\frac{d}{dt}\int_{V_m(t)-\Sigma(t)} \mathbf{F}\cdot\mathbf{R}\, dV}_{\text{expand using Eq. (3.44)}} = \int_{V_m(t)-\Sigma(t)} \mathbf{B}\cdot\mathbf{R}\, dV + \underbrace{\int_{S_m(t)-\Sigma(t)} (\mathbf{T}^i n_i)\cdot\mathbf{R}\, dS}_{\text{expand using Eq. (3.40)}}. \tag{4.2}$$

Application of Eq. (3.44) to the right hand side and employing Eq. (3.40) to ex-

pand the surface force terms yields

$$\int_{V_m(t)-\Sigma(t)} \left(\mathbf{F}_{,0} + (\mathbf{F}v^i)_{,i}\right) \cdot \mathbf{R}\, dV + \int_{\Sigma(t)} \left(\left[\!\left[\mathbf{F}(D^i - v^i)\right]\!\right] \nu_i\right) \cdot \mathbf{R}\, dS$$
$$= \int_{V_m(t)-\Sigma(t)} \mathbf{B} \cdot \mathbf{R}\, dV + \int_{V_m(t)-\Sigma(t)} \mathbf{T}^i_{,i} \cdot \mathbf{R}\, dV -$$
$$\int_{\Sigma(t)} \left(\left[\!\left[\mathbf{T}^i\right]\!\right] \nu_i\right) \cdot \mathbf{R}\, dS, \quad (4.3)$$

where $w^i_{,i} = w^i_{,i} = v^i_{,i} = v^i_{,i}$ for material volumes. Now, Eq. (4.3) is an instantaneous expression, *i.e.* it holds at every moment in time. Furthermore, the material volume in Eq. (4.3) was never specified. In fact, at a fixed time, all closed volumes are material volumes since they enclose certain material at that instant. Thus, although Eq. (4.3) was necessarily derived using a material volume, it holds for any closed volume $V(t)$.

Thus, writing Eq. (4.3) for an arbitrary volume after rearrangement gives

$$\int_{V(t)-\Sigma(t)} \left(\mathbf{F}_{,0} + \overbrace{\left(\mathbf{F}v^i - \mathbf{T}^i\right)}^{\text{outer-flux}}{}_{,i} - \mathbf{B}\right) \cdot \mathbf{R}\, dV +$$
$$\int_{\Sigma(t)} \left(\underbrace{\left[\!\left[\mathbf{F}(D^i - v^i) + \mathbf{T}^i\right]\!\right]}_{\text{inner-flux}} \nu_i\right) \cdot \mathbf{R}\, dS = 0. \quad (4.4)$$

One should note the fluxes as identified in Eq. (4.4) which have been labeled according to the surface across which they pertain.

In the limit as $V(t)$ collapses onto $\Sigma(t)$, $V(t) \to 0$ leaving only a balance of

flux terms across the discontinuity:

$$\int_{\Sigma(t)} \left(\left[\!\left[\mathbf{F}(D^i - v^i) + \mathbf{T}^i \right]\!\right] \nu_i \right) \cdot \mathbf{R} \, dS = 0. \tag{4.5a}$$

With Eq. (4.5a), the conservation law given by Eq. (4.4) reduces to

$$\int_{V(t)-\Sigma(t)} \left(\mathbf{F}_{,0} + (\mathbf{F}v^i - \mathbf{T}^i_{,i} - \mathbf{B} \right) \cdot \mathbf{R} \, dV = 0. \tag{4.5b}$$

The integrals given by Eqs. (4.5) are a fundamental expression of the conservation law for a tensor field containing a surface discontinuity.

Introduction of a surface discontinuity into the domain of the integral conservation law, Eq. (4.1), separates the law into two expressions: Eq. (4.5a) describing conservation across the shock and Eq. (4.5b) describing the conservation over the exterior of the domain.

4.2 Differential conservation laws

Differential expressions of Eq. (4.5) are now considered. The surface discontinuity's motion is governed by an algebraic balance of the flux across the shock. The domain excluding the discontinuity is governed by a system of partial differential equations (PDE's). The complete differential algebraic equation (DAE) system is then given in a general form.

4.2.1 Conservation across the shock

Since the shock surface $\Sigma(t)$ in Eq. (4.5a) is arbitrary, the integrand must be zero giving

$$\left(\left[\!\left[\mathbf{F}(D^i - v^i) + \mathbf{T}^i\right]\!\right] \nu_i\right) \cdot \mathbf{R} = 0 \qquad \text{on} \qquad \Sigma(t). \tag{4.6}$$

Equation (4.6) is simply the definition of the Cartesian representation of the zero tensor. Since the zero tensor is identical in all coordinates,

$$\left[\!\left[\mathbf{F}(D^i - v^i) + \mathbf{T}^i\right]\!\right] \nu_i = 0 \qquad \text{on} \qquad \Sigma(t). \tag{4.7}$$

Thus, conservation across the shock yields an algebraic constraint which determines the shock speed normal to $\Sigma(t)$. Together, Eqs. (4.4) and (4.7) state that there is no jump in the inner-flux across the jump.

Letting $\bar{v}^i = v^i - D^i$, Eq. (4.7) becomes

$$\left[\!\left[-\mathbf{F}\bar{v}^i + \mathbf{T}^i\right]\!\right] \nu_i = 0 \qquad \text{on} \qquad \Sigma(t). \tag{4.8}$$

Physically, $\bar{v}^i$ is the velocity relative to the shock surface. Inspection of Eq. (4.8) reveals a balance of two different mechanisms at each point on the surface: material penetrating the shock surface and forces acting on the shock surface.

4.2.2 Conservation excluding the shock

Appealing to the arbitrary nature of $V(t)$, the integrand in Eq. (4.5b) is zero. Thus, the quantity in parentheses is the zero tensor yielding

$$\mathbf{F}_{,0} + (\mathbf{F}v^i - \mathbf{T}^i)_{,i} - \mathbf{B} = 0 \qquad \text{in} \qquad V(t) - \Sigma(t), \tag{4.9}$$

which expresses conservation exclusive of the shock as a differential equation. Of particular interest is the fact that Eq. (4.9) is identical to the system of PDE's which could be formed from Eq. (4.1) without consideration of the discontinuity. In other words, the effect of the discontinuity is limited to the shock locus itself.

One should also note that an alternative tensorial form of Eq. (4.9) is given by expanding the divergence operator and replacement of the time derivative by Eq. (2.32) giving

$$\frac{\delta \mathbf{F}}{\delta t} + \mathbf{F}v^i_{,i} - \mathbf{T}^i_{,i} = \mathbf{B} \qquad \text{in} \qquad V(t) - \Sigma(t).$$

Inconveniently, this form is often classified as "non-conservative" in much of the literature to distinguish it from Eq. (4.9), even though it is obviously a tensorially equivalent expression of conservation.

4.2.3 General form

If the outer-flux distinguished in Eq. (4.4) is denoted as

$$\mathbf{f}^i = \mathbf{F}v^i - \mathbf{T}^i \qquad \text{on} \qquad \Sigma(t), \tag{4.10}$$

Eq. (4.7) can be written as

$$D^i \nu_i \left[\!\left[\mathbf{F} \right]\!\right] - \left[\!\left[\mathbf{f}^i \right]\!\right] \nu_i = 0 \qquad \text{in} \qquad V(t) - \Sigma(t).$$

While the inner-flux is continuous across the shock from Eq. (4.7), the outer-flux suffers a jump which determines the behavior of the discontinuity.

Therefore, the DAE given by Eqs. (4.7) and (4.9) expressing the conservation law, Eq. (4.1), may be written as

$$\mathbf{F}_{,0} + \mathbf{f}^i_{,i} - \mathbf{B} = 0 \qquad \text{in} \qquad V(t) - \Sigma(t) \tag{4.11a}$$

and

$$D^i \nu_i = \frac{\left[\!\left[\mathbf{f}^i \right]\!\right] \nu_i}{\left[\!\left[\mathbf{F} \right]\!\right]} \qquad \text{on} \qquad \Sigma(t). \tag{4.11b}$$

Note that Eq. (4.11b) is actually a number of equations as indicated by the tensor $\mathbf{F}$ in the denominator. There is only one value for the shock speed at every point on Σ, but there are as many jump conditions as conserved quantities; the shock speed is over-constrained.

Although it appears as though all spatial derivatives appear in a single divergence operator in Eq. (4.11a), one must remember that spatial derivatives can also appear inside the tensorial time derivative (cf. Eq. (2.28)). Nonetheless, Eqs. (4.11) do embody conservation of the quantity $\mathbf{F}$. Integrating Eq. (4.11a) over a fixed domain containing a shock gives

$$\int_{V-\Sigma(t)} \mathbf{F}_{,0} \cdot \mathbf{R} dV + \int_{V-\Sigma(t)} \mathbf{f}^i_{,i} \cdot \mathbf{R} dV - \int_{V-\Sigma(t)} \mathbf{B} \cdot \mathbf{R} dV = 0.$$

Using Eq. (3.40) the divergence term can be rewritten to give

$$\int_{V-\Sigma(t)} \mathbf{F}_{,0} \cdot \mathbf{R} dV + \int_{\Sigma(t)} \left([\![\mathbf{f}^i]\!] \, \nu_i \right) \cdot \mathbf{R} dS + \int_{S-\Sigma(t)} \left(\mathbf{f}^i n_i \right) \cdot \mathbf{R} dS - \int_{V-\Sigma(t)} \mathbf{B} \cdot \mathbf{R} dV = 0;$$

however, $[\![\mathbf{f}^i]\!] \, \nu_i = [\![\mathbf{F}]\!] \, D^i \nu_i$ on $\Sigma(t)$ from Eq. (4.11b) so that

$$\int_{V-\Sigma(t)} \mathbf{F}_{,0} \cdot \mathbf{R} dV + \int_{\Sigma(t)} \left([\![\mathbf{F}]\!] \, D^i \nu_i \right) \cdot \mathbf{R} dS + \int_{S-\Sigma(t)} \left(\mathbf{f}^i n_i \right) \cdot \mathbf{R} dS - \int_{V-\Sigma(t)} \mathbf{B} \cdot \mathbf{R} dV = 0. \quad (4.12)$$

Finally, employing Eq. (3.44) with $w^i = 0$ for a volume whose outer boundary is stationary, Eq. (4.12) becomes

$$\frac{d}{dt} \int_V \mathbf{F} \cdot \mathbf{R} dV + \int_S \mathbf{f}^i n_i \cdot \mathbf{R} dS - \int_V \mathbf{B} \cdot \mathbf{R} dV = 0, \quad (4.13)$$

where piecewise continuous integrals are denoted simply. Equation (4.13) states that the change in the total amount of $\boldsymbol{F} = \mathbf{F} \cdot \mathbf{R}$ in the domain V is equal to the amount produced by the source $\boldsymbol{B} = \mathbf{B} \cdot \mathbf{R}$ over V minus the flux of $\boldsymbol{f}^i n_i = (\mathbf{f}^i n_i) \cdot \mathbf{R}$ out of V. Thus, the conservative character of the governing equations is seen explicitly. In particular, the integral of $\boldsymbol{F}$ is increasing according to a rate which is a function of the flux of $\boldsymbol{f}^i$ over the outer boundary only.

With $\mathbf{f}^i$ defined by Eq. (4.10), Eqs. (4.1) and (4.13) express the same conservation law. One should note the difference between the integrands of the surface flux terms in Eqs. (4.1) and (4.13) arising from the different control volumes chosen. Included in Eq. (4.10) is a term corresponding to the flux of the of $\boldsymbol{F}$ across the control volume surface, whereas no such flux occurs across a volume moving with

the material.

4.3 Conservative form

In practice, considering discontinuities explicitly is often avoided; instead one manipulates the given governing PDE's into the form reminiscent of Eq. (4.11a) and then arrives at a jump condition from inspection. In fact, the form of the shock speed is assumed known *a priori*, introducing a number of subtleties into the resulting solutions. Unfortunately, inspection of such derivative forms of the governing PDE's over a domain containing discontinuities can yield a system which is inconsistent with the original physical conservation law [5].

Generalizing Eqs. (4.11a) such that the tensorial derivatives are replaced by simple partial derivatives, one has

$$\frac{\partial}{\partial t}\left(\mathbf{F}(x^i,t)\right)+\frac{\partial \mathbf{f}^{(i)}}{\partial x^i}-\mathbf{B}(x^i,t)=0 \qquad \text{in} \qquad V(t)-\Sigma(t), \tag{4.14}$$

where all terms involve simply n-tuples without any tensorial meaning ascribed to indices. In Eq. (4.14), $\mathbf{f}$ is known as the flux vector although it need not behave as a tensor. The domain is restricted to exclude the shock locus where the discontinuity renders the PDE's invalid. Equation (4.14) is known as the conservative form of the PDE's.

The system given by Eq. (4.14) is classified as hyperbolic if the Cauchy problem is well posed for it [31, pg. 42]: solutions propagate in waves along real characteristics. For such systems, the domain of dependence and the range of influence are used to geometrically describe the motion of information as the solution evolves

[4]. In the simple case of a scalar where the flux vector can be written

$$\mathbf{f} = \mathbf{f}(\mathbf{F}) \tag{4.15}$$

Eq. (4.14) is hyperbolic if the Jacobian $\frac{\partial \mathbf{f}}{\partial \mathbf{F}}$ is diagonalizable with real eigenvalues. It is strictly hyperbolic of each of the eigenvalues is unique.

4.3.1 Conservation and conservative form

The purely mathematical form, Eq. (4.14), may also be integrated over a fixed domain involving a discontinuity:

$$\int\limits_{V-\Sigma(t)} \frac{\partial}{\partial t}\left(\mathbf{F}(x^i,t)\right) dV + \int\limits_{V-\Sigma(t)} \frac{\partial \mathbf{f}^{(i)}}{\partial x^i} dV - \int\limits_{V-\Sigma(t)} \mathbf{B}(x^i,t) dV = 0.$$

Using Eq. (3.37), the divergence term can be rewritten to give

$$\int\limits_{V-\Sigma(t)} \frac{\partial}{\partial t}\left(\mathbf{F}(x^i,t)\right) dV + \int\limits_{\Sigma(t)} \left[\!\left[\mathbf{f}^{(i)}\right]\!\right] \nu_i dS + \int\limits_{S-\Sigma(t)} \mathbf{f}^{(i)} n_i dS - \int\limits_{V-\Sigma(t)} \mathbf{B}(x^i,t) dV = 0.$$

The total change in $\mathbf{F}(x^i,t)$ over the domain V is introduced through Eq. (3.42) yielding

$$\frac{d}{dt}\int\limits_{V-\Sigma(t)} \mathbf{F}(x^i,t) dV + \int\limits_{\Sigma(t)} \left[\!\left[\mathbf{f}^{(i)} - \mathbf{F}(x^i,t)\left.\frac{dx^i}{dt}\right|_{\Sigma}\right]\!\right] \nu_i dS + \int\limits_{S-\Sigma(t)} \mathbf{f}^{(i)} n_i dS - \int\limits_{V-\Sigma(t)} \mathbf{B}(x^i,t) dV = 0, \tag{4.16}$$

where $\frac{dx^i}{dt}\Big|_\Sigma = D^i - U^{(i)}$ is the shock velocity relative to the moving coordinates. Equation (4.16) is actually the modified form of a conservation law which must be satisfied by Eq. (4.14).

As demonstrated in Section 4.2.2, a single integral conservation law yields a DAE consisting of both the differential equations and the shock jump conditions; however, analysis originating solely in PDE's of the form Eq. (4.14) does necessarily produce either the jump condition or a conservation law of the form Eq. (4.13).

Now, the integral domains in Eq. (4.16) are arbitrary. In order for

$$\int_{\Sigma(t)} \left[\!\!\left[\mathbf{f}^{(i)} - \mathbf{F}(x^i,t)\, \frac{dx^i}{dt}\Big|_\Sigma \right]\!\!\right] \nu_i dS = 0,$$

the integrand itself must be zero. Thus, *if and only if* one constrains

$$\left[\!\!\left[\mathbf{f}^{(i)} - \mathbf{F}(x^i,t)(D^i - U^{(i)}) \right]\!\!\right] \nu_i = 0 \qquad \text{on} \qquad \Sigma(t) \tag{4.17}$$

(*cf.* Eq. (4.11b)), *then*

$$\frac{d}{dt}\int_V \mathbf{F}(x^i,t)dV + \int_S \mathbf{f}^{(i)} n_i dS - \int_V \mathbf{B}(x^i,t)dV = 0, \tag{4.18}$$

which is a typical conservation law (*cf.* Eq. (4.13)) where again piecewise integration is denoted simply. This last step is not trivial and should be contrasted with the analogous step in Section 4.2.2. It is necessary to impose either a jump condition or a constraint on total conservation in order that Eqs. (4.17) and (4.18) follow from Eq. (4.14).

Rearranging Eq. (4.17) gives

$$\left(D^i - U^{(i)}\right)\nu_i = \frac{[\![\mathbf{f}^{(i)}]\!]}{[\![\mathbf{F}(x^i,t)]\!]}\nu_i \qquad \text{on} \qquad \Sigma(t), \tag{4.19}$$

which contains an extra term in comparison with then tensorial jump condition Eq. (4.11b). Whereas the tensorial equation gives the shock velocity necessarily independent of any particular coordinates, the mathematical equation gives the shock motion relative to the coordinates chosen. Thus the mathematical expression subtracts off the grid velocity and gives the normal shock speed as it would be measured in the moving frame.

4.3.2 Summary remarks

Having developed the conservative form of a generic system of PDE's, a number of properties should be emphasised. First, the simple correspondence of the terms between the conservative form, Eq. (4.14), and the integral conservation law, Eq. (4.18), should be immediately apparent. It is this correspondence which gives the conservative form its useful analytic character: the conserved quantities and fluxes can be found by inspection. Thus, it is a trivial matter to substitute these quantities into Eq. (4.17) to arrive at the *a priori* shock speed.

However, a number of assumptions made in the analysis of Eq. (4.14) must also be recognized, preventing overestimation of the form's intrinsic worth. First, a system of PDE's may be manipulated into more than one conservative form which have different "conserved quantities." A simple illustrative example using

Burgers' equation in conservative form,

$$\frac{\partial u}{\partial t} + \frac{\partial}{\partial x}\left(\frac{1}{2}u^2\right) = 0, \tag{4.20a}$$

is given by [5, pg. 35]. Multiplying through by $2u$ gives the mathematically equivalent conservative form

$$\frac{\partial u^2}{\partial t} + \frac{\partial}{\partial x}\left(\frac{2}{3}u^3\right) = 0. \tag{4.20b}$$

Blindly applying Eq. (4.17) gives different results for the shock speed D. Yet the crux of the discrepancy is not that the derivatives have been incorrectly manipulated in the presence of a shock: neither of Eqs. (4.20) is more fundamental or is valid at a shock. Both satisfy Eq. (4.16) for an *arbitrary* shock speed. In fact both require conservation to be imposed at the shock from a more fundamental integral form.

Thus, the the conservative form of a system of PDE's is not i) unique or ii) more fundamental, nor does it contain iii) more information than other mathematically equivalent forms of the PDE's. Ironically, the conservative form of the PDE's neither dictates conservation across the shock or in the entire domain. To clarify that nature of the conservative form found in subsequent chapters, those for which the assumption Eq. (4.17) is valid are known as physically conservative forms.

Thus far, the most significant benefit conferred by the conservative form is the abstraction of physical principles of conservation to generic systems of PDE's. However, the real power of this mathematical form is realized in Section 6 when it is coupled with a conservative numerical scheme.

4.4 Explicit differential versions

In this section, the PDE's derived from the physical conservation law Eq. (4.1) are given explicitly. First, the first order tensorial form is expanded revealing its complexity. Rearrangement then gives a physically conservative form. This motivates seeking a simpler physically conservative form. A partial transformation is used resulting in such a form for a tensorial equation of arbitrary order. Again, the first order tensor form is given. In each case, the shock jump conditions given by Eq. (4.11b) complete the system of PDE's to give the DAE commensurate with Eq. (4.1). In this section, the domain of validity for the PDE's is assumed to exclude the shock.

4.4.1 Tensorially based forms

First, expanding the time derivative in Eq. (4.11a) using Eq. (2.28) gives

$$\frac{\partial F^i}{\partial t} + F^j U^{(i)}_{,j} - F^i_{,j} U^{(j)} + f^{ij}_{,j} = B^i. \tag{4.21}$$

Now expanding the spatial derivatives gives

$$\frac{\partial F^i}{\partial t} + F^j \left(\frac{\partial U^{(i)}}{\partial x^j} + \left\{ {}_k{}^i{}_j \right\} U^{(k)} \right) - U^{(j)} \left(\frac{\partial F^i}{\partial x^j} + \left\{ {}_k{}^i{}_j \right\} F^k \right) + \frac{\partial f^{ij}}{\partial x^j} + \left\{ {}_k{}^i{}_j \right\} f^{kj} + \frac{1}{\sqrt{g}} \frac{\partial \sqrt{g}}{\partial x^j} f^{ij} = B^i, \tag{4.22}$$

where repeated indices must still be summed. Although Eq. (4.11a) is a very compact tensorial formulation of a generic conservation law, it is practically limited in its direct application to specific problems. Because the mathematical complexity of tensorial differentiation is hidden by the subscript notion, it is generally not

trivial to implement for any one coordinate system.

Alternatively, one has $F^i_{,j}U^{(j)} = \left(F^iU^{(j)}\right)_{,j} - F^iU^{(j)}_{,j}$ and so replacing this term in Eq. (4.21) and rearrangement gives

$$\frac{\partial F^i}{\partial t} + \left(F^i(v^j - U^{(j)}) - T^{ij}\right)_{,j} = -F^iU^{(j)}_{,j} - F^jU^{(i)}_{,j} + B^i. \tag{4.23}$$

Expansion, leaving the partial derivatives of the flux on the left hand side gives

$$\begin{aligned}\frac{\partial F^i}{\partial t} + \frac{\partial}{\partial x^j}\left(F^i(v^j - U^{(j)}) - T^{ij}\right) = \\ - \left\{ {}_l{}^i{}_j \right\}(F^l(v^j - U^{(j)}) - T^{lj}) - \frac{1}{\sqrt{g}}\frac{\partial\sqrt{g}}{\partial x^j}(F^i(v^j - U^{(j)}) - T^{ij}) \\ - F^i\left(\frac{\partial U^{(j)}}{\partial x^j} - \frac{1}{\sqrt{g}}\frac{\partial\sqrt{g}}{\partial x^j}U^{(j)}\right) - F^j\left(\frac{\partial U^{(i)}}{\partial x^j} + U^{(l)}\left\{ {}_l{}^i{}_j \right\}\right) + B^i.\end{aligned} \tag{4.24}$$

Equation (4.24) is the conservative form for time-dependent coordinates. Note that although the source term in Eq. (4.24) contains derivatives, they are only derivatives of the coordinates themselves, which are guaranteed to be well defined across the discontinuity by construction.

Applying Eq. (4.19) to Eq. (4.24), one first notes that the conserved quantity is F^i, and the flux is given by $f^{ij} = F^i(v^j - U^{(j)}) - T^{ij}$. The jump condition then gives

$$\begin{aligned}\left(D^j - U^{(j)}\right)\nu_j &= \frac{[\![F^i(v^j - U^{(j)}) - T^{ij}]\!]}{[\![F^i]\!]}\nu_j \\ &= \frac{[\![F^iv^j - T^{ij}]\!]}{[\![F^i]\!]}\nu_j - \frac{[\![F^i]\!]\,U^{(j)}}{[\![F^i]\!]}\nu_j \\ &= \frac{[\![F^iv^j - T^{ij}]\!]}{[\![F^i]\!]}\nu_j - U^{(j)}\nu_j\end{aligned}$$

on $\Sigma(t)$. Therefore

$$D^j \nu_j = \frac{[\![F^i v^j - T^{ij}]\!]}{[\![F^i]\!]} \nu_j \qquad \text{on} \qquad \Sigma(t), \tag{4.25}$$

which is identical to the tensorial jump condition Eq. (4.11b). Thus Eq. (4.24) is a physically conservative form.

4.4.2 A simple conservative form

In order to arrive at a simple physically conservative form of Eq. (4.11a) valid for arbitrary time-dependent coordinates, a transformation is considered such that Cartesian components of the tensor equations are retained and written in the curvilinear coordinates.

Following the work of Viviand [32], Eq. (4.11a) is first written according to its Cartesian representation:

$$\frac{\partial \boldsymbol{F}}{\partial t} + \frac{\partial \boldsymbol{f}^i}{\partial y^i} = \boldsymbol{B}. \tag{4.26}$$

Using the chain rule gives

$$\frac{\partial \boldsymbol{F}}{\partial t} + \frac{\partial \boldsymbol{F}}{\partial x^j}\frac{\partial x^j}{\partial t} + \frac{\partial \boldsymbol{f}^i}{\partial x^j}\frac{\partial x^j}{\partial y^i} = \boldsymbol{B}, \tag{4.27}$$

introducing the curvilinear coordinates.

Now $\sqrt{g} = \left|\frac{\partial y}{\partial x}\right|$ by definition where g is the determinant of the metric tensor for the shock-fitted coordinates. In general, g will be a function of time.

Multiplying through by $\sqrt{g}$ and rearranging using the product rule gives

$$\frac{\partial}{\partial t}\left(\sqrt{g}\boldsymbol{F}\right)+\frac{\partial}{\partial x^j}\left(\sqrt{g}\boldsymbol{F}\frac{\partial x^j}{\partial t}+\sqrt{g}\boldsymbol{f}^i\frac{\partial x^j}{\partial y^i}\right) \\ -\boldsymbol{F}\underbrace{\left(\frac{\partial}{\partial t}\left(\sqrt{g}\right)+\frac{\partial}{\partial x^j}\left(\sqrt{g}\frac{\partial x^j}{\partial t}\right)\right)}_{①}-\boldsymbol{f}^i\underbrace{\frac{\partial}{\partial x^j}\left(\sqrt{g}\frac{\partial x^j}{\partial y^i}\right)}_{②}=\sqrt{g}\boldsymbol{B} \tag{4.28}$$

The derivatives of $\sqrt{g}$ are given using Eq. (3.9) as

$$\frac{\partial}{\partial y^\alpha}\left(\sqrt{g}\right)=-\frac{\partial}{\partial x^j}\left(\frac{\partial x^j}{\partial y^\alpha}\right)\sqrt{g} \tag{4.29}$$

where $\alpha\in\{0,1,2,3\}$.

Thus, expanding term ① gives

$$\begin{aligned}\frac{\partial}{\partial t}\left(\sqrt{g}\right)+\frac{\partial}{\partial x^j}\left(\sqrt{g}\frac{\partial x^j}{\partial t}\right)&=\frac{\partial}{\partial t}\left(\sqrt{g}\right)+\frac{\partial x^j}{\partial t}\frac{\partial}{\partial x^j}\left(\sqrt{g}\right)+\sqrt{g}\frac{\partial}{\partial x^j}\left(\frac{\partial x^j}{\partial t}\right)\\&=\frac{\partial}{\partial t}\left(\sqrt{g}\right)+\sqrt{g}\frac{\partial}{\partial x^j}\left(\frac{\partial x^j}{\partial t}\right)\\&=0,\end{aligned}$$

as shown from Eq. (4.29) with $\alpha=0$. Similarly term ② is expanded to

$$\begin{aligned}\frac{\partial}{\partial x^j}\left(\sqrt{g}\frac{\partial x^j}{\partial y^i}\right)&=\frac{\partial\sqrt{g}}{\partial x^j}\frac{\partial x^j}{\partial y^i}+\sqrt{g}\frac{\partial}{\partial x^j}\left(\frac{\partial x^j}{\partial y^i}\right)\\&=\frac{\partial\sqrt{g}}{\partial y^i}+\sqrt{g}\frac{\partial}{\partial x^j}\left(\frac{\partial x^j}{\partial y^i}\right)\\&=0,\end{aligned}$$

from Eq. (4.29) with $\alpha=i$.

Thus Eq. (4.28) can be simplified to the conservative form

$$\frac{\partial}{\partial t}\left(\sqrt{g}\boldsymbol{F}\right)+\frac{\partial}{\partial x^j}\left(\sqrt{g}\boldsymbol{F}\frac{\partial x^j}{\partial t}+\sqrt{g}\boldsymbol{f}^i\frac{\partial x^j}{\partial Y^i}\right)=\sqrt{g}\boldsymbol{B}, \tag{4.30a}$$

where $\sqrt{g}\boldsymbol{F}$ appears as the new conserved quantity and $\frac{\partial x^j}{\partial t}=-\frac{\partial x^j}{\partial Y^i}U^{(i)}$ is a vector with respect to the curvilinear basis, according to Eq. (2.17b). Substitution and rearrangement gives

$$\frac{\partial}{\partial t}\left(\sqrt{g}\boldsymbol{F}\right)+\frac{\partial}{\partial x^j}\left(\sqrt{g}\frac{\partial x^j}{\partial Y^i}\left(\boldsymbol{f}^i-\boldsymbol{F}\frac{\partial Y^i}{\partial t}\right)\right)=\sqrt{g}\boldsymbol{B}. \tag{4.30b}$$

One should recognize $\left(\boldsymbol{f}^i-\boldsymbol{F}\frac{\partial Y^i}{\partial t}\right)$ as the Cartesian flux of the conserved quantity $\boldsymbol{F}$ relative to the moving coordinates. Furthermore, $\frac{\partial x^j}{\partial Y}=\boldsymbol{g}^{(j)}$ is the reciprocal basis for the shock fitted coordinates. Thus using Eqs. (2.17), Eq. (4.30b) can be written in Gibbs notation as

$$\frac{\partial}{\partial t}\left(\sqrt{g}\boldsymbol{F}\right)+\frac{\partial}{\partial x^j}\left(\left(\sqrt{g}\boldsymbol{f}-\sqrt{g}\boldsymbol{F}\boldsymbol{U}\right)\cdot\boldsymbol{g}^{(j)}\right)=\sqrt{g}\boldsymbol{B}, \tag{4.30c}$$

where $\left(\sqrt{g}\boldsymbol{f}-\sqrt{g}\boldsymbol{F}\boldsymbol{U}\right)$ is simply the Cartesian flux of the new conserved quantity, $\sqrt{g}\boldsymbol{F}$. Multiplying this Cartesian tensor flux vector by $\boldsymbol{g}^{(j)}$ gives the contravariant representation of that flux component, *i.e.* one flux component is given according the the $\boldsymbol{g}_{(j)}$ basis.

If Eq. (4.30) is a physically conservative forms, then use of Eq. (4.19) will

reduce to the actual shock speed. Application of Eq. (4.19) to Eq. (4.30a) gives

$$\begin{aligned}\left(D^j - U^{(j)}\right)\nu_j &= \frac{\left[\!\left[\sqrt{g}\boldsymbol{F}\frac{\partial x^j}{\partial t} + \sqrt{g}\boldsymbol{f}^i\frac{\partial x^j}{\partial y^i}\right]\!\right]}{\left[\!\left[\sqrt{g}\boldsymbol{F}\right]\!\right]}\nu_j \\ &= \frac{\sqrt{g}\left[\!\left[\boldsymbol{F}\right]\!\right]\frac{\partial x^j}{\partial t}\nu_j + \sqrt{g}\left[\!\left[\boldsymbol{f}^i\right]\!\right]\frac{\partial x^j}{\partial y^i}\nu_j}{\sqrt{g}\left[\!\left[\boldsymbol{F}\right]\!\right]} \\ &= \frac{\left[\!\left[\boldsymbol{f}^i\right]\!\right]}{\left[\!\left[\boldsymbol{F}\right]\!\right]}\nu_i - U^{(j)}\nu_j, \end{aligned} \tag{4.31}$$

where all quantities are evaluated at the shock. Thus, once again the correct shock speed, Eq. (4.11b), is given and Eqs. (4.30) are a physically conservative form.

Lastly, consider generalizing Eqs. (4.30) and (4.31) such that none of the hidden indices are tensorial. Although the introduction of Eq. (4.26) was done assuming that all quantities were Cartesian tensors, there is never a step in the subsequent development with transforms any of them to a curvilinear representation. This is important for later numerical development where $\boldsymbol{F}$, $\boldsymbol{f}^i$, and $\boldsymbol{B}$ are taken to be a concatenation of physically conservative Cartesian conservation laws. Retaining the tensorial character of the explicit i^{th} order of $\boldsymbol{f}^i$ provides for an interpretation of the "flux vector" in a curvilinear direction, according Eq. (4.30c).

CHAPTER 5

SHOCK-FITTING

Shock-fitting is an analytic technique for effectively removing a discontinuity from a flow. A coordinate line is constrained *a prior* to conform exactly to the shock locus, *i.e.* fitted. By isolating the discontinuity along a single coordinate line, the remaining solution domain is split into two partitions; neither of these contains the fitted shock. The solutions over each sub-domain can be found using different techniques and matched at the discontinuity by balancing the outer-flux along the shock coordinate line.

From a numerical perspective, the key benefit shock-fitting confers is the potential for a high rate of convergence of the numerical solution, provided a high order method is used and all shocks are fitted. Since the shock is fitted to the numerical grid, there is no smearing of the shock locus or need for interpolation between grid points to track the shock. Disadvantages of this method include the inability to deal with shocks which unexpectedly evolve in the domain and a practical restriction to simple shock contours.

This solution technique has a variety of applications. It is often referred to in the solution of moving or free boundary problems. Alexiades and Solomon [3] give a good introduction to the general method and apply this technique to the study of phase transitions. Moretti *et al.* [11, 12] apply this technique to solve problems involving inert shocks. Valorani *et al.* [33] coupled shock-fitting with non-trivial

reaction kinetics, developing a numerical method solving non-equilibrium shocked flows around blunt bodies. More recently, Brooks [14] has also used this technique to accurately model supersonic flow around a blunt body with spectral accuracy.

In this chapter, only a single fitted shock is considered. In order to augment the robustness of the chosen solution technique, a conservative numerical formulation is chosen. When combined with a conservative numerical discretization, the resulting scheme correctly captures unanticipated shocks; however, such captured shocks degrade the accuracy of the solution to first order at best.

5.1 Shock evolution equations

Denoting the shock as Σ, the fitted coordinates are defined such that

$$\Sigma : \quad x^2(y^i, t) = 0. \tag{5.1}$$

Equation (5.1) is an implicit function defining $x^2 = 0$ to be a curve in the Cartesian space which gives the exact location of the shock. In order for a transformation satisfying Eq. (5.1) to be proper, it must exist for all (y^1, y^2, t) and (x^1, x^2, t). The general form of such a transformation is given in Eqs. (2.13) and is guaranteed to exist and be invertible if the total Jacobian of the transformation, $\frac{\partial x}{\partial y}$, does not vanish in the region of interest:

$$\begin{vmatrix} \frac{\partial x^1}{\partial y^1} & \frac{\partial x^2}{\partial y^1} & \frac{\partial t}{\partial y^1} \\ \frac{\partial x^1}{\partial y^2} & \frac{\partial x^2}{\partial y^2} & \frac{\partial t}{\partial y^2} \\ \frac{\partial x^1}{\partial t} & \frac{\partial x^2}{\partial t} & \frac{\partial t}{\partial t} \end{vmatrix} \neq 0. \tag{5.2}$$

Tensors described according to such time-dependent coordinates are described in Section 2.6. The associated metrics are given in Appendix B.

5.1.1 Shock kinematics

Along the coordinate line fitted to the shock, the grid kinematic terms introduced in Section 2.6.1 must now be interpreted in terms of the shock motion. Since $\frac{\partial}{\partial t}$ is the derivative with respect to time keeping the shock coordinates constant, $U^{(i)}\big|_{\Sigma} = \frac{\partial y^i}{\partial t}$ is the velocity of the shock coordinates relative to the Cartesian frame. Conversely $\frac{\partial x^i}{\partial \tau}$ is the velocity of the Cartesian position relative to the shock-attached frame. The Cartesian representation $\frac{\partial y^i}{\partial t}$ of the vector $\boldsymbol{U}$ admits an intuitive geometrical interpretation, while $-\frac{\partial x^i}{\partial \tau}$ are the components according to the contravariant shock-attached bases, which in general are non-orthogonal.

A mathematical description of the shock and its evolution over time is needed. Thus, consider the shock to be described by a level curve

$$\Sigma(y^i, \tau) = 0.$$

The time rate of change of such a curve is

$$\frac{\partial \Sigma}{\partial t} = \frac{\partial \Sigma}{\partial \tau} + \frac{\partial \Sigma}{\partial y^i}\frac{\partial y^i}{\partial t} = 0 \tag{5.3a}$$

where $\frac{\partial y^i}{\partial t} = U^{(i)}\big|_{\Sigma} = D^i$ is the shock velocity and $\frac{\partial \Sigma}{\partial y^i}$ is simply the gradient of the level curve Σ. Since

$$\frac{\partial \Sigma}{\partial y^i} = |\nabla \Sigma| \, n_i, \tag{5.3b}$$

where n_i is the unit vector normal to Σ and $\nabla\Sigma$ is the spatial gradient, Equation (5.3) may then be rewritten as

$$\frac{\partial \Sigma}{\partial t} + |\nabla\Sigma| \, D^i n_i = 0, \tag{5.3c}$$

or, denoting the scalar detonation speed in the normal direction as D_n,

$$\frac{\partial \Sigma}{\partial t} + D_n \, |\nabla\Sigma| = 0. \tag{5.3d}$$

Note that the sign convention for D_n is determined by the direction of n_i. Equations (5.3) are kinematic in nature, giving a mathematical constraint which must be satisfied in order for Σ to describe the shock. In particular, Eqs. (5.3) state that the change in Σ with respect to time must balance that caused by the curve's motion in space. Thus $-\frac{\partial \Sigma}{\partial t}$ is a measure of the total change in Σ at a given position in order that the $\Sigma = 0$ level curve will continue to coincide with the shock.

Here, the primary concern is the movement of the shock surface in which shock-fitted coordinates have been embedded; the shock is defined to lie along $x^2 = 0$, and the level curves of the surface Σ are simply x^2 coordinate lines. Letting $\Sigma = x^2$ in Eq. (5.3a) gives

$$\frac{\partial x^2}{\partial t} + \frac{\partial x^2}{\partial y^i} \frac{\partial y^i}{\partial t} = 0, \tag{5.4}$$

which one should compare with Eq. (2.15). In particular, Eq. (5.4) is simply the transformation rule for the grid velocities. In other words, the level set equation

is identical the tensor transformation rule in the x^2 direction.

$$U^{(2)} = \frac{\partial x^2}{\partial Y^i} U^{(i)} \qquad \text{or} \qquad U^{(2)} = \boldsymbol{g}^{(2)} \cdot \boldsymbol{U},$$

according to Eqs. (2.17b) and (2.18a).

Furthermore, with $\Sigma = x^2$, the gradient of the level curve becomes

$$\frac{\partial \Sigma}{\partial Y^i} = \left.\frac{\partial x^2}{\partial Y^i}\right|_{\Sigma} = \boldsymbol{g}^{(2)}|_{\Sigma}, \tag{5.5}$$

i.e. the gradient is simply the reciprocal basis vector normal to the shock surface. Thus the unit normal $\boldsymbol{n}$ in Eq. (5.3c) is simply

$$\boldsymbol{n} = \boldsymbol{e}^{(2)}|_{\Sigma}. \tag{5.6}$$

One should note that restricting the shock to lie along $x^2 = 0$ requires the the contravariant basis vector $\boldsymbol{g}_{(1)}\big|_{\Sigma}$ to be tangent to the shock. This in agreement with the definition of the normal, Eq. (5.6), since $\boldsymbol{g}^{(2)}$ is everywhere perpendicular to $\boldsymbol{g}_{(1)}$ by construction.

The unit normal can be written according to the covariant basis as

$$\boldsymbol{n} = n_1 \, \boldsymbol{g}^{(1)}\big|_{\Sigma} + n_2 \, \boldsymbol{g}^{(2)}\big|_{\Sigma} \tag{5.7}$$

$$= n_2 \, \boldsymbol{g}^{(2)}\big|_{\Sigma} \,, \tag{5.8}$$

since $\boldsymbol{n} \parallel \boldsymbol{g}^{(2)}\big|_{\Sigma}$. Furthermore, since $\boldsymbol{n}$ is a unit vector,

$$\boldsymbol{n} \cdot \boldsymbol{n} = 1 = (n_2)^2 \left(\boldsymbol{g}^{(2)} \cdot \boldsymbol{g}^{(2)} \right) \Big|_{\Sigma} \tag{5.9}$$

$$= (n_2)^2 \, g^{22}\big|_{\Sigma} \, , \tag{5.10}$$

or

$$n_2 = \frac{1}{\sqrt{g^{22}\big|_{\Sigma}}}, \tag{5.11}$$

where the positive root is choosen since $\boldsymbol{n}$ and $\boldsymbol{g}^{(2)}\big|_{\Sigma}$ are in the same direction. Equation (5.11) gives a simple relationship between the covariant representation of $\boldsymbol{n}$ and the conjugant metric tensor.

Along the coordinate line $x^2 = 0$, the grid motion is coincident with the shock: $\boldsymbol{U}|_{\Sigma} = \boldsymbol{D}$ and, consequently, $U^{(2)}\big|_{\Sigma} = D^2$. Therefore at the shock, Eqs. (2.18c) and (2.19) give

$$D^2 = D_n \sqrt{g^{22}|_{\Sigma}}, \tag{5.12a}$$

$$D(2) = \frac{D_n}{\cos \alpha}, \tag{5.12b}$$

respectively. Replacing $g^{22}|_{\Sigma}$ in Eq. (5.12a) using Eq. (5.11) gives

$$D^2 = \frac{D_n}{n_2}. \tag{5.12c}$$

Equations (5.12) give different froms of the kinematic constraint imposed on the grid motion by requiring the shock be fitted to an x^2 coordinate line.

5.1.2 Shock dynamics

Thus far, the development of the shock motion has remain purely kinematic by refraining from relating the shock motion to the forces in the flow. The motion of such shocks due to the discontinuity which they introduce into the flow field is derived in detail in Section 4.2.3. The resulting constraint is given in Eq. (4.11b) in which the jump in the surface forces across the shock is balance by the flux of the conserved quantity induced by the shock's motion.

Now $\boldsymbol{\nu}$ in Eq. (4.11b) is constrained to be normal to the shock surface, but its direction is arbitrary (*cf.* Section 3.38). In order to connect the kinematic constraint give by Eqs. (5.12) with the kinetic constraint given in Eq. (4.11b), the constraint

$$\mathbf{n} \equiv \boldsymbol{\nu} \tag{5.13}$$

is imposed forcing the unit normal to the shock to be chosen according to the gradient of level surface describing the shock. Equation (5.13) is essentially a geometric constraint giving the shock curve a specific orientation, fixing the sign convention of the jump operator to be in the direction dictated by the shock-fitted transformation.

Writing Eq. (4.11b) for a Cartesian representation gives

$$D_n \equiv D^i n_i = \frac{[\![\boldsymbol{f}^i]\!]}{[\![\boldsymbol{F}]\!]} n_i, \tag{5.14}$$

where Eq. (5.13) has been enforced. All jump operators are understood to be evaluated at the Σ unless otherwise noted. As noted in Section 4.2.3, Eq. (5.14) gives a jump condition on the shock speed for every conserved quantity. Since

each is equivalent, one may choose any of the jump conditions. Such ambiguity is denoted by $\boldsymbol{F}$ in the denominator.

In order to integrate the kinematic and kinetic constraints, substitute Eq. (5.14) into Eq. (5.3d) giving

$$\frac{\partial \Sigma}{\partial t} + \frac{[\![\boldsymbol{f}^i]\!]}{[\![\boldsymbol{F}]\!]} \frac{\partial \Sigma}{\partial y^i} = 0 \tag{5.15}$$

after use of Eq. (5.3b). Now, the surface of which Σ is a contour is continuous and so may be brought into the jump operator to give

$$\frac{\partial \Sigma}{\partial t} + \frac{\left[\!\!\left[\boldsymbol{f}^i \frac{\partial \Sigma}{\partial y^i} \right]\!\!\right]}{[\![\boldsymbol{F}]\!]} = 0. \tag{5.16}$$

Now $\Sigma = x^2$, so substituting from Eq. (5.5) gives

$$\left. \frac{\partial x^2}{\partial t} \right|_\Sigma + \frac{[\![\boldsymbol{f} \cdot \boldsymbol{g}^{(2)}]\!]}{[\![\boldsymbol{F}]\!]} = 0, \tag{5.17}$$

5.1.3 Geometric interpretation

In order to clarify Eqs. (5.12) and (5.14), consider Eq. (2.17a) at the shock:

$$\frac{\partial x^i}{\partial t} + \frac{\partial x^i}{\partial y^j} \frac{\partial y^j}{\partial t} = 0 \qquad \text{on} \qquad \Sigma,$$

which is the relationship between the shock velocity in curvilinear and Cartesian coordinates. The term $\left. \frac{\partial y^j}{\partial t} \right|_\Sigma$ gives the shock velocity; however, *only one* of the shock coordinates actually designates that the shock is being followed. In this case, $x^2 = 0$ is all that is required in order to be fixed to the shock. The other coordinate, x^1, identifies the particular *shock surface particle* which is being followed,

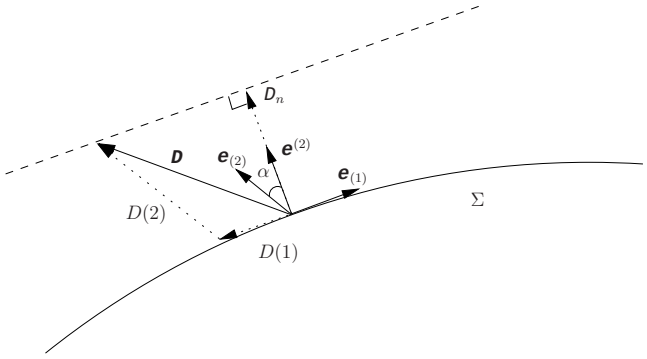

Figure 5.1. D_n and the physical components of $\mathbf{D}$.

as defined by the transformation. Such particles have no physical significance, serving only to uniquely identify each part of the shock surface. The motion of the x^1 coordinate is thus unconstrained, contributing only to the artificial tangential component of the shock velocity, whereas the jump conditions, Eqs. (5.14), constrain the the evolution of the x^2 coordinate normal to the shock.

Figure 5.1 shows the geometry involved. The normalized contravariant basis vectors, $\boldsymbol{e}_{(1)}$ and $\boldsymbol{e}_{(2)}$, are used to give the physical components of the velocity vector, $D(1)$ and $D(2)$. The corresponding reciprocal base vector normal to Σ is also shown. The angle α, as introduces in Section 2.6.1, is measured between basis vectors for two different coordinate systems; in general, α is not the angle between the grid velocity vector and the normal.

The remaining degree of freedom for the two-dimensional shock velocity manifests itself through the artifical component tangent to the shock. As seen, the physical component counterparts of both $-\frac{\partial x^1}{\partial t}\Big|_\Sigma = D^1$ and $-\frac{\partial x^2}{\partial t}\Big|_\Sigma = D^2$ partially determine this tangential component of the shock velocity, while $D(2) = D^2 \sqrt{g_{22}}\big|_\Sigma$ alone determines the normal shock velocity. At the illustrated point, the total

shock velocity can be any vector between the origin and the dotted line, effectively fixing the $D(2)$ component such that the shock-fitted constraint $\boldsymbol{D}\cdot\boldsymbol{e}^{(2)} = D_n$ is satisfied. From Fig. 5.2, it is clear that $D(2) \geq D_n$ due to the motion (or non-motion) of the x^1 coordinate embedded in the shock surface.

Of particular interest in the detonation community is the propagation of a shock along a particular line, for instance the centerline of a charge. Such a quantity is known as the phase speed, D_o, and is most easily defined as the speed of the intersection point between the shock surface and a line. The phase speed can be found by fixing the x^1 coordinate lines parallel to the line of interest. This both aligns $\boldsymbol{g}_{(2)}$ in the correct direction and forces $D^1 = 0$. The phase speed is then simply given by

$$D_o = D(2), \tag{5.18}$$

which gives a measure of the velocity of the shock surface particles which have been constrained to move only along x^1 coordinate lines.

5.1.4 A simple example

At this point, the major features of shock level curve and its associated grid velocity have been developed; nonetheless, a simple example will help to clarify the meaning of Eqs. (5.12) and (5.18). Consider a shock described by

$$\Sigma : x^2(y^1, y^2, t) = 0.$$

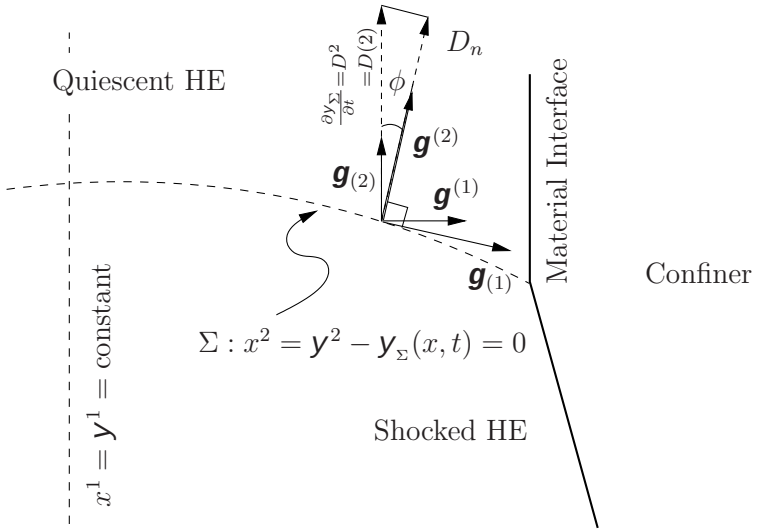

Figure 5.2. Generalized shock motion in curvilinear coordinates.

Provided that $\frac{\partial x^2}{\partial y^2} \neq 0$, this serves to implicitly define $y^2 = y_\Sigma(y^1, t)$. Thus, a transformation between the two coordinate systems is defined according to

$$\begin{aligned} x^1 &= y^1, \\ x^2 &= y^2 - y_\Sigma(y^1, t), \end{aligned} \tag{5.19}$$

consistent with the definition of Σ as $x^2 = 0$. Application of this transformation to the model problem is seen in Fig. 5.2. In particular, note that y^1 coordinate lines are fixed parallel to the undeflected material interface.

First, it is clear from Eqs. (2.17b) and (5.19) that the grid velocity $\boldsymbol{D}$ along the shock can be represented according to the the shock-fitted or Cartesian basis as

$$D^i = -\left.\frac{\partial x^i}{\partial t}\right|_\Sigma = \begin{pmatrix} 0 \\ \frac{\partial y_\Sigma}{\partial t} \end{pmatrix} \qquad \text{and} \qquad D^i = \left.\frac{\partial y^i}{\partial t}\right|_\Sigma = \begin{pmatrix} 0 \\ \frac{\partial y_\Sigma}{\partial t} \end{pmatrix},$$

where $\frac{\partial y_\Sigma}{\partial t} = \frac{\partial y_\Sigma}{\partial t}$ from Eqs. (2.14) and (5.19). Note that $D^i = D^i$ for this simple transformation. Having fixed x^1 coordinate lines accordingly, the phase speed along the unshocked material interface is given by $D_o = D(2)$.

The contravariant and covariant basis vectors are calculated to be

$$\boldsymbol{g}_{(1)} = \begin{pmatrix} 1 \\ \frac{\partial y_\Sigma}{\partial x^1} \end{pmatrix}, \qquad \boldsymbol{g}_{(2)} = \begin{pmatrix} 0 \\ 1 \end{pmatrix}, \qquad \boldsymbol{g}^{(1)} = \begin{pmatrix} 1 \\ 0 \end{pmatrix}, \qquad \text{and} \qquad \boldsymbol{g}^{(2)} = \begin{pmatrix} -\frac{\partial y_\Sigma}{\partial y^1} \\ 1 \end{pmatrix},$$

where $\frac{\partial y_\Sigma}{\partial x^1} = \frac{\partial y_\Sigma}{\partial y^1}$ is known in the literature as the shock slope. Note that for this example, $\boldsymbol{e}_{(2)} = \boldsymbol{g}_{(2)}$ since $g_{22} = \boldsymbol{g}_{(2)} \cdot \boldsymbol{g}_{(2)} = 1$; thus, the contravariant and physical component are identical: $D(2) = D^2$.

Since $g^{22} = \boldsymbol{g}^{(2)} \cdot \boldsymbol{g}^{(2)} = 1 + \left(\frac{\partial y_\Sigma}{\partial y^1}\right)^2$, Eq. (5.12a) gives an expression relating D^2 to either the shock slope or its arc length:

$$\begin{aligned} D^2 &= D_n \sqrt{1 + \left(\frac{\partial y_\Sigma}{\partial y^1}\right)^2} \\ &= D_n \frac{ds}{dy^1}, \end{aligned} \tag{5.20}$$

where s is the arc length along the shock. Equations (5.20) reiterate the fact the D^2 is related to D_n through the shock geometry. Since in this case $D^2 = D(2) = D_o$, Eq. (5.20) can be rewritten

$$D_o = \frac{\partial y_\Sigma}{\partial t} = D_n \sqrt{1 + \left(\frac{\partial y_\Sigma}{\partial y^1}\right)^2}, \tag{5.21}$$

a result which is verified by Stewart and Bdzil [34].

In the literature, it is more common to see the the phase speed written as $\frac{\partial y_\Sigma}{\partial t}$. Such a notion implicitly assumes a coordinate transformation of the form

Eq. (5.19). For steady shock waves, the shape of y_Σ is constant giving a phase speed which is not just independent of t but y^1 as well. The phase speed is a particularly important quantity since it can be empirically measured during the sandwich test.

The geometric interpretation is made complete by considering Eq. (5.12b) where α is simply the angle between the shock normal and $\boldsymbol{g}_{(2)}$. Since in this case $D^1 = 0$ and the unshocked HE is stationary, α is identical to ϕ, the shock angle as introduced in Appendix G.7.

In three dimensions, a similar geometric interpretation is possible.

5.2 Shock-fitted conservation laws

The representation of conservation laws according to time-dependent coordinates, such as those used in shock fitting, is explored in depth in Section 4. In particular, three first order formulations given by Eqs. (4.22), (4.24), and (4.30) are derived, the last two of which are physically conservative formulations. While it is not necessary to choose a conservative formulation to implement shock-fitting, such a formulation is selected foreseeing the use of a conservative numerical method to capture unanticipated shocks. The remainder of this work is focused on the form given by Eq. (4.30), in which transformation chosen retains the Cartesian tensor components. The main motivation for this choice is its simplicity; although, the completely transformed system, Eq. (4.24), may also be used and may provide for a more simple implementation of boundary conditions.

For both formulations, the shock jump conditions in the shock-fitted coordinates reduce to constraints in which the shock speed does not explictly appear.

For shock fitted coordinates, $U^{(i)}\big|_{\Sigma} = D^i$ reducing Eq. (4.19) to

$$\left.\frac{dx^i}{dt}\right|_{\Sigma} = \frac{[\![\mathbf{f}^{(i)}]\!]}{[\![\mathbf{F}(x^i,t)]\!]}\nu_i = 0.$$

Thus two facts are clarified. First, the shock is stationary in the transformed system as expected. Second, the outer-flux of the shock-attached formulation is continuous across the shock, effectively concealing the shock speed. Just as a moving observer cannot determine his own speed without reference to another frame, it impossible to determine the physical shock speed exclusively from quantities measured in the shock-attached frame. Therefore, use must be made of the jump conditions as measured in the lab frame to complete the system.

5.3 Summary of conservative form with constraints

Thus far, the development of shock fitted conservation laws has resulted in a differential algebraic system of equations. The general form of the conservation law is given by Eq. (4.30a) as

$$\frac{\partial}{\partial t}\left(\sqrt{g}\boldsymbol{F}\right) + \frac{\partial}{\partial x^j}\left(\sqrt{g}\boldsymbol{F}\frac{\partial x^j}{\partial t} + \sqrt{g}\boldsymbol{f}^i\frac{\partial x^j}{\partial y^i}\right) = \sqrt{g}\boldsymbol{B}. \tag{4.30a}$$

One could substitute Eq. (4.24) for Eq. (4.30a) without sacrificing the conservative form of the governing PDE's. Fitting the coordinates to the shock yields two constraints at the shock surface. The first is kinematic and given by Eq. (5.12a) as

$$D^2 = -\left.\frac{\partial x^2}{\partial t}\right|_{\Sigma} = D_n\sqrt{g^{22}\big|_{\Sigma}}. \tag{5.12a}$$

Examination of the kinematic constraint gives the temporal metric, or grid speed, in terms of the D_n and the spatial metric g^{22} (*cf.* Eq. (B.5b)). The second dynamic constraint, given by Eq. (5.14), dictates the normal shock speed through the jump conditions to be

$$D_n = \frac{[\![\boldsymbol{f}^i]\!]}{[\![\boldsymbol{F}]\!]} n_i = \frac{[\![\mathbf{f}^i]\!]}{[\![\mathbf{F}]\!]} n_i, \tag{5.14}$$

where the geometric constraint, Eq. (5.13), has been assumed; thus, the $[\![\,]\!]$ operator is defined as the difference in the direction of $\boldsymbol{g}^{(2)}$.

A single constraint embodying both Eqs. (5.12a) and (5.14) is given by Eqs. (5.17):

$$\left.\frac{\partial x^2}{\partial t}\right|_{\Sigma} = -\frac{[\![\boldsymbol{f} \cdot \boldsymbol{g}^{(2)}]\!]}{[\![\boldsymbol{F}]\!]}, \tag{5.17}$$

describing the motion of the of the shock fit coordinate line it terms of the jump in the Cartesian representation of the conserved quantities, $\boldsymbol{F}$. Alternatively, this constraint may be expressed compactly in terms of a jump in $\mathbf{F}$, the curvilinear representation of the conserved quantities. Substituting Eq. (5.14) into Eq. (5.12a) gives

$$\begin{aligned} -\left.\frac{\partial x^2}{\partial t}\right|_{\Sigma} &= \frac{[\![\mathbf{f}^i]\!]}{[\![\mathbf{F}]\!]} n_i \sqrt{g^{22}|_{\Sigma}} \qquad \text{or} \\ &= \frac{[\![\mathbf{f}^2]\!]}{[\![\mathbf{F}]\!]}, \end{aligned} \tag{5.22}$$

after substituting from Eq. (5.11), with n_1 identically zero. For the case that $\boldsymbol{F} = F = F$ is a scalar, $\boldsymbol{f} = f^i$ is a vector so that $\boldsymbol{f} \cdot \boldsymbol{g}^2 \equiv f^2$ and Eqs. (5.17) and (5.22) are equivalent.

CHAPTER 6

NUMERICAL TECHNIQUES

As discussed in Section 1, the numerical method of interest is a shock-fitting scheme which will accurately resolve the relevant structures at the intersection of the material interface and the shock locus. The use of a discretely conservative scheme away from the fitted shock allows the method to correctly capture unanticipated shocks in the interior of the domain. The relevant preliminary numeric concepts to be considered are conservation, weighted essentially non-oscillatory (WENO) schemes, and Local Lax-Friedrichs flux splitting. A brief presentation of the novel conservative numerical scheme, developed by Henrick *et al.* [35] for this work is given.

In the development of the numerical schemes in this chapter, a one-dimensional analogue is used which can be easily extended to multiple dimensions. The uniform grid spacing shown in Fig. 6.1, is assumed. The position of node i is denoted by x_i where $i = 0, 1, \ldots, N_x$. Similarly, functional values at node i will be denoted by a subscript i ($e.g$ $f_i = f(x_i)$). Half indices indicate the edge of cells across which fluxes will be calculated. Spacing is maintained such that $x_i = x_0 + i\Delta x$, where $\Delta x = \frac{x_{N_x} - x_0}{N_x}$.

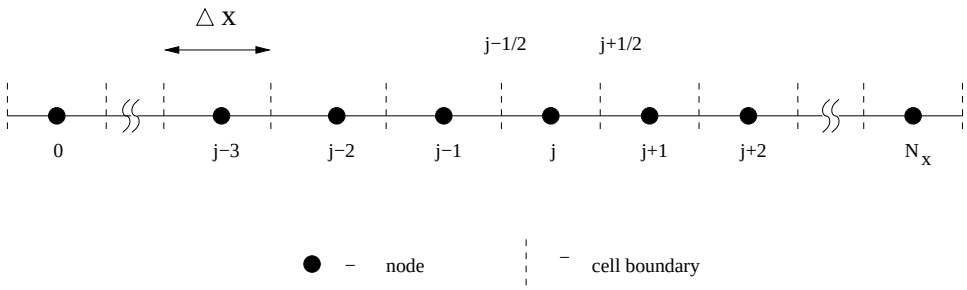

Figure 6.1. Uniform grid spacing discretization and node labeling.

6.1 Conservative numerical solvers

The role of conservation in the development of numerical solutions to hyperbolic equations involving shock waves is outlined by LeVeque [5]. There are two different primary meanings that conservation can have in this context. First, it is used to classify a particular type of hyperbolic PDE. This was clarified in Section 4.3. Second, it is used to describe a particular type of numerical method. Explanation of such methods is the purpose of this section.

One should note that the conservative form developed in Chapter 4 and utilized here is more general than forms traditionally considered in the numerical community (see Refs. [4, 5]). Because the rate term in Eq. (2.1e) acts as a distributed source, notions of conservation and the conservative form where developed to include a general source term. For a given Arrhenius reaction scheme, this source term will be approximately zero except in localized neighborhoods in the reaction zone. Addition of such source terms is not a trivial matter. In particular, conservation laws involving stiff source terms are considered by LeVeque and Yee [36]. Their analysis reveals the absolute necessity of resolving the effect of these source terms in order to propagate captured shocks at correct wave speeds.

Conservative numerical schemes guarantee that captured shocks propagate correctly, although they may be smeared due to numerical viscosity. This is demonstrated by the integral of the conserved quantity increasing at the correct rate [5, pg. 129]. The addition of a distributed source term to the model should be reflected in any numerical approximation by a global dependence on the total rate of production due to that source term.One must keep in mind, however, that discrete conservation does not guarantee that all discontinuities are captured correctly [5]. In particular a conservative numerical scheme can also yield weak solutions which are non-physical.

In physical fluid flows which experience large gradients in velocity, the fluid viscosity acts to regulate the flow and prevents discontinuities from forming. The desired weak solutions of the hyperbolic model problem are those are those observed in the limit of vanishing viscosity; thus, non-physical weak solutions are also known as non-viscosity limiting solutions. Such weak solutions are particularly relevant for conservative shock capturing methods since many practical examples exist in which a conservative numerical scheme does not converge to the physical solution. Almost all of these examples involve a sonic rarefaction which is captured and propagated as a shock. Such solutions are correct in the weak sense but, nonetheless, non-physical. Since a rarefaction is an isentropic process, such weak solutions are known in the literature as entropy violating. Refs. [4, 5] outline a number of corrections allowing conservative schemes to converge to the physically correct sonic rarefaction solution.

6.1.1 Numerical conservation

Numerically conservative schemes are valuable because they propagate discontinuities at the correct speeds. In order to achieve this goal, use is made of a physically conservative form of the governing PDE's, Eq. (4.14). As seen in Section 4.3, the analytic solution to such governing PDE's does not necessarily satisfy the desired global conservation of the conserved quantities, Eq. (4.18); however, *if* such global conservation is satisfied, *then* the analytic solution does propagate shocks at the desired physical shock speeds.

Thus, a consistent, stable numerical discretization of a conservative form which enforces global conservation should converge to the analytic solution that propagate shocks at the correct speed. Such a numerical scheme will be called conservative. To form a conservative discretization of Eq. (4.14), consider a physically conservative one-dimensional form:

$$\frac{\partial F}{\partial t} + \frac{\partial f}{\partial x} - B = 0, \tag{6.1a}$$

which should should satisfy Eq. (4.19)

$$D - U = \frac{[\![f]\!]}{[\![F]\!]}. \tag{6.1b}$$

The constraint on global conservation, Eq. (4.18), becomes

$$\frac{d}{dt} \int_{x_{-1/2}}^{x_{N_x+1/2}} F dx + f(x_{N_x+1/2}) - f(x_{-1/2}) - \int_{x_{-1/2}}^{x_{N_x+1/2}} B dx = 0, \tag{6.2}$$

where $x \in [x_{-1/2}, x_{N_x+1/2}]$ is the fixed numerical domain. Again, the integral of F

is increasing according to a rate which is a function of the flux of f over the outer boundary only.

A simple and intuitive way of ensuring discrete conservation is by using a central difference operator to approximate the spatial derivative and requiring that a single flux be used to define the flux both in and out of a cell. An illustration of the flux requirement is seen in Fig. 6.2. Approximating the spatial derivative in Eq. (6.1a) with the central difference operator yields

$$\frac{dF_i}{dt} + \frac{f_{i+1/2} - f_{i-1/2}}{\Delta x} - B_i = 0. \tag{6.3}$$

Multiplying this equation by Δx and summing over the $N_x + 1$ nodes gives

$$\frac{d}{dt}\left(\sum_{i=0}^{N_x} F_i \Delta x\right) + \left(f_{N_x+1/2} - f_{-1/2}\right) - \sum_{j=0}^{N_x} B_j \Delta x = 0.$$

Comparing this equation to Eq. (6.2), it is clear that the chosen discretization yields a conservative numerical scheme.

6.1.2 WENO schemes

In formulating the exact form of the spatial derivative to be used in Eq. (6.3), one may ask how to retain the conservative nature of the scheme and simultaneously increase its accuracy. Also important for consideration is the reduction of spurious oscillations in approximate numerical solutions containing discontinuities. This section gives the history and development of schemes which address both these issues. A particular scheme developed for this work by Henrick *et al.* [35] is given in detail.

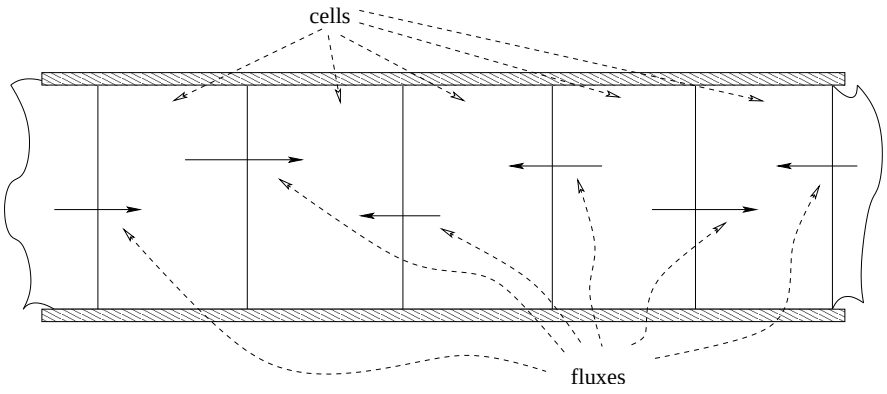

Figure 6.2. Conservation as a constraint on inter-cell fluxes.

6.1.2.1 History

Development of conservative numerical schemes is founded on the work of Van Leer [37, 38]. Later, Harten *et al.* [39] introduced Essentially Non-Oscillatory (ENO) schemes. Instead of using a single fixed stencil to approximate numerical fluxes, an r^{th} order ENO scheme uses a set of r candidate stencils. A measure of smoothness, known in the literature as the indicator of smoothness, is used to determine how smooth the solution is over each stencil. The stencil over which the solution is smoothest is then chosen in an attempt to diminish the effect of a discontinuity on neighboring cells. This method was further developed by Shu and Osher [40, 41] who introduced pointwise ENO schemes which involve significantly fewer computations for multidimensional problems with inhomogeneous source terms than their cell averaged counterparts.

Subsequently, Liu *et al.* [42] introduced Weighted ENO (WENO) schemes, again using a cell-averaged approach. In such schemes, spatial derivatives are calculated using a convex combination of the numerical fluxes associated with each candidate stencil. This is accomplished by weighting the contribution of each flux

according to the smoothness of the solution over each stencil. Using the indicator of smoothness introduced by Liu *et al.*, an r^{th} order ENO scheme can be converted to an $(r+1)^{th}$ order WENO scheme. Jiang and Shu [43] then developed WENO5, a pointwise WENO scheme. WENO5 converges at fifth order in special cases and is distinguished from other WENO schemes by the weights used in Ref. [43]. Balsara and Shu [44] showed that an $(2r-1)^{th}$ order WENO scheme can be constructed from the stencils of an r^{th} order ENO scheme for $r \in \{4, 5, 6, 7\}$. Also, Fedkiw *et al.* [10, 45] have noted that ϵ, a parameter in these schemes which introduces a numerical bound on the weights, is a dimensional quantity and have suggested an appropriate scaling.

6.1.2.2 General WENO schemes

Consideration of Eq. (6.3) reveals that even if f is inconsistent with the actual flux function, the scheme remains conservative due to the telescoping cancellation of the fluxes between cells. Substituting a different function h for f in Eq. (6.3) can increase the accuracy of the scheme.

In order to maximize accuracy, the function selected as a replacement for the actual flux is subject to the constraint

$$\left.\frac{\partial f}{\partial x}\right|_{x=x_j} = \frac{h_{j+1/2} - h_{j-1/2}}{\Delta x}. \tag{6.4}$$

Following Shu and Osher [40], $h(x)$ is defined implicitly by

$$f(x) = \frac{1}{\Delta x} \int_{x-\Delta x/2}^{x+\Delta x/2} h(\xi) d\xi. \tag{6.5}$$

Differentiation of Eq. (6.5) and evaluation at $x = x_j$ verifies that $h(x)$ satisfies

Eq. (6.4) exactly. Unfortunately, $h(x)$ is known in the literature as the numerical flux function even though it is obviously analytic. Further clarification of the relationship between the numerical and actual flux is given in Appendix A.

Different discrete approximations for $h(x)$ determine different conservative schemes. Using the functional notation given in Appendix A, Eq. (6.4) can be approximated as

$$\left.\frac{df}{dx}\right|_{x_j} \approx \frac{\hat{h}[f]_{j+1/2} - \hat{h}[f]_{j-1/2}}{\Delta x}. \tag{6.6}$$

Since a single functional, $\hat{h}_{j+1/2}$, approximates the numerical flux at every cell boundary in the domain, one need only shift each index by -1 to arrive at the corresponding $\hat{h}_{j-1/2}$. Furthermore, it was shown by Henrick *et al.* [35] that using different functional approximations for $\hat{h}_{j\pm1/2}$ in Eq. (6.6) can cause a decrease in convergence rates. Thus only one means of approximating the numerical flux should be used at every cell interface.

To formulate a specific functional approximation, one first selects a particular form and corresponding stencil for $\hat{h}(x)$ (*e.g.* a polynomial of n order and an n point stencil). Substituting this form for $h(\xi)$ in Eq. (6.5) and integrating, the resulting expression is evaluated at each point in the stencil, yielding a system of constraints for the unknown coefficients in the form chosen. Solving for the coefficients in terms of the fluxes at each point, f_i, one then substitutes back into the assumed form to arrive at a simplified expression for $\hat{h}[f](x)$. Evaluating this expression at $x_{j+1/2}$ gives $\hat{h}[f]_{j+1/2}$. Such a process is carried out in detail in Ref. [35].

A WENO scheme uses a convex combination of different approximations to $h_{j+1/2}$ from overlapping stencils in order to minimize the overall effect of a dis-

continuity on the composite approximation to the numerical flux. This is accomplished by weighting the different approximations to the numerical flux according to an indicator of smoothness, β.

6.1.2.3 WENO5M

The WENO5 Mapped (WENO5M) scheme is a corrected form of the WENO5 scheme [43] which gives optimal convergence even near critical points. This scheme is developed in detail in Ref. [35]. Here the scheme is presented in its final form.

WENO5M chooses the approximation $\hat{h}_{j+1/2}$ to be given by a weighted average of the stencils shown in Fig. 6.3. This weighted average takes the form

$$\hat{h}_{j+1/2} = \sum_{k=0}^{2} \omega_k^{(M)} q_k \tag{6.7}$$

where the third order stencils are given by

$$\begin{aligned} q_0 &= \frac{1}{6}(2f_{j-2} - 7f_{j-1} + 11f_j), \\ q_1 &= \frac{1}{6}(-f_{j-1} + 5f_j + 2f_{j+1}), \qquad \text{and} \\ q_2 &= \frac{1}{6}(2f_j + 5f_{j+1} - f_{j+2}). \end{aligned} \tag{6.8}$$

The $\omega_k^{(M)}$'s are determined in order to reduce the influence of a discontinuity on neighboring nodes. In the absence of a discontinuity, the choice of these weights which allows Eq. (6.6) to converge at fifth order are known as the ideal weights. They are given by

$$\bar{\omega}_0 = 1/10, \qquad \bar{\omega}_1 = 6/10, \qquad \bar{\omega}_2 = 3/10.$$

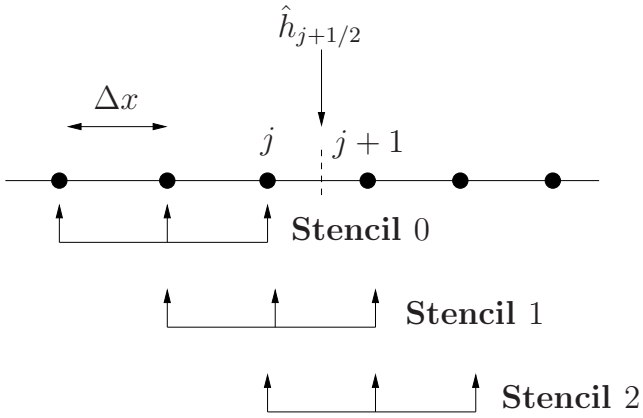

Figure 6.3. Constitutive stencils of the WENO5M scheme.

Such fifth order convergence is the best possible given the composite five point stencil shown in Fig. 6.4.

Once a discontinuity is introduced into the domain, the weights are determined by

$$\omega_k^{(M)} = \frac{\alpha_k^*}{\sum_{i=0}^{2} \alpha_i^*} \qquad \text{where} \qquad \alpha_k^* = g_k(\omega_k^{(JS)}).$$

The g_k are given by

$$g_k(\omega) = \frac{\omega(\bar{\omega}_k + \bar{\omega}_k^2 - 3\bar{\omega}_k\omega + \omega^2)}{\bar{\omega}_k^2 + (1 - 2\bar{\omega}_k)\omega}, \qquad \omega \in [0, 1]$$

and the $\omega_k^{(JS)}$ are the original weights used in Ref. [43]. In effect, g_k maps the k^{th} weight given by Ref. [43] to a more accurate value such that fifth order convergence is maintained near critical points.

The $\omega_k^{(JS)}$ are given by

$$\omega_k^{(JS)} = \frac{\alpha_k}{\sum_{i=0}^{2} \alpha_i}, \qquad \text{where} \qquad \alpha_k = \frac{\bar{\omega}_k}{(\epsilon + \beta_k)^p}.$$

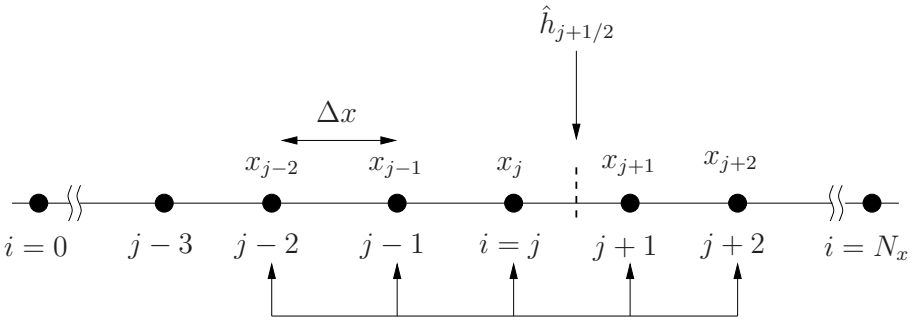

Figure 6.4. Composite stencil for the WENO5M scheme.

The indicators of smoothness are defined as

$$\begin{aligned}
\beta_0 &= \frac{13}{12}(f_{j-2} - 2f_{j-1} + f_j)^2 + \frac{1}{4}(f_{j-2} - 4f_{j-1} + 3f_j)^2, \\
\beta_1 &= \frac{13}{12}(f_{j-1} - 2f_j + f_{j+1})^2 + \frac{1}{4}(f_{j+1} - f_{j-1})^2, \\
\beta_2 &= \frac{13}{12}(f_j - 2f_{j+1} + f_{j+2})^2 + \frac{1}{4}(3f_j - 4f_{j+1} + f_{j+2})^2.
\end{aligned} \tag{6.9}$$

Here, ϵ is the small parameter which keeps the weights bounded. Eqs. (6.6) through Eqs. (6.9) define the fifth order spatial conservative discretization used.

In order to encapsulate the complexity of the WENO5M approximation to the numerical flux, Eq. (6.7) may be represented simply as a special interpolator:

$$\hat{h}[f]_{j+1/2} = \mathcal{F}(f_{j-2}, f_{j-1}, \ldots, f_{j+2}), \tag{6.10}$$

where $\mathcal{F}$ is the functional form of the WENO5M interpolant. With reference to Fig. 6.1 and 6.4, Eq. (6.10) takes the flux at nodal values around $j + 1/2$ and interpolates to give a flux at that inter-cell boundary allowing a conservative numerical scheme to be formed.

For the WENO5M scheme described by Eq. (6.10), information is forced to propagate from left to right by the stencil bias as shown in Fig. 6.4. An equivalent scheme which propagates information to the left can be easily constructed by reflecting the indices about the $(j+1/2)^{th}$ interface:

$$\hat{h}[f]_{j+1/2} = \begin{cases} \mathcal{F}(f_{j-2}, f_{j-1}, \ldots, f_{j+2}) & \text{for } \rightarrow \text{ waves,} \quad (6.11a) \\ \mathcal{F}(f_{j+3}, f_{j+2}, \ldots, f_{j-1}) & \text{for } \leftarrow \text{ waves.} \quad (6.11b) \end{cases}$$

It remains, however, to construct a scheme which would remain stable for a system in which information propagation is bi-directional.

6.1.3 Local Lax-Friedrichs flux splitting

Thus far, numerical stability has not been discussed. In the context of hyperbolic equations, the stability of a numerical approximation is closely related to the propagation of information in the correct direction [4, 5, 46]. In essence, the domain of dependence of the numerical scheme must contain that of the analytic solution. The direction of information propagation can be found by means of a characteristic analysis of the original hyperbolic system. Such an analysis is given for the one-dimensional Euler equations with reaction in Appendix F. As this analysis reveals, it is common for information in such systems to propagate in both directions simultaneously.

Many robust numerical schemes exist which maintain stability by allowing information to flow bi-directionally [4, 5, 47]. For this work, the local Lax-Friedrichs (LF) flux splitting method was chosen. This scheme is explained in detail by Katzer and Osher [48] and is based upon splitting the flux into two different terms: each propagating information in the opposite direction from the other. Appropriate finite differencing can then be applied to yield a conservative numerical

scheme.

The Lax-Friedrichs flux splitting technique is inspired by traditional flux vector splitting concepts, notably Steger-Warming splitting [4, pg. 270]; however, it depends neither on linearization nor the homogeneity of the flux vector f. In fact, a discretization of the "non-conservative system" known in the literature as the Split-Coefficient Matrix Scheme [4, pg. 267], would result in a loss of accuracy at points where the sign of an eigenvalue changes. This is due to a changing of the interpolant across a node which prevents the desired cancellation of error terms [35].

Consider again a one-dimensional model problem,

$$\frac{\partial \mathbf{F}}{\partial t} + \frac{\partial}{\partial x}\left(\mathbf{f}(\mathbf{F}(x))\right) = \mathbf{B}. \tag{6.12a}$$

Using the chain rule, Eq. (6.12a) becomes

$$\frac{\partial \mathbf{F}}{\partial t} + \frac{\partial \mathbf{f}}{\partial \mathbf{F}}\frac{\partial \mathbf{F}}{\partial x} = \mathbf{B}, \tag{6.12b}$$

where $\frac{\partial \mathbf{f}}{\partial \mathbf{F}}$ denotes a Jacobian matrix whose eigenvalues represent the wave speeds present in a given problem. Since Eq. (6.12a) is hyperbolic, the diagonlization of $\frac{\partial \mathbf{f}}{\partial \mathbf{F}}$ yields $\mathbf{\Lambda}$: a complete, real diagonal matrix of the system's eigenvalues. The sign of each eigenvalues determines whether the corresponding characteristic information propagates in the $\pm x$ direction.

The largest eigenvalue, in an absolute sense, defines the norm $|\cdot|$ such that

$$\alpha = \left|\frac{\partial \mathbf{f}}{\partial \mathbf{F}}\right| \tag{6.13}$$

is the largest wave speed of the system. The flux vector is now rewritten as

$$\frac{\partial \mathbf{F}}{\partial t} + \frac{\partial}{\partial x}\left(\frac{1}{2}\left(\mathbf{f} + \alpha\mathbf{F} + \mathbf{f} - \alpha\mathbf{F}\right)\right) = \mathbf{B},$$

allowing the flux to be split:

$$\frac{\partial \mathbf{F}}{\partial t} + \frac{1}{2}\left(\frac{\partial \mathbf{f}^{+}}{\partial x} + \frac{\partial \mathbf{f}^{-}}{\partial x}\right) = \mathbf{B} \quad \text{where} \quad \mathbf{f}^{\pm} = \mathbf{f} \pm \alpha\mathbf{F}. \tag{6.14}$$

The Jacobians of the split flux matrices are

$$\frac{\partial \mathbf{f}^{\pm}}{\partial \mathbf{F}} = \frac{\partial \mathbf{f}}{\partial \mathbf{F}} \pm \mathbf{I}\alpha, \tag{6.15}$$

where $\mathbf{I}$ is the identity matrix. Diagonalization of Eqs. (6.15) gives

$$\mathbf{\Lambda}^{+} = \mathbf{\Lambda} + \mathbf{I}\alpha \geq 0 \qquad \text{and} \qquad \mathbf{\Lambda}^{-} = \mathbf{\Lambda} - \mathbf{I}\alpha \leq 0, \tag{6.16}$$

confirming that the $\mathbf{f}^{\pm}$ fluxes correspond to waves traveling in the $\pm x$ directions.

The conservative numerical implementation of this flux splitting technique is known as a local Lax-Friedrichs flux splitting. Denoting $\hat{h}[\mathbf{f}^{\pm}]_{j+1/2}$ as $\hat{\mathbf{h}}^{\pm}_{j+1/2}$, Eq. (6.6) is used to conservatively discretized both derivatives in Eq. (6.14):

$$\begin{aligned}
\left.\frac{\partial \mathbf{f}}{\partial x}\right|_{x=x_j} &\approx \frac{1}{2}\left(\frac{\hat{\mathbf{h}}^{+}_{j+1/2} - \hat{\mathbf{h}}^{+}_{j-1/2}}{\Delta x} + \frac{\hat{\mathbf{h}}^{-}_{j+1/2} - \hat{\mathbf{h}}^{-}_{j-1/2}}{\Delta x}\right) \\
&\approx \frac{1}{\Delta x}\left(\frac{\hat{\mathbf{h}}^{+}_{j+1/2} + \hat{\mathbf{h}}^{-}_{j+1/2}}{2} - \frac{\hat{\mathbf{h}}^{+}_{j-1/2} + \hat{\mathbf{h}}^{-}_{j-1/2}}{2}\right) \\
&\approx \frac{\hat{\mathbf{f}}_{j+1/2} - \hat{\mathbf{f}}_{j-1/2}}{\Delta x},
\end{aligned} \tag{6.17a}$$

where

$$\begin{aligned}\hat{\mathbf{f}}_{j+1/2} &= \frac{1}{2}\left(\hat{\mathbf{h}}^{+}_{j+1/2} + \hat{\mathbf{h}}^{-}_{j+1/2}\right) \\ &= \frac{1}{2}\left(\hat{h}[\mathbf{f}^{+}]_{j+1/2} + \hat{h}[\mathbf{f}^{-}]_{j+1/2}\right)\end{aligned} \tag{6.17b}$$

is the total flux at each $j+1/2$ cell boundary. The component LF fluxes around the $j+1/2$ interface are

$$\mathbf{f}^{\pm} = \mathbf{f} \pm \alpha_{j+1/2}\mathbf{F}, \tag{6.17c}$$

where the local maximum wave speed is approximated by

$$\alpha_{j+1/2} = \max\left(\left|\frac{\partial \mathbf{f}}{\partial \mathbf{F}}\right|_{j}, \left|\frac{\partial \mathbf{f}}{\partial \mathbf{F}}\right|_{j+1}\right). \tag{6.17d}$$

Equations (6.17) completely define LF flux splitting without explicitly coupling the scheme with any particular numerical approximation to $h(x)$. It is, however assumed that $\hat{\mathbf{h}}^{\pm}_{j+1/2}$ are biased to match the wave motion of the $\mathbf{f}^{\pm}$ (*cf.* Eq. (6.11)). In the case that WENO5M is used,

$$\hat{h}[\mathbf{f}^{+}]_{i+1/2} = \mathcal{F}(\mathbf{f}^{+}_{i-2}, \mathbf{f}^{+}_{i-1}, \ldots, \mathbf{f}^{+}_{i+2}), \tag{6.18}$$

$$\hat{h}[\mathbf{f}^{-}]_{i+1/2} = \mathcal{F}(\mathbf{f}^{-}_{i+3}, \mathbf{f}^{-}_{i+2}, \ldots, \mathbf{f}^{-}_{i-1}), \tag{6.19}$$

where local LF fluxes, $\mathbf{f}^{\pm}_{j}$, are required for $j \in \{i-2, \ldots, i+3\}$.

6.2 Hamilton-Jacobi solvers

Hamilton-Jacobi (HJ) equations are a type of first order, nonlinear PDE's which describe a variety of phenomena, including the evolution of level curves. The general form of a one-dimensional HJ equation is

$$\frac{\partial g}{\partial t} + H\left(\frac{\partial g}{\partial x}\right) = 0; \qquad g(x,0) = g_0(x), \tag{6.20}$$

where the function H is known as the Hamiltonian. For this one-dimensional case, an immediate relationship to conservation laws is found by differentiating Eq. (6.20) with respect to x and defining $\phi = \frac{\partial g}{\partial x}$ giving

$$\frac{\partial \phi}{\partial t} + \frac{\partial}{\partial x}\left(H(\phi)\right) = 0; \qquad \phi(x,0) = \frac{\partial g_0}{\partial x}. \tag{6.21}$$

Equation (6.21) is the conservative PDE corresponding to the HJ equation.

Relating Eq. (6.20) to Eq. (6.21) provides a number of insights into solutions of the HJ equation. First, the solutions ϕ can suffer a discontinuity. Second, such discontinuities in derivative appear as kinks in the integrated solution g [10, pg. 48]. Most importantly, the well established numerical methods used to solve Eq. (6.21) supply a basis for construction of numerical schemes to solve Eq. (6.20).

Constructing a low order conservative, Lax-Friedrichs spatial discretization of Eq. (6.21) is simple given the methods presented in Section 6.1; however, the resulting numerical scheme can also be rearranged to solve Eq. (6.20) at a *higher order*. The development given here roughly follows that given by Osher *et al.* [49].

Before explicitly developing the HJ numerical scheme from its conservative LF counterpart, two clarifications should be made. First, the only data assumed to be given is the value of g at each node j; the initial condition on ϕ must be generated

from this data. Second, the conservative LF scheme given by Eqs. (6.17) leaves $\hat{h}$ unspecified; the simplest choice is to select the LF flux itself as the approximation to the numerical flux function.

Since only g_j is assumed to be given, the initial data for Eq. (6.21) must be produced. Let $\phi_{j-1/2}$ be given by centered differences applied to g_j:

$$\phi_{j-1/2} = \frac{g_j - g_{j-1}}{\Delta x} \qquad \text{or} \qquad \phi_i = \frac{g_{i+1/2} - g_{i-1/2}}{\Delta x}, \tag{6.22}$$

where a shifted index $i = j - 1/2$ is used giving the initial condition of ϕ at each location $x_i = x_{j-1/2}$. Thus the quantites ϕ_i and g_j are known and are offset from each other by $\frac{\Delta x}{2}$. Alternation between the i and j indices will occur as needed for brevity.

Discretizing Equation (6.21) at the i^{th} node and applying Eq. (6.17a) to the spatial derivative gives

$$\frac{d\phi_i}{dt} + \frac{\hat{H}_{i+1/2} - \hat{H}_{i-1/2}}{\Delta x} = 0, \tag{6.23a}$$

where $\hat{H}_{i\pm1/2}$ is the total LF flux at $x_{i\pm1/2}$ (*cf.* $\hat{f}_{i\pm1/2}$ in Eq. (6.17b)).

Choosing the approximation of the numerical flux function in Eq. (6.17b) to be simply the component LF flux itself gives

$$\begin{aligned} \hat{H}_j &= \frac{1}{2}\left(\hat{h}[H^+]_j + \hat{h}[H^-]_j\right) \\ &= \frac{1}{2}\left(H_j^+ + H_j^-\right), \end{aligned} \tag{6.23b}$$

where $\hat{h}[H^\pm] \equiv H^\pm$. However, since only the ϕ_i are known, $H_j^\pm$ must be computed

via interpolation:

$$\hat{h}[H^{\pm}]_j \equiv H_j^{\pm} = H(\phi_j^{\pm}) \pm \alpha_j \phi_j^{\pm}, \tag{6.23c}$$

where $\phi_j^{\pm}$ are biased to match the component LF fluxes and

$$\alpha_j = \max\left(\left|\frac{\partial H}{\partial \phi}\right|_{j-1/2}, \left|\frac{\partial H}{\partial \phi}\right|_{j+1/2} \right) \tag{6.23d}$$

from Eq. (6.17d) applied to Eq. (6.21). Such an approximation for the numerical flux function will only yield $\frac{\partial H}{\partial x}$ to second order (*cf.* Appendix A); thus the scheme appears to have limited accuracy as an approximation *of the conservation law*.

In order to apply this solution method to the HJ equation, ϕ_i is first removed from Eqs. (6.23a) giving

$$\frac{d}{dt}\left(\frac{g_{i+1/2} - g_{i-1/2}}{\Delta x}\right) + \frac{\hat{H}_{i+1/2} - \hat{H}_{i-1/2}}{\Delta x} = 0 \tag{6.24}$$

or

$$\left(\frac{d}{dt}\left(g_{i+1/2}\right) + \hat{H}_{i+1/2}\right) - \left(\frac{d}{dt}\left(g_{i-1/2}\right) + \hat{H}_{i-1/2}\right) = 0. \tag{6.25}$$

In order for Eq. (6.25) to be satisfied for any i,

$$\frac{d}{dt}\left(g_{i+1/2}\right) + \hat{H}_{i+1/2} = 0 \qquad \text{or} \qquad \frac{d}{dt}\left(g_j\right) + \hat{H}_j = 0. \tag{6.26}$$

Equation (6.26) is a discrete form of the HJ equation, Eq. (6.20); in the literature $\hat{H}_j$ is known as the "numerical Hamiltonian." Thus, the numerical discretization given by Eq. (6.23a) for the conservation law leads directly to a numerical scheme

for the HJ equation, where the Hamiltonian is replaced by a numerical flux.

While Eqs. (6.23) may only solve the conservation problem at second order, it is still possible for Eq. (6.26) to yield a high order solution to Eq. (6.20). This is possible by selecting the interpolator for $\phi_j^{\pm}$ in Eq. (6.23c) to be the numerical flux function; as shown in Appendix A.2, it restores the exact derivative of a function given its centered differences. In the case that WENO5M is chosen as the approximation to the numerical flux function,

$$\hat{h}[\phi]_j = \begin{cases} \phi_j^+ = \mathcal{F}(\phi_{i-2}, \phi_{i-1}, \ldots, \phi_{i+2}) & \text{(6.27a)} \\ \phi_j^- = \mathcal{F}(\phi_{i+3}, \phi_{i+2}, \ldots, \phi_{i-1}), & \text{(6.27b)} \end{cases}$$

where the interpolation has been biased to match the Lax-Friedrichs flux.

Substituting Eq. (6.23b) into Eq. (6.23c) gives

$$\hat{H}_j = \frac{H(\phi_j^+) + H(\phi_j^-)}{2} + \alpha_j \left(\frac{\phi_j^+ - \phi_j^-}{2} \right),$$

where α_j can be interpreted as a viscosity coefficient. The two Hamiltonian evaluations can be reduced to one without loss of accuracy:

$$\hat{H}_j = H\left(\frac{\phi_j^+ + \phi_j^-}{2} \right) + \alpha_j \left(\frac{\phi_j^+ - \phi_j^-}{2} \right). \tag{6.28}$$

Equation (6.28) is the normal form of the LF numerical Hamiltonian given in the literature [10, 50].

6.3 Time integration

An explicit pointwise spatial differencing give by Eq. (6.4) applied to a continuous system of PDE's yields a discrete system of ODE's at each point which are

amenable to solution by the method of lines. Thus a wide variety of standard numerical techniques, explicit and implicit, could be employed to solve the resulting system. For the work presented, an explicit six stage Runge-Kutta scheme [51] with fifth order temporal accuracy is chosen.

Most Runge-Kutta schemes of fourth order or higher are easier to code and require less storage when the Butcher formulation [51] is chosen rather than the more commonplace $\alpha - \beta$ form. Consider an autonomous system of ODE's and initial condition of the form

$$\frac{d\mathbf{u}}{dt} = \mathbf{L}(\mathbf{u}) \qquad \text{and} \qquad \mathbf{u}(t^n) = \mathbf{u}^n, \tag{6.29a}$$

where $\mathbf{L}$ is a general nonlinear operator of the same dimension as $\mathbf{u}$. The solution at $t^{n+1} = t^n + \Delta t^n$, for a constant time step Δt^n, is constructed in the following manner. Denoting the new solution $\mathbf{u}(t^{n+1}) = \mathbf{u}^{n+1}$, the generic s-stage Butcher formulation of Runge-Kutta schemes take the form

$$\bar{\mathbf{u}}^1 = \mathbf{u}^n, \tag{6.30a}$$

$$\bar{\mathbf{u}}^j = \mathbf{u}^n + \Delta t_n \sum_{k=1}^{j-1} a_k^j \left(\mathbf{L}(\bar{\mathbf{u}}^k\right), \tag{6.30b}$$

where $\bar{\mathbf{u}}^j$ are the intermediate solutions at each j-stage corresponding to a time

$$\bar{t}^j = t^n + c^j \Delta t^n. \tag{6.30c}$$

The solution at the next time step is given by

$$\mathbf{u}^{n+1} = \mathbf{u}^n + \Delta t^n \sum_{j=1}^{s} b_j \left(\mathbf{L}(\bar{\mathbf{u}}^j)\right). \tag{6.30d}$$

TABLE 6.1

RUNGE-KUTTA STAGE WEIGHTS.

a_k^j						b_j
	$k=1$	$k=2$	$k=3$	$k=4$	$k=5$	$b_1 = \frac{1}{24}$
$j=2$	1					$b_2 = 0$
$j=3$	$\frac{1}{4}$	$\frac{1}{4}$				$b_3 = 0$
$j=4$	$\frac{2046}{15625}$	$-\frac{454}{15625}$	$\frac{1533}{15625}$			$b_4 = \frac{125}{336}$
$j=5$	$-\frac{739}{5625}$	$\frac{511}{5625}$	$-\frac{566}{16875}$	$\frac{20}{27}$		$b_5 = \frac{27}{56}$
$j=6$	$\frac{11822}{21875}$	$-\frac{6928}{21875}$	$-\frac{4269}{21875}$	$-\frac{4}{7}$	$\frac{54}{35}$	$b_6 = \frac{5}{48}$

The quadrature weights a_k^j and b_j in Eqs. (6.30b) and (6.30d) are give in Table 6.1. The time coefficients c_j are given by

$$c^j = \sum_{k=1}^{j-1} a_k^j \tag{6.31}$$

and become important in the implementation of time-dependent boundary conditions.

CHAPTER 7

MODEL PROBLEM FORMULATION

Thus far, the development of the shock fitted formulation has culminated in Eqs. (4.30a) and (5.17) which are valid for general conservation laws. In this chapter, the formulation is specialized for the two-dimensional Euler equations with reaction bounded by the geometry imposed by the model problem introduced in Chapter 1. First, the numerical coordinates are developed and the corresponding metrics are given. Next the precise formulation of the two-dimensional differential-algebraic system amenable to solution with the method of lines is given. Finally, this formulation is applied to the Euler equations with reaction.

7.1 Boundary-fitted coordinates

First, coordinates matching the geometry of the model problem proposed in Chapter 1 are designed. For simplicity, the Cartesian lab frame and the shock-attached frame are denoted in this section as

$$\{x, y, t\} \qquad \text{and} \qquad \{\xi, \eta, \tau\},$$

respectively. The three dynamic surfaces which must be fit are the shock and the two material interfaces, as seen in Fig. 1.1.

Consider

$$x(\xi,\eta,\tau) = x_l(\eta,\tau)\frac{k_r-\xi}{k_r-k_l} + x_r(\eta,\tau)\frac{\xi-k_l}{k_r-k_l} \tag{7.1a}$$

$$y(\xi,\eta,\tau) = y_\Sigma(\xi,\tau) + \eta \tag{7.1b}$$

$$t(\xi,\eta,\tau) = \tau, \tag{7.1c}$$

where $\xi \in [k_l, k_r]$, $y_\Sigma(\xi,\tau)$ defines the shock locus, and $x_l(\eta,\tau)$ and $x_r(\eta,\tau)$ describe the x location and motion of the left and right boundaries, respectively. The limits on ξ are chosen to coincide with the initial shock shape: $k_l = x_l(0,0)$ and $k_r = x_r(0,0)$.

Equation (7.1b) relates y and η linearly, offseting them by the y position of the shock. Equation (7.1a) is reminiscent of the Lagrange interpolating polynomial and uniformly distributes the x positional coordinates along lines of constant η. The shape of the shocked HE region is simply a rectangle in the curvilinear frame: $\eta = 0$ is the shock-fitted coordinate line while $\xi = k_l$ and $\xi = k_r$ are the left and right boundaries along the confiner/HE material interface. An example numerical grid with deflected side boundaries can be seen in Fig. 7.1.

While Eqs. (7.1) give a simple expression for the Cartesian position as a function of the fitted coordinates, the inverse relationship cannot be given in closed form. As long as Eq. (5.2) is satisfied, the inverse transformation does indeed exist locally, but may be prohibitively complex. Since the closed form given by Eqs. (7.1) allows the metrics to be calculated analytically by a simple function evaluation, it is desirable that all geometric derivatives be written with respect the the fitted coordinates. This is facilitated by the by the inverse metric relationships derived in Appendix B.

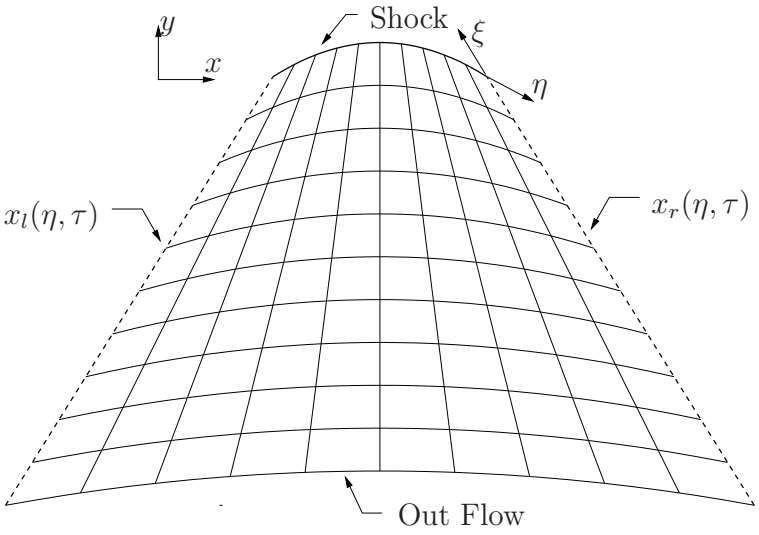

Figure 7.1. Example shock fit coordinates for the two-dimensional model problem.

The grid velocity and the contravariant basis vectors for the transformation Eq. (7.1) are

$$U^{(i)} = \begin{pmatrix} \frac{\partial x}{\partial \tau} \\ \frac{\partial y}{\partial \tau} \end{pmatrix} = \begin{pmatrix} \frac{\partial x_l}{\partial \tau}\frac{k_r-\xi}{k_r-k_l} + \frac{\partial x_r}{\partial \tau}\frac{\xi-k_l}{k_r-k_l} \\ \frac{\partial y_\Sigma}{\partial \tau} \end{pmatrix} \tag{7.2a}$$

$$\boldsymbol{g}_{(1)} = \begin{pmatrix} \frac{\partial x}{\partial \xi} \\ \frac{\partial y}{\partial \xi} \end{pmatrix} = \begin{pmatrix} \frac{x_r(\eta,\tau)-x_l(\eta,\tau)}{k_r-k_l} \\ \frac{\partial y_\Sigma}{\partial \xi} \end{pmatrix} \tag{7.2b}$$

$$\boldsymbol{g}_{(2)} = \begin{pmatrix} \frac{\partial x}{\partial \eta} \\ \frac{\partial y}{\partial \eta} \end{pmatrix} = \begin{pmatrix} \frac{\partial x_l}{\partial \eta}\frac{k_r-\xi}{k_r-k_l} + \frac{\partial x_r}{\partial \eta}\frac{\xi-k_l}{k_r-k_l} \\ 1 \end{pmatrix}. \tag{7.2c}$$

Using the inverse metrics derived in Appendix B, the covariant basis vector normal

to the shock is given by

$$\boldsymbol{g}^{(2)} = \begin{pmatrix} \frac{\partial \eta}{\partial x} \\ \frac{\partial \eta}{\partial y} \end{pmatrix} = \frac{1}{\sqrt{\mathcal{G}}} \begin{pmatrix} -\frac{\partial y}{\partial \xi} \\ \frac{\partial x}{\partial \xi} \end{pmatrix} = \frac{1}{\sqrt{\mathcal{G}}} \begin{pmatrix} -\frac{\partial y_\Sigma}{\partial \xi} \\ \frac{x_r(\eta,\tau)-x_l(\eta,\tau)}{k_r-k_l} \end{pmatrix}, \tag{7.3}$$

where each components is given explicitly by differentiation of Eqs. (7.1).

Inspection of Eqs. (7.2) shows that the transformation metrics depend on x_l and $x_r(\eta,\tau)$, their partial derivatives, and the partial derivatives of $y_\Sigma(\xi,\tau)$. For purposes of the proposed work, $x_l(\eta,\tau)$ and $x_r(\eta,\tau)$ are prescribed for all space and time. All that is given with respect the the shock is its initial condition $y_\Sigma(\xi,0)$; thus, at any position and time, $\frac{\partial y_\Sigma}{\partial \tau}$ and $\frac{\partial y_\Sigma}{\partial \xi}$ are unknown and must be computed as part of the numerical solution.

While in general, $x_l(0,\tau)$ and $x_r(0,\tau)$ are not constant, for the case of the LANL confinement test they are. This corresponds to a shock confined to propagate in the y direction. In this case, $\frac{\partial x}{\partial \xi}\Big|_\Sigma \equiv 1$ and $D^1 = \frac{\partial x}{\partial \tau}\Big|_\Sigma = 0$ giving a significant simplification to the shock fitted formulation.

At the shock, Eqs. (7.2) become

$$U^i\big|_\Sigma = D^i = \begin{pmatrix} 0 \\ \frac{\partial y_\Sigma}{\partial \tau} \end{pmatrix} \tag{7.4a}$$

$$\boldsymbol{g}_{(1)}\big|_\Sigma = \begin{pmatrix} 1 \\ \frac{\partial y_\Sigma}{\partial \xi} \end{pmatrix} \tag{7.4b}$$

$$\boldsymbol{g}_{(2)}\big|_\Sigma = \begin{pmatrix} \frac{\partial x_l}{\partial \eta}\Big|_\Sigma \frac{k_r-\xi}{k_r-k_l} + \frac{\partial x_r}{\partial \eta}\Big|_\Sigma \frac{\xi-k_l}{k_r-k_l} \\ 1 \end{pmatrix}. \tag{7.4c}$$

The normal covariant base vector becomes

$$\boldsymbol{g}^{(2)}\big|_{\Sigma} = \frac{1}{\sqrt{g}|_{\Sigma}} \begin{pmatrix} -\frac{\partial y_{\Sigma}}{\partial \xi} \\ 1 \end{pmatrix}. \tag{7.5}$$

7.2 Shock-fitted formulation

In this section, the differential conservation law and the shock-fitted constraint, Eqs. (4.30a) and (5.17), are adapted to a form amenable to solution using the method of lines; it is assumed that the flux functions and source terms are functions of the conserved quantities alone. Because the shock is fitted, the coordinate transformation is itself part of the solution, as articulated in Section 7.1; the system is written directly in term of the metrics, Eqs. (7.2), which either are given analytically from Eqs. (7.1) or evolve with the motion of the shock. In this context the shock jump condition is distinguished as both an algebraic constraint and as a HJ equation. A simple conservative system of PDE's is possible by differentiating the jump condition. Lastly, the shock change equation is derived, giving the shock acceleration.

7.2.1 Conservation laws

The physically conservative form, Eq. (4.30b), can be written as

$$\begin{aligned} \frac{\partial}{\partial \tau}\left(\sqrt{g}\boldsymbol{F}\right) + \frac{\partial}{\partial \xi}\left(\frac{\partial y}{\partial \eta}\left(\boldsymbol{f}_x - \boldsymbol{F}\frac{\partial x}{\partial \tau}\right) - \frac{\partial x}{\partial \eta}\left(\boldsymbol{f}_y - \boldsymbol{F}\frac{\partial y}{\partial \tau}\right)\right) \\ + \frac{\partial}{\partial \eta}\left(-\frac{\partial y}{\partial \xi}\left(\boldsymbol{f}_x - \boldsymbol{F}\frac{\partial x}{\partial \tau}\right) + \frac{\partial x}{\partial \xi}\left(\boldsymbol{f}_y - \boldsymbol{F}\frac{\partial y}{\partial \tau}\right)\right) = \sqrt{g}\boldsymbol{B}, \end{aligned} \tag{7.6}$$

where $\boldsymbol{f}_x \equiv \boldsymbol{f}^1$ and $\boldsymbol{f}_y \equiv \boldsymbol{f}^2$ are the fluxes in the x and y directions, respectively. Equations (B.4) have been used to write the metrics in terms of curvilinear deriva-

tives. The motion of the quantity $\sqrt{g}\boldsymbol{F}$ is described by the new fluxes in the ξ and η directions. Note that none of the hidden orders of $\boldsymbol{F}$, $\boldsymbol{f}_x$, or $\boldsymbol{f}_y$ needs to be tensorial (*cf.* the last paragraph of Section 4.4.2). The only tensorial relationships assumed are $\mathbf{f}_\xi = \left[\begin{smallmatrix}\boldsymbol{f}_x \\ \boldsymbol{f}_y\end{smallmatrix}\right] \cdot \boldsymbol{g}^{(1)}$, $\mathbf{f}_\eta = \left[\begin{smallmatrix}\boldsymbol{f}_x \\ \boldsymbol{f}_y\end{smallmatrix}\right] \cdot \boldsymbol{g}^{(2)}$, and $U^{(i)} = \boldsymbol{U} \cdot \boldsymbol{g}^{(i)}$.

7.2.2 Shock-fitting constraint

Given the transformation, Eqs. (7.1), an expression for the evolution of $y_\Sigma(\xi, \tau)$ is required which satisfies the shock-fitting constraint; all the metrics in Eqs. (7.2) are known except $\frac{\partial y_\Sigma}{\partial \tau}$ and $\frac{\partial y_\Sigma}{\partial \xi}$. Expressions for the evolution of both quantities is found from the shock jump condition.

Substituting Eqs. (B.6b) and (7.3) into Eq. (5.17) gives the shock jump condition with respect to $\{\xi, \eta, \tau\}$:

$$\frac{1}{\sqrt{g}|_\Sigma}\left(-\frac{\partial y}{\partial \xi}\frac{\partial x}{\partial \tau} + \frac{\partial x}{\partial \xi}\frac{\partial y}{\partial \tau}\right)\bigg|_\Sigma = \frac{1}{\sqrt{g}|_\Sigma}\frac{\left[\!\left[-\boldsymbol{f}_x\frac{\partial y}{\partial \xi} + \boldsymbol{f}_y\frac{\partial x}{\partial \xi}\right]\!\right]}{[\![\boldsymbol{F}]\!]}\bigg|_\Sigma, \tag{7.7}$$

where the jump operator is in the direction of $\boldsymbol{g}^{(2)}$, *i.e.* the shocked state minus the unshocked state. Since $\frac{\partial y}{\partial \tau}\big|_\Sigma = \frac{\partial y_\Sigma}{\partial \tau}$, Eq. (7.7) may be rearranged as

$$\frac{\partial y_\Sigma}{\partial \tau} = \frac{1}{\frac{\partial x}{\partial \xi}}\left(\frac{\left[\!\left[-\boldsymbol{f}_x\frac{\partial y}{\partial \xi} + \boldsymbol{f}_y\frac{\partial x}{\partial \xi}\right]\!\right]}{[\![\boldsymbol{F}]\!]} + \frac{\partial y}{\partial \xi}\frac{\partial x}{\partial \tau}\right)\bigg|_\Sigma, \tag{7.8}$$

where $\frac{\partial x}{\partial \tau}\big|_\Sigma = D^1$. Equation (7.8) gives the required expression for the metric $\frac{\partial y_\Sigma}{\partial \tau}$.

Differentiating Eq. (7.8) with respect to ξ gives an evolution equation for the

shock slope:

$$\frac{\partial}{\partial\tau}\left(\frac{\partial y_\Sigma}{\partial\xi}\right) = \frac{\partial}{\partial\xi}\left(\frac{\partial x}{\partial\xi}^{-1}\left(\frac{\left[\!\left[-\boldsymbol{f}_x\frac{\partial y_\Sigma}{\partial\xi}+\boldsymbol{f}_y\frac{\partial x}{\partial\xi}\right]\!\right]}{[\![\boldsymbol{F}]\!]}+\frac{\partial y_\Sigma}{\partial\xi}\frac{\partial x}{\partial\tau}\right)\right)\Bigg|_\Sigma, \tag{7.9}$$

since differentiation with respect to ξ and τ commute. One should notice the Eq. (7.9) is in conservative form.

Again, the presence of the $\boldsymbol{F}$ in the denominator of Eqs. (7.8) and (7.9) indicates that a jump condition exists for each of the conserved quantities. In solving for the surface evolution, only one of the jump conditions is necessary; however, care should be exercised in its selection to ensure that the resulting expression is well behaved.

7.2.3 Solvable systems

In order to clarify the nature of the system formed from Eqs. (7.6), (7.8), and (7.9), consider naming the new conserved quantity

$$\mathbf{u} = \sqrt{g}\boldsymbol{F}. \tag{7.10a}$$

The Cartesian flux functions ($\boldsymbol{f}_x$ and $\boldsymbol{f}_y$) and the source term ($\boldsymbol{B}$) are assumed to be functions of $\boldsymbol{F}$ alone; however, consider if they are also homogeneous such that

$$\sqrt{g}\boldsymbol{f}_x(\boldsymbol{F}) = \boldsymbol{f}_x(\sqrt{g}\boldsymbol{F}) = \boldsymbol{f}_x(\mathbf{u}), \tag{7.10b}$$

$$\sqrt{g}\boldsymbol{f}_y(\boldsymbol{F}) = \boldsymbol{f}_y(\sqrt{g}\boldsymbol{F}) = \boldsymbol{f}_y(\mathbf{u}), \tag{7.10c}$$

$$\sqrt{g}\boldsymbol{B}(\boldsymbol{F}) = \boldsymbol{B}(\sqrt{g}\boldsymbol{F}) = \boldsymbol{B}(\mathbf{u}). \tag{7.10d}$$

Using Eqs. (7.10), Eq. (7.6) can be rewritten

$$\frac{\partial \mathbf{u}}{\partial \tau} = -\frac{\partial}{\partial \xi}\left(\frac{1}{\sqrt{g}}\left(\frac{\partial y}{\partial \eta}\left(\boldsymbol{f}_x(\mathbf{u}) - \mathbf{u}\frac{\partial x}{\partial \tau}\right) - \frac{\partial x}{\partial \eta}\left(\boldsymbol{f}_y(\mathbf{u}) - \mathbf{u}\frac{\partial y}{\partial \tau}\right)\right)\right)$$
$$-\frac{\partial}{\partial \eta}\left(\frac{1}{\sqrt{g}}\left(-\frac{\partial y}{\partial \xi}\left(\boldsymbol{f}_x(\mathbf{u}) - \mathbf{u}\frac{\partial x}{\partial \tau}\right) + \frac{\partial x}{\partial \xi}\left(\boldsymbol{f}_y(\mathbf{u}) - \mathbf{u}\frac{\partial y}{\partial \tau}\right)\right)\right) + \boldsymbol{B}(\mathbf{u}), \quad (7.11a)$$

where the right hand side is a function of $\mathbf{u}$ and the metrics. Multiplying numerator and denominator of the jump term in Eqs. (7.8) by the continuous Jacobian $\sqrt{g}|_\Sigma$ gives

$$\frac{\partial y_\Sigma}{\partial \tau} = \left.\frac{\partial x}{\partial \xi}\right|_\Sigma^{-1}\left(\frac{\left[\!\left[-\boldsymbol{f}_x(\mathbf{u})\frac{\partial y_\Sigma}{\partial \xi} + \boldsymbol{f}_y(\mathbf{u})\frac{\partial x}{\partial \xi}\right]\!\right]}{[\![\mathbf{u}]\!]} + \frac{\partial y_\Sigma}{\partial \xi}\frac{\partial x}{\partial \tau}\right)\Bigg|_\Sigma, \quad (7.11b)$$

after substituting from Eqs. (7.10). Similarly, Eq. (7.9) becomes

$$\frac{\partial}{\partial \tau}\left(\frac{\partial y_\Sigma}{\partial \xi}\right) = \frac{\partial}{\partial \xi}\left(\frac{\partial x}{\partial \xi}^{-1}\left(\frac{\left[\!\left[-\boldsymbol{f}_x(\mathbf{u})\frac{\partial y_\Sigma}{\partial \xi} + \boldsymbol{f}_y(\mathbf{u})\frac{\partial x}{\partial \xi}\Big|_\Sigma\right]\!\right]}{[\![\mathbf{u}]\!]} + \frac{\partial y_\Sigma}{\partial \xi}\frac{\partial x}{\partial \tau}\right)\right)\Bigg|_\Sigma. \quad (7.11c)$$

All other metrics are computed analytically from from Eqs. (7.1).

If the fluxes of the new conserved quantity $\mathbf{u}$ are denoted

$$\mathbf{g}_\xi(\mathbf{u}, \frac{\partial y_\Sigma}{\partial \tau}) = \frac{1}{\sqrt{g}}\left(\frac{\partial y}{\partial \eta}\left(\boldsymbol{f}_x(\mathbf{u}) - \mathbf{u}\frac{\partial x}{\partial \tau}\right) - \frac{\partial x}{\partial \eta}\left(\boldsymbol{f}_y(\mathbf{u}) - \mathbf{u}\frac{\partial y}{\partial \tau}\right)\right), \quad (7.12a)$$
$$\mathbf{g}_\eta(\mathbf{u}, \frac{\partial y_\Sigma}{\partial \tau}, \frac{\partial y_\Sigma}{\partial \xi}) = \frac{1}{\sqrt{g}}\left(-\frac{\partial y}{\partial \xi}\left(\boldsymbol{f}_x(\mathbf{u}) - \mathbf{u}\frac{\partial x}{\partial \tau}\right) + \frac{\partial x}{\partial \xi}\left(\boldsymbol{f}_y(\mathbf{u}) - \mathbf{u}\frac{\partial y}{\partial \tau}\right)\right), \quad (7.12b)$$

and H is defined to be

$$H(\mathbf{u}, \frac{\partial y_\Sigma}{\partial \xi}) = -\left.\frac{\partial x}{\partial \xi}\right|_\Sigma^{-1}\left(\frac{\left[\!\left[-\boldsymbol{f}_x(\mathbf{u})\frac{\partial y_\Sigma}{\partial \xi} + \boldsymbol{f}_y(\mathbf{u})\frac{\partial x}{\partial \xi}\right]\!\right]}{[\![\mathbf{u}]\!]} + \frac{\partial y_\Sigma}{\partial \xi}\frac{\partial x}{\partial \tau}\right)\Bigg|_\Sigma, \quad (7.12c)$$

then the entire original DAE may be written down simply as

$$\frac{\partial \mathbf{u}}{\partial \tau} = -\frac{\partial}{\partial \xi}\left(\mathbf{g}_\xi(\mathbf{u}, \frac{\partial y_\Sigma}{\partial \tau})\right) - \frac{\partial}{\partial \eta}\left(\mathbf{g}_\eta(\mathbf{u}, \frac{\partial y_\Sigma}{\partial \tau}, \frac{\partial y_\Sigma}{\partial \xi})\right) + \mathbf{B}(\mathbf{u}) \tag{7.13a}$$

$$\frac{\partial y_\Sigma}{\partial \tau} = -H(\mathbf{u}_\Sigma, \frac{\partial y_\Sigma}{\partial \xi}), \tag{7.13b}$$

where $\mathbf{u}_\Sigma$ denotes the tuple of conserved quantities evaluated at the shock.

As its original formulation as an algebraic jump condition suggests, Eq. (7.13b) is primarily a constraint on the metric fitted to the shock. Substituting Eq. (7.13b) into Eq. (7.13a) removes explicit dependence on $\frac{\partial y_\Sigma}{\partial \tau}$:

$$\frac{\partial}{\partial \tau}\begin{bmatrix} \mathbf{u} \\ y_\Sigma \end{bmatrix} = -\begin{bmatrix} \frac{\partial}{\partial \xi}\left(\mathbf{g}_\xi(\mathbf{u}, -H)\right) + \frac{\partial}{\partial \eta}\left(\mathbf{g}_\eta(\mathbf{u}, -H, \frac{\partial y_\Sigma}{\partial \xi})\right) - \mathbf{B}(\mathbf{u}) \\ H(\mathbf{u}_\Sigma, \frac{\partial y_\Sigma}{\partial \xi}) \end{bmatrix}. \tag{7.14}$$

From Section 6.2, Eq. (7.13b) is a HJ equation for y_Σ with Hamiltonian H which can be solved numerically by forming an approximation to $\frac{\partial y_\Sigma}{\partial \xi}$ directly from y_Σ. Alternatively, Eq. (7.13a) is in conservative form and may be solved using a conservative LF discretization. Thus, using two different numerical techniques, Equations (7.14) give the most primitive numerically solvable form .

To form a simple system of PDE's, Eq. (7.13b) can be replaced by Eq. (7.11c) yielding

$$\frac{\partial}{\partial \tau}\begin{bmatrix} \mathbf{u} \\ \frac{\partial y_\Sigma}{\partial \xi} \end{bmatrix} = -\frac{\partial}{\partial \xi}\begin{bmatrix} \mathbf{g}_\xi(\mathbf{u}, -H) \\ H(\mathbf{u}_\Sigma, \frac{\partial y_\Sigma}{\partial \xi}) \end{bmatrix} - \frac{\partial}{\partial \eta}\begin{bmatrix} \mathbf{g}_\eta(\mathbf{u}, -H, \frac{\partial y_\Sigma}{\partial \xi}) \\ 0 \end{bmatrix} + \begin{bmatrix} \mathbf{B}(\mathbf{u}) \\ 0 \end{bmatrix}. \tag{7.15}$$

Each of the right hand sided of Eq. (7.15) are in conservative form making the entire system tractable to solution by a single numerical solution technique. In arriving at Eq. (7.15), it was necessary to differentiate the original shock jump

condition. Such an operation can change the critical points and behavior of the global dynamic system; thus solutions Eq. (7.15) are more nuanced than those of Eq. (7.14)

7.2.4 Shock acceleration

Lastly, the shock acceleration as given by the shock change equation is considered. In previous work given in Ref. [52], the shock change equation was mutually coupled with the differential conservation law; solutions depended explicitly on the shock acceleration. Here the shock change equation is presented as a means of determining the shock acceleration, *a posteriori*.

Substituting Eqs. (5.12a) and (7.3) into Eq. (5.17) gives

$$D_n \sqrt{g^{22}|_\Sigma} = \frac{1}{\sqrt{g}|_\Sigma} \left. \frac{\left[\!\left[-\boldsymbol{f}_x \frac{\partial y}{\partial \xi} + \boldsymbol{f}_y \frac{\partial x}{\partial \xi} \right]\!\right]}{[\![\mathbf{u}]\!]} \right|_\Sigma , \tag{7.16}$$

where $D^2 = -\left.\frac{\partial \eta}{\partial t}\right|_\Sigma$ and numerator and denominator have again been multiplied by the continuous Jacobian, $\sqrt{g}$. Substituting from Eq. (B.5b) and rearranging gives

$$D_n = \left. \frac{\left[\!\left[-\boldsymbol{f}_x \frac{\partial y}{\partial \xi} + \boldsymbol{f}_y \frac{\partial x}{\partial \xi} \right]\!\right]}{[\![\mathbf{u}]\!] \sqrt{\frac{\partial x}{\partial \xi}^2 + \frac{\partial x}{\partial \eta}^2}} \right|_\Sigma . \tag{7.17a}$$

D_n may also be given as a function of H from Eqs. (7.12c) and (7.17a) giving

$$D_n = \left. \frac{H(\mathbf{u}, \frac{\partial y_\Sigma}{\partial \xi}) \frac{\partial x}{\partial \xi} - \frac{\partial y}{\partial \xi} \frac{\partial x}{\partial \tau}}{\sqrt{\frac{\partial x}{\partial \xi}^2 + \frac{\partial x}{\partial \eta}^2}} \right|_\Sigma . \tag{7.17b}$$

Differentiating Eq. (7.17a) with respect to τ gives

$$\frac{\partial D_n}{\partial \tau} = \left.\frac{\frac{\partial}{\partial \tau}\left(\left[\!\left[-\boldsymbol{f}_x \frac{\partial y}{\partial \xi} + \boldsymbol{f}_y \frac{\partial x}{\partial \xi}\right]\!\right]\right)}{[\![\mathbf{u}]\!]\sqrt{\frac{\partial x}{\partial \xi}^2 + \frac{\partial x}{\partial \eta}^2}}\right|_\Sigma - \left.\frac{\frac{\partial}{\partial \tau}\left([\![\mathbf{u}]\!]\sqrt{\frac{\partial x}{\partial \xi}^2 + \frac{\partial x}{\partial \eta}^2}\right)}{[\![\mathbf{u}]\!]\sqrt{\frac{\partial x}{\partial \xi}^2 + \frac{\partial x}{\partial \eta}^2}}\right|_\Sigma D_n, \tag{7.18}$$

where Eq. (7.17a) has been substituted into its own derivative. Expanding the derivatives of Eq. (7.18) gives

$$\begin{aligned}\frac{\partial D_n}{\partial \tau} = &\left.\frac{\left[\!\left[-\frac{\partial \boldsymbol{f}_x}{\partial \tau}\frac{\partial y}{\partial \xi} - \boldsymbol{f}_x \frac{\partial}{\partial \xi}\left(\frac{\partial y}{\partial \tau}\right) + \frac{\partial \boldsymbol{f}_y}{\partial \tau}\frac{\partial x}{\partial \xi} + \boldsymbol{f}_y \frac{\partial}{\partial \tau}\left(\frac{\partial x}{\partial \xi}\right)\right]\!\right]}{[\![\mathbf{u}]\!]\sqrt{\frac{\partial x}{\partial \xi}^2 + \frac{\partial x}{\partial \eta}^2}}\right|_\Sigma \\ &- \left(\frac{\frac{\partial}{\partial \tau}\left(\sqrt{\frac{\partial x}{\partial \xi}^2 + \frac{\partial x}{\partial \eta}^2}\right)}{\sqrt{\frac{\partial x}{\partial \xi}^2 + \frac{\partial x}{\partial \eta}^2}} + \frac{[\![\frac{\partial \mathbf{u}}{\partial \tau}]\!]}{[\![\mathbf{u}]\!]}\right)_\Sigma D_n.\end{aligned} \tag{7.19}$$

Furthermore, $\boldsymbol{f}_x(\mathbf{u})$ and $\boldsymbol{f}_y(\mathbf{u})$ so that their derivatives can be calculated using the chain rule as

$$\frac{\partial \boldsymbol{f}_x}{\partial \tau} = \frac{\partial \boldsymbol{f}_x}{\partial \mathbf{u}} \cdot \frac{\partial \mathbf{u}}{\partial \tau} \qquad \text{and} \qquad \frac{\partial \boldsymbol{f}_y}{\partial \tau} = \frac{\partial \boldsymbol{f}_y}{\partial \mathbf{u}} \cdot \frac{\partial \mathbf{u}}{\partial \tau}. \tag{7.20}$$

Letting $\frac{\partial \mathbf{u}}{\partial \tau} = \mathbf{G}$, both $\mathbf{G}$ and H are already explicitly calculated for each solution of Eqs. (7.13). Taking advantage of this fact, Eq. (7.19) can be written in terms of $\mathbf{G}$ and H as

$$\begin{aligned}\frac{\partial D_n}{\partial \tau} = &\left.\frac{\left[\!\left[-\left(\frac{\partial \boldsymbol{f}_x}{\partial \mathbf{u}} \cdot \mathbf{G}\right)\frac{\partial y}{\partial \xi} - \boldsymbol{f}_x \frac{\partial}{\partial \xi}(-H) + \left(\frac{\partial \boldsymbol{f}_y}{\partial \mathbf{u}} \cdot \mathbf{G}\right)\frac{\partial x}{\partial \xi} + \boldsymbol{f}_y \frac{\partial^2 x}{\partial \xi \partial \tau}\right]\!\right]}{[\![\mathbf{u}]\!]\sqrt{\frac{\partial x}{\partial \xi}^2 + \frac{\partial x}{\partial \eta}^2}}\right|_\Sigma \\ &- \left(\frac{1}{2}\frac{\partial}{\partial \tau}\ln\left(\frac{\partial x}{\partial \xi}^2 + \frac{\partial x}{\partial \eta}^2\right) + \frac{[\![\mathbf{G}]\!]}{[\![\mathbf{u}]\!]}\right)_\Sigma D_n,\end{aligned} \tag{7.21}$$

where $D_n(\mathbf{u}, \frac{\partial y_\Sigma}{\partial \xi})$ from Eq. (7.17b).

7.3 Numerical implementation

In order to numerically solve Eqs. (7.14) or Eqs. (7.15) using the method of lines, the numerical approximations to the spatial derivatives $\frac{\partial \mathbf{g}_{xi}}{\partial \xi}$, $\frac{\partial \mathbf{g}_\eta}{\partial \eta}$, $\frac{\partial y_\Sigma}{\partial \xi}$, and $\frac{\partial H}{\partial \xi}$ are specified using the techniques presented in Section 6. Giving particular attention to nodes near the boundaries, the numerical grid is presented, and the corresponding discretization of the differential system is given. The finite difference schemes used in each region of the grid are then made explicit.

7.3.1 Grid

Numerical solutions are approximated on a discrete grid over the domain

$$\{\xi \in [k_l, k_r], \eta \in [\eta_{min}, 0]\}$$

as shown in Fig. 7.2. The position of node (i, j) is denoted (ξ_i, η_j) where $i \in [0, N_\xi]$ and $j \in [0, N_\eta]$. Functional values at node (i, j) are denoted by a subscript (i, j), *e.g* $f_{(i,j)} = f(\xi_i, \eta_j)$. Uniform spacing is used in each direction such that $\xi_i = \xi_0 + i\Delta\xi$ and $\eta_j = \eta_0 + j\Delta\eta$.

Five different types of nodes are shown in Fig. 7.2. In particular, ghost nodes are represented with unfilled circles. Ghost nodes may be active or inactive depending on the boundary condition enforced along the side boundaries; the outflow ghost nodes, for which $\eta_j \in [\eta_{-3}, \eta_{-1}]$, are always used.

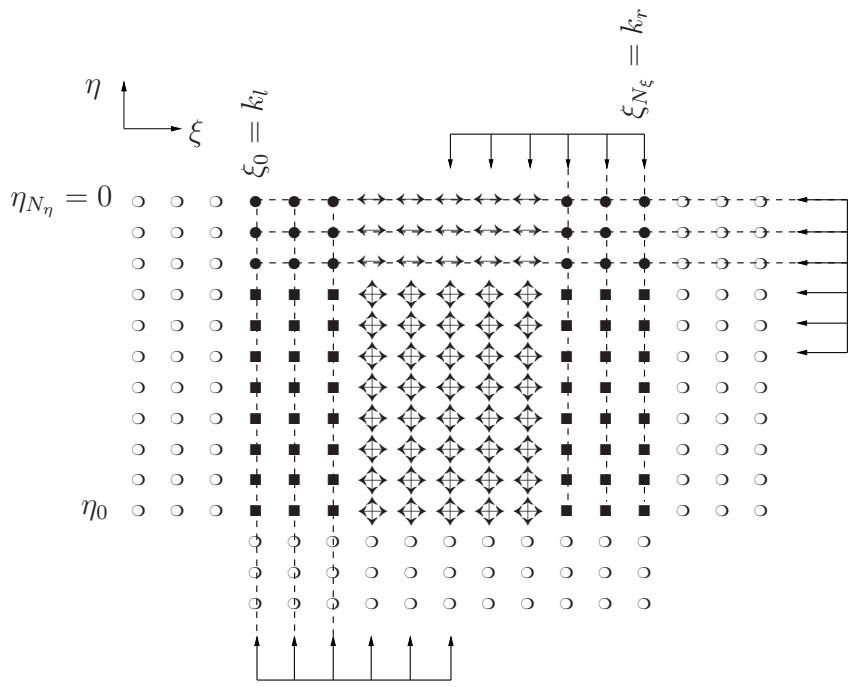

Figure 7.2. A coarse numerical grid highlighting the various nodal domains according to spatial discretization. Arrows indicate use of the WENO5M discretization to compute derivatives in that direction. Left and right boundary nodes are marked with solid symbols; discretization at these points depends on the boundary condition chosen. Unfilled circles indicate ghost nodes.

7.3.2 Hybrid method

In order to solve the system Eqs. (7.13), the union of both formulations Eqs. (7.14) and (7.15) is discretizated spatially:

$$\frac{d}{d\tau}\begin{bmatrix}\mathbf{u}\\ \frac{\partial y_\Sigma}{\partial \xi}\\ y_\Sigma\end{bmatrix}_{(i,j)} = -\frac{\partial}{\partial \xi}\begin{bmatrix}\mathbf{g}_\xi(\mathbf{u},-H)\\ H(\mathbf{u},\frac{\partial y_\Sigma}{\partial \xi})\\ 0\end{bmatrix}_{(i,j)} - \frac{\partial}{\partial \eta}\begin{bmatrix}\mathbf{g}_\eta(\mathbf{u},-H,\frac{\partial y_\Sigma}{\partial \xi})\\ 0\\ 0\end{bmatrix}_{(i,j)} + \begin{bmatrix}\mathbf{B}(\mathbf{u})\\ 0\\ H(\mathbf{u},\frac{\partial y_\Sigma}{\partial \xi})\end{bmatrix}_{(i,j)}. \tag{7.22}$$

The source term $\mathbf{B}$ can be simply evaluated at each point, since its dependence is restricted to the conserved quantities themselves. The dependence of the Hamiltonian $H(\mathbf{u},\frac{\partial y_\Sigma}{\partial \xi})$ on $\frac{\partial y_\Sigma}{\partial \xi}$ requires a special discretization as given in Section 6.2.

One need not solve the entire system given by Eqs. (7.22); rather, only the conservative system given by the first two equations have been used in the following work. Further iterations of the numerical scheme using the HJ equation explicitly have been tested and are currently in development.

For each type of non-ghost node, a particular discretization of the spatial derivatives is employed. In the following sections, the discretization of $\frac{\partial \mathbf{g}}{\partial \eta}$ and $\frac{\partial \mathbf{g}}{\partial \eta}$ at each type of node is treated individually for an arbitary function $\mathbf{g}(\mathbf{u})$. Furthermore, the numerical discretization of the Hamiltonian is give explicitly in Section 7.3.8, making used of the derivative approximations as needed.

7.3.3 $\frac{\partial}{\partial \eta}$ for $(\xi_i,\eta_j) : j \in [0, N_\eta - 3]$

For these nodes, the WENO5M discretization of the LF flux given in Sections 6.1.2.3 and 6.1.3 is used to approximate the derivative. Approximating $\frac{\partial \mathbf{g}}{\partial \eta}$

by Eqs. (6.17) gives

$$\left.\frac{\partial \mathbf{g}}{\partial \eta}\right|_{(i,j)} = \frac{\hat{\mathbf{g}}_{(i,j+1/2)} - \hat{\mathbf{g}}_{(i,j-1/2)}}{\Delta\eta}, \tag{7.23a}$$

where the numerical flux function is approximated by WENO5M yielding

$$\hat{\mathbf{g}}_{(i,j+1/2)} = \frac{1}{2}\left(\hat{h}[\mathbf{g}^+]_{(i,j+1/2)} + \hat{h}[\mathbf{g}^-]_{(i,j+1/2)}\right), \tag{7.23b}$$

$$\hat{h}[\mathbf{g}^+]_{(i,j+1/2)} = \mathcal{F}(\mathbf{g}^+_{(i,j-2)}, \mathbf{g}^+_{(i,j-1)}, \ldots, \mathbf{g}^+_{(i,j+2)}), \tag{7.23c}$$

$$\hat{h}[\mathbf{g}^-]_{(i,j+1/2)} = \mathcal{F}(\mathbf{g}^-_{(i,j+3)}, \mathbf{g}^-_{(i,j+2)}, \ldots, \mathbf{g}^-_{(i,j-1)}), \tag{7.23d}$$

and

$$\mathbf{g}^\pm = \mathbf{g} \pm \alpha_{\eta(i,j+1/2)}\mathbf{u}. \tag{7.23e}$$

The absolute value of the largest wave speed in the η direction is α_η (*cf.* Eq. (6.17d)). The WENO5M interpolant, $\mathcal{F}$, is given in Section 6.1.2.3.

7.3.4 $\frac{\partial}{\partial\eta}$ for $(\xi_i, \eta_j) : j \in [N_{\eta-2}, N_\eta]$

In this region it is not possible to use the scheme given by Eqs. (7.23) since the presence of the shock prevents the LF fluxes from being computed. Instead, the stencil shown on the left hand side of Fig. 7.2 is used to simply computed the

derivative via finite differences:

$$\left.\frac{\partial \mathbf{g}}{\partial \eta}\right|_{(i,N_\eta-2)} = \frac{1}{12\Delta\eta}\Big(\mathbf{g}_{(i,N_\eta-4)} - 8\mathbf{g}_{(i,N_\eta-3)} + 8\mathbf{g}_{(i,N_\eta-1)} - \mathbf{g}_{(i,N_\eta)}\Big) + O(\Delta\eta^4), \tag{7.24a}$$

$$\begin{aligned}\left.\frac{\partial \mathbf{g}}{\partial \eta}\right|_{(i,N_\eta-1)} = \frac{1}{12\Delta\eta}\Big(&- \mathbf{g}_{(i,N_\eta-4)} + 6\mathbf{g}_{(i,N_\eta-3)} \\ &- 18\mathbf{g}_{(i,N_\eta-2)} + 10\mathbf{g}_{(i,N_\eta-1)} + 3\mathbf{g}_{(i,N_\eta)}\Big) + O(\Delta\eta^4),\end{aligned} \tag{7.24b}$$

$$\begin{aligned}\left.\frac{\partial \mathbf{g}}{\partial \eta}\right|_{(i,N_\eta)} = \frac{1}{60\Delta\eta}\Big(&- 12\mathbf{g}_{(i,N_\eta-5)} + 75\mathbf{g}_{(i,N_\eta-4)} - 200\mathbf{g}_{(i,N_\eta-3)} \\ &+ 300\mathbf{g}_{(i,N_\eta-2)} - 300\mathbf{g}_{(i,N_\eta-1)} + 137\mathbf{g}_{(i,N_\eta)}\Big) + O(\Delta\eta^5).\end{aligned} \tag{7.24c}$$

7.3.5 $\frac{\partial}{\partial \xi}$ for $(\xi_i, \eta_j) : i \in [3, N_\xi - 3]$

Similar to Eqs. (7.23), $\frac{\partial \mathbf{g}}{\partial \xi}$ is approximated using the WENO5M discretization of the LF flux:

$$\left.\frac{\partial \mathbf{g}}{\partial \xi}\right|_{(i,j)} = \frac{\hat{\mathbf{g}}_{(i+1/2,j)} - \hat{\mathbf{g}}_{(i-1/2,j)}}{\Delta\xi}, \tag{7.25a}$$

where the numerical flux function is approximated by WENO5M yielding

$$\hat{\mathbf{g}}_{(i+1/2,j)} = \frac{1}{2}\left(\hat{h}[\mathbf{g}^+]_{(i+1/2,j)} + \hat{h}[\mathbf{g}^-]_{(i+1/2,j)}\right), \tag{7.25b}$$

$$\hat{h}[\mathbf{g}^+]_{(i+1/2,j)} = \mathcal{F}(\mathbf{g}^+_{(i-2,j)}, \mathbf{g}^+_{(i-1,j)}, \ldots, \mathbf{g}^+_{(i+2,j)}), \tag{7.25c}$$

$$\hat{h}[\mathbf{g}^-]_{(i+1/2,j)} = \mathcal{F}(\mathbf{g}^-_{(i+3,j)}, \mathbf{g}^-_{(i+2,j)}, \ldots, \mathbf{g}^-_{(i-1,j)}), \tag{7.25d}$$

and

$$\mathbf{g}^{\pm} = \mathbf{g} \pm \alpha_{\xi(i+1/2,j)}\mathbf{u}. \tag{7.25e}$$

Again, the largest wave speed magnitude is the ξ direction is α_{ξ}. The WENO5M interpolant, $\mathcal{F}$, is given in Section 6.1.2.3.

7.3.6 $\frac{\partial}{\partial\xi}$ for $(\xi_i, \eta_j) : i \in [0, 2]$

Although the model problem shown in Fig. 1.1 is of primary interest, it is also beneficial to be able to employ a periodic boundary condition as well. It is for this purpose that the ghost nodes seen on the right of Fig. 7.2 can be used. When imposing a periodic boundary condition, these ghost nodes allow for the scheme given in Eqs. (7.25) to be used; no special discretization need be employed at the boundary.

However, for the model problem the boundary $\xi = k_l$ is treated as rigid wall across which the solution is unknown. Thus, the stencil seen at the bottom of Fig. 7.2 is used in conjunction with Taylor series approximations to the derivative:

$$\begin{aligned}\left.\frac{\partial \mathbf{g}}{\partial \xi}\right|_{(0,j)} = \frac{1}{60\Delta\eta}\Big(&- 137\mathbf{g}_{(0,j)} + 300\mathbf{g}_{(1,j)} - 300\mathbf{g}_{\eta(2,j)} \\ &+ 200\mathbf{g}_{(3,j)} - 75\mathbf{g}_{(4,j)} + 12\mathbf{g}_{(5,j)}\Big) + O(\Delta\xi^5)\end{aligned} \tag{7.26a}$$

$$\begin{aligned}\left.\frac{\partial \mathbf{g}}{\partial \xi}\right|_{(1,j)} = \frac{1}{12\Delta\xi}\Big(&- 3\mathbf{g}_{(0,j)} - 10\mathbf{g}_{(1,j)} \\ &+ 18\mathbf{g}_{(2,j)} - 6\mathbf{g}_{(3,j)} + \mathbf{g}_{(4,j)}\Big) + O(\Delta\xi^4)\end{aligned} \tag{7.26b}$$

$$\left.\frac{\partial \mathbf{g}}{\partial \xi}\right|_{(2,j)} = \frac{1}{12\Delta\xi}\Big(\mathbf{g}_{(0,j)} - 8\mathbf{g}_{(1,j)} + 8\mathbf{g}_{(3,j)} - \mathbf{g}_{(4,j)}\Big) + O(\Delta\xi^4) \tag{7.26c}$$

7.3.7 $\frac{\partial}{\partial \xi}$ for $(\xi_i, \eta_j) : i \in [N_\xi - 2, N_\xi]$

Here the same considerations stated in Section 7.3.6 determine the behavior of the ghost nodes and the subsequent approximation of the derivative. For the case of periodic boundary conditions, the scheme presented in Eqs. (7.25) is used again. For a rigid wall, Taylor series again give an appropriate approximation to the derivatives:

$$\left.\frac{\partial \mathbf{g}}{\partial \xi}\right|_{(N_\xi-2,j)} = \frac{1}{12\Delta\xi}\Big(\mathbf{g}_{(N_\xi-4,j)} - 8\mathbf{g}_{(N_\xi-3,j)} + 8\mathbf{g}_{(N_\xi-1,j)} - \mathbf{g}_{(N_\eta,j)}\Big) + O(\Delta\xi^4) \tag{7.27a}$$

$$\left.\frac{\partial \mathbf{g}}{\partial \xi}\right|_{(N_\xi-1,j)} = \frac{1}{12\Delta\xi}\Big(- \mathbf{g}_{(N_\xi-4,j)} + 6\mathbf{g}_{(N_\xi-3,j)} - 18\mathbf{g}_{(N_\xi-2,j)} + 10\mathbf{g}_{(N_\eta-1,j)} + 3\mathbf{g}_{(i,N_\xi)}\Big) + O(\Delta\xi^4) \tag{7.27b}$$

$$\left.\frac{\partial \mathbf{g}}{\partial \xi}\right|_{(N_\xi,j)} = \frac{1}{60\Delta\xi}\Big(- 12\mathbf{g}_{(N_\xi-5,j)} + 75\mathbf{g}_{(N_\xi-4,j)} - 200\mathbf{g}_{(N_\xi-3,j)} + 300\mathbf{g}_{(N_\xi-2,j)} - 300\mathbf{g}_{(N_\xi-1,j)} + 137\mathbf{g}_{(N_\xi,j)}\Big) + O(\Delta\xi^5) \tag{7.27c}$$

7.3.8 $\hat{H}$ along $j = N_\eta$

Along the shock, the discretization of the last of Eqs. (7.22) is also needed. The discretization selected is a conservative LF scheme which employs the WENO5M approximation to the numerical flux. The resulting numerical Hamiltonian $\hat{H}$ is given by Eq. (6.28):

$$\hat{H}(\mathbf{u}, \phi^+, \phi^-)_i = H\left(\mathbf{u}, \frac{\phi_i^+ + \phi_i^-}{2}\right) + \alpha_i\left(\frac{\phi_i^+ - \phi_i^-}{2}\right), \tag{7.28}$$

where

$$\phi_i^+ = \mathcal{F}(\phi_{i-5/2}, \phi_{i-3/2}, \ldots, \phi_{i+3/2}), \tag{7.29}$$

$$\phi_i^- = \mathcal{F}(\phi_{i+5/2}, \phi_{i+3/2}, \ldots, \phi_{i-3/2}), \tag{7.30}$$

$$\phi_{(i-1/2,j)} = \frac{y_{(i,N_\eta)} - y_{(i-1,N_\eta)}}{\Delta\xi}, \tag{7.31}$$

and α is give by Eq. (6.23d).

7.4 Formulation for Euler equations with reaction

All that remains is the specification of the conserved quantities, fluxes, source terms, and boundary conditions for the model problem. The dominant physical mechanisms considered in detonation modeling are pressure waves and reaction, as discussed in Appendix C. The resulting hyperbolic system in two-dimensions is given in a physically conservative, tensorial form. As indicated in Section 4.3, it is a simple matter of inspection to determine the requisite conserved quantities and fluxes. The boundary conditions are chosen according model problem of Fig. 1.1. At the shock, the Rankine-Hugoniot jump conditions give the shocked state of the as a function of the quiescent state and the shock velocity. No flux of material is allowed along the interface between the HE and inert confiner. A simple Neumann condition is used along the rear of the domain. Lastly, a concatenated form of the conserved quantities, fluxes, and source terms allows the system to be expressed as a single equation without loss of generality.

7.4.1 The Euler equations with reaction

The system Eqs. (2.1e) consists of mass, momentum, energy, and species conservation. Each conservation law may be re-written according to Eq. (4.11a) in Cartesian coordinates as

$$\frac{\partial \boldsymbol{F}}{\partial t} + \frac{\partial \boldsymbol{f}^i}{\partial Y^i} = \boldsymbol{B} \qquad \text{or} \qquad \frac{\partial \boldsymbol{F}}{\partial t} + \frac{\partial \boldsymbol{f}_x}{\partial x} + \frac{\partial \boldsymbol{f}_y}{\partial y} = \boldsymbol{B}. \tag{7.32}$$

Equation (7.32) is identical to Eq. (4.26) and so identifies the corresponding terms in Eq. (7.6):

$$\boldsymbol{F} = \rho, \qquad \boldsymbol{f}^i = \rho v^i = \begin{bmatrix} \rho u \\ \rho v \end{bmatrix}, \qquad \boldsymbol{B} = 0, \tag{7.33a}$$

$$\begin{aligned} \boldsymbol{F} &= \begin{bmatrix} \rho u \\ \rho v \end{bmatrix}, & \boldsymbol{f}^i &= \rho v^i v^j + p\delta^{ij}, & \boldsymbol{B} &= \begin{bmatrix} 0 \\ 0 \end{bmatrix}, \\ & & &= \begin{bmatrix} \rho u^2 + p & \rho uv \\ \rho vu & \rho v^2 + p \end{bmatrix} \end{aligned} \tag{7.33b}$$

$$\begin{aligned} \boldsymbol{F} &= \rho(e + \frac{1}{2}(u^2 + v^2)), & \boldsymbol{f}^i &= \rho v^i \left(e + \frac{v^j v_j}{2} + \frac{p}{\rho} \right), & \boldsymbol{B} &= 0, \\ & & &= \begin{bmatrix} \rho u \left(e + \frac{1}{2}(u^2 + v^2) + \frac{p}{\rho} \right) \\ \rho v \left(e + \frac{1}{2}(u^2 + v^2) + \frac{p}{\rho} \right) \end{bmatrix} \end{aligned} \tag{7.33c}$$

$$\boldsymbol{F} = \rho Y_{(i)}, \qquad \boldsymbol{f}^i = \rho Y_{(i)} v^i = \begin{bmatrix} \rho Y_{(i)} u \\ \rho Y_{(i)} v \end{bmatrix}, \qquad \boldsymbol{B} = M_{(i)} \dot{\omega}_{(i)}. \tag{7.33d}$$

With Eqs. (7.33), Eq. (7.32) is a physically conservative tensorial form which may be easily used in conjunction with Eq. (4.11b) to determine the physical shock speed.

7.4.2 Reaction kinetics and equations of state

Consider the irreversible Arrhenius unimolecular reaction

$$A \rightarrow B$$

between two species A and B. Because only two species are involved and the stoichiometric coefficient is unity, the molecular weight of A and B must be identical and

$$Y_{(A)} = 1 - Y_{(B)}.$$

Thus, Eqs. (2.1e) corresponding to Eq. (7.33d) can be reduced to a single equation for $\rho Y_{(B)}$:

$$\frac{\partial}{\partial t}\left(\rho Y_{(B)}\right) + \frac{\partial}{\partial x}\left(\rho Y_{(B)} u\right) + \frac{\partial}{\partial y}\left(\rho Y_{(B)} v\right) = M_{(B)}\dot{\omega}_{(B)}.$$

Furthermore, the only remaining reaction rate will be denoted ζ and is specified to be

$$\begin{aligned} \zeta &= M_{(B)}\dot{\omega}_{(B)}, \\ &= a\rho(1 - Y_{(B)}) \exp\left(\frac{-E\rho}{p}\right), \end{aligned}$$

where a is a collision frequency factor with dimensions of inverse time and E is the activation energy. Note the the only quantity not directly related to one of the conserved quantities, Eq. (7.33) is the pressure.

Still required to complete the system are the thermal and caloric equations of state. Once they are specified, the thermodynamic quantities of pressure and internal energy can be given in terms of the other state variables. Here the HE material is modeled as a calorically perfect ideal gas mixture as in Appendix D where only two species with identical specific heats are involved. Initially, the material is composed entirely of species A: $Y_{(A)} = 1$ and $Y_{(B)} = 0$. The reaction reaches completion when species A is exhausted yielding $Y_{(A)} = 0$ and $Y_{(B)} = 1$. For the sake of comparison with the literature, $Y_{(B)}$ will be denoted as λ and is termed the progress variable.

Denoting the mass fraction of the reaction products to be λ, the equations of state reduce to

$$p = \rho R T, \tag{7.34a}$$

$$e = \frac{1}{\gamma - 1} + q\lambda, \tag{7.34b}$$

where q is the heat release due to reaction. Since e and ρ appear explicitly in the conserved quantities, Eqs. (7.33), the most useful form of Eq. (7.34b) is

$$p = \rho(\gamma - 1)(e + q\lambda). \tag{7.35}$$

7.4.3 Boundary conditions

In this section, the boundary conditions for the model problem are specified. The quiescent, non-shocked HE state is denoted with a subscript "o". The velocity vector is denoted as $\boldsymbol{u} = \begin{bmatrix} u \\ v \end{bmatrix}$, consistent with the notation of the grid speed, $\boldsymbol{U} = \begin{bmatrix} \frac{\partial x}{\partial \tau} \\ \frac{\partial y}{\partial \tau} \end{bmatrix}$, and shock speed, $\boldsymbol{D} = \begin{bmatrix} \frac{\partial x}{\partial \tau} \\ \frac{\partial y}{\partial \tau} \end{bmatrix}_{\Sigma}$. Because many of the jump conditions constrain the physical components of the velocity, recall that they are denoted

${}_{(\mathrm{i})}\bar{u} = \bar{\boldsymbol{u}} \cdot \boldsymbol{e}^{(i)}$ and $\bar{u}_{(\mathrm{i})} = \bar{\boldsymbol{u}} \cdot \boldsymbol{e}_{(i)}$. The physical bases are such that $\{\boldsymbol{e}_{(2)}, \boldsymbol{e}^{(1)}\}$ are tangential and normal to the material interface along $\xi = k_l$ or k_r and $\{\boldsymbol{e}_{(1)}, \boldsymbol{e}^{(2)}\}$ are tangential and normal to the shock along $\eta = 0$ (*cf.* Fig. 5.2).

7.4.3.1 Material interface conditions

At the material interface between the HE and inert confiner, it is required that the normal component of velocity in the shock-attached frame is zero:

$$(\boldsymbol{u}_p - \boldsymbol{U}) \cdot \boldsymbol{e}^{(1)} = 0 \qquad \text{along } \xi = k_l \text{ or } k_r, \tag{7.36}$$

where $\boldsymbol{u}_p = \begin{bmatrix} u_p \\ v_p \end{bmatrix}$ is the velocity after the boundary condition has been applied. To achieve this condition at each point on the material interface, the relative velocity vector is projected onto the vector tangent to the interface. Letting $\bar{\boldsymbol{u}} = \boldsymbol{u} - \boldsymbol{U}$, the relative velocity vector is split into two orthonormal components

$$\bar{\boldsymbol{u}} = {}_{(1)}\bar{u}\ \boldsymbol{e}^{(1)} + \underbrace{\bar{u}_{(2)}\ \boldsymbol{e}_{(2)}}_{\bar{\boldsymbol{u}}_p} \qquad \text{along } \xi = k_l \text{ or } k_r.$$

Solving for the projection $\bar{\boldsymbol{u}}_p$ and simplifying gives

$$\begin{bmatrix} u_p \\ v_p \end{bmatrix} = \begin{bmatrix} u \\ v \end{bmatrix} - \frac{\bar{u}\frac{\partial y}{\partial \eta} - \bar{v}\frac{\partial x}{\partial \eta}}{\frac{\partial y}{\partial \eta}^2 + \frac{\partial x}{\partial \eta}^2} \begin{bmatrix} \frac{\partial y}{\partial \eta} \\ -\frac{\partial x}{\partial \eta} \end{bmatrix} \qquad \text{along } \xi = k_l \text{ or } k_r. \tag{7.37}$$

Equation (7.37) gives the required boundary condition.

7.4.3.2 Rankine-Hugoniot jump conditions

Applying the shock jump condition Eq. (4.11b) to Eqs. (7.32) and (7.33) gives the jump conditions in an Eulerian flow across a shock, known as the Rankine-Hugoniot jump conditions. They are developed in Appendix G, giving a pointwise condition across the shock. With the relative velocity tangential and normal to the shock denoted $\bar{\boldsymbol{u}} \cdot \boldsymbol{e}_{(1)} \equiv \bar{u}_{(1)}$ and $\bar{\boldsymbol{u}} \cdot \boldsymbol{e}^{(2)} \equiv {}_{(2)}\bar{u}$, respectively, they may be written

$$p_\Sigma - p_o = (\rho \bar{\boldsymbol{u}} \cdot \boldsymbol{e}^{(2)})\Big|_o^2 \left(\frac{1}{\rho_o} - \frac{1}{\rho_\Sigma}\right), \tag{7.38a}$$

$$e_\Sigma - e_o = \frac{1}{2}(p_\Sigma + p_o)\left(\frac{1}{\rho_o} - \frac{1}{\rho_\Sigma}\right), \tag{7.38b}$$

$$(\rho \bar{\boldsymbol{u}} \cdot \boldsymbol{e}^{(2)})\Big|_\Sigma = (\rho \bar{\boldsymbol{u}} \cdot \boldsymbol{e}^{(2)})\Big|_o, \tag{7.38c}$$

$$\bar{\boldsymbol{u}} \cdot \boldsymbol{e}_{(1)}\Big|_\Sigma = \bar{\boldsymbol{u}} \cdot \boldsymbol{e}_{(1)}\Big|_o, \tag{7.38d}$$

$$Y_{(i)}\Big|_\Sigma = Y_{(i)}\Big|_o, \tag{7.38e}$$

where a subscript Σ denotes the shocked value. To form a complete system, the equation of state must be specified to give an additional relationship for $e(p, \rho)$. Since the HE is assumed to be a calorically perfect ideal gas mixture, Appendix D gives the desired relationship as

$$e_\Sigma - e_o = \frac{1}{\gamma - 1}\left(\frac{p_\Sigma}{\rho_\Sigma} - \frac{p_o}{\rho_o}\right), \tag{7.39}$$

since there is no reaction at the shock according to Eq. (7.38e).

With Eq. (7.39), Eqs. (7.38) forms a system of five equations in five unknown which can be solved for ρ_Σ, p_Σ, ${}_{(2)}u\big|_\Sigma$, $u_{(1)}\big|_\Sigma$, and $Y_{(i)}\big|_\Sigma$ as a function of the

quiescent state and the shock velocity:

$$\rho_\Sigma = \frac{(\gamma+1)\rho_o^2 \left(\bar{\boldsymbol{u}}\cdot\boldsymbol{e}^{(2)}\right)\big|_o^2}{(\gamma-1)\rho_o \left(\bar{\boldsymbol{u}}\cdot\boldsymbol{e}^{(2)}\right)\big|_o^2 + 2\gamma p_o}, \tag{7.40a}$$

$$p_\Sigma = -\frac{\gamma-1}{\gamma+1}p_o + \frac{2\rho_o \left(\bar{\boldsymbol{u}}\cdot\boldsymbol{e}^{(2)}\right)\big|_o^2}{(\gamma+1)}, \tag{7.40b}$$

$${}_{(2)}u\big|_\Sigma = \frac{(\gamma-1)\rho_o \left(\bar{\boldsymbol{u}}\cdot\boldsymbol{e}^{(2)}\right)\big|_o^2 + 2\gamma p_o}{(\gamma+1)\rho_o \left(\bar{\boldsymbol{u}}\cdot\boldsymbol{e}^{(2)}\right)\big|_o} + D_n \tag{7.40c}$$

$$u_{(1)}\big|_\Sigma = \boldsymbol{u}_o\cdot\boldsymbol{e}_{(1)}, \tag{7.40d}$$

$$Y_{(i)}\big|_\Sigma = Y_{(i)}\big|_o, \tag{7.40e}$$

where all quantities are evaluated at the shock.

All that remains is to write the velocity in Cartesian components. Writing the velocity vector as $\boldsymbol{u} = u_{(1)}\ \boldsymbol{e}_{(1)} + {}_{(2)}u\ \boldsymbol{e}^{(2)}$ gives

$$\begin{bmatrix} u \\ v \end{bmatrix} = \frac{1}{\sqrt{\frac{\partial x}{\partial \xi}^2 + \frac{\partial y}{\partial \xi}^2}} \left(u_{(1)} \begin{bmatrix} \frac{\partial x}{\partial \xi} \\ \frac{\partial y}{\partial \xi} \end{bmatrix} + {}_{(2)}u \begin{bmatrix} -\frac{\partial y}{\partial \xi} \\ \frac{\partial x}{\partial \xi} \end{bmatrix} \right). \tag{7.41}$$

7.4.3.3 Rear boundary condition

Because the structured solution inside the reaction zone is of primary interest, the rear boundary condition is not as critical as the others. This is due to the fact that the solution domain of interest normally lies between the shock and sonic loci, which is unaffected by perturbations introduced due to the rear boundary. Thus, it is sufficient to constrain all rear boundary ghost node values to the last computed value of its nearest neighbor in the computational domain. This homogeneous Neumann boundary condition effectively sets the flux to zero along the rear boundary at low order.

7.4.4 Final numerical form

Concatenating Eqs. (7.33) gives a form more amenable to numerical manipulation. Using the simplified notation of Eq. (7.6), Eqs. (7.33) may be regrouped as

$$\boldsymbol{F} = \begin{pmatrix} \rho \\ \rho u \\ \rho v \\ \rho(e + \frac{1}{2}(u^2 + v^2)) \\ \rho\lambda \end{pmatrix}, \qquad \boldsymbol{B} = \begin{pmatrix} 0 \\ 0 \\ 0 \\ 0 \\ \zeta \end{pmatrix}, \tag{7.42a}$$

$$\boldsymbol{f}_x = \begin{pmatrix} \rho u \\ \rho u^2 + p \\ \rho v u \\ \rho u \left(e + \frac{1}{2}(u^2 + v^2) + \frac{p}{\rho}\right) \\ \rho\lambda u \end{pmatrix}, \quad \boldsymbol{f}_y = \begin{pmatrix} \rho v \\ \rho u v \\ \rho v^2 + p \\ \rho v \left(e + \frac{1}{2}(u^2 + v^2) + \frac{p}{\rho}\right) \\ \rho\lambda v \end{pmatrix}. \tag{7.42b}$$

With the conserved quantities, fluxes and sources now defined in Eqs. (7.42), either system Eq. (7.14) or Eq. (7.15) can now be formed directly from Eqs. (7.10) and (7.12). The numerical discretization used given in Section 7.3 combined with the time integration in Section 6.3 .

CHAPTER 8

GASEOUS DETONATION: ONE-DIMENSIONAL RESULTS

In this chapter, the methods developed in Chapter 7 are applied to a classical unsteady detonation problem to generate solutions with unprecedented accuracy. The one-dimensional reactive Euler equations for a calorically perfect mixture of ideal gases whose reaction is described by single-step irreversible Arrhenius kinetics are solved in a series of calculations in which the activation energy is varied. In contrast with nearly all known simulations of this problem, which converge at a rate no greater than first order as the spatial and temporal grid is refined, the present method is shown to converge at a rate consistent with the fifth order accuracy of the spatial and temporal discretization schemes. This high accuracy enables more precise verification of known results and prediction of heretofore unknown phenomena. To five significant figures, the scheme faithfully recovers the stability boundary, growth rates, and wave-numbers predicted by an independent linear stability theory in the stable and weakly unstable regime. As the activation energy is increased, a series of period-doubling events are predicted, and the system undergoes a transition to chaos. Consistent with general theories of non-linear dynamics, the bifurcation points are seen to converge at a rate for which the Feigenbaum constant is 4.66 ± 0.09, in close agreement with the true value of $4.669201\ldots$. As activation energy is increased further, domains are identified in which the system undergoes a transition from a chaotic state back to one

whose limit cycles are characterized by a small number of non-linear oscillatory modes. This result is consistent with behavior of other non-linear dynamical systems, but not typically considered in detonation dynamics. The period and average detonation velocity are calculated for a variety of asymptotically stable limit cycles. The average velocity for such pulsating detonations is found to be slightly greater than the Chapman-Jouguet velocity.

Unsteady detonations predicted by the model employed here have been widely studied for over forty years. A partial list [1, 9, 53–63] summarizes some of the many approaches: linear stability via normal modes analysis, asymptotic techniques, method of characteristics, and direct numerical simulation using shock-capturing, shock-tracking and/or adaptive mesh refinement techniques. Linear stability analysis gives the most rigorous results, but cannot capture the non-linear dynamics or long-time limit cycle behavior. The method of characteristics, when coupled with a high order method for solution of ordinary differential equations, can give accurate results, at the expense of algorithmic complexity and difficulty in accommodating flows with multiple discontinuities. Shock capturing techniques are easy to implement, but results are corrupted by order one errors at the shock which propagate into the entire flow field, rendering it difficult to precisely identify fine scale dynamics [64–67]. Methods which do have high order accuracy for continuous solutions, when coupled with a shock-capturing scheme, always reduce that accuracy to at most first order. Although shock-tracking [9, 54, 56, 57] and shock-fitting schemes [1] can in principle eliminate the order one errors at the shock, high rates of global convergence have not been demonstrated to date.

The true high order accuracy of the new numerical algorithm is the principal novelty of this work; less accurate versions of most results have appeared pre-

viously in the literature. We compare our results with two of the best recent studies: Kasimov and Stewart [1] and Ng, *et al.* [63]. Several test problems are exploited to verify the accuracy of the scheme. In particular, for unstable detonations it becomes possible to predict, with high precision and moderate resolution, both the growth rates and frequencies of the same unstable modes which have been independently predicted by linear stability analysis. The results are then extended into the non-linear regime to predict the ultimate limit cycle behavior. Relative to recent related calculations [1, 63], those presented here are resolved in roughly two orders of magnitude more detail, which allows a clearer elucidation of the structurally rich bifurcation phenomena. In particular, new windows of parameter space are identified in which low frequency behavior is predicted in an otherwise chaotic region.

The plan of this chapter is as follows. First, the governing equations and associated jump conditions are specified. An evolution equation for the shock velocity is derived, which is commonly referred to as the shock-change equation [19]. A description of the fifth order scheme is then presented. The solutions to various test problems is given. These include comparisons with the stable Zel'dovich-von Neumann-Döring (ZND) solution, growth rate and frequency of linearly unstable ZND waves, and fully time-dependent and non-linear detonation pulsation flows. A detailed bifurcation diagram shows how the long-time limit of the detonation wave speed behaves as activation energy is varied. Period-doubling bifurcations, identified earlier [60, 63], are found to much greater precision, and several new modes of behavior are given. It is also confirmed that the convergence of the period-doubling bifurcation points is in agreement with the general theory of Feigenbaum [68, 69]. The limit cycle period and average detonation speed

are given for asymptotically stable flows with a variety of activation energies; the average detonation speed is found to be slightly greater than the Chapman-Jouguet speed.

8.1 Governing equations

The one-dimensional unsteady reactive Euler equations for a calorically perfect ideal gas which undergoes a single irreversible reaction are expressed in conservative form as

$$\frac{\partial \rho}{\partial t} + \frac{\partial}{\partial \xi}(\rho u) = 0, \tag{8.1a}$$

$$\frac{\partial}{\partial t}(\rho u) + \frac{\partial}{\partial \xi}\left(\rho u^2 + p\right) = 0, \tag{8.1b}$$

$$\frac{\partial}{\partial t}\left(\rho\left(e + \frac{1}{2}u^2\right)\right) + \frac{\partial}{\partial \xi}\left(\rho u\left(e + \frac{1}{2}u^2 + \frac{p}{\rho}\right)\right) = 0, \tag{8.1c}$$

$$\frac{\partial}{\partial t}(\rho\lambda) + \frac{\partial}{\partial \xi}(\rho u\lambda) = k\rho(1-\lambda)\exp\left(-\frac{\rho E}{p}\right), \tag{8.1d}$$

$$e = \frac{1}{\gamma - 1}\frac{p}{\rho} - \lambda q. \tag{8.1e}$$

Here, the laboratory frame Cartesian spatial coordinate is ξ, and time is t. The dependent variables in Eqs. (8.1) are density ρ, particle velocity u, pressure p, specific internal energy e, and reaction progress λ. The parameters are the reaction kinetic rate constant k, activation energy E, ratio of specific heats γ, and heat release per unit mass q. Equations (8.1) are expressions of, respectively, the conservation of mass, ξ-momentum, and energy, evolution of species, and a caloric state relation. Equation (8.1d) models the irreversible reaction $A \rightarrow B$ in which species A and B have identical molecular masses and specific heats. The mass fractions of each species, Y_A and Y_B, are given in terms of the reaction progress

variable by the relations $Y_A = 1 - \lambda$ and $Y_B = \lambda$.

Equations (8.1) are supplemented by the following standard Rankine-Hugoniot conditions at the shock jump:

$$\rho_s(D(t) - u_s) = \rho_o(D(t) - u_o), \tag{8.2a}$$

$$p_s - p_o = (\rho_o(D(t) - u_o))^2 \left(\frac{1}{\rho_o} - \frac{1}{\rho_s}\right), \tag{8.2b}$$

$$e_s - e_o = \frac{1}{2}(p_s + p_o)\left(\frac{1}{\rho_o} - \frac{1}{\rho_s}\right), \tag{8.2c}$$

$$\lambda_s = \lambda_o. \tag{8.2d}$$

Here, D is the shock velocity, which in general is time-dependent; the subscript s denotes the shock state, and the subscript o denotes the constant ambient state. Note that the shock states in Eqs. (8.2) can be determined in terms of the ambient state and the shock velocity. It is assumed that no reaction takes place upstream of the shock; *i.e.* the source term in Eq. (8.1d) is activated only for fluid particles which have passed through the shock.

For the shock-fitting numerical scheme, Eqs. (8.1) are transformed to a frame that is fixed to the shock front. To this end, a new spatial variable is taken to be

$$x = \xi - \int_0^t D(\tau)d\tau, \tag{8.3}$$

where the shock is initially presumed to be at $\xi = 0$, and thus for all time the shock locus is $x = 0$. Under this transformation, one recovers the following conservation

laws:

$$\frac{\partial \rho}{\partial t} + \frac{\partial}{\partial x}\left(\rho(u-D)\right) = 0, \tag{8.4a}$$

$$\frac{\partial}{\partial t}\left(\rho u\right) + \frac{\partial}{\partial x}\left(\rho u(u-D) + p\right) = 0, \tag{8.4b}$$

$$\frac{\partial}{\partial t}\left(\rho\left(e + \frac{1}{2}u^2\right)\right) + \frac{\partial}{\partial x}\left((u-D)\rho\left(e + \frac{1}{2}u^2\right) + up\right) = 0, \tag{8.4c}$$

$$\frac{\partial}{\partial t}\left(\rho\lambda\right) + \frac{\partial}{\partial x}\left(\rho(u-D)\lambda\right) = k\rho(1-\lambda)\exp\left(-\frac{\rho E}{p}\right). \tag{8.4d}$$

The particle velocity, u, is still measured in the laboratory frame. Up to this point, there is nothing different from earlier shock-fitting formulations [1].

Equations (8.4) do not yet form a complete system of equations; an expression for the change in shock velocity, D, with time is still required. In order to close the system, consider that the boundary condition provided at the shock by Eqs. (8.2) is a function of D alone for a given ambient state. Thus, the state variables are all coupled through D at the shock and cannot evolve independently if they are to satisfy the boundary condition; however, Eqs. (8.2) can also be solved to find an expression for the shock velocity in terms the state variables at the shock. This observation combined with the governing PDEs provides the basis for the derivation of the shock velocity evolution equation, otherwise known as the shock-change equation [19].

The shock-change equation describes the evolution of the shock velocity as a function of time. This relationship can take on various forms which are mathematically equivalent. A new and particularly useful form is derived here. First, assuming $\lambda_o = 0$, one determines the momentum at the shock state from Eqs. (8.1e)

and (8.2) to be

$$\rho_s u_s = \frac{\rho_o(D-u_o)\left(\gamma(\rho_o(D-u_o)u_o - 2p_o) + \rho_o(2D^2 - 3Du_o + u_o^2)\right)}{\gamma(2p_o + \rho_o(D-u_o)^2) - \rho_o(D-u_o)^2}. \tag{8.5}$$

As Eq. (8.5) is a function of D alone, one has

$$\frac{dD}{dt} = \left(\frac{d(\rho_s u_s)}{dD}\right)^{-1} \frac{d}{dt}(\rho_s u_s), \tag{8.6}$$

from the chain rule. Note that the derivative of the momentum at the shock with respect to the shock velocity, $d(\rho_s u_s)/dD$, can be obtained in closed form from Eq. (8.5) but is omitted here due to its complexity. Thus, the only term remaining in Eq. (8.6) to compute is $d(\rho_s u_s)/dt$.

Now

$$\frac{d}{dt}(\rho_s u_s) = \left.\frac{d}{dt}\right|_{x=0} (\rho u) \tag{8.7}$$

is the intrinsic derivative of the momentum following the shock. This derivative is given by

$$\left.\frac{d}{dt}\right|_{x=0} = \left.\frac{\partial}{\partial t}\right|_{x=0} + \underbrace{\left.\frac{dx}{dt}\right|_{x=0}}_{=0} \left.\frac{\partial}{\partial x}\right|_{x=0} = \left.\frac{\partial}{\partial t}\right|_{x=0}, \tag{8.8}$$

since the velocity of the shock in the fitted coordinate system is zero. Thus, at the shock, rearrangement of Eq. (8.4b) gives

$$\left.\frac{d\left(\rho_s u_s\right)}{dt}\right|_{x=0} = -\frac{\partial}{\partial x}\left(\rho u(u-D) + p\right)|_{x=0}, \tag{8.9}$$

the intrinsic derivative of the momentum following the shock in terms of a spatial

derivative at the shock. Lastly, substituting Eq. (8.9) into Eq. (8.6) yields the shock-change equation

$$\frac{dD}{dt} = -\left(\frac{d(\rho_s u_s)}{dD}\right)^{-1}\left(\frac{\partial}{\partial x}\left(\rho u(u-D)+p\right)\right)\Big|_{x=0}. \tag{8.10}$$

Equation (8.10) relates the shock acceleration to the momentum flux gradient at the shock. Other, mathematically equivalent forms of the shock-change equation could have been used, but there are two reasons this particular form was chosen. First, the momentum flux gradient is a quantity that will already be computed throughout the flow, eliminating the need to perform a special characteristic decomposition of the equations at the shock [1, 70]. More importantly, it scales easily with shock velocity, so that the first term on the right hand side of Eq. (8.10) is well behaved in both the weak and strong shock limits; this quality would not be exhibited if mass rather than momentum conservation was used to derive the shock-change equation. Other combinations of the equations may also be amenable in these limits, but Eq. (8.10) is adequate for what follows in the next section.

8.2 Numerical method

Here, the details of the high order shock-fitting numerical algorithm are presented. A point-wise method of lines approach [40] is used. This method simplifies the required coding, allows separate temporal and spatial discretizations, and also allows for the incorporation of source terms. In the following sections, the computational grid will be defined, the WENO5M spatial discretization scheme [35] will be outlined, and the temporally fifth order Runge-Kutta scheme for time discretization [51] will be given.

Written in vector notation, Eqs. (8.4) take on the form

$$\frac{\partial}{\partial t}\mathbf{u} + \frac{\partial}{\partial x}\mathbf{f}\left(\mathbf{u}\right) = \mathbf{s}\left(\mathbf{u}\right). \tag{8.11}$$

Here the vector $\mathbf{u}$ is used to denote the set of conserved dependent variables,

$$\mathbf{u} = \left(\rho, \rho u, \rho\left(e + \frac{1}{2}u^2\right), \rho\lambda\right)^T. \tag{8.12}$$

Strictly speaking, $\rho\lambda$ is not conserved, but evolves due to the reaction source term. It is traditional to label it a conserved variable as well, as it is the proper divergence formulation of the reaction kinetics model. The vector $\mathbf{f}$ is a set of fluxes of each conserved quantity, and $\mathbf{s}$ is a source.

8.2.1 Grid

A uniform Cartesian grid is used to discretize the domain $x \in [x_{min}, x_{max}]$, with $N_x + 1$ equally spaced nodes, $x_{min} < 0$, and $x_{max} = 0$. One allows the semi-discretizations $\mathbf{u}(x,t) \rightarrow \mathbf{u}_i(t)$ and $\mathbf{u}(x,t) \rightarrow \mathbf{u}^n(x)$ as well as the full discretization $\mathbf{u}_i(t) \rightarrow \mathbf{u}_i^n$ of the solution vector $\mathbf{u}$. Here, i is the spatial node number corresponding to the location $x_i = x_{min} + i\Delta x$, where $\Delta x = -x_{min}/N_x$, and n is the time level corresponding to $t_n = \sum_{m=1}^{n} \Delta t_m$, where Δt_m is the time step for each integration step. Half indices are used to denote the spatial midpoint between nodes across which the fluxes are calculated: $i \pm 1/2$ corresponds to the midpoint between nodes i and $i \pm 1$.

8.2.2 Spatial discretization

Following spatial discretization, Eq. (8.11) can be approximated as a system of ordinary differential equations in t:

$$\frac{d\mathbf{u}_i}{dt} = \mathbf{L}(\mathbf{u})|_{x=x_i}\,, \tag{8.13}$$

where the operator $\mathbf{L}$ is a discrete approximation to the continuous convection and source operators of Eq. (8.11):

$$\mathbf{L}(\mathbf{u})|_{x=x_i} \approx \left(-\frac{\partial}{\partial x}\mathbf{f}\left(\mathbf{u}\right) + \mathbf{s}\left(\mathbf{u}\right)\right)\Bigg|_{x=x_i}. \tag{8.14}$$

It is understood that the evaluation of the discrete spatial operator $\mathbf{L}(\mathbf{u})$ at x_i will involve values of $\mathbf{u}$ other than just $\mathbf{u}_i$.

In this section, the definition of $\mathbf{L}$ for various nodes is given as shown in Fig. 8.1. First, however, the essentially non-oscillatory high order numerical flux interpolator employed in this scheme is described.

8.2.2.1 WENO5M

A weighted essentially non-oscillatory scheme is used to approximate spatial derivatives. Besides its essentially non-oscillatory character over both smooth and discontinuous solutions, such schemes are conservative and guarantee that captured shocks will propagate at the correct speeds. This is important for studying unstable detonations since secondary shocks can form in the flow behind the lead shock and cause simpler finite differencing schemes to become unstable. One should note that, in spite of the fact that such secondary shocks are not fitted, the scheme presented here retains its high order accuracy at least throughout the

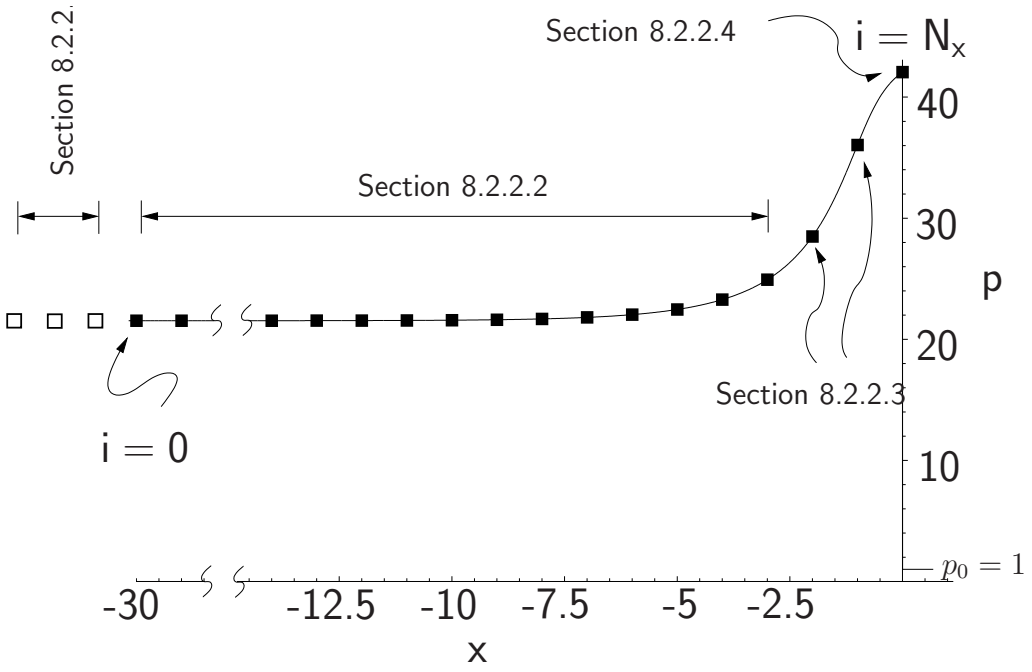

Figure 8.1. Artificially coarse numerical grid highlighting boundary points. The section detailing the spatial discretization used at each node is also given. The pressure profile shown is that of the ZND solution used as an initial condition for the case $E = 25$, $q = 50$, and $\gamma = 1.2$

domain of dependence of the fitted shock: from $x = 0$ to the limiting characteristic [1, 71].

In particular, the fifth order WENO5M scheme developed in Ref. [35] is used. In order to encapsulate the complexity of the method, the WENO5M scheme is presented simply as a special interpolator:

$$\hat{f}_{j+1/2} = \begin{cases} \mathcal{F}(f_{j-2}, f_{j-1}, \ldots, f_{j+2}) & \text{for } \rightarrow \text{ waves,} \quad (8.15a) \\ \mathcal{F}(f_{j+3}, f_{j+2}, \ldots, f_{j-1}) & \text{for } \leftarrow \text{ waves.} \quad (8.15b) \end{cases}$$

Both Eqs. (8.15) give an approximation of the numerical flux function [35, 43] at $j+1/2$ such that a high order conservative discretization of spatial derivatives can be formed. The difference between Eqs. (8.15) lies in the selection and ordering of the functional arguments. Equation (8.15a) propagates information to the right, while Eq. (8.15b) propagates information to the left. This distinction will become important in the creation of a stable numerical scheme for systems involving the propagation of waves simultaneously in both directions.

Thus, given the values of a function f at the specified nodes, the WENO5M interpolant $\hat{f}_{j+1/2}$ can be computed. The functional form of $\mathcal{F}$ is given by

$$\mathcal{F}(f_{j-2}, f_{j-1}, \ldots, f_{j+2}) = \sum_{k=0}^{2} \omega_k q_k, \quad (8.16)$$

where the ω_k's are the WENO5M weights and the component stencils q_k are

$$q_0 = \frac{1}{6}(2f_{j-2} - 7f_{j-1} + 11f_j), \quad (8.17a)$$

$$q_1 = \frac{1}{6}(-f_{j-1} + 5f_j + 2f_{j+1}), \quad (8.17b)$$

$$q_2 = \frac{1}{6}(2f_j + 5f_{j+1} - f_{j+2}). \quad (8.17c)$$

Next, the formulation of the ω_k's is given in two steps.

As a first approximation of the final weights, those developed in Ref. [43] are calculated. These are given by

$$\omega_k^* = \frac{\alpha_k}{\sum_{i=0}^{2} \alpha_i}, \qquad \text{where} \qquad \alpha_k = \frac{\bar{\omega}_k}{(\epsilon + \beta_k)^p}. \tag{8.18}$$

The ideal weights, $\bar{\omega}_k$, are constants given by

$$\bar{\omega}_0 = 1/10, \qquad \bar{\omega}_1 = 6/10, \qquad \bar{\omega}_2 = 3/10, \tag{8.19}$$

and the indicators of smoothness, β_k, are defined as

$$\beta_0 = \frac{13}{12}(f_{j-2} - 2f_{j-1} + f_j)^2 + \frac{1}{4}(f_{j-2} - 4f_{j-1} + 3f_j)^2, \tag{8.20a}$$

$$\beta_1 = \frac{13}{12}(f_{j-1} - 2f_j + f_{j+1})^2 + \frac{1}{4}(f_{j+1} - f_{j-1})^2, \tag{8.20b}$$

$$\beta_2 = \frac{13}{12}(f_j - 2f_{j+1} + f_{j+2})^2 + \frac{1}{4}(3f_j - 4f_{j+1} + f_{j+2})^2. \tag{8.20c}$$

Here, ϵ is the small parameter which keeps the weights bounded. In all computations presented here, $\epsilon = 10^{-40}$, as suggested in Ref. [35].

Next, the ω_k^*'s are mapped to the corrected ω_k's, such that the accuracy of the method is fifth order in general. This is done through the mappings

$$g_k(\omega) = \frac{\omega(\bar{\omega}_k + \bar{\omega}_k^2 - 3\bar{\omega}_k\omega + \omega^2)}{\bar{\omega}_k^2 + (1 - 2\bar{\omega}_k)\omega}. \tag{8.21}$$

The final corrected weights are given by

$$\omega_k = \frac{g_k(\omega_k^*)}{\sum_{i=0}^{2} g_i(\omega_i^*)}. \tag{8.22}$$

8.2.2.2 Nodes $0 \leq i \leq N_x - 3$

Next, general nodes in the interior of the domain are considered. For $\mathbf{L}(\mathbf{u})|_{x=x_i}$ the WENO5M scheme [35] with a local Lax-Friedrichs solver is used. This scheme is a conservative flux difference method, which has been shown to be stable, and yields the proper viscosity-vanishing solution to Eqs. (8.1). The derivation of the difference operator $\mathbf{L}(\mathbf{u})|_{x=x_i}$ in Eq. (8.14) is done in two parts. First the flux is split into two parts representing right and left moving waves. Then each of these fluxes is numerically approximated using the WENO5M discretization. The final form of the operator is then given in a simplified form.

First, a local Lax-Friedrichs flux splitting of the spatial derivative in Eq. (8.14) gives

$$\left.\frac{\partial \mathbf{f}}{\partial x}\right|_{x=x_i} = \frac{1}{2}\left.\left(\frac{\partial \mathbf{f}^+}{\partial x} + \frac{\partial \mathbf{f}^-}{\partial x}\right)\right|_{x=x_i}, \tag{8.23}$$

where

$$\mathbf{f}_i^{\pm} = \mathbf{f}_i \pm \alpha \mathbf{u}_i, \tag{8.24}$$

and α is the largest local wave speed in an absolute value sense. This splitting yields $\mathbf{f}_i^+$ and $\mathbf{f}_i^-$ which correspond to the flux vectors for right and left moving waves, respectively.

Next the flux derivatives in Eq. (8.23) are approximated at each node i by

$$\left.\frac{\partial \mathbf{f}^{\pm}}{\partial x}\right|_{x=x_i} = \frac{\hat{\mathbf{f}}^{\pm}_{i+1/2} - \hat{\mathbf{f}}^{\pm}_{i-1/2}}{\Delta x} + O(\Delta x^5), \tag{8.25}$$

where $\hat{\mathbf{f}}^{\pm}_{i\pm1/2}$ is the WENO5M interpolant of $f^{\pm}$ at $i \pm 1/2$. For the $i + 1/2$ case,

application of Eqs. (8.15) gives

$$\begin{aligned} \hat{f}^+_{i+1/2} &= \mathcal{F}(f^+_{i-2}, f^+_{i-1}, f^+_i, f^+_{i+1}, f^+_{i+2}), \\ \hat{f}^-_{i+1/2} &= \mathcal{F}(f^-_{i+3}, f^-_{i+2}, f^-_{i+1}, f^-_i, f^-_{i-1}), \end{aligned} \tag{8.26}$$

where either Eq. (8.15a) or Eq. (8.15b) have been chosen to match the direction of information propagation for the f^+ and f^- waves, respectively. Since Eq. (8.26) gives the numerical flux approximations midway between each node i and $i+1$ in this domain, it is only necessary to consider the interpolant for the $i+1/2$ case; the $i-1/2$ case is given simply by shifting i by -1.

Substitution of Eq. (8.25) into Eq. (8.23) gives

$$\begin{aligned} \left.\frac{\partial \mathbf{f}}{\partial x}\right|_{x=x_i} &= \frac{1}{2}\left(\frac{\hat{\mathbf{f}}^+_{i+1/2} - \hat{\mathbf{f}}^+_{i-1/2}}{\Delta x} + \frac{\hat{\mathbf{f}}^-_{i+1/2} - \hat{\mathbf{f}}^-_{i-1/2}}{\Delta x}\right) + O(\Delta x^5) \\ &= \frac{1}{\Delta x}\left(\frac{\hat{\mathbf{f}}^+_{i+1/2} + \hat{\mathbf{f}}^-_{i+1/2}}{2} - \frac{\hat{\mathbf{f}}^+_{i-1/2} + \hat{\mathbf{f}}^-_{i-1/2}}{2}\right) + O(\Delta x^5) \\ &= \frac{\hat{\mathbf{f}}_{i+1/2} - \hat{\mathbf{f}}_{i-1/2}}{\Delta x} + O(\Delta x^5), \end{aligned} \tag{8.27}$$

where

$$\hat{\mathbf{f}}_{i+1/2} = \frac{1}{2}\left(\hat{\mathbf{f}}^+_{i+1/2} + \hat{\mathbf{f}}^-_{i+1/2}\right) \tag{8.28}$$

defines a single value for the approximate numerical flux in between nodes i and $i+1$.

The flux between nodes i and $i+1$ is calculated using values of f^+ and f^- as

given in Eq. (8.24) where α can now be defined locally as

$$\alpha = \max\left(\left|\left|\frac{\partial \mathbf{f}}{\partial \mathbf{u}}\right|\right|_{x=x_i}, \left|\left|\frac{\partial \mathbf{f}}{\partial \mathbf{u}}\right|\right|_{x=x_{i+1}}\right), \tag{8.29}$$

where the norm of the Jacobian matrix, $\partial \mathbf{f}/\partial \mathbf{u}$, is the largest eigenvalue in an absolute value sense.

Substitution of Eq. (8.27) into Eq. (8.14) gives the definition of $\mathbf{L}$ in the interior of the domain:

$$\mathbf{L}(\mathbf{u})|_{x=x_i} = -\frac{\hat{\mathbf{f}}_{i+1/2} - \hat{\mathbf{f}}_{i-1/2}}{\Delta x} + \mathbf{s}\left(\mathbf{u}_i\right), \tag{8.30}$$

where $\mathbf{s}\left(\mathbf{u}_i\right)$ is a simple evaluation of the source terms at node x_i.

Because the WENO5M discretization at node i requires information at the nodes $i-3, ..., i+3$, fluxes at the three nodes in the neighborhood of the shock are calculated separately. For these nodes, either a discretization is used which does not require information differencing across the fitted shock or the shock jump conditions Eqs. (8.2) are used directly.

8.2.2.3 Nodes $N_x - 2 \leq i \leq N_x - 1$

At these nodes, the flux derivatives are approximated by explicit formula biased in such a manner that no nodes $i > N_x$ are used. These are derived from standard Taylor series expansions (TSE). These approximations are given by

$$\frac{\partial}{\partial x}\left(f\left(\mathbf{u}_{N_x-2}\right)\right) \approx \frac{1}{60\Delta x}\left(-2f\left(\mathbf{u}_{N_x-5}\right) + 15f\left(\mathbf{u}_{N_x-4}\right) - \right.$$
$$\left. 60f\left(\mathbf{u}_{N_x-3}\right) + 20f\left(\mathbf{u}_{N_x-2}\right) + 30f\left(\mathbf{u}_{N_x-1}\right) - 3f\left(\mathbf{u}_{N_x}\right)\right), \tag{8.31}$$

and

$$\frac{\partial}{\partial x}\left(f\left(\mathbf{u}_{N_x-1}\right)\right) \approx \frac{1}{12\Delta x}\left(-f\left(\mathbf{u}_{N_x-4}\right)+6f\left(\mathbf{u}_{N_x-3}\right)-\right.$$
$$\left.18f\left(\mathbf{u}_{N_x-2}\right)+10f\left(\mathbf{u}_{N_x-1}\right)+3f\left(\mathbf{u}_{N_x}\right)\right). \quad (8.32)$$

According to TSE, Equation (8.31) is fifth order accurate, while Eq. (8.32) is fourth order accurate. Use of this fourth order stencil at node $N_x - 1$ appears necessary to ensure linear numerical stability; however, no noticeable loss in the global fifth order convergence rate of the scheme is incurred (see Sections 8.3.1 and 8.3.5). Since the line $\xi(x_{N_x-1}, t)$ is not along a characteristic, the fourth order spatial errors suffered at this line do not accumulate along any one characteristic solution. The source term, $\mathbf{s}\left(\mathbf{u}_i\right)$, is still just an evaluation at these two nodes.

8.2.2.4 Node $i = N_x$

At the shock locus, $i = N_x$, the solution is only a function of the shock velocity, D. At this point, only Eq. (8.10) is solved. Only the momentum flux gradient needs to be computed to update the shock velocity. Here, a biased fifth order stencil,

$$\frac{\partial}{\partial x}\left(f\left(\mathbf{u}_{N_x}\right)\right) \approx \frac{1}{60\Delta x}\left(-12f\left(\mathbf{u}_{N_x-5}\right)+75f\left(\mathbf{u}_{N_x-4}\right)-200f\left(\mathbf{u}_{N_x-3}\right)+\right.$$
$$\left.300f\left(\mathbf{u}_{N_x-2}\right)-300f\left(\mathbf{u}_{N_x-1}\right)+137f\left(\mathbf{u}_{N_x}\right)\right), \quad (8.33)$$

is used to calculate the momentum flux gradient.

The conservative state variables at the shock are given from the shock jump

relations, Eqs. (8.2). No source terms enter at this nodal point, since this is exactly a shock state. Also, the numerical method is discretely conservative everywhere, except at $i = N_x$, since the state there is constrained to be at a shock state, and so itself cannot be discretely conservative. Errors in conservation are of the order of the truncation error of the scheme, and so are small.

8.2.2.5 Nodes $i < 0$

At nodes for which $i < 0$, which are necessary for calculation of some fluxes, a zero gradient condition is enforced. Formally, this introduces spurious waves at the boundary. However, as a check, the forward characteristic emanating from this boundary was calculated, and it was guaranteed that the domain was sufficiently large so as to prevent corruption of the shock and reaction zone structure from this downstream acoustic noise.

8.2.3 Temporal discretization

With the discrete operator $\mathbf{L}$ now defined, Eqs. (8.13) could be solved by a wide variety of standard numerical techniques, explicit or implicit, which have been developed over the years for large systems of ordinary differential equations. Here, an explicit six-stage Runge-Kutta scheme [51] with fifth order temporal accuracy is chosen.

Most Runge-Kutta schemes of fourth or higher order are easier to code and seem to require less storage when the Butcher formulation [51, 72] is chosen rather than the more commonplace $\alpha-\beta$ form [40]. Given a solution $\mathbf{u}_i^n$ at t_n, the solution $\mathbf{u}_i^{n+1}$ at t_{n+1} is constructed in the following manner. The generic s-stage Butcher

formulation of Runge-Kutta schemes takes on the form

$$\begin{aligned} \bar{\mathbf{u}}_i^1 &= \mathbf{u}_i^n, \\ \bar{\mathbf{u}}_i^j &= \mathbf{u}_i^n + \Delta t_n \sum_{k=1}^{j-1} a_{jk}\, \mathbf{L}(\bar{\mathbf{u}}^k)\big|_{x=x_i}, \end{aligned} \tag{8.34}$$

where $\bar{\mathbf{u}}_i^j$ are the intermediate solution states at each j-stage, and the solution at the next time step is given by

$$\mathbf{u}_i^{n+1} = \mathbf{u}_i^n + \Delta t_n \sum_{j=1}^{s} b_j\, \mathbf{L}(\bar{\mathbf{u}}^j)\big|_{x=x_i}. \tag{8.35}$$

The coefficients, a_{jk} and b_j in Eqs. (8.34) and (8.35) are given in Tables 6.1, respectively.

In this problem, for which the effect of the source term has been resolved, it is convection which dictates the time step restriction. All computations performed here have $0.8 < CFL < 1.5$, where CFL represents the traditional Courant-Friedrichs-Lewy number. The high order of the Runge-Kutta method enables CFL to be slightly greater than unity while maintaining numerical stability. The results were verified to be insensitive to small changes in CFL.

8.3 Results

Results are given for a set of standard test cases. All calculations were performed using double precision and 64-bit arithmetic. The typical computation time for any single case was ten minutes. A few calculations which required long integration times took as long as two weeks to complete. The equations have been scaled in such a fashion that the ambient density and pressure are $\rho_o = 1$ and

$p_o = 1$, the half-reaction zone length, $L_{1/2}$, is unity, and other parameters take the values $q = 50$, and $\gamma = 1.2$. Here $L_{1/2}$ is the distance from the shock to the point at which λ takes on the value $1/2$ for the steady ZND structure. This now standard approach requires one to vary k from case to case in order to maintain $L_{1/2} = 1$; for $E = 25$, one has $k = 35.955584760859722$, where the high precision is needed to guarantee the high precision of the results.

Here, interest is focused on self-sustained detonation waves, known commonly as Chapman-Jouguet (CJ) [19]. This results in a steady detonation velocity of

$$D_{CJ} = \sqrt{11} + \sqrt{\frac{61}{5}} \approx 6.80947463. \tag{8.36}$$

Interest is further focused on how increase in the activation energy, E, affects the propagation of the detonation wave. Linear stability analysis [55] reveals that for $E < 25.26$, the steady ZND detonation wave structure [19] will be linearly stable, and for $E > 25.26$, the steady detonation structure is linearly unstable. In all cases considered, the exact, to machine precision, ZND solution is used as the initial condition. Note that using 64-bit machine precision translates to roughly 16 significant figures. A second comparison case is presented in the following subsection for $E = 26$.

In all unstable cases considered, the predicted non-linear behavior has its origin in a single unstable low frequency mode identified by linear theory. While evermore high frequency modes are predicted by the linear theory as E increases through a series of threshold values, here, E is increased only moderately. As a consequence, the high frequency instabilities are not activated, while still admitting a rich spectrum of low frequency non-linear behavior.

TABLE 8.1

NUMERICAL ACCURACY OF ALGORITHM PRESENTED BY KASIMOV [1].

$N_{1/2}$	ΔD	r_c
100	1.90×10^{-2}	-
200	9.40×10^{-3}	1.01

8.3.1 Linearly stable ZND, $E = 25$

The new algorithm is first tested on a stable problem, $E = 25$, and results are compared with those of a recent shock-fitting study [1]. For this case, the steady solution is stable, and thus it is the exact solution for all time. This can also serve as a test problem for verification of the numerical scheme. As done in Ref. [1] the numerically calculated detonation velocity can be plotted as a function of time. In particular, it is important to measure the error produced as a function of numerical resolution. Following Ref. [1], one defines the number of numerical zones in the half reaction zone length to be $N_{1/2}$, so that $\Delta x = 1/N_{1/2}$. Figure 8.2 shows the result of Kasimov and Stewart's numerical method for $N_{1/2} = 100$ and $N_{1/2} = 200$. At relatively long times, this numerical method attains $D_{N_{1/2}=100} \approx 6.8285$ and $D_{N_{1/2}=200} \approx 6.8189$. Considering the numerical errors, ΔD, are then 0.0190 and 0.0094, respectively, it is concluded that the error of the scheme of Ref. [1] scales directly with Δx, and is thus first order accurate. These results are summarized in Table 8.1, where r_c is the rate of convergence. The lack of high order convergence

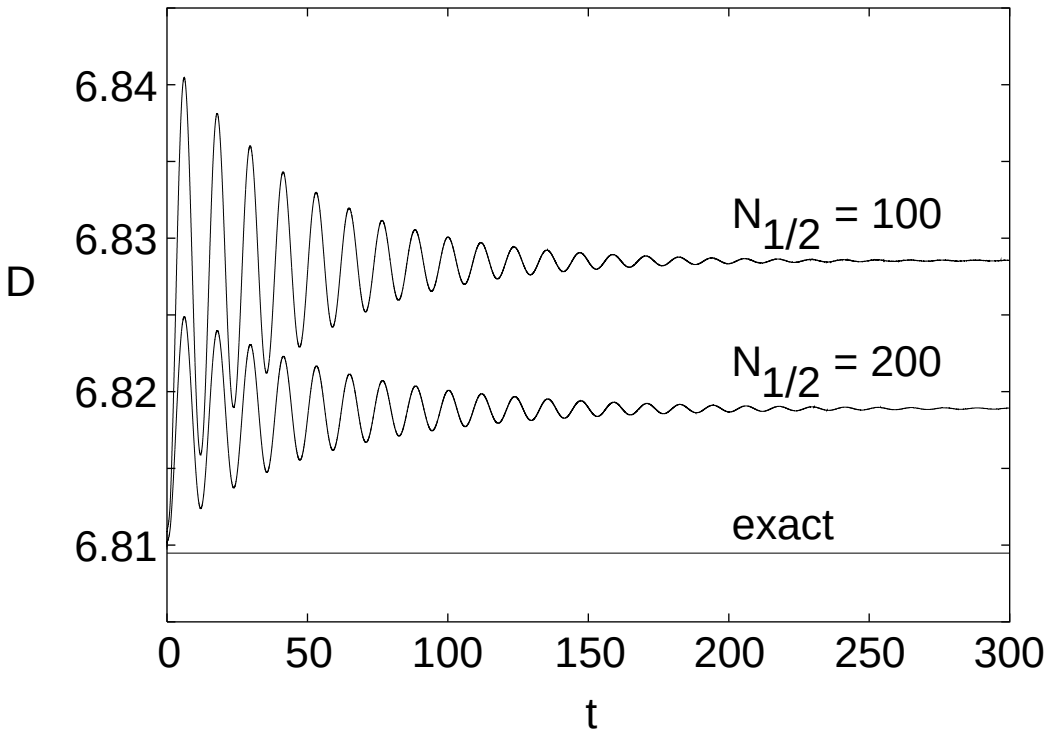

Figure 8.2. Numerically generated detonation velocity, D versus t, using the shock-fitting scheme of Kasimov and Stewart, $E = 25$, $q = 50$, $\gamma = 1.2$, with $N_{1/2} = 100$ and $N_{1/2} = 200$ [1].

is due to the first order finite differencing of the shock-change equations.

The prediction of the high order shock-fitting algorithm of the previous section, utilizing a coarser grid, $N_{1/2} = 20$, is displayed in Fig. 8.3. A few important facts should be noted. First, the error in shock speed has been greatly reduced by the high order shock-fitting scheme, even utilizing a much coarser grid. This is evident because of greatly reduced scale on the detonation velocity in Fig. 8.3. Also, not only are the errors greatly reduced, but the rate of convergence is shown to be fifth order as seen in Table 8.2. Thus, for this stable problem, the new high order shock-fitting scheme produces very accurate solutions with moderate mesh size.

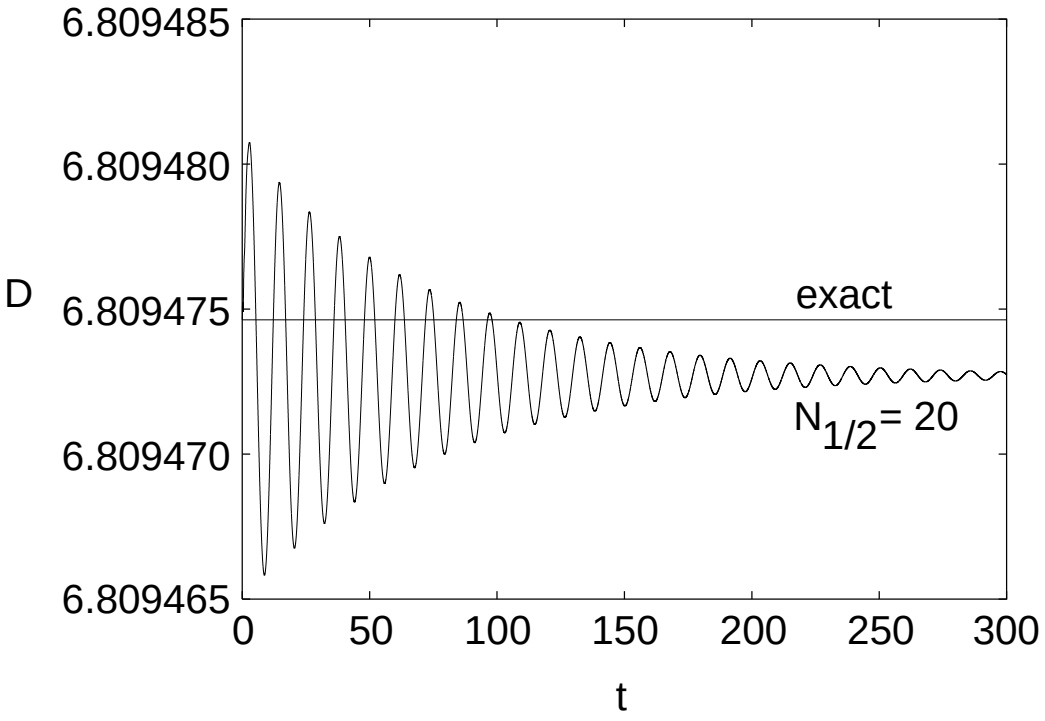

Figure 8.3. Numerically generated detonation velocity, D versus t, using the high order shock-fitting scheme, $E = 25$, $q = 50$, $\gamma = 1.2$, with $N_{1/2} = 20$.

TABLE 8.2

NUMERICAL ACCURACY OF HIGH ORDER SHOCK-FITTING SCHEME.

$N_{1/2}$	ΔD	r_c
20	2.13×10^{-6}	-
40	6.00×10^{-8}	5.01

8.3.2 Linearly unstable ZND, stable limit cycle, $E = 26$

Next, an unstable problem, $E = 26$, is analyzed, as also done in Ref. [1]. For $E = 26$, linear stability theory [60] predicts a single unstable mode, with growth rate, $\sigma_r = 0.03710$, and a frequency, $\sigma_i = 0.52215$. Figure 8.4 gives a plot of the numerical prediction of detonation velocity, D, as a function of time, with $N_{1/2} = 20$. The growth of the unstable mode is triggered by the small numerical truncation error. Figure 8.4 shows a clearly oscillatory exponential growth of $D(t)$ at early times ($t < 300$). Postulating that the numerical predictions could be fit by an equation of the form

$$D(t) \sim a_0 + a_1 e^{a_2 t} \sin\left(a_3 t + a_4\right), \tag{8.37}$$

a least squares curve fit of the data over the range $0 < t < 100$ revealed that

$$a_0 = 6.80947239809145 \pm 7.506 \times 10^{-10}, \tag{8.38a}$$

$$a_1 = 0.00000643598884 \pm 4.549 \times 10^{-10}, \tag{8.38b}$$

$$a_2 = 0.03709980167992 \pm 7.983 \times 10^{-7}, \tag{8.38c}$$

$$a_3 = 0.52214295442142 \pm 8.615 \times 10^{-7}, \tag{8.38d}$$

$$a_4 = 0.18145671900944 \pm 7.455 \times 10^{-5}. \tag{8.38e}$$

Note that the growth rate a_2 and wavenumber a_3 both agree strikingly to four significant figures with the predictions of linear stability theory.

Note from Fig. 8.4 that the long time behavior appears to be that of a stable periodic limit cycle. One can thus infer that the non-linear effects are stabilizing the linear instability, and that the amplitude of the long time limit cycle is dictated

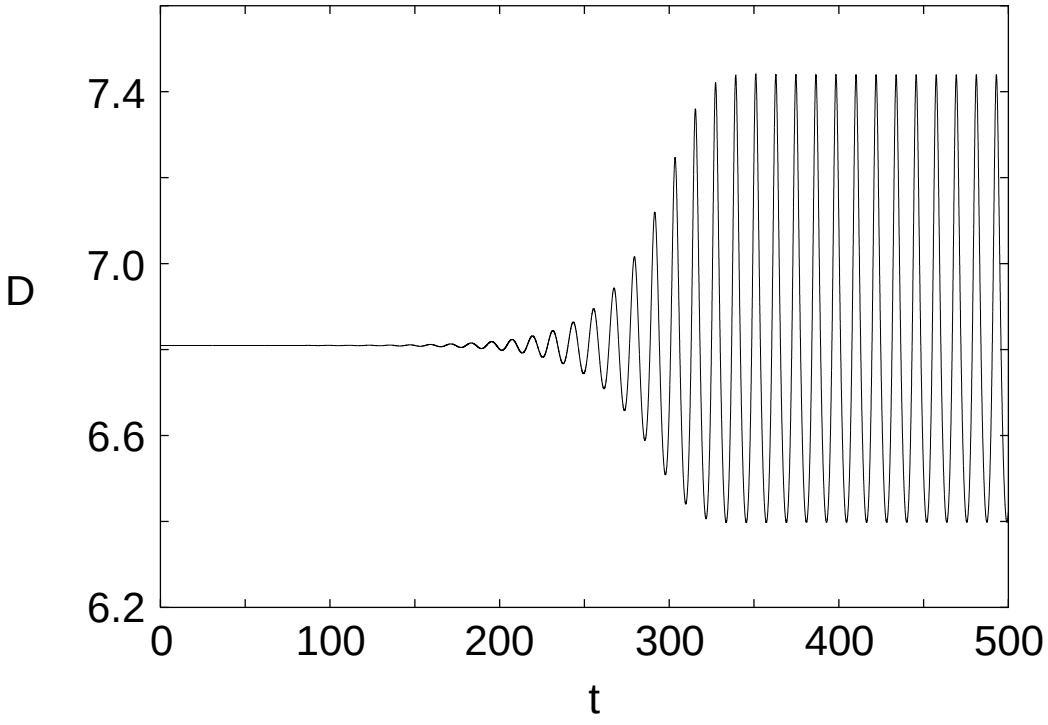

Figure 8.4. Numerically generated detonation velocity, D versus t, using the high order shock-fitting scheme, $E = 26$, $q = 50$, $\gamma = 1.2$, with $N_{1/2} = 20$. Period-1 oscillations shown.

by a balance struck between linear growth and non-linear decay. It is useful to plot the results in the phase plane, dD/dt versus D [58]. This is easily and accurately accomplished, since the shock acceleration, dD/dt, is already computed from the shock-change equation (8.10). Figure 8.5 is the parametric plot of dD/dt versus D, where both the acceleration and velocity are known parametrically as functions of t. The solution starts at $dD/dt(t = 0) = 0$, and $D(t = 0) = D_{CJ}$. A spiral trajectory commences at this point and has a radius of curvature which increases with arc length which is indicative of the linear instability. At late times, $t > 350$, the solution has effectively relaxed to a steady cyclic behavior. It is also noted that through several numerical simulations, the linear stability boundary was determined to be located at $E = 25.265 \pm 0.005$, in excellent agreement with the prediction of linear stability theory.

8.3.3 Period-doubling and Feigenbaum's universal constant

As noted in Ref. [62], and later in Ref. [63], if the activation energy is increased to $E \approx 27.2$, one predicts a period-doubling phenomena, reminiscent of that predicted by the simple logistic map [73, 74]. Figure 8.6 shows the time history of the detonation velocity for the case $E = 27.35$. It is evident that in the long time limit, the solution possesses two distinct relative maxima, namely $D \approx 8.225$ and $D \approx 7.676$; whereas for $E = 26$, only a single relative maximum, $D \approx 7.439$ is predicted. The corresponding phase plane is shown in Fig. 8.7. Performing several simulations, with $N_{1/2} = 20$, to long times (up to $t = 30000$), one can bisect the region $26 < E < 27.35$, in an attempt to find the bifurcation point, *i.e.* the point where the single periodic cycle gives way to the period-2 solution. The activation energy at this point will be denoted by E_1. Likewise, as noted in Ref. [63], there

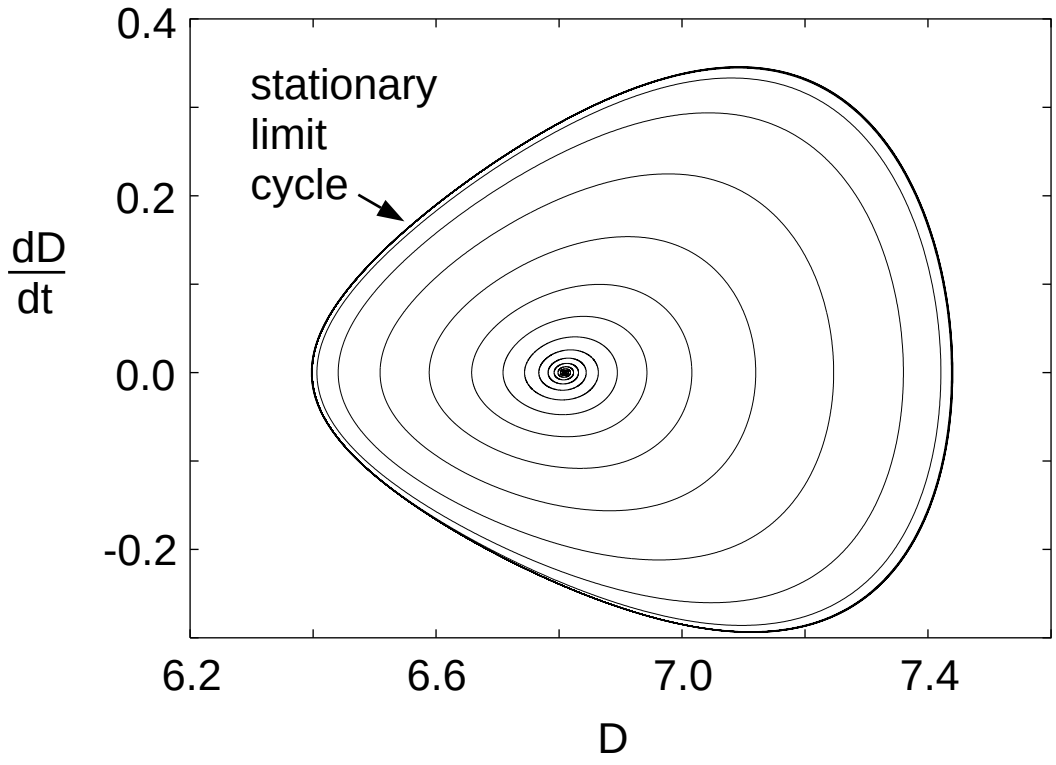

Figure 8.5. Numerically generated phase portrait dD/dt versus D, using the high order shock-fitting scheme, $E = 26$, $q = 50$, $\gamma = 1.2$, with $N_{1/2} = 20$. Period-1 oscillations shown.

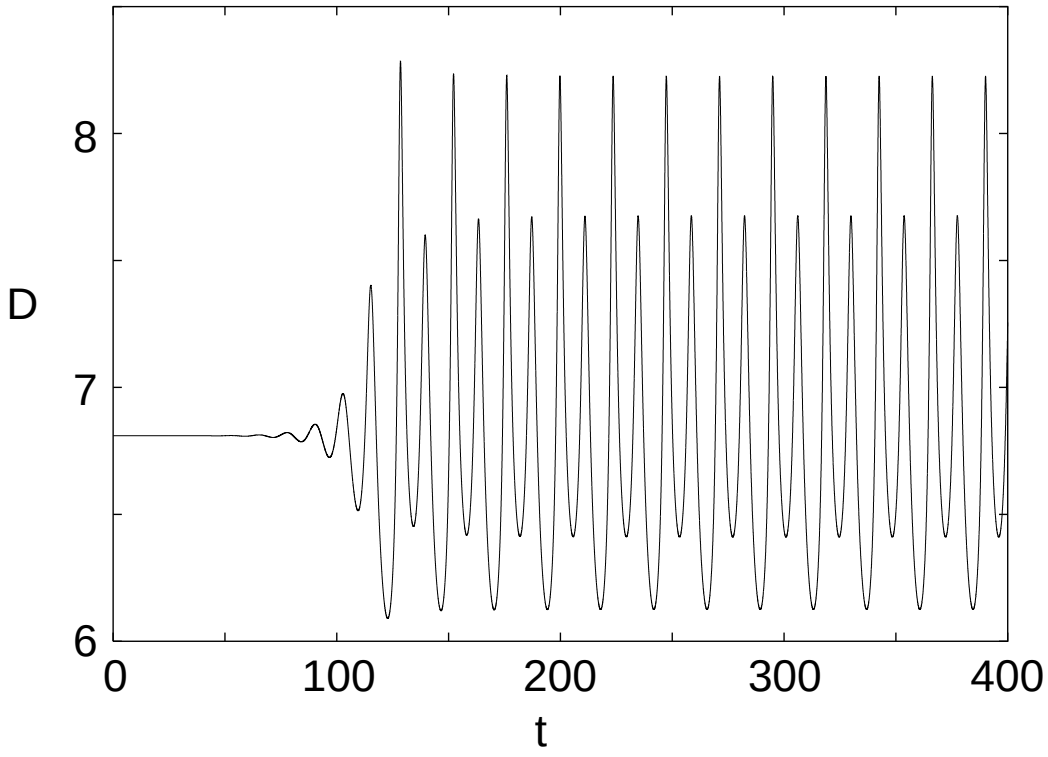

Figure 8.6. Numerically generated detonation velocity, D versus t, using the high order shock-fitting scheme, $E = 27.35$, $q = 50$, $\gamma = 1.2$, with $N_{1/2} = 20$. Period-2 oscillations shown.

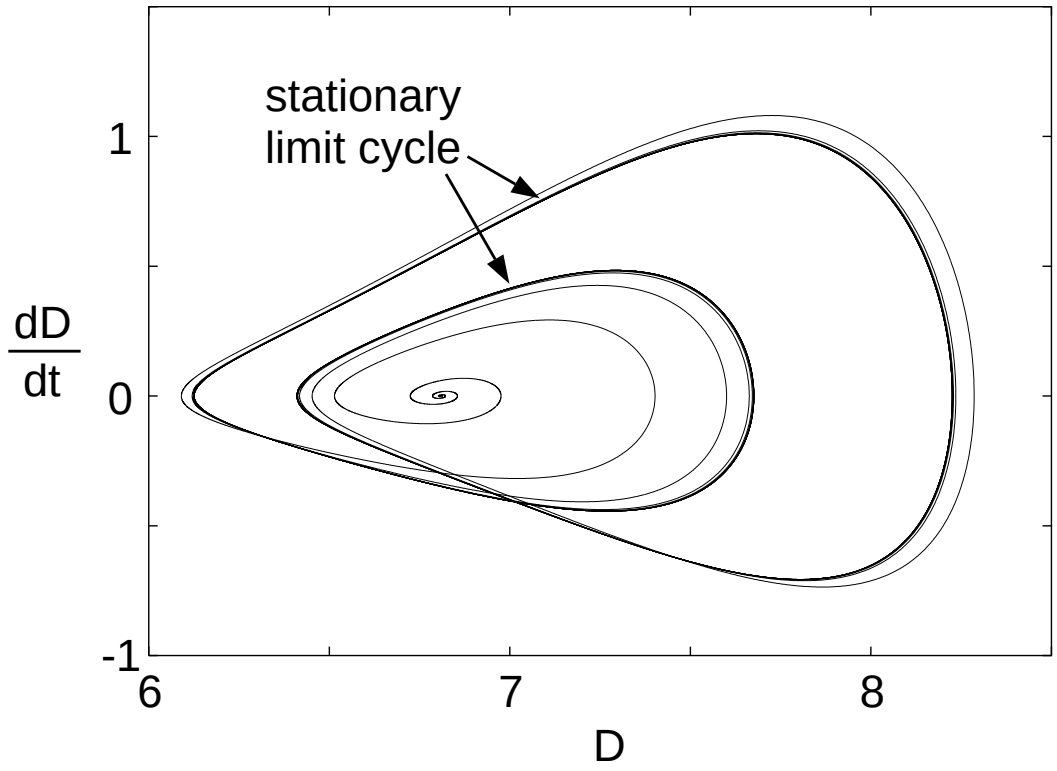

Figure 8.7. Numerically generated phase portrait dD/dt versus D using the high order shock-fitting scheme, $E = 27.35$, $q = 50$, $\gamma = 1.2$, with $N_{1/2} = 20$. Period-2 oscillations shown.

are other period-doubling bifurcation values of E_n, where the solution transits from a period-2^{n-1} to a period-2^n. The point at which one predicts the transition from a steady solution (linear stability) to a periodic solution (period-1 solution) will be designated by E_0. These bifurcation points and the associated numerical uncertainties are given in Table 8.3. Also calculated are the differences between these points, $E_{n+1} - E_n$, and the relative change in the differences, δ_n:

$$\delta_n = \frac{E_n - E_{n-1}}{E_{n+1} - E_n}. \tag{8.39}$$

It was predicted by Feigenbaum [68, 69], using models of several different physical and mathematical phenomena, that in the limit as $n \to \infty$, that δ_n approaches a universal constant, $\delta_\infty \approx 4.669201$, now commonly known as Feigenbaum's number. Table 8.3 shows three progressively better approximations, δ_1, δ_2, and δ_3, to δ_∞. It is seen that δ_3 is in agreement with δ_∞, with an uncertainty of 2%.

8.3.4 Bifurcation diagram, semi-periodic solutions, odd periods, windows and chaos

Given that the solutions obtained, even for $N_{1/2} = 20$, are so accurate and efficient to calculate, a detailed bifurcation diagram can be constructed with much greater detail than any to date. It is noted that Ref. [63] did show the first bifurcation diagram for this model, albeit with only twenty-five different activation energies. Here, the bifurcation diagram is constructed by sampling over a thousand different activation energies, with $25 < E < 28.8$ with $\Delta E = 0.0025$. At each value of E, the exact ZND solution is used as the initial condition. For each

TABLE 8.3

NUMERICALLY DETERMINED BIFURCATION POINTS AND APPROXIMATIONS TO FEIGENBAUM'S NUMBER.

n	E_n	$E_{n+1} - E_i$	δ_n
0	25.265 ± 0.005	-	-
1	27.1875 ± 0.0025	1.9225 ± 0.0075	3.86 ± 0.05
2	27.6850 ± 0.001	0.4975 ± 0.0325	4.26 ± 0.08
3	27.8017 ± 0.0002	0.1167 ± 0.0012	4.66 ± 0.09
4	27.82675 ± 0.00005	0.02505 ± 0.00025	-

E, the solution is integrated to $t = 7000$, and all the relative maxima in D are recorded for $5000 < t < 7000$ (*i.e.* the late time behavior). This composite plot of predicted, late time, relative maxima in D versus E is presented in Fig. 8.8. The qualitative similarities to the logistic map are striking. One clearly notices the various period-doubling bifurcations up to roughly $E_\infty \approx 27.8324$. One then notes various regions of semi-periodic behavior, and various odd-periodic regions. For example in the vicinity of $E = 28.2$, a large period-3 window opens in the bifurcation diagram; as E is increased further, the period-3 solution bifurcates. In regions where the bifurcation points are very dense, it is likely that the system has underwent a transition to chaos.

Figure 8.9 gives several plots of D versus t as activation energy is increased. Specific values of E are listed in the caption. In Fig. 8.9a), a period-4 solution is shown. As E is increased, the system continues a bifurcation process, and a

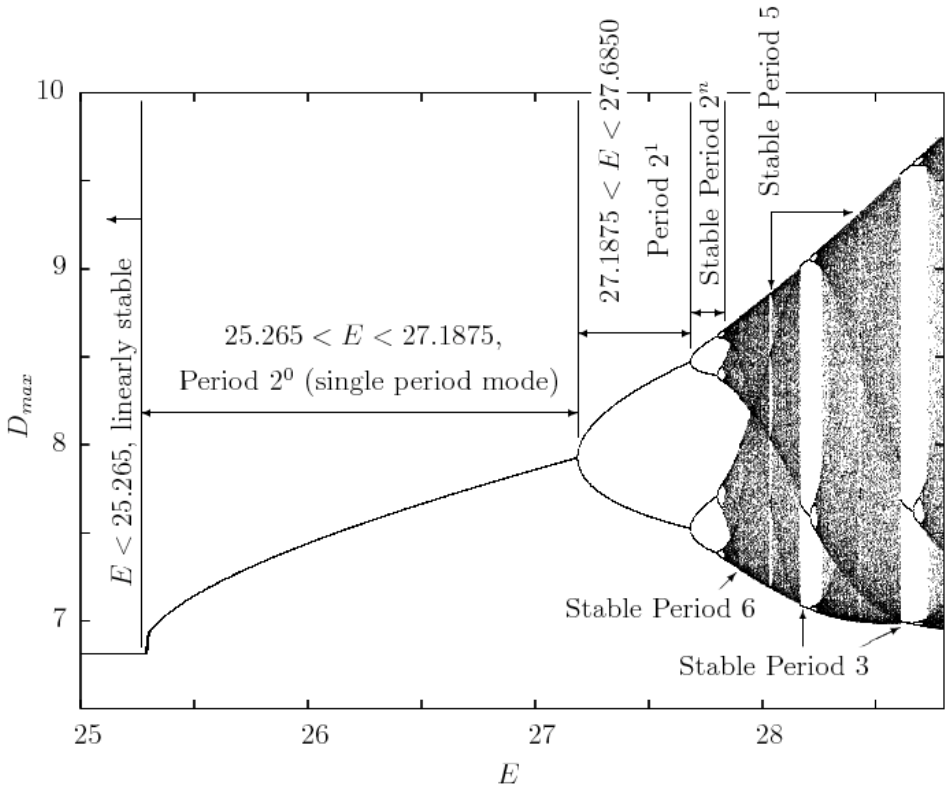

Figure 8.8. Numerically generated bifurcation diagram, $25 < E < 28.8$, $q = 50$, $\gamma = 1.2$.

chaotic state is realized in general. However, in b), c), and d) examples are found which are within windows of order in an otherwise chaotic region. Periods of 6, 5, and 3 are found, respectively. In e), a chaotic solution is shown. In f) another structured solution is found with period-3.

Note that as the system becomes more chaotic, the solution remains resolved. This is because the periods are increasing, not decreasing. However, for much higher activation energies, roughly $E > 30$, higher frequency instabilities are excited, and finer resolution would be necessary. Moreover, at such high activation energies, secondary captured shocks may overtake the fitted lead shock, which would negate the advantage of the present shock-fitting method.

8.3.5 Asymptotically stable limit cycles

Further studies of the limit cycle behavior for detonations with

$$E \in \{26, 26.5, 27, 27.5, 28.2, 28.65\} \tag{8.40}$$

were also performed. In particular, two limit cycle properties were examined: the period and the average detonation speed.

The period of the limit cycle is the smallest amount of time T such that

$$\mathbf{u}(t+T) = \mathbf{u}(t). \tag{8.41}$$

Thus a small window in the phase plane $(D, dD/dt)$ is selected such that the solution trajectory passes through it once per cycle as a single valued function. Within this window, a fixed value $D = D^*$ is selected. By finding the unique times at which the solution passes through D^* for consecutive cycles, the period can be

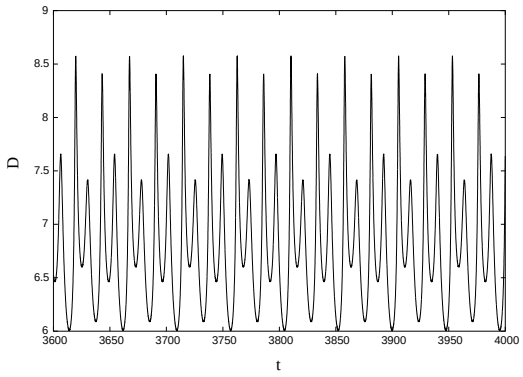

8.9.1: $E = 27.75$, period-4

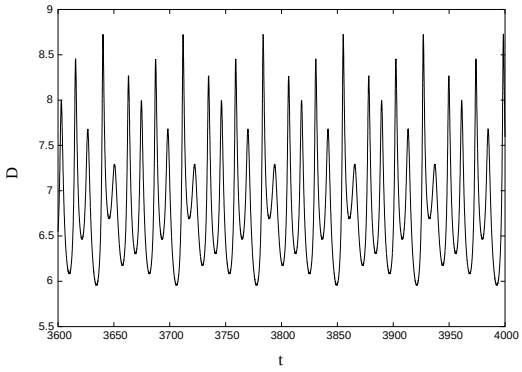

8.9.2: $E = 27.902$, period-6

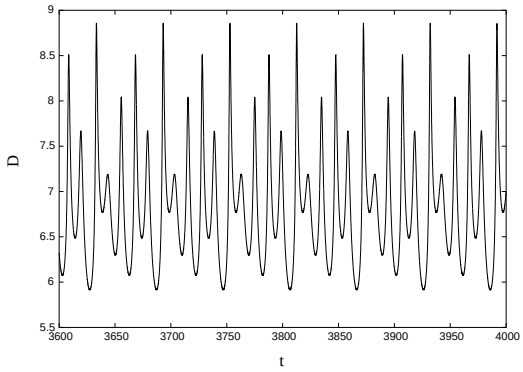

8.9.3: $E = 28.035$, period-5

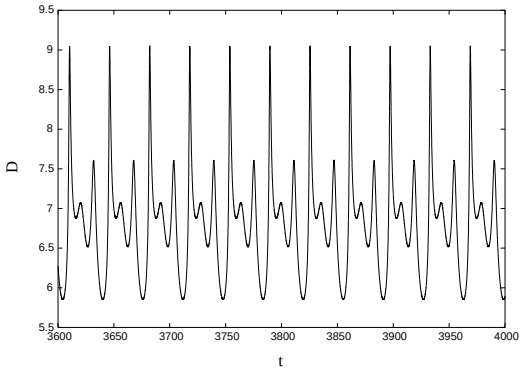

8.9.4: $E = 28.2$, period-3

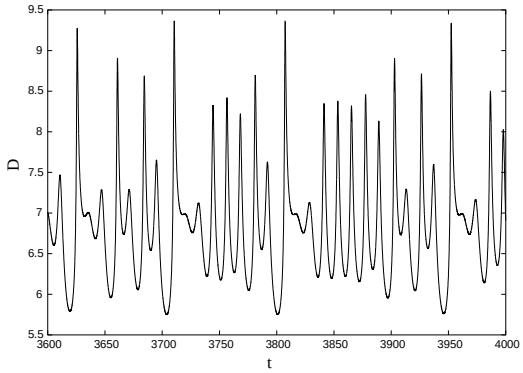

8.9.5: $E = 28.5$, chaotic

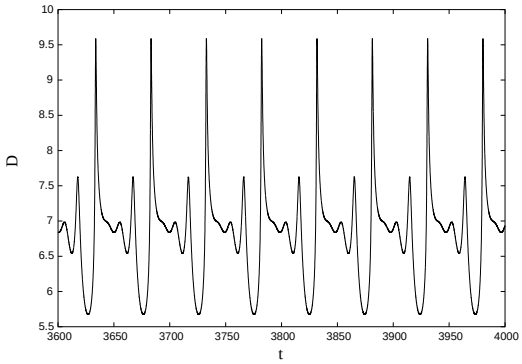

8.9.6: $E = 28.66$, period-3

Figure 8.9. Numerically generated detonation velocity, D versus t, using the high order shock-fitting scheme, $q = 50$, $\gamma = 1.2$, with $N_{1/2} = 20$.

approximated. Since numerical solutions give $t(D)$ discretely, the value of t at which $D = D^*$ is found by interpolation. For the n^{th} cycle, five data points (D, t) in the neighborhood of D^* are captured, and a Lagrange interpolating polynomial is passed through them. Evaluation of this polynomial at $D = D^*$ gives t_n, a fifth order approximation of the time at which the solution passed through D^* during the n^{th} cycle. Here D^* was chosen to be D_{CJ}, and thus the period is simply

$$T = t_{n+1}(D_{CJ}) - t_n(D_{CJ}). \tag{8.42}$$

Having found the period, the average velocity was then computed from

$$D_{avg} = \frac{\xi_0(t_{n+1}(D_{CJ})) - \xi_0(t_n(D_{CJ}))}{T}, \tag{8.43}$$

where $\xi_0(t) = \xi(x = 0, t)$ is the shock location in the lab frame found from Eq. (8.3).

The converged period and average velocity for each activation energy in Eq. (8.40) are given in Table 8.4 for $N_{1/2} = 80$. A new and particularly interesting result is that the average detonation speed increases as E increases and only equals D_{CJ} for the linearly stable case of $E < 25.26$. This is illustrated in Fig. 8.10.

Furthermore, for a single asymptotically stable value of E, both the period and its self convergence rate can be calculated over a number of resolutions. The case of $E = 28.2$ is shown in Table 8.5. The period convergence rate indicates that the method is also fifth order convergent in the linearly unstable case, as anticipated from the convergence result of Table 8.2.

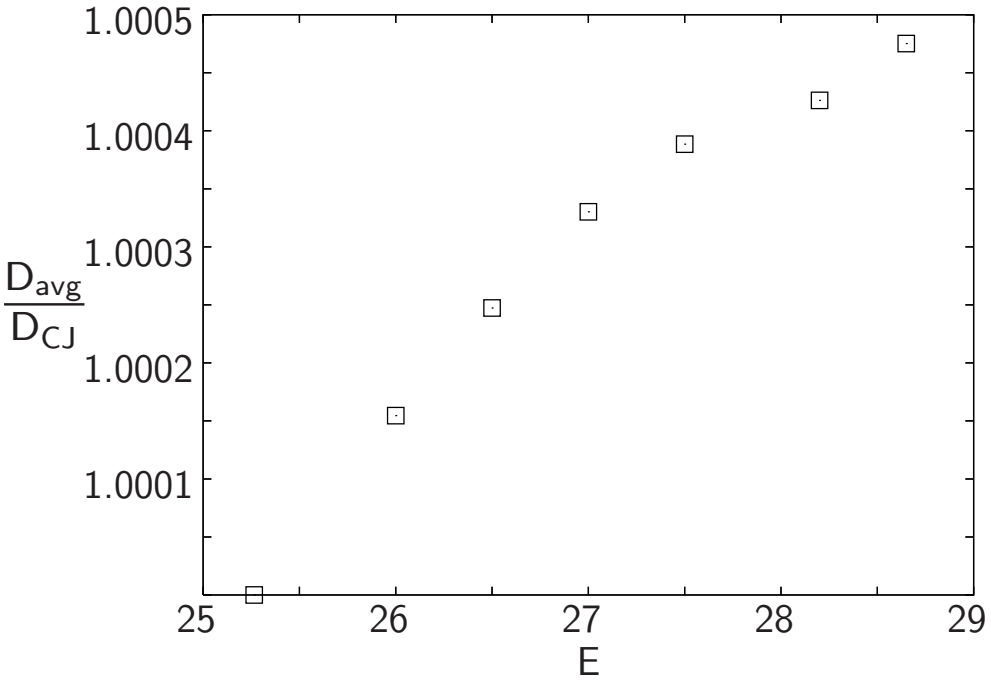

Figure 8.10. Normalized average detonation velocity as a function of activation energy for selected periodic cases. For all cases, $N_{1/2} = 80$.

TABLE 8.4

CONVERGED PERIOD AND AVERAGE DETONATION SPEED FOR $\Delta x = 0.0125$.

E	Period	D_{avg}
26	11.82102781	6.810527134
26.5	11.838380175	6.811158675
27	11.877201192	6.811723287
27.5	23.790471808	6.812119710
28.2	35.859529390	6.812377052
28.65	49.514811239	6.812710499

8.4 Conclusions

Investigation of the model one-dimensional unsteady detonation problem using shock-fitting coupled with a high order discretization scheme has clarified the behavior of linearly unstable detonations for a select range of activation energies. The resulting fifth order scheme allows for quantification of the chaotic and limit cycle behavior of the system. Bifurcation behavior and transition to chaos while varying the activation energy is demonstrated and found to be reminiscent of that governing the logistic map. In particular, the period and average detonation velocity for asymptotically stable solutions are studied, and the average detonation velocity for each case is seen to be slightly larger than the Chapman-Jouguet speed.

TABLE 8.5

CONVERGENCE RATES OF THE LIMIT CYCLE PERIOD FOR $E = 28.2$.

Δx	Period	r_c
1/20	35.86111963	–
1/40	35.859442127	4.2648
1/80	35.859529390	4.6210
1/160	35.859532936	4.9407
1/320	35.859533052	–

CHAPTER 9

CONDENSED PHASE DETONATION: ONE- AND TWO- DIMENSIONAL RESULTS

This chapter gives numerical results in one- and two- dimensional for the model problem introduced in Chapter 1 subject to the idealized condensed phase assumption. The idealized condensed phase model assumes a strong shock limit with $\gamma = 3$ and a zero activation energy. The convergence properties of the two dimensional code are first verified using the Sedov blast wave problem.

9.1 Code verification: Sedov blast explosion

In order to demonstrate the convergence properties of the numerical scheme given in Chapter 7, the Sedov blast wave problem was solved. The initial condition is taken to be $\rho_o = 1$ in the strong shock limit with $\gamma = 1.4$. The analytic solution is given in detail in Appendix I. This analytic solution provides a boundary condition for the numerical solution and allows for the error to be directly computed for any given time or location.

The convergence behavior of the scheme is seen in Fig. 9.1 for a number of different CFL numbers, where

$$\text{CFL} = \frac{\Delta t}{\Delta x}.$$

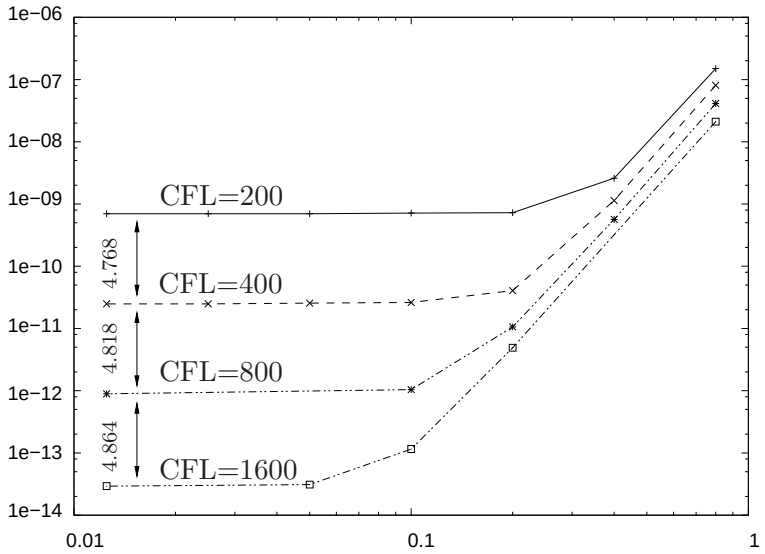

Figure 9.1. Sedov convergence.

Along the horizontal axis, a fixed Δt for a particular numerical solution is given. The vertical axis gives the corresponding L_∞ error, as computed in the shock-attached frame over the numerical domain excluding a strip near the rear boundary. As the CFL number is increased for a particular Δt the spatial grid size decreases cooerspondingly. From Fig. 9.1, one can see that it is necessary to take Δt to be excessively small to realize the desired fifth order convergence. For larger fixed Δt, the convergence properties degrade suggesting that Δt must vanish faster that Δx to achieve high order convergence.

Assuming that the truncation error term dominating this behavior follows the form

$$\text{error} = c_o \frac{\Delta t^n}{\Delta x^m},$$

a modified CFL restriction of $\Delta t \sim \Delta x^{5/3}$ is required to converge at fifth order.

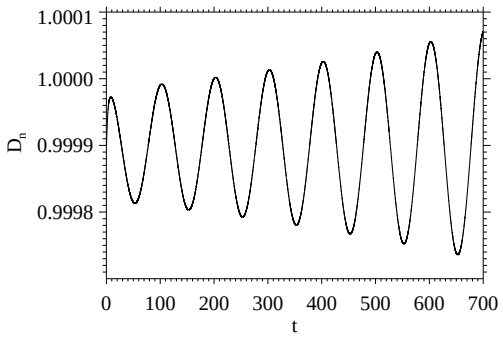

9.2.1: $n = 5.95$

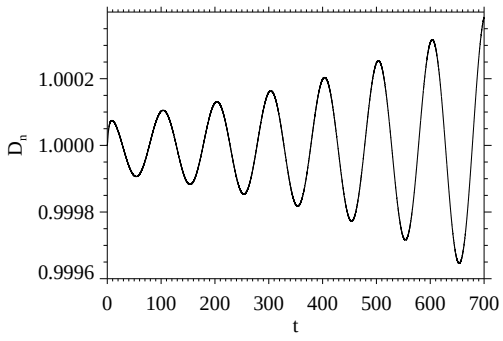

9.2.2: $n = 6$.

Figure 9.2. Evolution of the detonation front speed D_n at early time calculated for $f = 1$, $\nu = 1/2$. The grid resolution was 80 pts/hrl.

9.2 Linear stability study

Comparisons between the growth rates of unstable one- and two-dimensionally perturbed ZND detonations calculated using shock fitting and those calculated using normal mode analysis are given. All the calculations given her were performed on a uniform spatial grid, and the resolution in each case is indicated by the number of points (pts) per half reaction length (hrl) that are placed in the initial ZND wave. The initial conditions consisted of the ZND detonation structure for a supported CJ or overdriven detonation structure. A small amplitude quadratic perturbation in the reaction progress variable λ is added to the ZND structure, and the system allowed to evolve in time.

9.2.1 One-dimensional evolution

Figure 9.2 shows the early time evolution of the detonation shock speed D_n calculated for $f = 1$, $\nu = 1/2$ and for $n = 5.95$ and $n = 6$. Each shows a form of

TABLE 9.1

ONE-DIMENSIONAL GROWTH RATES AND FREQUENCIES

		Normal mode analysis		DNS		
f	n	Re(α)	Im(α)	Growth rate	Frequency	Res
1	5.906	.0000503	.062878	.0000502	.062877	80
1	5.95	.0010547	.062870	.0010546	.062867	80
1	6	.0022082	.062837	.0022082	.062834	80
1.1	4.28	.0001348	.087987	.0001352	.087981	40
1.05	4.5	.0024044	.063625	.0024013	.063624	40

oscillatory, exponential growth. The growth rates and frequencies of the evolution are extracted by fitting a function of the form $D_n = a_0 + a_1 \exp(a_2 t) \sin(a_3 t + a_4)$ to the data shown Fig. 9.2. The results of this fitting are shown in Table 9.1 for the two cases in Fig. 9.2 as well as for $n = 5.906$. Also shown in Table 9.1 are the corresponding predictions of the normal-mode analysis. In all cases, the agreement is excellent. Similarly good agreement is obtained for moderately overdriven waves. Cases for $\nu = 1/2$, $f = 1.1$, $n = 4.28$ and $f = 1.05$, $n = 4.5$ are shown in Table 9.1.

9.2.2 Two-dimensional evolution

Table 9.2 shows a comparison between the growth rate of a two-dimensional unstable detonation for $f = 1$, $\nu = 1/2$ and $n = 2.4$, characterized by a wavelength $L = 6$ (wavenumber $k = 2\pi/L = 1.0472$) as calculated via the normal mode

TABLE 9.2

TWO-DIMENSIONAL GROWTH RATED AND FREQUENCIES

			Normal mode analysis		DNS		
f	n	L	Re(α)	Im(α)	Growth rate	Frequency	Res
1	2.4	6	.00908726	0.731900	.00908759	0.731917	80
1.05	2.4	6	.00869689	0.730839	.00882749	0.731175	10
					.00857121	0.730811	20
1.05	2.2	5.7	.00152091	0.764230	.00024641	0.763367	10
					.00076171	0.763886	20
					.00125331	0.764115	40
1.05	2.2	7.3	.00244835	0.598937	.00147256	0.598540	10
					.00210797	0.598732	20

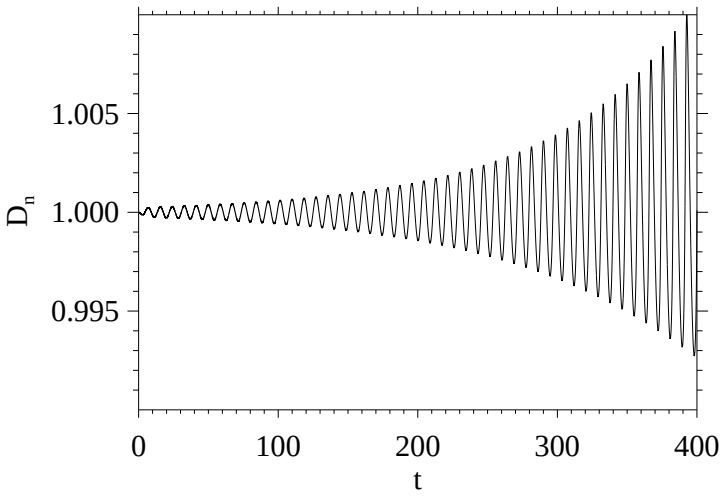

Figure 9.3. Evolution of the detonation front speed D_n for early time calculated along $z = 0$ in a two-dimensional periodic channel for $f = 1$, $\nu = 1/2$, $n = 2.4$ and $L = 6$. The grid resolution was 80 pts/hrl.

analysis and shock fitting. Numerical integration is carried in a channel of width $0 \leq z \leq L$ with periodic boundary conditions applied along $z = 0$ and $z = L$. The time evolution of the detonation shock velocity (D_n) along the boundary $z = 0$ is given in Fig. 9.3. The agreement between the growth rates and frequencies shown in Table 9.2 is again excellent.

In addition, Table 9.2 shows comparisons between shock-fitted numerical and the normal mode solutions for three overdriven cases in a two-dimensional periodic channel ($0 \leq z \leq L$). It should be noted that the resolution used in the overdriven cases is lower than that typically employed for the Chapman-Jouguet simulations. The overdriven detonation wave simulations are conducted on significantly larger domains to prevent any numerically spurious reflections of disturbances from the downstream outflow boundary over a given time span, which we have shown can

affect the linear evolution of the wave. For the case with $f = 1.05$, $n = 2.4$ and $L = 6$, the agreement between the growth rates and frequencies is excellent given the 20 pts/hrl resolution. The two cases with $f = 1.05$, $n = 2.2$ and either $L = 5.7$ or $L = 7.3$ lie close to the two-dimensional neutral stability boundary. The agreement between the frequencies is excellent. It is also satisfactory for the growth rates, which are clearly converging towards the normal mode results under increasing resolution. In particular, the two cases for $f = 1.05$ and $n = 2.2$ with channel widths of $L = 5.7$ and $L = 7.3$ lie within two neighboring unstable regions of the oscillatory variation in the neutral stability boundary location. Moreover, the numerical solution for $f = 1.05$, $n = 2.2$ and $L = 6.5$ reveals that the detonation is linearly stable, a confirmation of the validity of the unusual wavy variation found by normal modes analysis for $f = 1.05$. In summary, we have demonstrated an excellent agreement between the growth rates and frequencies of unstable disturbances obtained from a normal mode analysis and from a direct numerical integration for both Chapman-Jouguet and overdriven systems with square-root depletion ($\nu = 1/2$). Other cases we have calculated for $\nu > 1/2$ show similarly excellent agreement.

9.2.3 Stable evolution for $\nu = 1/2$.

Figure 9.4.1 shows the evolution of the detonation shock speed in time for $f = 1$, $\nu = 1/2$ and $n = 5.9$ calculated using shock fitting. For this case, $K_p = -0.002892$ (see §6.2). A calculation from the linear stability analysis shows that $\mathrm{Re}(\alpha) = -8.60 \times 10^{-5}$ and $\mathrm{Im}(\alpha) = 0.062878$, so that $K_p < \mathrm{Re}(\alpha) < 0$. An exponential fit of the form described in Ref. [75] to the slowly decaying amplitude of D_n in Fig. 9.4.1 gives $\mathrm{Re}(\alpha) = -8.61 \times 10^{-5}$ and $\mathrm{Im}(\alpha) = 0.062877$, an excellent

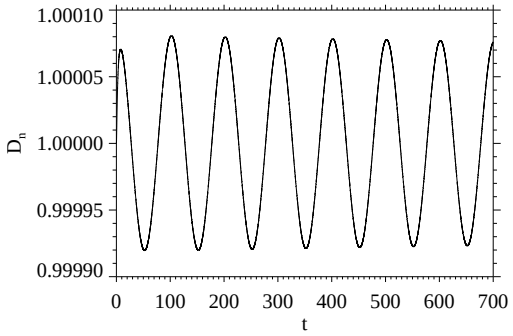

9.4.1: one-dimensional evolution for $n = 5.9$

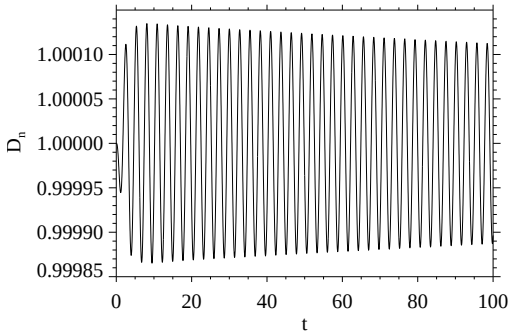

9.4.2: two-dimensional periodic channel evolution along $z = 0$ for $n = 2.4$ and $L = 1.9$.

Figure 9.4. Detonation front speed D_n for early time calculated by DNS for $f = 1$, $\nu = 0.5$; The grid resolution was 80 pts/hrl in each case.

agreement between the two results. Figure 9.4.2 shows the decay in amplitude of D_n along $z = 0$ arising after a weak perturbation of the steady ZND wave for $f = 1$, $n = 2.4$ and $\nu = 1/2$ in a periodic two-dimensional channel with $L = 1.9$ For this case, $K_p = -0.024134$. For a periodic channel of width $L = 1.9$, the wavenumber $k = 3.3069$. A linear stability analysis calculation gives $\mathrm{Re}(\alpha) = -0.0019355$ and $\mathrm{Im}(\alpha) = 2.295462$ for these parameters. A fit to the numerical solution shown in Fig. 9.4.2 gives $\mathrm{Re}(\alpha) = -0.0019365$ and $\mathrm{Im}(\alpha) = 2.295464$. These results show that for $f = 1$ and $\nu = 1/2$, modal solutions of the exponential form given in Ref. [75] are possible provided $K_p < \mathrm{Re}(\alpha) < 0$ and that the agreement between the linear stability analysis and a numerical simulation of the early time damping behavior of D_n is excellent.

9.3 Nonlinear evolution of unstable Chapman-Jouguet detonations for the idealized condensed phase model

In the final section, we discuss some long-time evolution calculations of one-dimensional pulsating and two-dimensional unstable Chapman-Jouguet detonations for the idealized condensed phase model. Again, these are calculated by direct numerical integration of Eqs. (7.42) using the shock-fitting, shock-attached strategy.

9.3.1 Pulsating instabilities

Figures 9.5, 9.6 and 9.7 show the long-time evolution of the detonation shock speed of an initially supported, steady CJ detonation for $\nu = 1/2$, and $n = 5.95$, $n = 5.975$ and $n = 6$. For $n = 5.95$ (Fig. 9.4), the linear stage of the growth persists over a long time, due to the slow growth rate of the unstable mode ($\mathrm{Re}(\alpha) = 0.00105$). The growth initially appears to saturate at around $t = 4500$, but there is a second growth stage for $5500 < t < 6500$, before the oscillatory amplitude of D_n saturates, and the detonation front enters a periodic limit-cycle state with period $T = 91.8$ and an amplitude of around 3.5% of the initial CJ velocity. The late-time periodic behavior for $(39000 < t < 40000)$ is shown in the $(dD_n/dt, D_n)$ phase portrait in Fig. 9.8.1. The evolution of D_n for $n = 5.975$ is shown in Fig. 9.6. The initial stages of the nonlinear saturation behavior appear to indicate a 'beating' form of evolution, but the amplitude of the beating cycle decays in time and for $t > 40000$, the shock speed evolution appears to have limited to a single-mode periodic state. The phase portrait for $n = 5.975$ where $39000 < t < 40000$ is shown in Fig. 9.8.2. The evolution of D_n for $n = 6$ is shown in Fig. 9.6. After the nonlinear saturation point for $t > 2500$,

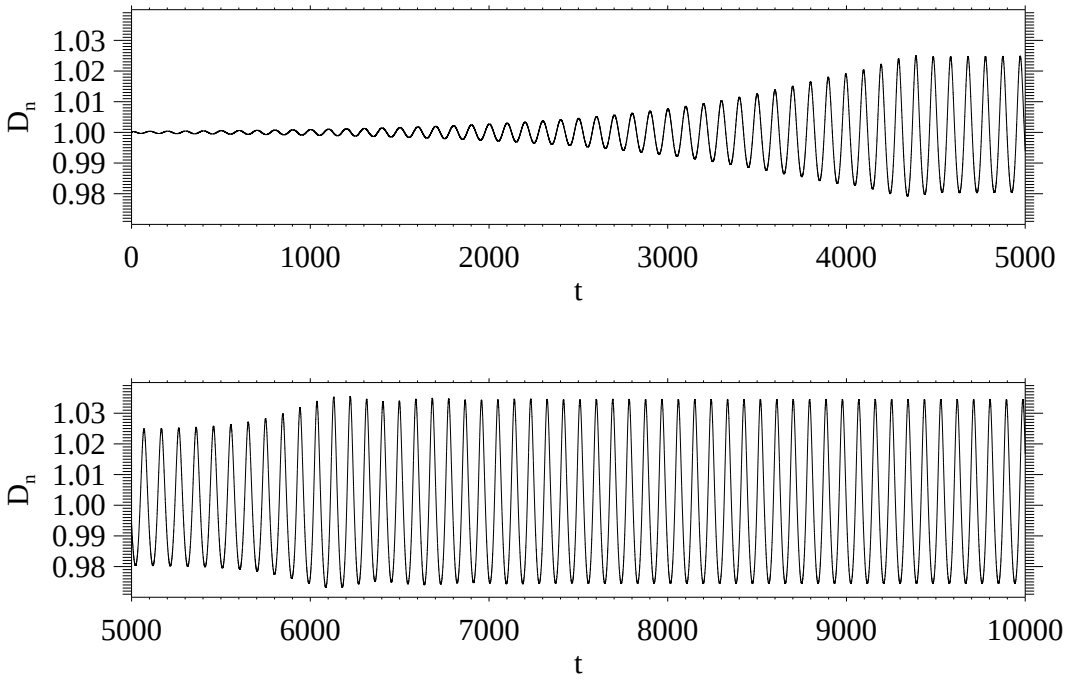

Figure 9.5. Long-time evolution of the detonation front speed calculated by DNS for $f = 1$, $\nu = 1/2$ and $n = 5.95$. The grid resolution was 40 pts/hrl.

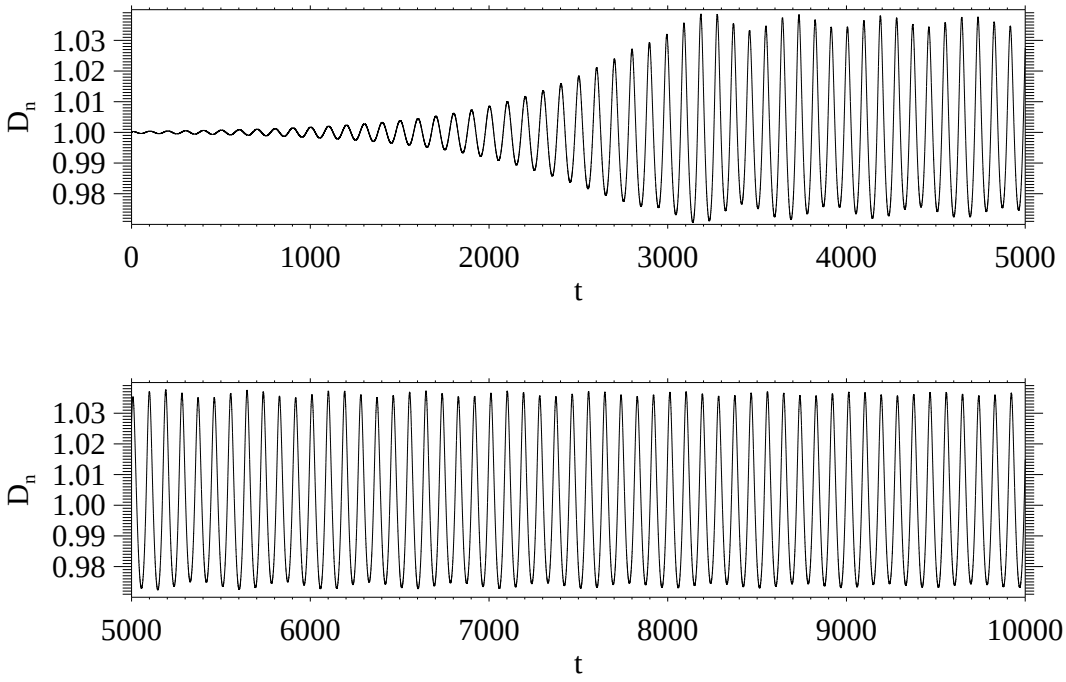

Figure 9.6. Long-time evolution of the detonation front speed calculated by DNS for $f = 1$, $\nu = 1/2$ and $n = 5.975$. The grid resolution was 40 pts/hrl.

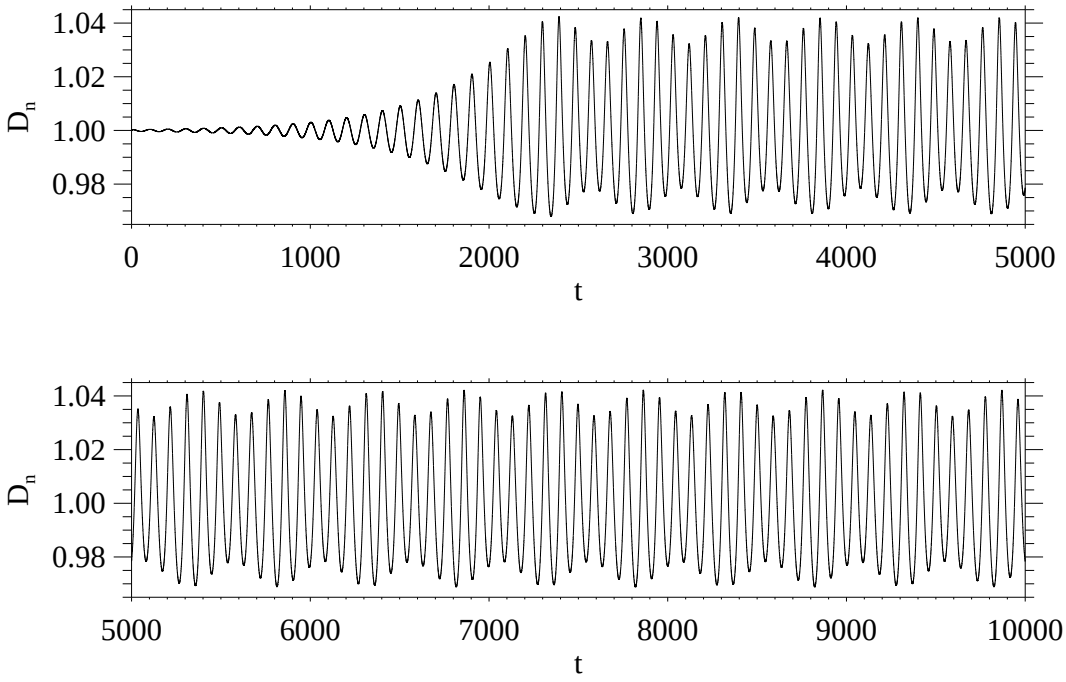

Figure 9.7. Long-time evolution of the detonation front speed calculated by DNS for $f = 1$, $\nu = 1/2$ and $n = 6$. The grid resolution was 40 pts/hrl.

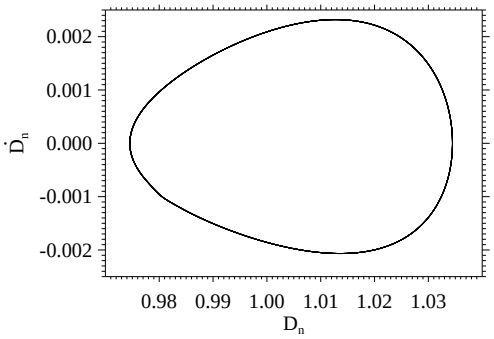

9.8.1: $n = 5.95$

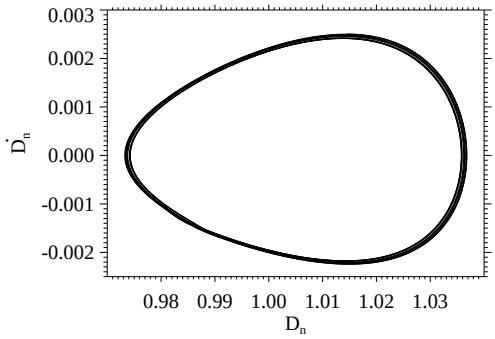

9.8.2: $n = 5.975$

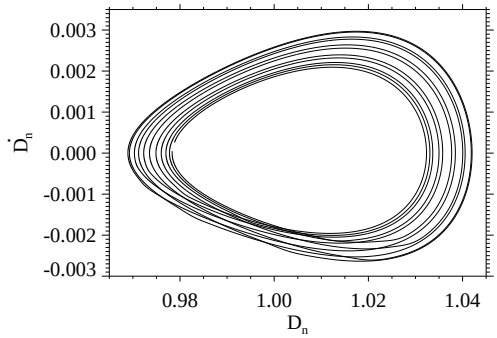

9.8.3: $n = 6$

Figure 9.8. Phase plane $(dD_n/dt, D_n)$ representation of the detonation front evolution calculated by DNS for $f = 1$, $\nu = 1/2$. The time interval over which each phase plane is shown is $t \in [39000, 40000]$. The grid resolution was 40 pts/hrl.

there is a sustained "beating" form of evolution in the amplitude variation of D_n. The total amplitude variations of the oscillation in D_n are approximately 4% of the initial CJ speed, with the beating oscillation having an amplitude of about 1% of the initial CJ speed. In this case, we do not observe any decay of the beating cycle, and there is no evidence of any periodic behavior for $t < 60000$. This apparently multi-mode evolution is observed in the phase portrait shown in Fig. 9.8.3 for $39000 < t < 40000$. A striking feature of the above nonlinear 1D dynamics (which is repeated for a range of other simulations we have conducted) is the relatively small magnitude of the detonation shock velocity departures in the saturated nonlinear equilibrium state from the underlying ZND value ($D_n = 1$) as the pressure exponent (n) is increased significantly from its neutrally stable value. This property is markedly different to that previously observed for 1D pulsating detonations in the idealized gas phase model.

9.3.2 Cellular instabilities

Figure 9.9 shows the long-time evolution of the detonation shock speed (D_n) corresponding to the case shown in Fig. 9.3, *i.e.* for a two-dimensional unstable detonation with $f = 1$, $n = 2.4$ and $\nu = 1/2$ in a channel $0 \leq z \leq 6$, with periodic boundaries on $z = 0$ and $z = 6$. A cellular, diamond-like, pattern is clearly evident in the channel that is reminiscent of the dynamics of cellular detonations formed under the idealized gas phase model. Along any line of fixed z, the evolution involves alternating periods of shock acceleration and deceleration. The black lines in Fig. 9.9 show the locus of the incident shock at various times in the evolution. There are a number of interesting features to this plot; the first is the relatively small deflections in the shock locus across the channel. The second is the relatively

small departures of the detonation shock velocity from the steady CJ value $D_n = 1$ (up to 7%). Finally, the time-scale over which a complete detonation cell is formed is 8.6, as determined from Fig. 9.9. This compares to the linear analysis where the completion of a period in the detonation speed along any fixed z, occurs over a time-scale of $2\pi/\mathrm{Im}(\alpha) = 2\pi/0.7319 = 0.858$ (Table 9.2), almost identical to that recovered from the simulation. Further insights into the reason for the small deflections in the shock locus across the channel can be obtained from Fig. 9.10, which shows various snap-shots of the density variation behind the incident shock during the cell cycle. Transverse shock waves and slip lines are clearly evident in a triple point configuration; however, the gradient discontinuity in the incident shock locus is small at the shock intersection point. Figure 9.11 shows snap-shots of density and pressure variations at one time superimposed with constant pressure and density contours, demonstrating that the transverse shock wave is weak in amplitude.

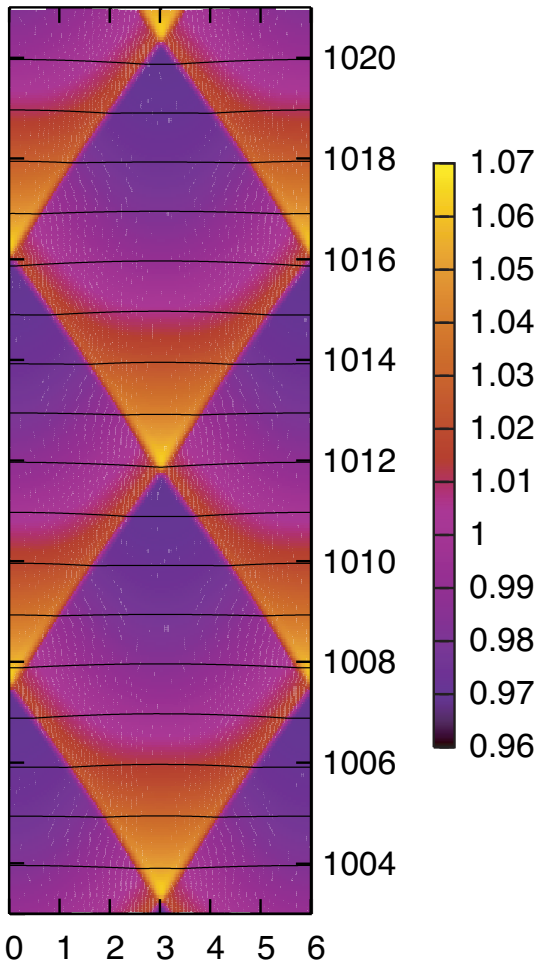

Figure 9.9. Evolution of the detonation front speed D_n in time for $f = 1$, $\nu = 0.5$ and $n = 2.4$ in a periodic channel $0 \leq z \leq L$, where $L = 6$. The black lines are the locus of the incident shock.

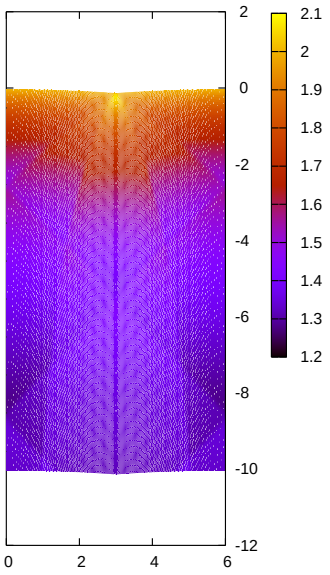

9.10.1: $t = 1003.40$

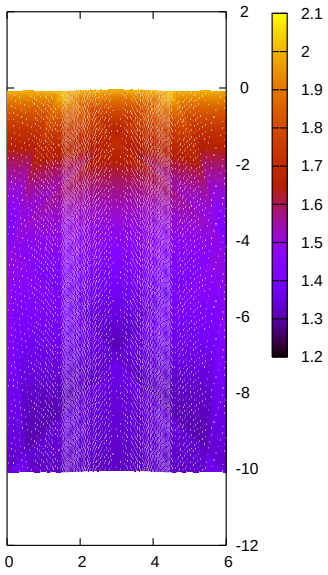

9.10.2: $t = 1005.55$

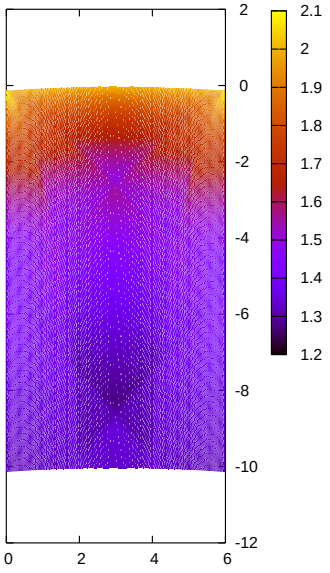

9.10.3: $t = 1007.71$

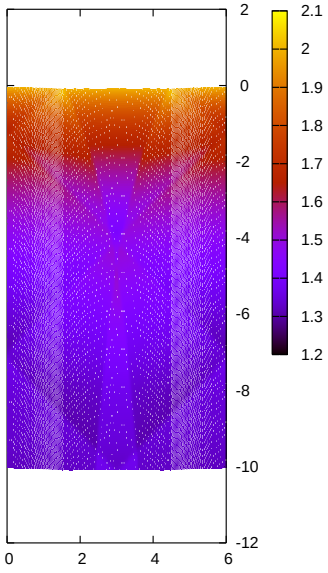

9.10.4: $t = 1009.86$

Figure 9.10. Snap-shots of the density variation behind the detonation front in the periodic channel $0 \leq z \leq 6$. The variations are shown in the longitudinal coordinate frame $x = x^l - Dt$.

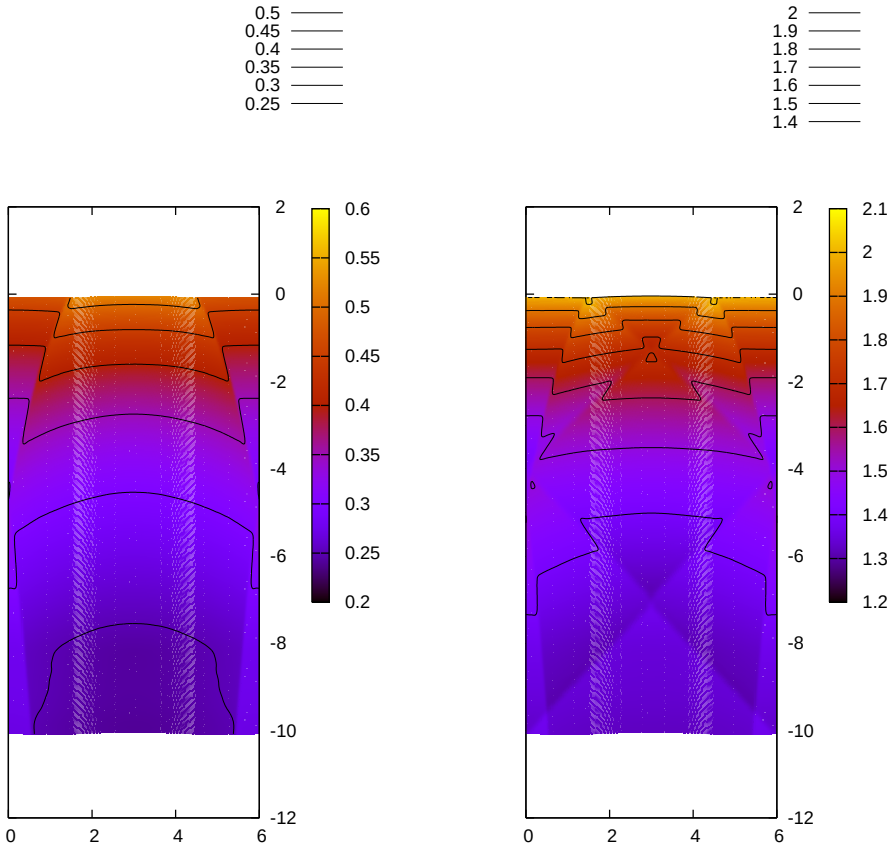

9.11.1: Pressure field

9.11.2: Density field

Figure 9.11. Snap-shots at $t = 1005.55$. The black lines indicate contours of constant pressure and density.

CHAPTER 10

CONCLUSIONS AND FUTURE WORK

Shock-fitting is an attractive method for solving problems with an embedded shock. A conservative formulation for a general conservation law was rigorously derived and implemented for the Euler equations with reaction in both one- and two-dimensions. This formally high order method was verified using an inert shock problem, and highly accurate detonation solutions were obtained at relatively small computation cost. In summary, shock-fitting is a successful means of obtaining highly accurate, resolved detonation solutions.

Shock-fitting is not, however, without its own distinctive complications. First, it is a mathematically intensive exercise to correctly formulate governing equations in time-dependent curvilinear coordinates. This added complexity contributes to practical difficulties in implementing the method. More importantly, this complexity greatly limits the types of problems for which shock-fitting is useful: in practice only a single smooth shock can be fitted. For problems with evolving shocks, shock-fitting can still be employed to precisely define a single shock surface; however, the presence of other shocks degrades the convergence properties of the method to first order at best. Furthermore, depending on the type of transformation chosen, the correct implementation of boundary conditions can be difficult.

To augment the robustness of the method, the conservative numerical scheme WENO5M was developed. This scheme correctly captures shocks and simultaneously provides a formally fifth order interior solver. WENO5M is an effective improvement to a well known high order scheme and has served to clarify and extend weighted essentially non-oscillatory schemes.

The results for the model problem suggest that when properly employed, algorithm craftsmanship in the form of shock-fitting coupled with a high order spatio-temporal discretization can yield remarkable gains in accuracy of many orders of magnitude relative to existing algorithms for certain specialized problems. This then admits solution in more rapid fashion or enables existing computational resources to be used to predict new phenomena. This includes precise quantitative description of the dynamical system behavior of pulsating one-dimensional detonations. For the idealized condensed phase model, long-time direct numerical simulations reveal that for unstable, one-dimensional CJ detonations, the evolution occurs in a form of pulsating instability, while for unstable two-dimensional detonations, detonation cells appear to form.

There are promising avenues for future work in this area. First, exploration of the fully transformed, conservative formulation may provide for a more straightforward implementation of boundary conditions. Deflected boundary problems are yet to be reported; extension of the solution domain in the model problem to include the confiner material behavior would provide the correct deflected boundary conditions. Lastly, three-dimensional shock-fitting problems should be considered and would be a straightforward extension of the work presented here.

APPENDIX A

THE NUMERICAL FLUX FUNCTION

The numerical flux function is defined according to Eqs. (6.4) and (6.5) such that "the real flux divergence is a finite difference of numerical fluxes [10]." Despite its natural connotation, the numerical flux is not a numerical approximation to the flux. As Section 6.1.2 elaborates, high order conservative numerical schemes are formed by making a numerical approximation to the numerical flux function itself. In this section, the analytic character of the numerical flux is given.

A.1 An approximation to the actual flux

First, as suggested in Ref. [10] the numerical flux function is exactly a second order approximation to the exact flux function for any fixed, non-zero Δx. Beginning with the midpoint integration rule, one has

$$\int_{x-\Delta x/2}^{x+\Delta x/2} h(\xi)d\xi = h(x)\Delta x + \frac{1}{24}h''(x)\Delta x^3 + \frac{1}{1920}h^{(4)}\Delta x^5 + O(\Delta x^7).$$

Dividing by Δx gives

$$f(x) = \frac{1}{\Delta x}\int_{x-\Delta x/2}^{x+\Delta x/2} h(\xi)d\xi = h(x) + \frac{1}{24}h''(x)\Delta x^2 + \frac{1}{1920}h^{(4)}\Delta x^5 + O(\Delta x^6) \quad \text{(A.1)}$$

which is the definition of numerical flux function.

Solving Eq. (A.1) for $h(x)$ and differentiating gives

$$h(x) = f(x) - \frac{1}{24}h''(x)\Delta x^2 - \frac{1}{1920}h^{(4)}\Delta x^5 + O(\Delta x^6), \tag{A.2a}$$

$$h''(x) = f''(x) - \frac{1}{24}h^{(4)}(x)\Delta x^2 + O(\Delta x^4), \tag{A.2b}$$

$$h^{(4)}(x) = f^{(4)}(x) + O(\Delta x^2). \tag{A.2c}$$

Substituting Eq. (A.2c) in Eq. (A.2b) gives

$$h''(x) = f''(x) - \frac{1}{24}f^{(4)}(x)\Delta x^2 + O(\Delta x^4). \tag{A.3}$$

Substituting Eqs. (A.2c) and (A.3) into Eq. (A.2a) gives

$$h(x) = f(x) - \frac{1}{24}\Delta x^2\left(f''(x) - \frac{1}{24}f^{(4)}(x)\Delta x^2\right) - \frac{1}{1920}\Delta x^5 f^{(4)} + O(\Delta x^6). \tag{A.4}$$

Finally, simplification of Eq. (A.4) yields

$$h(x) = f(x) - \frac{1}{24}f''(x)\Delta x^2 + \frac{7}{5760}f^{(4)}(x)\Delta x^4 + O(\Delta x^6), \tag{A.5}$$

which is the Taylor series expansion of the numerical flux function in terms of the actual flux. Equations (A.1) and (A.5) together allow the flux and numerical flux to be expressed, each in terms of the other; they are second order approximations of each other.

Evaluation of Eq. (A.5) for a particular value of $x = x_{i+1/2}$ yields a functional

taking an arbitrary function f:

$$h[f]_{i+1/2} = f(x_{i+1/2}) - \frac{1}{24} f''(x_{i+1/2})\Delta x^2 + \frac{7}{5760} f^{(4)}(x_{i+12})\Delta x^4 + O(\Delta x^6). \tag{A.6}$$

Representing a series approximation to $h(x)$ by $\hat{h}(x)$, an approximation to the numerical flux, for a given flux f at $x_{i+1/2}$, can be easily denoted $\hat{h}[f]_{i+1/2}$. For brevity, where the functional argument is omitted, it is assumed from the context.

A.2 A means of computing first derivatives

The numerical flux function may also be used as a means of obtaining the exact first derivative of a function from its centered finite differences. Consider a function

$$g(x) = \int_a^x h(\xi) d\xi, \tag{A.7}$$

where a is a fixed constant. Taking the central difference operator to be defined as

$$\delta g(x) = \frac{g(x + \frac{\Delta x}{2}) - g(x - \frac{\Delta x}{2})}{\Delta x}, \tag{A.8}$$

Eq. (6.5) can now be extended to incorporate $g(x)$ such that

$$\frac{1}{\Delta x} \int_{x-\Delta x/2}^{x+\Delta x/2} h(\xi) d\xi = \delta g(x). \tag{A.9}$$

But from the fundamental theorem of calculus, differentiation of Eq. (A.7) gives

$$g'(x) = h(x). \tag{A.10}$$

Thus, given Eq. (A.7), the numerical flux function is identical to the derivative of $g(x)$. The numerical flux function satisfies and satisfies Eq. (A.9) exactly. Thus, any series approximation $\hat{h}(x)$ truncated at order $O(\Delta x^n)$ gives an n^{th} order approximation to the derivative of $g(x)$ when operating on the the centered differences:

$$g'(x) = \hat{h}[\delta g(x)] + O(\Delta x^n) \tag{A.11}$$

WENO5M is a robust, fifth order approximation to $h(x)$ given in Section 6.1.2.3.

APPENDIX B

TWO-DIMENSIONAL TIME-DEPENDENT METRICS

A summary of the spatial and temporal metrics relating derivatives of Cartesian and time-dependent curvilinear coordinates are given. Spatial derivatives in each coordinate system are related through the the partial derivatives

$$\begin{pmatrix} \frac{\partial}{\partial x^1} \\ \frac{\partial}{\partial x^2} \end{pmatrix} = \left(\begin{array}{c} \boldsymbol{g}_{(1)} \\ \hdashline \boldsymbol{g}_{(2)} \end{array}\right) \begin{pmatrix} \frac{\partial}{\partial y^1} \\ \frac{\partial}{\partial y^2} \end{pmatrix} \tag{B.1a}$$

$$= \begin{pmatrix} \frac{\partial y^1}{\partial x^1} & \frac{\partial y^2}{\partial x^1} \\ \frac{\partial y^1}{\partial x^2} & \frac{\partial y^2}{\partial x^2} \end{pmatrix} \begin{pmatrix} \frac{\partial}{\partial y^1} \\ \frac{\partial}{\partial y^2} \end{pmatrix}. \tag{B.1b}$$

Inverting Eqs. (B.1b) gives

$$\begin{pmatrix} \frac{\partial}{\partial y^1} \\ \frac{\partial}{\partial y^2} \end{pmatrix} = \left(\begin{array}{c:c} \boldsymbol{g}^{(1)} & \boldsymbol{g}^{(2)} \end{array}\right) \begin{pmatrix} \frac{\partial}{\partial x^1} \\ \frac{\partial}{\partial x^2} \end{pmatrix} \tag{B.2a}$$

$$= \frac{1}{\sqrt{g}} \begin{pmatrix} \frac{\partial y^2}{\partial x^2} & -\frac{\partial y^2}{\partial x^1} \\ -\frac{\partial y^1}{\partial x^2} & \frac{\partial y^1}{\partial x^1} \end{pmatrix} \begin{pmatrix} \frac{\partial}{\partial x^1} \\ \frac{\partial}{\partial x^2} \end{pmatrix}, \tag{B.2b}$$

where

$$\sqrt{g} = \begin{vmatrix} \boldsymbol{g}_{(1)} \\ \boldsymbol{g}_{(2)} \end{vmatrix} \tag{B.3a}$$

$$= \frac{\partial y^1}{\partial x^1}\frac{\partial y^2}{\partial x^2} - \frac{\partial y^1}{\partial x^2}\frac{\partial y^2}{\partial x^1} \tag{B.3b}$$

is just the square root of the metric tensors' determinant. Often in the literature, $\frac{1}{\sqrt{g}}$ is denoted J. Application of Eq. (B.2b) to x^1 and x^2 gives, respectively

$$\frac{\partial x^1}{\partial y^1} = \frac{1}{\sqrt{g}}\frac{\partial y^2}{\partial x^2}, \tag{B.4a}$$

$$\frac{\partial x^1}{\partial y^2} = -\frac{1}{\sqrt{g}}\frac{\partial y^1}{\partial x^2}, \tag{B.4b}$$

$$\frac{\partial x^2}{\partial y^1} = -\frac{1}{\sqrt{g}}\frac{\partial y^2}{\partial x^1}, \tag{B.4c}$$

$$\frac{\partial x^2}{\partial y^2} = \frac{1}{\sqrt{g}}\frac{\partial y^1}{\partial x^1}. \tag{B.4d}$$

Lastly,

$$\sqrt{g^{22}} = \sqrt{\boldsymbol{g}^{(2)} \cdot \boldsymbol{g}^{(2)}} \tag{B.5a}$$

$$= \frac{1}{\sqrt{g}}\sqrt{\left(\frac{\partial y^2}{\partial x^1}\right)^2 + \left(\frac{\partial y^1}{\partial x^1}\right)^2} \tag{B.5b}$$

is given explicitly for use in the shock-fitting constraints.

The temporal metrics, otherwise known as the grid velocity components, are explored in Section 2.6.1 and given by Eq. (2.17a). For completeness, they are repeated here in component form where Eqs. (B.4) have been used to write all

spatial derivatives with respect to the curvilinear coordinates:

$$-\frac{\partial x^1}{\partial t} = \frac{1}{\sqrt{g}}\left(\frac{\partial y^2}{\partial x^2}\frac{\partial y^1}{\partial t} - \frac{\partial y^1}{\partial x^2}\frac{\partial y^2}{\partial t}\right), \tag{B.6a}$$

$$-\frac{\partial x^2}{\partial t} = \frac{1}{\sqrt{g}}\left(-\frac{\partial y^2}{\partial x^1}\frac{\partial y^1}{\partial t} + \frac{\partial y^1}{\partial x^1}\frac{\partial y^2}{\partial t}\right). \tag{B.6b}$$

Equations (B.6) have been verified for the general time-dependent transformation given by Eq. (2.13) by Steger [76].

APPENDIX C

THE EULER EQUATIONS WITH REACTION

"The rapid and violent form of combustion called detonation differs from other forms in that all the important energy transfer is by mass flow in strong compression waves, with negligible contributions from other processes like heat conduction which are so important in flames [19]." Thus, the Euler equations with reaction are considered to describe the relevant physics for many detonation problems. They are the focus of proposed research and are placed in this appendix for reference and for use in subsequent appendices. In deriving these equations, *body forces, radiation, and species diffusion are neglected, and the fluid is assumed to be adiabatic and inviscid.*

In Einstein notation, the conservation form of the equations is given by

$$\frac{\partial \rho}{\partial t} + \left(\rho v^i\right)_{,i} = 0, \tag{C.1a}$$

$$\frac{\partial}{\partial t}(\rho v^i) + \left(\rho v^i v^j + p g^{ji}\right)_{,j} = 0, \tag{C.1b}$$

$$\frac{\partial}{\partial t}\left(\rho\left(e + \frac{1}{2}v^j v_j\right)\right) + \left(\rho v^i\left(e + \frac{1}{2}v^k v_k + \frac{p}{\rho}\right)\right)_{,i} = 0, \tag{C.1c}$$

$$\frac{\partial}{\partial t}(\rho Y_{(i)}) + \left(\rho v^j Y_{(i)}\right)_{,j} = M_{(i)}\dot{\omega}_{(i)}, \tag{C.1d}$$

where t is the time coordinate, superscripts denote contravariance and subscripts denote covariance, g^{ij} is the metric tensor, ρ is the density, v^i is the velocity, p is

the pressure, e is the internal energy, $Y_{(i)}$ and $M_{(i)}$ are the mass fraction and molar mass of the i^{th} species, and $\dot{\omega}_{(i)}$ is the production rate of the molar concentration for the i^{th} species. This particular conservation form is physical in that it yields correct shock speeds, whereas other mathematically equivalent conservation forms do not.

In one dimension, Eq. (C.1) becomes

$$\frac{\partial \rho}{\partial t} + \frac{\partial}{\partial x}(\rho u) = 0, \tag{C.2a}$$

$$\frac{\partial}{\partial t}(\rho u) + \frac{\partial}{\partial x}(p + \rho u^2) = 0, \tag{C.2b}$$

$$\frac{\partial}{\partial t}\left(\rho\left(e + \frac{1}{2}u^2\right)\right) + \frac{\partial}{\partial x}\left(\rho u\left(e + \frac{1}{2}u^2 + \frac{p}{\rho}\right)\right) = 0, \tag{C.2c}$$

$$\frac{\partial}{\partial t}(\rho Y_{(i)}) + \frac{\partial}{\partial x}(\rho u Y_{(i)}) = M_{(i)}\dot{\omega}_{(i)}, \tag{C.2d}$$

where u is the velocity in the x direction.

For use with characteristic analysis, it is more convenient to expand the derivative operators in Eq. (C.2). Further simplification yields the non-conservative form:

$$\frac{\partial \rho}{\partial t} + u\frac{\partial \rho}{\partial x} + \rho\frac{\partial u}{\partial x} = 0, \tag{C.3a}$$

$$\left(\frac{\partial u}{\partial t} + u\frac{\partial u}{\partial x}\right) + v\frac{\partial p}{\partial x} = 0, \tag{C.3b}$$

$$\left(\frac{\partial e}{\partial t} + u\frac{\partial e}{\partial x}\right) + p\left(\frac{\partial v}{\partial t} + u\frac{\partial v}{\partial x}\right) = 0, \tag{C.3c}$$

$$\frac{\partial Y_{(i)}}{\partial t} + u\frac{\partial Y_{(i)}}{\partial x} = r_{(i)}(p, \rho, Y_{(j)}), \tag{C.3d}$$

where $v = 1/\rho$ is the specific volume, and the $r_{(i)} = M_{(i)}\dot{\omega}_{(i)}/\rho$ is the rate law associated with the i^{th} species.

APPENDIX D

CALORIC EQUATION OF STATE FOR AN IDEAL GAS MIXTURE

For a mixture

$$e = \sum_{i=1}^{N} Y_i e_i, \tag{D.1}$$

where e_i is the internal energy of the i^{th} species and N is the number of species in the system. Parentheses surrounding non-tensorial indices have been dropped for brevity. For a calorically perfect ideal gas,

$$e_i = h^0_{f,i} + c_{p,i}(T - T_0) - R_i T, \tag{D.2}$$

where the constants $c_{p,i}$ and $h^0_{f,i}$ are the specific heat and the heat of formation for the i^{th} species, respectively. The ideal gas constant for the i^{th} species is given by $R_i = \Re/M_i$ where $\Re$ is the universal gas constant. A "0" superscript indicated evaluation at the reference pressure, and T_0 is the reference temperature.

Now the ideal gas constant is related to the specific heats by

$$R_i = c_{p,i} - c_{v,i} \qquad \text{or} \qquad R = c_p - c_v, \tag{D.3}$$

where $R = \sum_{i=1}^{N} Y_i R_i$, $c_p = \sum_{i=1}^{N} Y_i c_{p,i}$, and $c_v = \sum_{i=1}^{N} Y_i c_{v,i}$.

For the case that the specific heats for each species i satisfy $c_{p,i} = c_p$ and $c_{v,i} = c_v$, the ideal gas constants, as well as the molar masses, must also be equal:

$R_i = R$ and $M_i = M$. With these assumptions, Eq. (D.2) becomes

$$e_i = h^0_{f,i} + c_p(T - T_0) - RT. \tag{D.4}$$

Substituting Eq. (D.4) in Eq. (D.1) gives

$$e = \sum_{i=1}^{N} Y_i h^0_{f,i} + c_p(T - T_0) - RT,$$

since the sum of the mass fractions is unity by definition. Furthermore, R may be replaced by Eq. (D.3) and the total energy is given by

$$e = \sum_{i=1}^{N} Y_i h^0_{f,i} - c_p T_0 + c_v T. \tag{D.5}$$

Replacing T using the ideal gas law yields

$$e = \sum_{i=1}^{N} Y_i h^0_{f,i} - c_p T_0 + \frac{c_v}{R}\frac{p}{\rho}.$$

Furthermore, $\sum_{i=1}^{N} Y_i h^0_{f,i} - c_p T_0$ is a function of Y_i alone, and $\frac{c_v}{R} = \frac{1}{\gamma - 1}$ where $\gamma = \frac{c_p}{c_v}$. Thus the energy equation becomes

$$e = \underbrace{\sum_{i=1}^{N} Y_i h^0_{f,i} - c_p T_0}_{f(Y_i)} + \frac{1}{\gamma - 1}\frac{p}{\rho}. \tag{D.6}$$

Equation (D.6) simplifies greatly for the case of two species:

$$e = Y_1 h^0_{f,1} + Y_2 h^0_{f,2} - c_p T_0 + \frac{1}{\gamma - 1}\frac{p}{\rho}.$$

Since the sum of the mass fractions is unity, one may write $Y_1 = 1 - Y_2$. Substituting for Y_1 gives

$$e = Y_2(h^0_{f,2} - h^0_{f,1}) + h^0_{f,1} - c_p T_0 + \frac{1}{\gamma - 1}\frac{p}{\rho}.$$

Furthermore, the internal energy, e, is only an *energy difference*. Thus, the constant $h^0_{f,1} - c_p T_0$ can be incorporated by shifting the original energy datum, yielding

$$e = Y_2(h^0_{f,2} - h^0_{f,1}) + \frac{1}{\gamma - 1}\frac{p}{\rho}. \tag{D.7}$$

For a binary mixture undergoing a unimolecular reaction from Y_1 to Y_2, it is customary to speak of Y_2 as the progress variable and to change its notation to λ such that

$$\lambda \in [0, 1].$$

Lastly, the quantity $h^0_{f,2} - h^0_{f,1}$ is simply the heat release accompanying the reaction and is denoted q. Equation (D.7) then becomes

$$e = \frac{1}{\gamma - 1}\frac{p}{\rho} + q\lambda. \tag{D.8}$$

APPENDIX E

THERMICITY COEFFICIENT IDENTITIES

The thermicity coefficients are defined as

$$\sigma_i = -\frac{1}{\rho c^2}\left[\frac{\left.\frac{\partial e}{\partial Y_i}\right|_{p,v}}{\left.\frac{\partial e}{\partial p}\right|_{v,Y}}\right]. \tag{E.1}$$

where subscripted variables following the unmatched right hand | are held constant and parenthesis surrounding non-tensorial indices have been dropped for brevity. Holding the mass fractions constant will be denoted by an undecorated subscript Y. In Eq. (E.1), $c^2 = \gamma pv$ is the frozen sound speed. For a single inert material, adiabatic gamma for general equation of state is

$$\gamma = \frac{dv}{dT}|_P \frac{dP}{dv}|_s.$$

It may be reduced to

$$\gamma = \frac{1}{pv}\left.\frac{\partial p}{\partial \rho}\right|_{s,Y}$$

and is simply the ratio of specific heats for a calorically perfect ideal gas.

More physically intuitive interpretations of the thermicity coefficient's can be give by appealing to thermodynamic identities and use of the chain rule for multivariable calculus. Using the volume expansion coefficient and the specific heat

at constant pressure,

$$\beta = \frac{1}{v}\left.\frac{\partial v}{\partial T}\right|_{p,Y} \quad \text{and} \quad c_p = \left.\frac{\partial h}{\partial T}\right|_{p,Y}, \tag{E.2}$$

an explicit expression of the thermicity coefficients in terms of "the volume increase due to reaction at constant pressure and the heat release of the reaction at constant pressure [19, pg. 78]" is derived. Here the enthalpy, h, is defined as $h = e + pv$. In the following manipulations, the mass fractions are assumed constant except where explicitly denoted otherwise.

In a simple, multispecies system a caloric equation of state exists such that $f(e, p, v, Y_i) = 0$. Differentials on this hypersurface are related by

$$df = \frac{\partial f}{\partial e}de + \frac{\partial f}{\partial p}dp + \frac{\partial f}{\partial v}dv + \frac{\partial f}{\partial Y_i}dY_i = 0.$$

Thus, a relationship between the partial derivatives of the independent variables may be formed:

$$\left.\begin{aligned} \left.\frac{\partial Y_i}{\partial e}\right|_{p,v} &= -\frac{\frac{\partial f}{\partial e}}{\frac{\partial f}{\partial Y_i}} \\ \left.\frac{\partial p}{\partial Y_i}\right|_{e,v} &= -\frac{\frac{\partial f}{\partial Y_i}}{\frac{\partial f}{\partial e}} \\ \left.\frac{\partial e}{\partial p}\right|_{Y,v} &= -\frac{\frac{\partial f}{\partial p}}{\frac{\partial f}{\partial e}} \end{aligned}\right\} \qquad \left.\frac{\partial Y_i}{\partial e}\right|_{p,v}\left.\frac{\partial p}{\partial Y_i}\right|_{e,v}\left.\frac{\partial e}{\partial p}\right|_{Y,v} = -1. \tag{E.3}$$

Taking into account that $\left(\left.\frac{\partial Y_i}{\partial e}\right|_{p,v}\right)^{-1} = \left.\frac{\partial e}{\partial Y_i}\right|_{p,v}$, rearrangement of Eq. (E.3) gives

$$\left.\frac{\partial p}{\partial Y_i}\right|_{e,v} = -\frac{\left.\frac{\partial e}{\partial Y_i}\right|_{p,v}}{\left.\frac{\partial e}{\partial p}\right|_{Y,v}}. \tag{E.4}$$

More generally, given an implicit differentiable function $f(w,x,y,z) = 0$, the partial derivatives may be related according to

$$\left.\frac{\partial x}{\partial y}\right|_{w,z} = -\frac{\left.\frac{\partial w}{\partial y}\right|_{x,z}}{\left.\frac{\partial w}{\partial x}\right|_{y,z}}. \tag{E.5}$$

Substituting Eq. (E.4) into Eq. (E.1) gives

$$\sigma_i = \frac{1}{\rho c^2}\left.\frac{\partial p}{\partial Y_i}\right|_{e,v}, \tag{E.6}$$

from which the thermicity coefficient for the i^{th} species is seen to the be proportional to the change in pressure per change in the mass fraction.

Now, β and c_p are introduced into Eqs. (E.1) and (E.6) through c. Writing the sound speed in terms of specific volume rather than density gives

$$c^2 = -v^2\left.\frac{\partial p}{\partial v}\right|_{s,Y}. \tag{E.7}$$

Instead of working with this isentropic expression, it is easier to work with the partial derivatives of entropy directly. Since an implicit function $f(s,p,v,Y_i) = 0$ describes the thermodynamic state, application of Eq. (E.5) gives

$$\left.\frac{\partial p}{\partial v}\right|_{s,Y} = -\frac{\left.\frac{\partial s}{\partial v}\right|_{p,Y}}{\left.\frac{\partial s}{\partial p}\right|_{v,Y}}. \tag{E.8}$$

Thus, substituting Eq. (E.8) into Eq. (E.7) and rearrangement gives

$$\rho c^2 = v\frac{\left.\frac{\partial s}{\partial v}\right|_{p,Y}}{\left.\frac{\partial s}{\partial p}\right|_{v,Y}}. \tag{E.9}$$

Now the thermicity coefficients can be written as

$$\sigma_i = -\rho \frac{\left.\frac{\partial s}{\partial p}\right|_{v,Y}}{\left.\frac{\partial s}{\partial v}\right|_{p,Y}} \left[\frac{\left.\frac{\partial e}{\partial Y_i}\right|_{p,v}}{\left.\frac{\partial e}{\partial p}\right|_{v,Y}} \right]. \tag{E.10}$$

by substituting Eq. (E.9) into Eq. (E.1).

Consider first $\left.\frac{\partial s}{\partial p}\right|_{v,Y}$. The entropy may be expressed in terms of energy by making use of the Gibbs equation

$$de = Tds - pdv. \tag{E.11}$$

Taking $s = s(v, p)$, this may be written

$$de = T \left.\frac{\partial s}{\partial p}\right|_{v,Y} dp + \left(T \left.\frac{\partial s}{\partial v}\right|_{p,Y} - p \right) dv, \tag{E.12}$$

where $ds = \left.\frac{\partial s}{\partial v}\right|_{p,Y} dv + \left.\frac{\partial s}{\partial p}\right|_{v,Y} dp$. Furthermore, $e = e(v, p)$ giving

$$de = \left.\frac{\partial e}{\partial p}\right|_{v,Y} dp + \left.\frac{\partial e}{\partial v}\right|_{p,Y} dv. \tag{E.13}$$

Comparing Eqs. (E.12) and (E.13) gives

$$\left.\frac{\partial e}{\partial p}\right|_{v,Y} = T \left.\frac{\partial s}{\partial p}\right|_{v,Y} \tag{E.14}$$

from inspection. Substitution of Eq. (E.14) into Eq. (E.10) gives

$$\begin{aligned}\sigma_i &= -\frac{v}{T}\frac{\left.\frac{\partial e}{\partial p}\right|_{v,Y}}{\left.\frac{\partial s}{\partial v}\right|_{p,Y}}\left[\frac{\left.\frac{\partial e}{\partial Y_i}\right|_{p,v}}{\left.\frac{\partial e}{\partial p}\right|_{v,Y}}\right], \\ &= -\frac{v}{T}\frac{1}{\left.\frac{\partial s}{\partial v}\right|_{p,Y}}\left.\frac{\partial e}{\partial Y_i}\right|_{p,v}.\end{aligned} \tag{E.15}$$

Since β and c_p are constant pressure properties involving the enthalpy, $\left.\frac{\partial s}{\partial v}\right|_{p,Y}$ is expanded in terms of h. Substituting $dh = de + pdv + vdp$ into Eq. (E.11) gives an equivalent Gibbs equation in terms of enthalpy:

$$dh = Tds + vdp. \tag{E.16}$$

Again taking $s = s(v,p)$, Eq. (E.16) be written as

$$dh = \left(T\left.\frac{\partial s}{\partial p}\right|_{v,Y} + v\right)dp + T\left.\frac{\partial s}{\partial v}\right|_{p,Y}dv. \tag{E.17}$$

Considering $h(v,p)$ gives

$$dh = \left.\frac{\partial h}{\partial p}\right|_{v,Y}dp + \left.\frac{\partial h}{\partial v}\right|_{p,Y}dv. \tag{E.18}$$

Inspection of Eqs. (E.17) and (E.18) gives

$$\left.\frac{\partial h}{\partial v}\right|_{p,Y} = T\left.\frac{\partial s}{\partial v}\right|_{p,Y}. \tag{E.19}$$

Now to arrive at an expression involving β and c_p, consider $h(v,p) = h(T(v,p),p)$ such that

$$\left.\frac{\partial h}{\partial v}\right|_{p,Y} = \left.\frac{\partial h}{\partial T}\right|_{p,Y}\left.\frac{\partial T}{\partial v}\right|_{p,Y},$$

or

$$\left.\frac{\partial h}{\partial v}\right|_{p,Y} = \frac{\rho c_p}{\beta}. \tag{E.20}$$

given the definitions of β and c_p in Eqs. (E.2). Eq. (E.19) then becomes

$$\left.\frac{\partial s}{\partial v}\right|_{p,Y} = \frac{\rho c_p}{\beta T}. \tag{E.21}$$

Finally substitution into Eq. (E.15) and rearrangement gives

$$\sigma_i = -\frac{\beta}{c_p}\left.\frac{\partial e}{\partial Y_i}\right|_{p,v}. \tag{E.22}$$

Thus, the thermicity coefficients are proportional to the internal energy change due to reaction. Physically, this energy change models the chemical bond energy which is released to the flow by reaction.

To separate Eq. (E.22) into components which show the explicit dependence of thermicity on isobaric, isothermal volume change and heat release, the dependence on volume must be explicitly reintroduced. Substituting for β and c_p using Eq. (E.20), Eq. (E.22) becomes

$$\sigma_i = -\frac{\rho}{\left.\frac{\partial h}{\partial v}\right|_{p,Y}}\left.\frac{\partial e}{\partial Y_i}\right|_{p,v}. \tag{E.23}$$

$\left.\frac{\partial e}{\partial Y_i}\right|_{p,v}$ may be expressed in terms of h by considering

$$\begin{aligned} dh &= de + pdv + vdp, \\ &= \left(\left.\frac{\partial e}{\partial p}\right|_{v,Y} dp + \left.\frac{\partial e}{\partial v}\right|_{p,Y} dv + \left.\frac{\partial e}{\partial Y_i}\right|_{v,p} dY_i \right) + pdv + vdp, \\ &= \left(\left.\frac{\partial e}{\partial p}\right|_{v,Y} + v \right) dp + \left(\left.\frac{\partial e}{\partial v}\right|_{p,Y} + p \right) dv + \left.\frac{\partial e}{\partial Y_i}\right|_{v,p} dY_i. \end{aligned}$$

Comparison with $h(p, v, Y_i)$ such that

$$dh = \left.\frac{\partial h}{\partial p}\right|_{v,Y} dp + \left.\frac{\partial h}{\partial v}\right|_{p,Y} dv + \left.\frac{\partial h}{\partial Y_i}\right|_{p,v} dY_i$$

reveals that

$$\left.\frac{\partial e}{\partial Y_i}\right|_{v,p} = \left.\frac{\partial h}{\partial Y_i}\right|_{v,p}. \tag{E.24}$$

Substituting Eq. (E.24) into Eq. (E.23) gives

$$\sigma_i = -\frac{\rho}{\left.\frac{\partial h}{\partial v}\right|_{p,Y}} \left.\frac{\partial h}{\partial Y_i}\right|_{v,p}.$$

Now, the term

$$\frac{\left.\frac{\partial h}{\partial Y_i}\right|_{v,p}}{\left.\frac{\partial h}{\partial v}\right|_{p,Y}} = -\left.\frac{\partial v}{\partial Y_i}\right|_{h,p}$$

by application of Eq. (E.5) so that the thermicity coefficients become

$$\sigma_i = \rho \left.\frac{\partial v}{\partial Y_i}\right|_{h,p}. \tag{E.25}$$

Thus thermicity is also proportional to the adiabatic volume change due to reac-

tion.

Now that an explicit dependence on v is introduced, considering $v(T, p, Y_i)$ and $T(h, p, Y_i)$ allows the reintroduction of β and c_p.

$$\begin{aligned} dv &= \left.\frac{\partial v}{\partial T}\right|_{p,Y} dT + \left.\frac{\partial v}{\partial p}\right|_{T,Y} dp + \left.\frac{\partial v}{\partial Y_i}\right|_{p,T} dY_i, \\ &= \left.\frac{\partial v}{\partial T}\right|_{p,Y} \left(\left.\frac{\partial T}{\partial h}\right|_{p,Y} dh + \left.\frac{\partial T}{\partial p}\right|_{h,Y} dp + \left.\frac{\partial T}{\partial Y_i}\right|_{h,p} dY_i \right) + \left.\frac{\partial v}{\partial p}\right|_{T,Y} dp + \left.\frac{\partial v}{\partial Y_i}\right|_{p,T} dY_i, \\ &= \left.\frac{\partial v}{\partial T}\right|_{p,Y} \left.\frac{\partial T}{\partial h}\right|_{p,Y} dh + \left(\left.\frac{\partial v}{\partial T}\right|_{p,Y} \left.\frac{\partial T}{\partial p}\right|_{h,Y} + \left.\frac{\partial v}{\partial p}\right|_{T,Y} \right) dp \\ &\qquad + \left(\left.\frac{\partial v}{\partial T}\right|_{p,Y} \left.\frac{\partial T}{\partial Y_i}\right|_{h,p} + \left.\frac{\partial v}{\partial Y_i}\right|_{p,T} \right) dY_i. \end{aligned}$$

Comparison with

$$dv = \left.\frac{\partial v}{\partial h}\right|_{p,Y} dh + \left.\frac{\partial v}{\partial p}\right|_{h,Y} dp + \left.\frac{\partial v}{\partial Y_i}\right|_{h,p} dY_i$$

gives

$$\left.\frac{\partial v}{\partial Y_i}\right|_{h,p} = \left.\frac{\partial v}{\partial T}\right|_{p,Y} \left.\frac{\partial T}{\partial Y_i}\right|_{h,p} + \left.\frac{\partial v}{\partial Y_i}\right|_{p,T}, \tag{E.26}$$

$$= v\beta \left.\frac{\partial T}{\partial Y_i}\right|_{h,p} + \left.\frac{\partial v}{\partial Y_i}\right|_{p,T}. \tag{E.27}$$

$\left.\frac{\partial T}{\partial Y_i}\right|_{h,p}$ may be rewritten using Eq. (E.5) to give

$$\left.\frac{\partial T}{\partial Y_i}\right|_{h,p} = -\frac{\left.\frac{\partial h}{\partial Y_i}\right|_{p,T}}{\left.\frac{\partial h}{\partial T}\right|_{p,Y}}, \tag{E.28}$$

$$= -\frac{1}{c_p} \left.\frac{\partial h}{\partial Y_i}\right|_{p,T}. \tag{E.29}$$

Finally, substitution of Eqs. (E.27) and (E.29) in Eq. (E.25) gives

$$\sigma_i = -\frac{\beta}{c_p}\left.\frac{\partial h}{\partial Y_i}\right|_{p,T} + \frac{1}{v}\left.\frac{\partial v}{\partial Y_i}\right|_{p,T}. \tag{E.30}$$

Thus thermicity is divided into two terms due to reaction: heat release and volume change.

APPENDIX F

CHARACTERISTIC ANALYSIS OF EULER EQUATIONS WITH REACTION

A solution to Eqs. (C.3) can be found using the method of characteristics. From inspection, Eq. (C.3d) is already in characteristic form with

$$\frac{dY_i}{dt} = r_i(p, \rho, Y_j) \qquad \text{along} \qquad \frac{dx}{dt} = u. \tag{F.1}$$

Furthermore, Y_i does not appear explicitly in the remaining three equations. Thus, our characteristic analysis will only involve Eqs. (C.3a), (C.3b), and (C.3c). Also note that parentheses surrounding non-tensorial indices have been dropped for brevity.

F.1 Reformulating the energy equation

The energy equation, Eq. (C.3c), is also already in characteristic form with

$$\frac{de}{dt} + p\frac{dv}{dt} = 0 \qquad \text{along} \qquad \frac{dx}{dt} = u. \tag{F.2}$$

This equation cannot be neglected in the characteristic analysis since the pressure effectively couples the energy equation to the momentum equation. Thus, before beginning the characteristic analysis, it is useful to reduce the number of unknowns

in Eq. (C.3) by eliminating the internal energy in favor of the dependent variables p, v, and Y_i.

Making use of the caloric equation of state, $e = e(p, v, Y_i)$, an expression for $\frac{de}{dt}$ in terms of the p, v, and Y_i can be found. The differential is $de = \frac{\partial e}{\partial p}dp + \frac{\partial e}{\partial v}dv + \frac{\partial e}{\partial Y_i}dY_i$ with implicit summing on i from 1 to N. Thus

$$\frac{de}{dt} = \frac{\partial e}{\partial p}\frac{dp}{dt} + \frac{\partial e}{\partial v}\frac{dv}{dt} + \frac{\partial e}{\partial Y_i}\frac{dY_i}{dt}.$$

Substituting this expression into Eq. (F.2) gives

$$\frac{\partial e}{\partial p}\frac{dp}{dt} + \frac{\partial e}{\partial v}\frac{dv}{dt} + \frac{\partial e}{\partial Y_i}\frac{dY_i}{dt} + p\frac{dv}{dt} = 0 \tag{F.3}$$

along the characteristic defined by $\frac{dx}{dt} = u$. Since Eq. (F.1) is also valid along this characteristic, substitution of Eq. (F.1) into Eq. (F.3) removes $\frac{dY_i}{dt}$ in favor of $r_i(p, v, Y_i)$. This gives, after slight rearrangement,

$$\frac{dp}{dt} + \left[\frac{\frac{\partial e}{\partial v}\Big|_{p,Y} + p}{\frac{\partial e}{\partial p}\Big|_{v,Y}}\right]\frac{dv}{dt} + \left[\frac{\frac{\partial e}{\partial Y_i}\Big|_{p,v}}{\frac{\partial e}{\partial p}\Big|_{v,Y}}\right] r_i = 0. \tag{F.4}$$

where the variables held constant in each partial derivative are denoted as a subscript following the unmatched right hand $|$. Holding the mass fractions constant will be denoted by an undecorated subscript Y.

To clarify the bracketed thermodynamic quantities appearing in Eq. (F.4), one may also introduce the sound speed and thermicity. The first such quantity is readily identifiable as $\rho^2 c^2$, where c is the frozen sound speed. Frozen quantities are calculated for a set of constant mass fractions. They are in general different than values calculated at thermodynamic equilibrium. The second serves to define

the thermicity, $\sigma_i r_i$, according to

$$\frac{\left.\frac{\partial e}{\partial Y_i}\right|_{p,v}}{\left.\frac{\partial e}{\partial p}\right|_{v,Y}} = -\left.\frac{\partial P}{\partial Y_i}\right|_{v,e} = -\rho c^2 \sigma_i.$$

The thermicity coefficients, σ_i, are developed in detail in Appendix E. From this work, $\sigma_i r_i$ is seen to be "related to the net rate at which chemical bond energy is released to the flow by chemical reaction [19, pg. 101]".

Substituting these parameters into Eq. (F.4), the energy equation becomes

$$\frac{dp}{dt} + \rho^2 c^2 \frac{dv}{dt} - \rho c^2 \sigma_i r_i = 0.$$

As a final step, $v = 1/\rho$ is used to write everything in terms of ρ. This gives

$$\frac{dp}{dt} - c^2 \frac{d\rho}{dt} = \rho c^2 \sigma_i r_i \qquad \text{along} \qquad \frac{dx}{dt} = u,$$

or equivalently

$$\frac{\partial p}{\partial t} + u\frac{\partial p}{\partial x} - c^2\left(\frac{\partial \rho}{\partial t} + u\frac{\partial \rho}{\partial x}\right) = \rho c^2 \sigma_i r_i. \tag{F.5}$$

F.2 Characteristic form

Thus, characteristics of Eq. (C.3) are sought using the reduced system

$$\begin{aligned}
\frac{\partial \rho}{\partial t} + u\frac{\partial \rho}{\partial x} + \rho\frac{\partial u}{\partial x} &= 0, \\
\left(\frac{\partial u}{\partial t} + u\frac{\partial u}{\partial x}\right) + v\frac{\partial p}{\partial x} &= 0, \\
\frac{\partial p}{\partial t} + u\frac{\partial p}{\partial x} - c^2\left(\frac{\partial \rho}{\partial t} + u\frac{\partial \rho}{\partial x}\right) &= \rho c^2 \sigma_i r_i,
\end{aligned}$$

which may be written as

$$\begin{pmatrix} 1 & 0 & 0 \\ 0 & 1 & 0 \\ -c^2 & 0 & 1 \end{pmatrix} \begin{pmatrix} \frac{\partial \rho}{\partial t} \\ \frac{\partial u}{\partial t} \\ \frac{\partial p}{\partial t} \end{pmatrix} + \begin{pmatrix} u & \rho & 0 \\ 0 & u & 1/\rho \\ -c^2 u & 0 & u \end{pmatrix} \begin{pmatrix} \frac{\partial \rho}{\partial x} \\ \frac{\partial u}{\partial x} \\ \frac{\partial p}{\partial x} \end{pmatrix} = \begin{pmatrix} 0 \\ 0 \\ \rho c^2 \sigma_i r_i \end{pmatrix}.$$

This is of the form $A_{ij}\frac{\partial u_j}{\partial t} + B_{ij}\frac{\partial u_j}{\partial x} = C_i$ where $u_j = (\rho, u, p)^T$ [71, pp. 113ff.]. Linear combinations of the above equations are sought such that total derivatives along characteristic directions can be found. Such linear combinations are formed by multiplying by an unknown vector l_i such that

$$l_i A_{ij}\frac{\partial u_j}{\partial t} + l_i B_{ij}\frac{\partial u_j}{\partial x} = l_i C_i \tag{F.6}$$

can be written as

$$m_j\left(\frac{\partial u_j}{\partial t} + k\frac{\partial u_j}{\partial x}\right) = l_i C_i \qquad \text{or} \qquad m_j\frac{du_j}{dt} = l_i C_i \tag{F.7}$$

along $\frac{dx}{dt} = k$. Comparison of Eqs. (F.6) and (F.7) gives the constraints $l_i A_{ij} = m_j$ and $l_i B_{ij} = k m_j$ which can be combined to give $k l_i A_{ij} = l_i B_{ij}$. Rearrangement gives

$$l_i\left(kA_{ij} - B_{ij}\right) = 0, \tag{F.8}$$

which is reminiscent of the eigen-problem. Non-trivial solutions to Eq. (F.8) exist only for $|kA_{ij} - B_{ij}| = 0$.

For the case of the Euler equations with reaction, Eq. (F.8) becomes

$$\begin{pmatrix} l_1 & l_2 & l_3 \end{pmatrix} \begin{pmatrix} k-u & -\rho & 0 \\ 0 & k-u & -\frac{1}{\rho} \\ -c^2(k-u) & 0 & k-u \end{pmatrix} = \begin{pmatrix} 0 & 0 & 0 \end{pmatrix}.$$

Thus, setting

$$\begin{vmatrix} k-u & -\rho & 0 \\ 0 & k-u & -\frac{1}{\rho} \\ -c^2(k-u) & 0 & k-u \end{vmatrix} = 0,$$

we find our characteristic directions to be

$$\begin{aligned} k &= u, \\ k &= u + c, \qquad \text{and} \\ k &= u - c. \end{aligned} \tag{F.9}$$

The case $k = u$ is obviously associated with Eq. (C.3c) and has the trivial vector $l_i = \begin{pmatrix} 0 & 0 & 1 \end{pmatrix}$ associated with it. For $k = u \pm c$, Eq. (F.8) becomes

$$\begin{pmatrix} l_1 & l_2 & l_3 \end{pmatrix} \begin{pmatrix} \pm c & -\rho & 0 \\ 0 & \pm c & -\frac{1}{\rho} \\ \mp c^3 & 0 & \pm c \end{pmatrix} = \begin{pmatrix} 0 & 0 & 0 \end{pmatrix}$$

for which a solution is $l_i = \begin{pmatrix} c^2 & \pm\rho c & 1 \end{pmatrix}$. Substituting for l_i in Eq. (F.7), with $m_j = l_i A_{ij}$, gives

$$\pm\rho c \left(\frac{\partial u}{\partial t} + (u \pm c)\frac{\partial u}{\partial x} \right) + \left(\frac{\partial \rho}{\partial t} + (u \pm c)\frac{\partial u}{\partial x} \right) = \rho c^2 \sigma_i r_i.$$

Thus our final characteristic form of the Euler equations with reaction are:

$$\rho c \frac{du}{dt} + \frac{d\rho}{dt} = \rho c^2 \sigma_i r_i \qquad \text{on} \qquad \frac{dx}{dt} = u + c, \tag{F.10a}$$

$$-\rho c \frac{du}{dt} + \frac{d\rho}{dt} = \rho c^2 \sigma_i r_i \qquad \text{on} \qquad \frac{dx}{dt} = u - c, \tag{F.10b}$$

$$\frac{dp}{dt} - c^2 \frac{d\rho}{dt} = \rho c^2 \sigma_i r_i \qquad \text{on} \qquad \frac{dx}{dt} = u, \tag{F.10c}$$

$$\frac{dY_i}{dt} = r_i \qquad \text{on} \qquad \frac{dx}{dt} = u. \tag{F.10d}$$

APPENDIX G

RANKINE–HUGONIOT JUMP CONDITIONS

The Rankine–Hugoniot jump conditions are those which must hold across a discontinuity in an Eulerian flow. They are found by application of Eq. (4.8) to Eq. (C.1).

$$\mathbf{F} = \rho \quad \text{and} \quad \mathbf{T}^i = \mathbf{0} \quad \rightarrow \quad \left[\!\left[-\rho \bar{v}^i\right]\!\right] \nu_i = 0, \tag{G.1a}$$

$$\mathbf{F} = \rho v^i \quad \text{and} \quad \mathbf{T}^i = -p g^{ji} \quad \rightarrow \quad \left[\!\left[-\rho(\bar{v}^i + D^i)\bar{v}^j - p g^{ji}\right]\!\right] \nu_j = 0, \tag{G.1b}$$

$$\mathbf{F} = E \quad \text{and} \quad \mathbf{T}^i = -p v^i \quad \rightarrow \quad \left[\!\left[-E\bar{v}^i - (\bar{v}^i + D^i)p\right]\!\right] \nu_i = 0, \tag{G.1c}$$

$$\mathbf{F} = \rho Y_{(i)} \quad \text{and} \quad \mathbf{T}^i = \mathbf{0} \quad \rightarrow \quad \left[\!\left[-\rho Y_{(i)} \bar{v}^j\right]\!\right] \nu_j = 0, \tag{G.1d}$$

where $E = \rho(e + 1/2 v^j v_j)$ is the total energy per unit volume and $\bar{v}^i$ again represents the velocity relative to the shock surface.

In order to simplify the following analysis, it is useful to assume an orthogonal coordinate system which has one basis vector co-linear with ν_i. Thus, in this coordinate system,

$$\nu_i = \begin{pmatrix} 1 \\ 0 \\ 0 \end{pmatrix} \quad \text{and} \quad \bar{v}^i = \begin{pmatrix} \bar{u} \\ \bar{v} \\ \bar{w} \end{pmatrix}. \tag{G.2}$$

G.1 Mass jump condition

Substitution of Eqs. (G.2) into Eq. (G.1a) gives

$$\left[\!\left[-\rho\bar{u}\right]\!\right] = 0. \tag{G.3}$$

G.2 Momentum jump condition

Writing out the momentum jump condition, Eq. (G.1b), gives

$$\begin{aligned}\left[\!\left[-\rho\bar{v}^i\bar{v}^j - pg^{ji} - \rho D^i\bar{v}^j\right]\!\right]\nu_j &= 0,\\ \left[\!\left[-\rho\bar{v}^i\bar{v}^j - pg^{ji}\right]\!\right]\nu_j + D^i\underbrace{\left[\!\left[-\rho\bar{v}^j\right]\!\right]\nu_j}_{=0 \text{ from Eq. (G.1a)}} &= 0.\end{aligned}$$

Thus, a final general form of the momentum jump condition is given by

$$\left[\!\left[-\rho\bar{v}^i\bar{v}^j - pg^{ji}\right]\!\right]\nu_j = 0. \tag{G.4}$$

which is a vector equation. Substitution of Eqs. (G.2) into Eq. (G.4) yields

$$\left[\!\left[-\rho\bar{v}^i\bar{u} - p\nu^i\right]\!\right] = 0.$$

In the normal direction this gives

$$\left[\!\left[-\rho\bar{u}^2 - p\right]\!\right] = 0. \tag{G.5}$$

Consideration of the other two components of the momentum jump condition

is also revealing and yields

$$[\![\bar{v}]\!] = 0 \qquad \text{and} \qquad [\![\bar{w}]\!] = 0 \tag{G.6}$$

which states that *velocity components tangent to a shock wave in Eulerian flow are constant across the shock.*

G.3 Energy jump condition

The energy jump condition is given by Eq. (G.1c) and may be simplified to

$$\begin{aligned}
[\![-E\bar{v}^i - (\bar{v}^i + D^i)p]\!]\,\nu_i &= 0, \\
[\![-\rho\bar{v}^i(e + |\bar{v}^k + D^k|^2/2) - (\bar{v}^i + D^i)p]\!]\,\nu_i &= 0, \\
[\![-\rho\bar{v}^i(e + \bar{v}^k\bar{v}_k/2) - \bar{v}^i p - \rho\bar{v}^i(\bar{v}^k D_k + D^k D_k/2) - D^i p]\!]\,\nu_i &= 0, \\
[\![-\rho\bar{v}^i(e + \bar{v}^k\bar{v}_k/2 + p/\rho)]\!]\,\nu_i + D^k D_k/2\,[\![-\rho\bar{v}^i]\!]\,\nu_i + D_k\,[\![-\rho\bar{v}^i\bar{v}^k - pg^{ki}]\!]\,\nu_i &= 0,
\end{aligned}$$

where the second two jump terms are identically 0 from Eqs. (G.1a) and (G.4).

Substitution of Eqs. (G.2) for ν_i and $\bar{v}^i$ yields

$$[\![-\rho\bar{u}(e + \bar{u}^2/2 + p/\rho)]\!] = 0.$$

Since $[\![\rho\bar{u}]\!] = 0$ from Eq. (G.3), the energy jump condition reduces to

$$[\![e + \bar{u}^2/2 + p/\rho]\!] = 0. \tag{G.7}$$

G.4 Species jump condition

Substitution of Eqs. (G.2) into Eq. (G.1d) gives

$$\left[\!\left[\rho Y_{(i)}\bar{u}\right]\!\right] = 0;$$

however, simplification again by way of Eq. (G.3) gives $\left[\!\left[Y_{(i)}\right]\!\right] = 0$. Thus, the shock wave does not cause a jump in the mass fractions of the fluid mixture.

G.5 Normal shock relations

The jump condition can be made more explicit by writing out the jump operator for each of Eqs. (G.3),(G.5),(G.7),and (G.1d). Distinguishing the limiting value of the properties on one side of the shock with a subscript o, the jump conditions become

$$\rho\bar{u} = \rho_o\bar{u}_{o,} \tag{G.8a}$$

$$\rho\bar{u}^2 + p = \rho_o\bar{u}_o^2 + p_o, \tag{G.8b}$$

$$e + \frac{\bar{u}^2}{2} + \frac{p}{\rho} = e_o + \frac{\bar{u}_o^2}{2} + \frac{p_o}{\rho_o}, \tag{G.8c}$$

$$Y_i = Y_{io}. \tag{G.8d}$$

Eqs. (G.8a), (G.8b), and (G.8c) describe the jump in mass, momentum, energy across the shock for an unsteady Eulerian flow where $\bar{u}$ is the velocity normal to the shock surface

G.6 Rayleigh–Hugoniot analysis

In the majority of cases, the upstream thermodynamic state and velocity are known, and the state of the fluid downstream of the shock wave is desired. For such problems, Rayleigh-Hugoniot analysis has been developed. This analysis seeks solutions to the system of nonlinear jump conditions by examination of solution trajectories in the (v, p) plane. Here, v is the specific volume, $v = \rho^{-1}$.

In the following derivation, tensorial indices no longer appear, and parentheses around subscripts are no longer necessary. Quantities denoted with a subscript o are considered to be known, and the corresponding values across the shock are sought.

G.6.1 The Rayleigh line

The Rayleigh line is found by eliminating $\bar{u}$ in Eq. (G.8b) using Eq. (G.8a). Rearrangement and elimination of density in favor of specific volume gives

$$p = p_o - \rho_o^2 \bar{u}_o^2 \left(v - v_o\right), \tag{G.9}$$

which is a line in (v, p) space which represents momentum conservation. Given a known r state, the jumped state is a point on this line.

G.6.2 The Hugoniot curve

To derive the Hugoniot curve, first $\bar{u}$ is eliminated from Eq. (G.8c) using Eq. (G.8a). This gives, after rearrangement,

$$e - e_o = -\frac{1}{2}\bar{u}_o^2 \left(\frac{(\rho_o - \rho)(\rho_o + \rho)}{\rho^2}\right) + \frac{p_o}{\rho_o} - \frac{p}{\rho}.$$

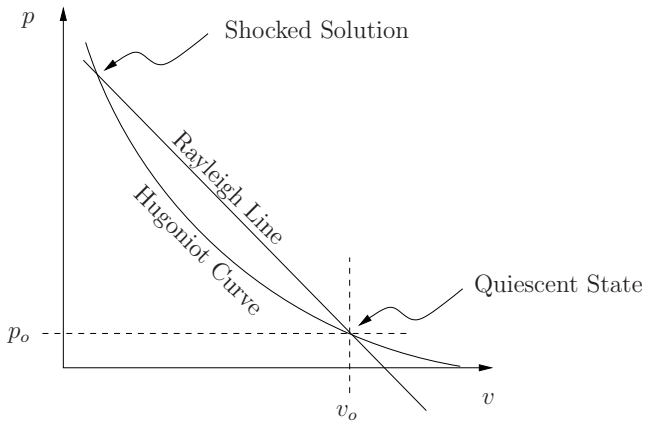

Figure G.1. Rayleigh-Hugoniot solution.

Now $\bar{u}_o^2$ is eliminated using Eq. (G.9) to give

$$e - e_o = -\frac{1}{2}\frac{p_o - p}{\rho_o^2}\left(\frac{1}{\rho} - \frac{1}{\rho_o}\right)^{-1}\left(\frac{(\rho_o - \rho)(\rho_o + \rho)}{\rho^2}\right) + \frac{p_o}{\rho_o} - \frac{p}{\rho}.$$

Simplification leads to

$$\begin{aligned} e - e_o &= -\frac{1}{2}\frac{p_o - p}{\rho_o \rho}(\rho_o + \rho) + \frac{p_o}{\rho_o} - \frac{p}{\rho}, \\ &= -\frac{1}{\rho}\left(\frac{p_o - p}{2} + p\right) - \frac{1}{\rho_o}\left(\frac{p_o - p}{2} + p_o\right). \end{aligned}$$

Thus the final form of this energy difference is given by

$$e - e_o = -\frac{p + p_o}{2}(v - v_o), \tag{G.10}$$

where specific volume has been used in place of density. Eq. (G.10) states that the change in internal energy is equal to minus the average pressure times the

change in specific volume.

Eq. (G.10) gives energy as a function of specific volume and pressure. To find a curve is (v, p) space, another expression for $e(v, p)$ is needed. Here, the caloric equation of state, Eq. (D.6) is used. Since $Y_{(i)}$ is constant across the shock, the energy difference for a calorically perfect ideal gas is

$$e - e_o = \frac{1}{\gamma - 1} \left(pv - p_o v_o \right).$$

Setting this equal to Eq. (G.10) and solving for p gives

$$p = \frac{p_o \left(\frac{\gamma+1}{\gamma-1} v_o - v \right)}{\frac{\gamma+1}{\gamma-1} v - v_o}. \tag{G.11}$$

This is the Hugoniot curve. For a given γ and quiescent state, the correct shocked state solution is a point on this curve.

As a final note, the Hugoniot curve can be shown to be a hyperbola in (v, p) space. Addition of $\frac{\gamma-1}{\gamma+1}$ to both sides of Eq. (H.18) and rearrangement reveals

$$\left(\frac{p}{p_o} + \frac{\gamma - 1}{\gamma + 1} \right) \left(\frac{v}{v_o} - \frac{\gamma - 1}{\gamma + 1} \right) = \frac{4\gamma}{(\gamma + 1)^2},$$

which is the form of a scale rectangular hyperbola.

G.6.3 Geometric considerations and solutions

Eqs. (G.9) and (G.11) must both be satisfied at both the shocked solution and the quiescent state. Plotting these two curves in the (v, p) plane provides a geometric visualization to such solutions and is seen in Fig. G.1.

An analytic solution to Eqs. (G.9) and (G.11) is possible. Setting the two

equations equal yields a quadratic equation in v which may be solved to give

$$v = v_o \frac{\gamma - 1}{\gamma + 1} \left(1 + \frac{2}{\gamma - 1} \frac{\gamma p_o}{u_o^2 \rho_o} \right) \tag{G.12}$$

at the shocked state. Having found v, it is a simple matter to find p and u at the shocked state by Eq. (G.11) and Eq. (G.4).

G.7 The shock polar equations

The shock polar equations describe oblique shock behavior in a two-dimensional Eulerian flow. All of the results derived thus far remain valid and may be used. A schematic showing the geometry involved in this problem is shown in Fig. G.2. The shock curve, denoted Σ, and a streamline are shown, as is an orthogonal coordinate system with x^1 co-linear with ν_i. From Eq. (G.6) it is clear that the component of velocity tangent to Σ will remain constant through the shock; thus, $\bar{v} = \bar{v}_o$. The velocity component normal to Σ however will suffer a jump as it crosses Σ which gives rise to a sharp streamline deflection.

As the streamline intersects Σ at an angle ϕ to the shock normal, it becomes deflected by an angle δ. A relationship is sought between these two angles, as well as the appropriate jump conditions parameterized in terms of these angles.

G.7.1 $\delta = f(\phi)$

The jump conditions across Σ for mass, momentum, energy, and species are given by Eq. (G.8). Similarly, the Rayleigh-Hugoniot analysis remains applicable. Thus, Eq. (G.12) may be used to immediately arrive at an expression for the ratio

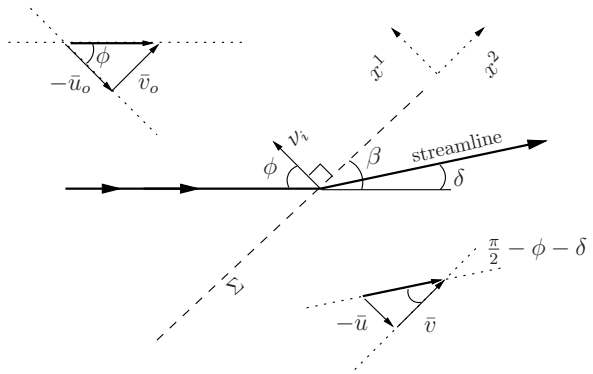

Figure G.2. Oblique shock geometry.

of specific volumes between the two states:

$$\frac{v}{v_o} = \frac{\gamma - 1}{\gamma + 1}\left(1 + \frac{2}{\gamma - 1}\frac{1}{M_n^2}\right) \tag{G.13}$$

where

$$M_n^2 = \frac{\bar{u}_o^2}{c}$$

is the Mach number normal to the shock surface with sound speed c. Eq. (G.8a) says that the ratio of the specific volumes is equal to the ratio of velocities; thus Eq. (G.13) becomes

$$\frac{\bar{u}}{\bar{u}_o} = \frac{\gamma - 1}{\gamma + 1}\left(1 + \frac{2}{\gamma - 1}\frac{1}{M_n^2}\right). \tag{G.14}$$

Now this ratio of velocities is directly related to the angles ϕ and δ by trigonometry. From Fig. G.2, one sees that

$$\tan\left(\frac{\pi}{2} - \phi - \delta\right) = \frac{-\bar{u}}{\bar{v}} \qquad \text{and} \qquad \tan\phi = \frac{\bar{v}_o}{-\bar{u}_o}. \tag{G.15}$$

Since $\bar{v}_o = \bar{v}$, multiplying these equations together gives

$$\frac{\bar{u}}{\bar{u}_o} = \tan\left(\frac{\pi}{2} - \phi - \delta\right)\tan\phi.$$

If $\beta = \frac{\pi}{2} - \phi$, then

$$\frac{\bar{u}}{\bar{u}_o} = \frac{\tan(\beta - \delta)}{\tan\beta}, \tag{G.16}$$

since $\tan(\frac{\pi}{2} - \beta) = \cot\beta$.

Setting Eqs. (G.14) and (G.16) equal to one another gives

$$\frac{\tan(\beta - \delta)}{\tan\beta} = \frac{\gamma - 1}{\gamma + 1}\left(1 + \frac{2}{\gamma - 1}\frac{1}{M_n}\right). \tag{G.17}$$

Furthermore,

$$M_n^2 = \frac{\bar{u}_o^2}{c^2} \qquad \text{and} \qquad M^2 = \frac{\bar{u}_o^2 + \bar{v}_o^2}{c^2}.$$

The ratio of these Mach numbers is simply

$$\begin{aligned} \frac{M^2}{M_n^2} &= \frac{\bar{u}_o^2 + \bar{v}_o^2}{\bar{u}_o^2}, \\ &= 1 + \frac{\bar{v}_o^2}{\bar{u}_o^2}, \\ &= 1 + \frac{1}{\tan^2\beta}, \\ &= \frac{1}{\sin^2\beta}. \end{aligned} \tag{G.18}$$

Thus, Eq. (G.17) becomes

$$\begin{aligned}\frac{\tan(\beta-\delta)}{\tan\beta} &= \frac{\gamma-1}{\gamma+1}\left(1+\frac{2}{\gamma-1}\frac{1}{M^2\sin^2\beta}\right),\\ &= \frac{\gamma-1}{\gamma+1}\left(\frac{(\gamma-1)M^2\sin^2\beta+2}{(\gamma-1)M^2\sin^2\beta}\right),\\ &= \frac{(\gamma-1)M^2\sin^2\beta+2}{(\gamma+1)M^2\sin^2\beta}.\end{aligned} \tag{G.19}$$

Multiplying Eq. (G.19) by $\tan\beta$ and substituting $\tan(\beta-\delta) = \frac{\tan\beta-\tan\delta}{1+\tan\beta\tan\delta}$ gives

$$\frac{\tan\beta-\tan\delta}{1+\tan\beta\tan\delta} = \tan\beta\frac{(\gamma-1)M^2\sin^2\beta+2}{(\gamma+1)M^2\sin^2\beta} \equiv \chi.$$

Solving for $\tan\delta$ and rearrangement yields

$$\begin{aligned}\tan\delta &= \frac{\tan\beta-\chi}{1+\chi\tan\beta},\\ &= \frac{\tan\beta-\tan\beta\frac{(\gamma-1)M^2\sin^2\beta+2}{(\gamma+1)M^2\sin^2\beta}}{1+\tan^2\beta\frac{(\gamma-1)M^2\sin^2\beta+2}{(\gamma+1)M^2\sin^2\beta}},\\ &= \frac{\tan\beta(\gamma+1)M^2\sin^2\beta-\tan\beta(\gamma-1)M^2\sin^2\beta-2\tan\beta}{(\gamma+1)M^2\sin^2\beta+\tan^2\beta(\gamma-1)M^2\sin^2\beta+2\tan^2\beta},\\ &= \frac{2\tan\beta M^2\sin^2\beta-2\tan\beta}{M^2\sin^2\beta((\gamma+1)+\tan^2\beta(\gamma-1))+2\tan^2\beta},\\ &= 2\tan\beta\frac{M^2\sin^2\beta-1}{M^2\sin^2\beta(\gamma(1+\tan^2\beta)+1-\tan^2\beta)+2\tan^2\beta}.\end{aligned}$$

Substituting the identities $1-\tan^2\beta = \frac{\cos(2\beta)}{\cos^2\beta}$ and $\tan^2\beta+1 = \frac{1}{\cos^2\beta}$ into this expression gives

$$\begin{aligned}\tan\delta &= \frac{2\tan\beta}{\tan^2\beta}\frac{M^2\sin^2\beta-1}{M^2(\gamma+\cos(2\beta))+2},\\ &= 2\cot\beta\frac{M^2\sin^2\beta-1}{M^2(\gamma+\cos(2\beta))+2}.\end{aligned}$$

Finally removing β in favor of ϕ yields a succinct expression for δ as a function of ϕ:

$$\delta = \arctan\left(2\tan\phi\frac{M^2\cos^2\phi - 1}{M^2(\gamma - \cos(2\phi)) + 2}\right). \tag{G.20}$$

G.7.2 $p = f(\phi)$

In order to find pressure as a function of the shock angle, the Hugoniot curve, Eq. (G.11), is used.

$$\begin{aligned}\frac{p}{p_o} &= \frac{\frac{\gamma+1}{\gamma-1}v_o - v}{\frac{\gamma+1}{\gamma-1}v - v_o},\\ &= \frac{\frac{\gamma+1}{\gamma-1} - \frac{v}{v_o}}{\frac{\gamma+1}{\gamma-1}\frac{v}{v_o} - 1}.\end{aligned}$$

Substituting Eq. (G.13) for the ratio of specific volumes gives

$$\begin{aligned}\frac{p}{p_o} &= \frac{\frac{\gamma+1}{\gamma-1} - \frac{\gamma-1}{\gamma+1}\left(1 + \frac{2}{(\gamma-1)M_n^2}\right)}{\frac{\gamma+1}{\gamma-1}\frac{\gamma-1}{\gamma+1}\left(1 + \frac{2}{(\gamma-1)M_n^2}\right) - 1},\\ &= \left(\frac{\gamma+1}{\gamma-1} - \frac{\gamma-1}{\gamma+1} - \frac{2}{(\gamma+1)M_n^2}\right)\frac{(\gamma-1)M_n^2}{2},\\ &= \frac{(\gamma+1)M_n^2}{2} - \frac{(\gamma-1)^2M_n^2}{2(\gamma+1)} - \frac{\gamma-1}{\gamma+1},\\ &= M_n^2\left(\frac{(\gamma+1)^2 - (\gamma-1)^2}{2(\gamma+1)}\right) - \frac{\gamma-1}{\gamma+1},\\ &= M_n^2\left(\frac{2\gamma}{\gamma+1}\right) - \frac{\gamma-1}{\gamma+1},\\ &= \frac{M_n^2 2\gamma - \gamma + 1}{\gamma+1}.\end{aligned}$$

Now, if γ is added and subtracted from the numerator, this gives

$$\begin{aligned}\frac{p}{p_o} &= \frac{\gamma+1+2\gamma M_n^2-2\gamma}{\gamma+1},\\ &= 1+\frac{2\gamma}{\gamma+1}\left(M_n^2-1\right).\end{aligned} \tag{G.21}$$

However, Eq. (G.18) gives M_n in terms of the true Mach number and β. Thus, the ratio of pressures across the oblique shock as a function of the incident shock angle is given by

$$\begin{aligned}\frac{p}{p_o} &= 1+\frac{2\gamma}{\gamma+1}\left(M^2\sin^2\beta-1\right),\\ &= 1+\frac{2\gamma}{\gamma+1}\left(M^2\cos^2\phi-1\right).\end{aligned} \tag{G.22}$$

G.8 The strong shock limit

In the strong shock limit, $p_o \to 0$ or $M \to \infty$. Thus, the shock polar equations, Eqs. (G.20) and (G.22), in this limit reduce to

$$\delta = \arctan\left(\frac{2\sin\phi\cos\phi}{\gamma+1-2\cos^2\phi}\right) \tag{G.23a}$$

and

$$\frac{p}{p_o} = \frac{2\gamma M^2\cos^2\phi}{\gamma+1}. \tag{G.23b}$$

G.9 Shock polar diagram

Having developed the shock polar equations, it is instructive to illustrate their behavior graphically. A typical shock polar diagram is show in Fig. G.3 where the mach number is held constant along each curve. For a given mach number and deflection angle, two possible shock angles exist. For the case of a zero deflection

angle, the two possible solutions are a normal shock or a mach wave where

$$\phi|_{\delta=0} = \begin{cases} 0 & \text{for a normal shock,} \\ \frac{\pi}{2} - \sin^{-1}\left(\frac{1}{M}\right) & \text{for a mach wave.} \end{cases}$$

The branch giving the mach wave solution is known as weak, while that giving the normal shock is strong. As the mach number increases, so does the deflection angle for a given shock angle, or the shock angle for a deflection angle.

The transition from the weak to the strong branch can be found by differentiating Eq. (G.20) with respect to ϕ and solving for the point of zero slope:

$$\phi = \cos^{-1}\left(\left(\frac{(\gamma+1)M^2 - 4}{4\gamma M^2} + \frac{\sqrt{(\gamma+1)\big((\gamma+1)^2M^4 + 8(\gamma-1)M^2 + 16\big)}}{4\gamma M^2}\right)^{\frac{1}{2}}\right). \quad \text{(G.24)}$$

This line is seen as a dotted line in Fig. G.3, separating the strong and weak branches of the shock polar.

Solutions are also classified according to the speed of the deflected flow relative to the shock. Such information determines the flow of information in solutions involving a shock, as in Section H.3. If the deflected flow is locally subsonic, disturbances may travel into and effect the shock; for supersonic outflow, no such interactions are possible. The sonic condition is given by

$$\frac{\bar{u}^2 + \bar{v}^2}{\gamma p v} = 1.$$

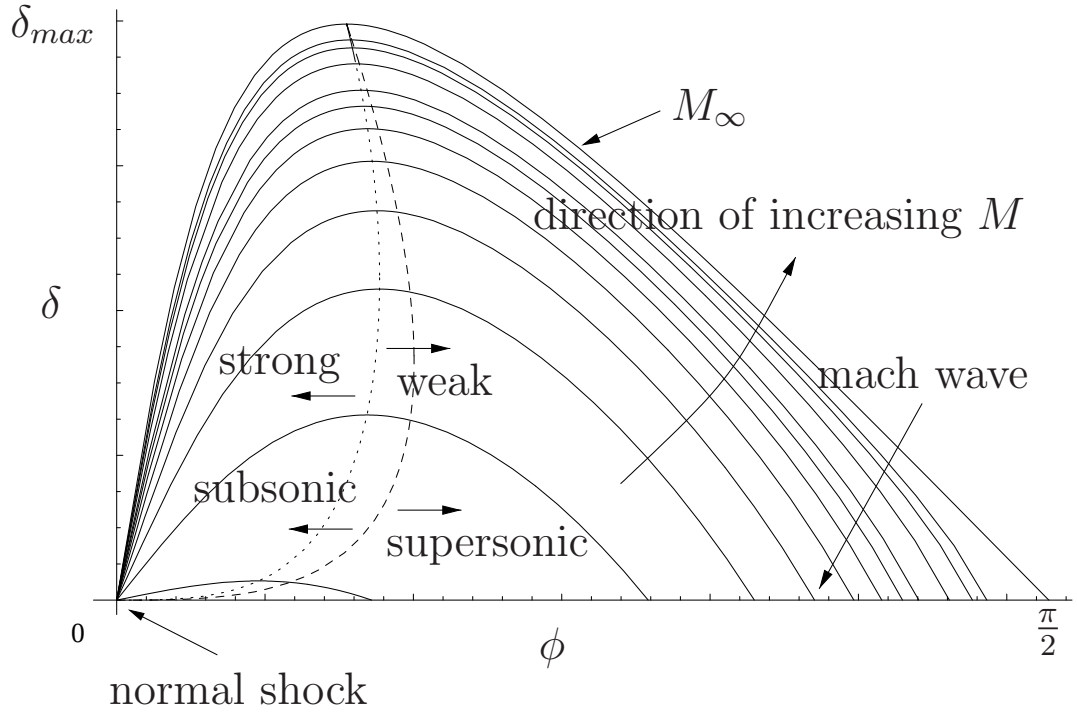

Figure G.3. General shock polar behavior.

Multiplying by unity in the form of $1 = \frac{p_o}{p_o} = \frac{v_o}{v_o} = \frac{u_o}{u_o}$ and simplifcation gives

$$\left(\frac{u_o}{c}\right)^2 \frac{\bar{u}}{\bar{u}_o}\left(1 + \frac{\bar{v}^2}{\bar{u}^2}\right) = \frac{p}{p_o}.$$

Recalling $M_n = \frac{\bar{u}_o}{c}$ and substituting Eqs. (G.14), (G.15), and (G.21) gives

$$M_n^2 \frac{\gamma - 1}{\gamma + 1}\left(1 + \frac{2}{\gamma - 1}M_n^{-2}\right)\left(1 + \tan^2\left(\frac{\pi}{2} - \phi - \delta\right)\right) = 1 + \frac{2\gamma}{\gamma + 1}\left(M_n^2 - 1\right).$$

Substituting for the deflection angle from Eq. (G.20) and for M_n fromEq. (G.18),

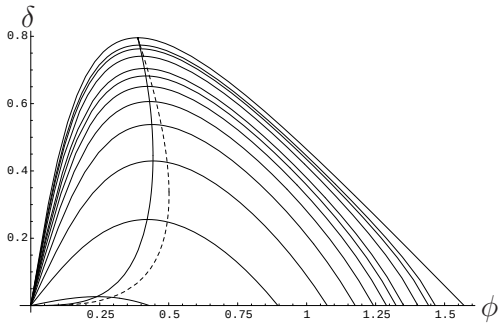

G.4.1: $\gamma = 1.4$

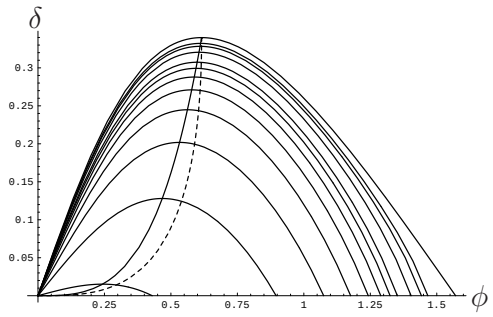

G.4.2: $\gamma = 3$

Figure G.4. Shock polars of varying M for a calorically perfect ideal gas.

the shock angle is for sonic flow if found to be

$$\phi = \cos^{-1}\left(\left(\frac{\gamma+1}{\gamma} + \frac{\gamma-3}{\gamma}M^{-2} + \frac{\sqrt{M^4(\gamma+1)\big((\gamma+1)M^4 + (2\gamma-6)M^2+9\big)}}{\gamma M^4}\right)^{\frac{1}{2}}\right). \quad \text{(G.25)}$$

This line is seen as a dashed line in Fig. G.3.

In the limit as $M \to \infty$, both Eqs. (G.24) and (G.25)

$$\phi = \cos^{-1}\left(\sqrt{\frac{\gamma+1}{2\gamma}}\right) \qquad \text{(strong shock limit)}, \quad \text{(G.26)}$$

giving the maximum possible deflection angle to be a sonic point. The domain of ϕ in this limit is extended to $\pi/2$.

The shock polars for a calorically perfect ideal gas are given in Fig. G.4 for $\gamma = 1.4$ and $\gamma = 3$, respectively. Increasing the ration of specific heats decreases the maximum achievable deflection. As before, all strong shocks yield subsonic flow

APPENDIX H

ZND ANALYSIS

In order to understand the basic structure of a steady traveling detonation wave, it is essential to have a working knowledge of the Zel'dovich-von Neumann-Doering model problem. This one-dimensional problem, known in the literature as the ZND problem, is important because it describes the relevant structures found in steady traveling detonation waves with a finite reaction rate where curvature effects are negligible. The authoritative reference on this problem is the work by Fickett and Davis [19].

A schematic of the ZND problem is shown in Fig. H.1. A shock wave propagates to the right at a constant speed D into a quiescent High Explosive (HE) material. The ZND analysis assumes the HE to be calorically perfect ideal gases (CPIG) with equal specific heats. As the shock wave passes, the HE jumps to an unreacted shocked state known as the von Neumann spike. A reaction then initiates in the shocked material causing heat release and a simultaneous pressure decrease. Two types of steady solutions are possible for flows involving a unimolecular reaction: either a self-propagating detonation wave or a detonation wave supported by a rear piston.

The governing equations for the ZND problem are the Euler equations with reaction. In one-dimension, these are given by in conservation form by Eqs. (C.2).

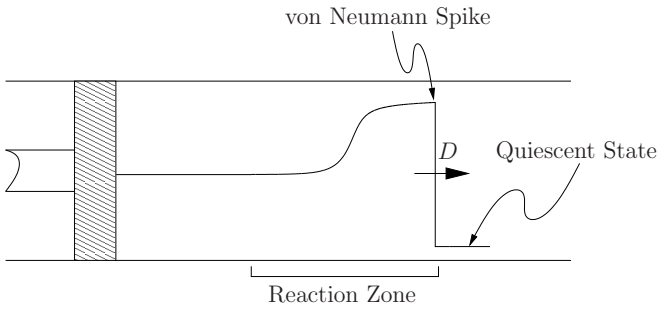

Figure H.1. ZND Problem.

Although the classical ZND problem assumes a single exothermic Arrhenius reaction, this analysis will consider a general multi-species system until a specific chemical kinetics scheme must be assumed in order to compute numerical solutions.

Using this simplified mathematical description, the Chapman-Jouguet (CJ) solution is found. The CJ solution is that of a self-propagating detonation wave without rear piston support. This solution is of primary importance and is used as the reference solution in much of the literature. Some weak detonation results are also presented to illustrate the behavior of the sonic locus in problems involving more complicated chemical kinetics, as well as in slightly divergent flows.

H.1 Steady wave frame solutions

Assuming a steady traveling wave with velocity D, the governing equations are found by transforming the Euler equations in conservative form to the steady

wave frame. This transformation is given by

$$\bar{x}(x,t) = x - Dt, \tag{H.1a}$$

$$\bar{t}(x,t) = t, \tag{H.1b}$$

where (x,t) is the physical space and $(\bar{x},\bar{t})$ is the steady wave frame. Differentiating Eq. (H.1a) with respect to time gives the velocity in the wave frame to be

$$\bar{u} = u - D. \tag{H.2}$$

Note that the proposed transformation given by Eqs. (H.1) is Galilean (i.e. the transformation involves a simple shift by a constant velocity). Thus, our governing equations will remain invariant under this transformation. Assuming that in this frame a steady solution exists, partial derivatives with respect to $\bar{t}$ are set to zero. Dropping parentheses around subscripts, Eqs. (C.2) become

$$\frac{d}{d\bar{x}}(\rho\bar{u}) = 0, \tag{H.3a}$$

$$\frac{d}{d\bar{x}}(p + \rho\bar{u}^2) = 0, \tag{H.3b}$$

$$\frac{d}{d\bar{x}}\left(\rho\bar{u}\left(e + \frac{1}{2}\bar{u}^2 + \frac{p}{\rho}\right)\right) = 0, \tag{H.3c}$$

$$\frac{d}{d\bar{x}}(\rho\bar{u}Y_i) = M\dot{\omega}_i. \tag{H.3d}$$

in the transformed coordinates.

Eqs. (H.3a), (H.3b), and (H.3d) can be integrated directly on either side of the

shock to give

$$\rho\bar{u} = C_1, \tag{H.4a}$$

$$p + \rho\bar{u}^2 = C_2, \tag{H.4b}$$

$$\rho\bar{u}\left(e + \frac{1}{2}\bar{u}^2 + \frac{p}{\rho}\right) = C_3, \tag{H.4c}$$

where C_1, C_2 and C_3 are constant. Since the material into which the shock wave propagates is at rest, this integrated form of the Euler equations is used to solve for the structure in the shocked, detonating material to the left of the shock wave.

Since the quiescent state is known and constant, only the properties of the shocked material must be determined by Eq. (H.4). The constants C_1, C_2, and C_3 are determined by the Rankine–Hugoniot jump conditions to be functions of the quiescent, unshocked material and the detonation wave speed.

H.1.1 The Rankine–Hugoniot jump conditions

These jump conditions for the Euler equations are derived in Appendix G. A schematic of the jump is shown in Fig. H.2. In the following analysis, a subscripts Σ and o refer to the variable values in the shocked and quiescent states, respectively.

Now the state to the right of the shock is quiescent with $u_o = 0$. Substitution into Eq. (H.2) gives

$$\bar{u}_o = -D. \tag{H.5}$$

Substitution of Eq. (H.5) into Eq. (G.8a) gives the mass jump condition:

$$\rho_\Sigma \bar{u}_\Sigma = -\rho_o D. \tag{H.6}$$

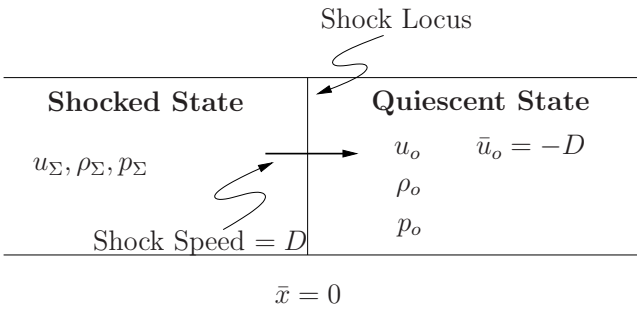

Figure H.2. ZND Transformed Problem.

The quantity $\rho_\Sigma \bar{u}_\Sigma$ is the momentum per unit volume of the material just after the shock wave has passed and acts as a boundary value for the continuum of shocked material. Thus, Eq. (H.6) is valid in the domain of Eq. (H.4a) and comparison gives $C_1 = -\rho_o D$.

Similarly, the momentum jump condition, Eq. (G.8b), becomes

$$\rho_\Sigma \bar{u}_\Sigma^2 + p_\Sigma = \rho_o D^2 + p_o. \tag{H.7}$$

Comparison with Eq. (H.4b) gives $C_2 = \rho_o D^2 + p_o$.

Lastly, the energy jump condition given by Eq. (G.8c) becomes

$$\rho_\Sigma \bar{u}_\Sigma \left(e_\Sigma + \frac{\bar{u}_\Sigma^2}{2} + \frac{p_\Sigma}{\rho_\Sigma} \right) = -\rho_o D \left(e_o + \frac{D^2}{2} + \frac{p_o}{\rho_o} \right),$$

after multiplying with Eq. (H.6). Comparison with Eq. (H.4c) gives $C_3 = -\rho_o D \left(e_o + \frac{D^2}{2} + \frac{p_o}{\rho_o} \right)$. The final form of the energy jump condition is given by substituting Eq. (H.5) into Eq. (G.8c) to give

$$e_\Sigma + \frac{\bar{u}_\Sigma^2}{2} + \frac{p_\Sigma}{\rho_\Sigma} = e_o + \frac{D^2}{2} + \frac{p_o}{\rho_o}. \tag{H.8}$$

Lastly, Eq. (G.8d) serves to demonstrate that the species mass fraction are constant across the jump:

$$Y_{i\Sigma} = Y_{io}. \tag{H.9}$$

Thus the mass, momentum, energy, and species jump conditions across a shock are given by Eqs. (H.6), (H.7), (H.8), and (H.9). One should also note that, although Eqs. (H.4) assume D to be constant, these jump conditions are valid for unsteady shock speeds.

H.1.2 Governing equations

Since the mass, momentum, and energy equations have been integrated, the only remaining differential equation is that governing the species mass fractions, Eqs. (H.3d). While the conservative form of the governing equations was convenient for derivation of the appropriate jump conditions, the non-conservative form of the species equation is the preferrable form for numerical integration, giving total derivatives of Y_i with respect to both $\bar{t}$ and $\bar{x}$.

Choosing the non-conservative form, species evolution is described by Eqs. (C.3d) with $r_i = \frac{M_i\dot{\omega}_i}{\rho}$ and $\frac{d}{dt} = \frac{\partial}{\partial t} + u\frac{\partial}{\partial x}$:

$$\frac{dY_i}{dt} = \frac{\partial Y_i}{\partial t} + u\frac{\partial Y_i}{\partial x} = \frac{M_i\dot{\omega}_i}{\rho}.$$

Again, these equations are invariant under the transformation given by Eqs. (H.1). Thus,

$$\frac{dY_i}{d\bar{t}} = \frac{\partial Y_i}{\partial \bar{t}} + \bar{u}\frac{\partial Y_i}{\partial \bar{x}} = \frac{M_i\dot{\omega}_i}{\rho}$$

describes species evolution in the wave frame. Assuming the solution is steady in

this frame requires $\frac{\partial}{\partial \bar{t}} = 0$ and gives

$$\frac{dY_i}{d\bar{t}} = \bar{u}\frac{dY_i}{d\bar{x}} = \frac{M_i\dot{\omega}_i}{\rho}, \tag{H.10}$$

where $\frac{d}{dt}$ represents the derivative following a fluid particle and $\frac{d}{d\bar{x}}$ represents the derivative at a position in the steady traveling wave frame.

Having found the C_i in Eq. (H.4) and rewritten the species equation, the final form of the transformed, steady Euler equations with reaction are given by

$$\rho\bar{u} = -\rho_o D, \tag{H.11a}$$

$$\rho\bar{u}^2 + p = \rho_o D^2 + p_o, \tag{H.11b}$$

$$e + \frac{\bar{u}^2}{2} + \frac{p}{\rho} = e_o + \frac{D^2}{2} + \frac{p_o}{\rho_o}, \tag{H.11c}$$

$$\frac{dY_i}{d\bar{t}} = \frac{M_i\dot{\omega}_i}{\rho} \quad \text{with} \quad Y_i|_{\bar{x}=0} = Y_{io}, \tag{H.11d}$$

where Eq. (H.9) serves as the initial condition for Eq. (H.11d).

H.2 Rayleigh-Hugoniot analysis

Notice that Eqs. (H.11a), (H.11b), and (H.11c) govern the entire solution of the ZND structure problem and are identical to the Rankine–Hugoniot equations, Eqs. (G.8), which govern the flow at the shock surface. Thus a Rayleigh–Hugoniot analysis similar to that performed in Appendix G.6 is used to interpret Eqs. (H.11) in the (v, p) plane. Here, however, reaction must be considered: the mass fractions are not constant. This results in a family of Hugoniot curves, each one describing a different chemical composition. To incorporate the heat release due to reaction, the caloric equation of state must again be considered.

H.2.1 The Rayleigh line

First, the Rayleigh line is quickly re-presented, as it does not depend on the mass fractions. Eq. (G.9) with $\bar{u}_o^2 = D^2$ gives

$$p = p_o - \rho_o^2 D^2 (v - v_o). \tag{H.12}$$

As seen in Fig. H.3, this line in the (v, p) space is parameterized by the constant

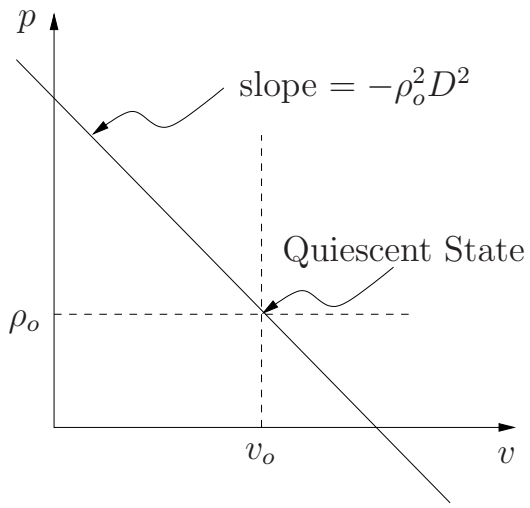

Figure H.3. Rayleigh line.

detonation speed D and the quiescent state. The slope is $-\rho_o^2 D^2$ and must be negative. All points in the (v, p) space which satisfy momentum conservation lie on this line. Thus, for a given value of D, our solution space is restricted to this line.

H.2.2 Energy change and heat release

The HE is assumed to be a CPIG mixture of N species and is described in Appendix D. The energy at the quiescent state is given by Eq. (D.5) evaluated with $T = T_o$ and the Y_i describing the initial mass fractions of the undetonated HE. If we further assume that the quiescent state is composed entirely of the first species, the quiescent mass fractions are given by $Y_1 = 1$ and $Y_i = 0$ for $i \neq 1$. Thus

$$e_o = h^0_{f,1} - c_p T_0 + c_v T_o. \tag{H.13}$$

Subtracting Eq. (H.13) from Eq. (D.5) gives

$$e - e_o = (Y_1 - 1)h^0_{f,1} + \sum_{i=2}^{N} Y_i h^0_{f,i} + c_v(T - T_o).$$

Since the mass fractions must sum to unity,

$$Y_1 - 1 = -\sum_{i=2}^{N} Y_i.$$

Thus

$$e - e_o = -\sum_{i=2}^{N} Y_i(h^0_{f,1} - h^0_{f,i}) + c_v(T - T_o). \tag{H.14}$$

To arrive at a form of this energy difference in terms of v and p, the ideal gas law is used to replace T:

$$e - e_o = -Q + \frac{c_v}{R}(pv - p_o v_o),$$

where

$$Q = \sum_{i=2}^{N} Y_i(h^0_{f,1} - h^0_{f,i}) \tag{H.15}$$

represents the total heat released by reaction for a particular set of mass fractions. Furthermore $\frac{c_v}{R} = \frac{1}{\gamma - 1}$, where $\gamma = \frac{c_p}{c_v}$. Thus our final form of the energy difference from the caloric equation of state is

$$e - e_o = -Q + \frac{1}{\gamma - 1}(pv - p_o v_o). \tag{H.16}$$

Having formulated the caloric equation of state such that an expression for $e(v, p)$ is known, the Hugoniot curve can now be developed.

H.2.3 The Hugoniot curve

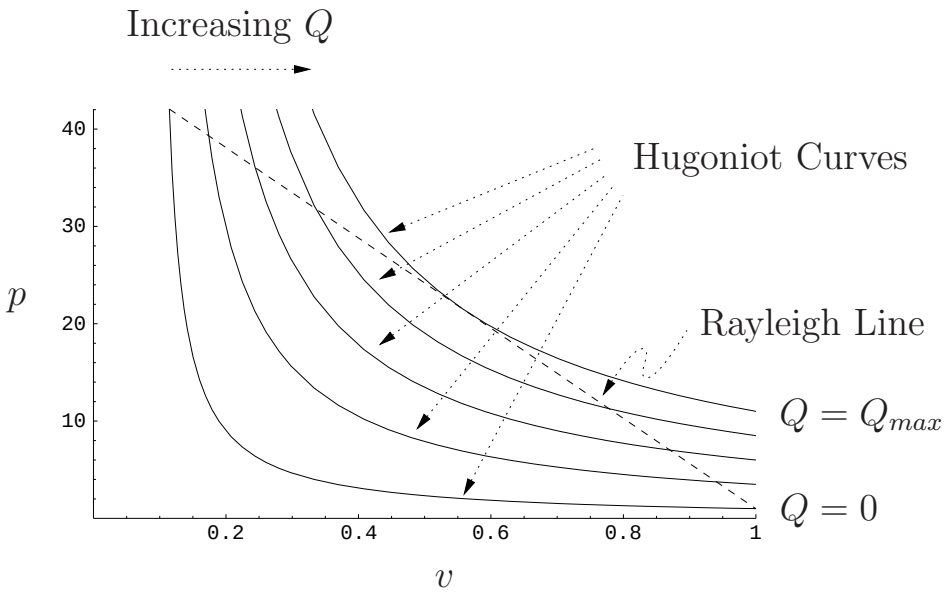

Figure H.4. Hugoniot curves parameterized by Q.

The development of the Hugoniot curve is the same as that given in Appendix G.6.2 up until Eq. (G.10):

$$e - e_o = -\frac{p + p_o}{2}(v - v_o). \tag{H.17}$$

Now, however, the equation of state describing the reacting HE is given by Eq. (H.16). Setting Eq. (H.17) equal to Eq. (H.16) and solving for p gives

$$p = \frac{2Q + p_o\left(\frac{\gamma+1}{\gamma-1}v_o - v\right)}{\frac{\gamma+1}{\gamma-1}v - v_o}. \tag{H.18}$$

These are the Hugoniot curves. For a given γ and quiescent state, the Hugoniot curves are parameterized by Q which changes as reaction takes place. Thus, a family of Hugoniot curves is associated with a given detonation. This is seen in Fig. H.4. The points along these Hugoniot curves satisfy energy conservation.

As a final note, the family of Hugoniot curves can be shown to be a family of hyperbolas in the (v, p) space. Addition of $\frac{\gamma-1}{\gamma+1}p_o$ to both sides of Eq. (H.18) and rearrangement reveals

$$\left(\frac{p}{p_o} + \frac{\gamma-1}{\gamma+1}\right)\left(\frac{v}{v_o} - \frac{\gamma-1}{\gamma+1}\right) = \frac{\gamma-1}{\gamma+1}\frac{2Q}{p_o v_o} + \frac{4\gamma}{(\gamma+1)^2},$$

which is the form of a scaled rectangular hyperbola. As the parameter Q increases, the semi-major axis of the corresponding hyperbola increases as illustrated in Fig. H.4.

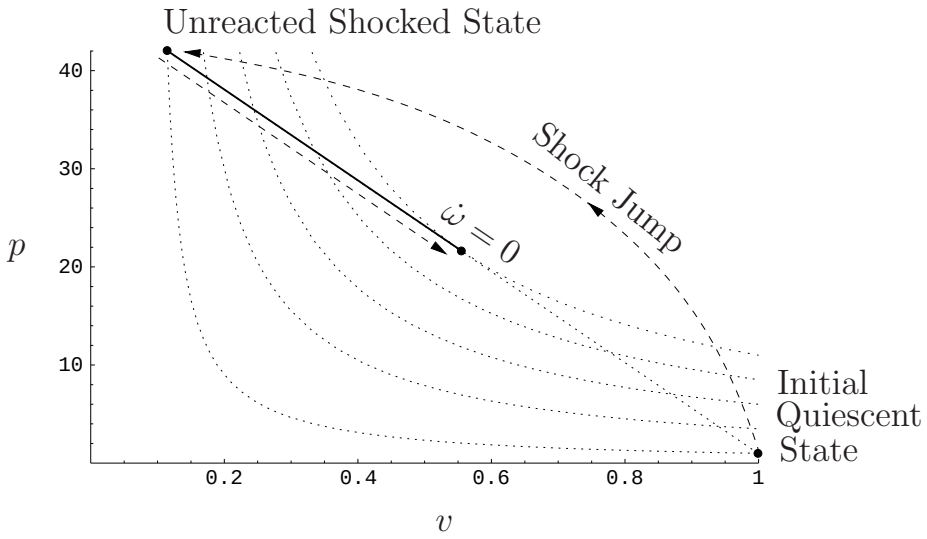

Figure H.5. ZND solution illustrated in the (v, p) plane.

H.2.4 Solutions in the (v, p) plane

Since both momentum and energy must be conserved, solutions to the ZND problem are restricted to points which intersect both the Rayleigh line and the appropriate family of Hugoniot curves. A typical (v, p) solution space is shown in Fig. H.4, where Q_{max} is the maximum possible heat release due to reaction. The $Q = 0$ and $Q = Q_{max}$ Hugoniot curves form the boundaries of the region to which solutions are constrained due to energy conservation. The Rayleigh line cuts across this region, further restricting the possible solutions.

The structure of the steady traveling reaction zone is found by considering the species equation. From Eq. (H.9), it is known that the mass fractions of the quiescent state and the state immediately following the shock are equal; thus, no reaction takes place through the discontinuity requiring $Q = 0$ across the shock. Since the Hugoniot curve is parameterized by Q alone, both the quiescent state

and the unreacted shocked state are given by the intersection of the Rayleigh line with the $Q = 0$ Hugoniot curve. This discontinuous change in in pressure and specific volume at the shock is seen in Fig. H.5.

This jump from the quiescent state to the unreacted shocked state is the only discontinuity in the system; all other solutions must be accessible by means of a continuous transformation along the Rayleigh line from the unreacted shocked state. In order for the reaction to go to completion, the Rayleigh line must intersect the Q_{max} Hugoniot curve. Since the Rayleigh line becomes steeper with increasing D, this given a minimum shock velocity such that the reaction is not prematurely quenched.

For the case of a unimolecular reaction, the point at which the Q_{max} and Hugoniot curves share a tangency condition gives the slowest moving steady detonation possible. This is the Chapman-Jouguet solution and is seen in Fig. H.5. From the unreacted shock state, the solution travels along the Rayleigh line until it intersects the Q_{max} Hugoniot curve. Other solutions besides the CJ solution exist for detonation traveling faster than D_{cj} and are known as over-driven solutions. For a complete discussion, see Fickett and Davis [19, pg. 141ff.].

H.2.5 D_{cj} behavior

By closing the system of equations given by Eqs. (H.11a), (H.11b), and (H.11c) with an equation of state, the behavior of the CJ velocity as a function of the quiescent state can be characterized for a particular material. Assuming a CPIG as described by Eq. (H.16), this relationship is

$$D_{cj}^2 = \gamma\frac{p_o}{\rho_o} + Q(\gamma^2-1) + \sqrt{Q(\gamma^2-1)\left(2\gamma\frac{p_o}{\rho_o} + Q(\gamma^2-1)\right)} \tag{H.19}$$

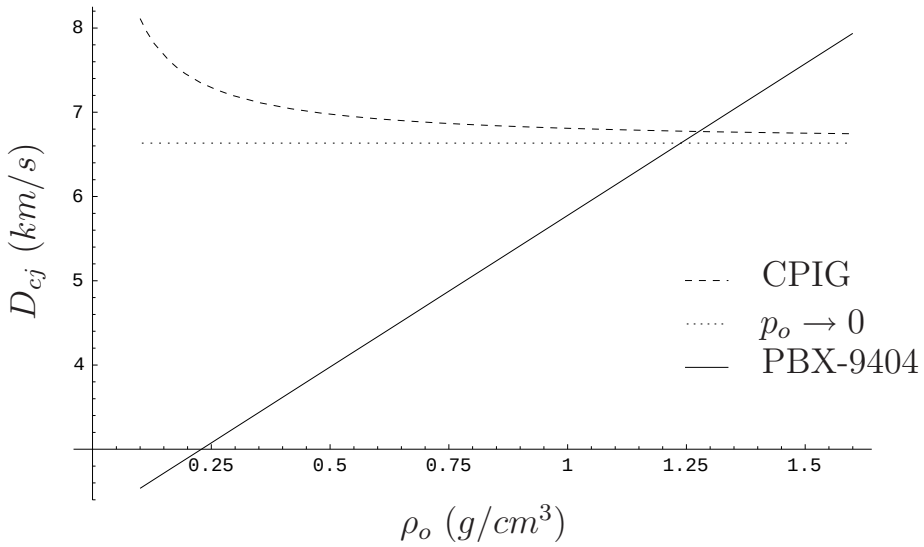

Figure H.6. D_{cj} as effected by density of quiescent HE. The CPIG shown is characterized by $\gamma = 1.2$, $Q = 50\ km^2/s^2$, $p_o = 1\ GPa$.

In the case of no heat release, $Q = 0$, Eq. (H.19) reduces to $D_{cj}^2 = \gamma \frac{p_o}{\rho_o}$; thus, disturbances simply propogate as acoustic waves. The strong shock limit is

$$\lim_{p_o \to 0} D_{cj}^2 = 2Q(\gamma^2 - 1). \tag{H.20}$$

Examples of Eqs. (H.19) and (H.20) are shown in Fig. H.6.

The equation of state for a CPIG allows for a simple analysis; although one which does not reproduce the behavior of solid HE materials well. This detonation velocity is seen to vary linearly with the initial density for most solid materials. Fig. H.6 illustrates this discrepancy between a CPIG and PBX-9404, a typical solid HE [17, pg. 124]. More complicated equations of state, usually known statistically in a narrow band around the Hugoniot curve, are used to describe real HE materials.

H.3 Characteristic considerations

Having made a preliminary analysis of the steady traveling wave solution in the (v, p) plane, it still remains to connect this solution to the corresponding characteristic analysis. Characteristics, as shown in Appendix F, are lines along which waves propagate. Thus, combining these two types of analysis yields important information about how information propagates in a steady solution.

It may seem that information propagation in a steady solution is a nonsensical notion; however, examination of Eq. (F.10) reveals that the information propagating along characteristics in reactive regions of the flow is, in general, not constant. Thus, while the overall wave form of the detonation is steady, the flow of information in the domain is non-trivial. Of primary importance is the information propagated along the $u + c$ characteristics given by Eq. (F.10a). This information will reveal how the reaction acts to support the detonation wave.

H.3.1 Sonic points

Before continuing to consider the structure of all such characteristics, it is useful to consider the special case of a $u + c$ characteristic which propagates at the same speed as the detonation wave itself.

Now $\frac{dx}{dt} = u + c$ defines the characteristic, while $\frac{dx}{dt} = D$ along the detonation front. Setting the two slopes equal and substituting for u from Eq. (H.2), $D = u+c$ becomes

$$-\bar{u} = c \tag{H.21}$$

in the transformed plane. Therefore, the flow in the steady wave frame is sonic at such points.

Since the wave speed at such positions is equal to the detonation speed, the

slope of the characteristics through these these positions in the $(\bar{x}, t)$ plane is vertical. Graphically this confirms that the characteristic direction of the detonation wave and the $u + c$ wave are the same.

In the transformed coordinates the solution at such positions is steady and the $u + c$ wave is stationary; thus, the total derivatives in the characteristic direction found in Eq. (F.10a) must be zero. Furthermore, since all the total derivatives in Eq. (F.10a) are zero,

$$\sigma_i r_i = 0$$

must be satisfied. In other words, at sonic points the rate of change of internal energy due to species creation is zero.

At this point, it may be anticipated that the point of tangency which determines the CJ solution, as seen in Appendix H.2.4, is a sonic point. The following consideration will prove that this is indeed the case.

H.3.2 The sonic locus

Such sonic points are instrumental in understanding the (v, p) plane. In this plane, the locus of all points at which the flow is sonic is called the sonic locus. Such points can be found by considering isentropes, Rayleigh lines, and Hugoniot curves.

The frozen sound speed is defined along an isentrope according to

$$\left.\frac{\partial p}{\partial \rho}\right|_{s,Y} = c^2 \qquad \text{or} \qquad \left.\frac{\partial p}{\partial v}\right|_{s,Y} = -\rho^2 c^2. \tag{H.22}$$

Thus the slope along an isentrope in the (v, p) plane is simply $-\rho^2 c^2$. Examination

of Eq. (H.12) gives the slope of a Rayleigh to be

$$\frac{dp}{dv} = -\rho_o^2 D^2, \tag{H.23a}$$

$$= \frac{p - p_o}{v - v_o}. \tag{H.23b}$$

At points where the Rayleigh line is tangent to an isentrope,

$$-\rho^2 c^2 = -\rho_o^2 D^2$$

from Eqs. (H.22) and (H.23a). However by Eq. (H.11a), $\rho_o D = \rho \bar{u}$; therefore,

$$-\rho^2 c^2 = -\rho^2 \bar{u}^2 \qquad \text{or} \qquad c = |\bar{u}|,$$

and the flow is sonic at such points.

Moreover, the sonic point divides the solutions space along a particular Rayleigh line into supersonic and subsonic domains. If the isentrope passing through a solution has a steeper negative slope than the Rayleigh line, then

$$\underbrace{-\rho^2 c^2}_{\text{isentrope slope}} < \underbrace{-\rho^2 \bar{u}^2}_{\text{Rayleigh slope}}$$

or $c > |\bar{u}|$. Thus the flow is subsonic. Similarly, those solutions where the Rayleigh line is steeper than the isentrope are supersonic with $c < |\bar{u}|$.

Eqs. (H.22) and (H.23b) give

$$\left.\frac{\partial p}{\partial v}\right|_{s,Y} = \frac{p - p_o}{v - v_o}. \tag{H.24}$$

The locus of all such points for a fixed quiescent state is known as the sonic

locus. Once an equation of state describing the selected HE is specified, $\frac{\partial p}{\partial v}\big|_{s,Y}$ is determined, and the sonic locus can be plotted in the (p, v) plane.

Along the Hugoniot curve, $e(p, v)$ is given by Eq. (H.17) for a general equation of state. An expression for $\frac{\partial p}{\partial v}\big|_{s,Y}$ along the Hugoniot is given by

$$\left.\frac{\partial p}{\partial v}\right|_{s,Y} = -\frac{\left.\frac{\partial e}{\partial v}\right|_{p,Y} + p}{\left.\frac{\partial e}{\partial p}\right|_{v,Y}}, \tag{H.25}$$

which is a general thermodynamic identity.

One should note, that Eq. (H.17) gives a surface $e = (v, p)$ along which energy is conserved; however, this surface is not a constitutive equation describing a particular material. Thus, while Eq. (H.25) may be applied at every point on this surface to give an isentropic derivative, the resulting equation will not describe a material property like the sound speed. A description for the sound speed in a material is recovered if Eq. (H.25) is used in conjunction with an equation of state.

Differentiation of Eq. (H.17) and insertion of the results into Eq. (H.25) gives

$$\left.\frac{\partial p}{\partial v}\right|_{s,Y} = \frac{p - p_o}{v - v_o} \tag{H.26}$$

along the Hugoniot curve. At points where the Hugoniot curve is tangent to an isentrope, Eq. (H.26) is identical to Eq. (H.24). Thus at a sonic point, the Rayleigh line, Hugoniot curve, and isentrope through that point are all tangent to one another. It should be noted that this result is valid for a general equation of state.

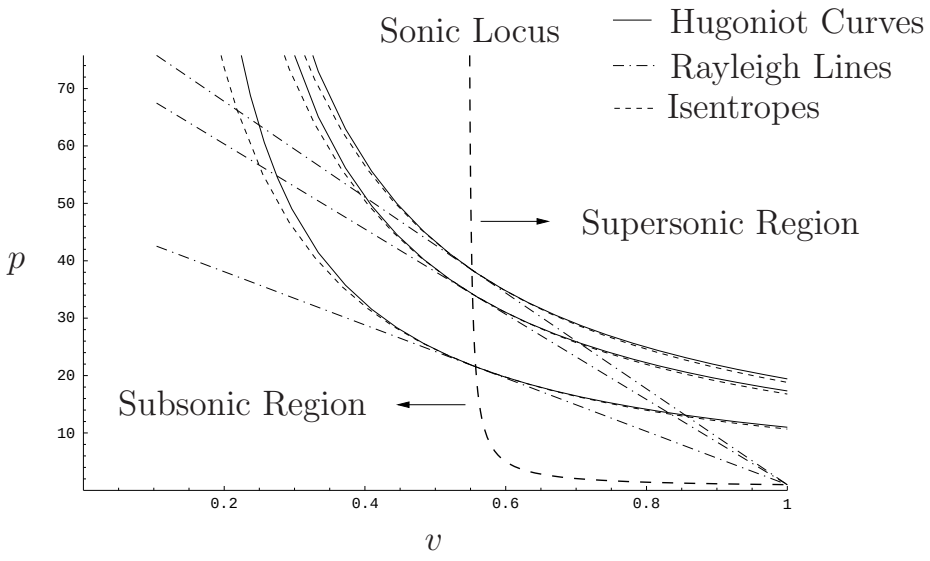

Figure H.7. The sonic locus and associate tangent conditions.

For the ideal gas described in Appendix D, the frozen isentropes are given by

$$pv^{\gamma} = k; \qquad k > 0 \tag{H.27}$$

where k is constant. These are always concave up in the quadrant of interest. To examine the sonic locus, consider that for an isentrope defined according to Eq. (H.27), there is a single Rayleigh line through the quiescent state such that the sonic condition is met. Implicit differentiation of Eq. (H.27) gives

$$\left.\frac{dp}{dv}\right|_{s,Y} = -\gamma\frac{p}{v} \qquad \text{along an isentrope.}$$

Substituting this result into Eq. (H.24) gives and solving for p gives

$$p = \frac{p_o v}{(\gamma+1)v - \gamma v_o}.$$

This is illustrated in Fig. H.7 for $\gamma = 1.2$. Shown are the Rayleigh lines associated with $D = \{6.80947, 8.61338, 9.13587\}$ and the associated tangent Hugoniot curves and isentropes.

H.3.3 Flow of information in the reaction zone

The distinction between subsonic and supersonic flow is quite important in context of the characteristic analysis done in Appendix F. From this analysis, it is known that the speed of information propagation from the left hand reacting flow toward the shock front is $u + c$. Now $\bar{u} < 0$, so for the subsonic flow $|\bar{u}| < c$ becomes $-\bar{u} < c$. Substitution from Eq. (H.2) and rearrangement gives

$$D < u + c,$$

which means that the shock is moving slower than acoustic information propagates. Thus, subsonic regions act to support the flow. Such characteristics are shown in Fig. H.8.

In a CJ detonation, the slope of the characteristics increases as the flow moves further down stream from the shock locus. This means that information propagates at a slower rate from regions further from the shock front than from regions closer to it. At a sonic point, the slope of the characteristics becomes vertical and information at this point moves at the speed of the shock. Moreover, for a CJ detonation, information emanating from a sonic point remains stationary with respect to the shock and, thus, can have no effect on the structure solution.

Besides the behavior illustrated in Fig. H.8, two other types of sonic points are illustrated in Fig. H.9. In the first case, information propagating from the back of the reaction zone passes through a stationary point and continues to effect the lead

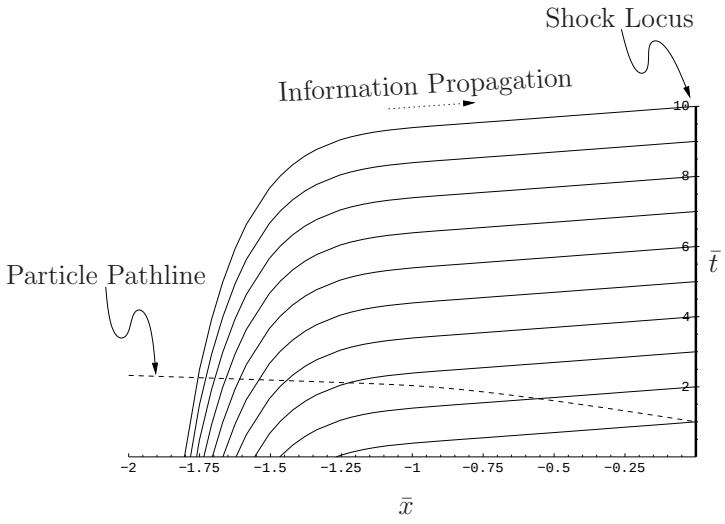

Figure H.8. $u + c$ and u characteristics of a CJ detonation.

shock. This is known as a strong eigen-detonation. In the second case, is known as a weak eigen-detonation, information cannot pass through the sonic point.

H.4 Reaction kinetics

The discussion to this point is valid for a general chemical kinetics scheme. Here the simple irreversible Arrhenius reaction

$$A \rightarrow B$$

between two species A and B is considered. Since only these two species exist in the system and the stoichiometric coefficient is 1, the problem is constrained to

$$M = M_B = M_A \quad \text{and} \quad Y_A = 1 - Y_B, \tag{H.28}$$

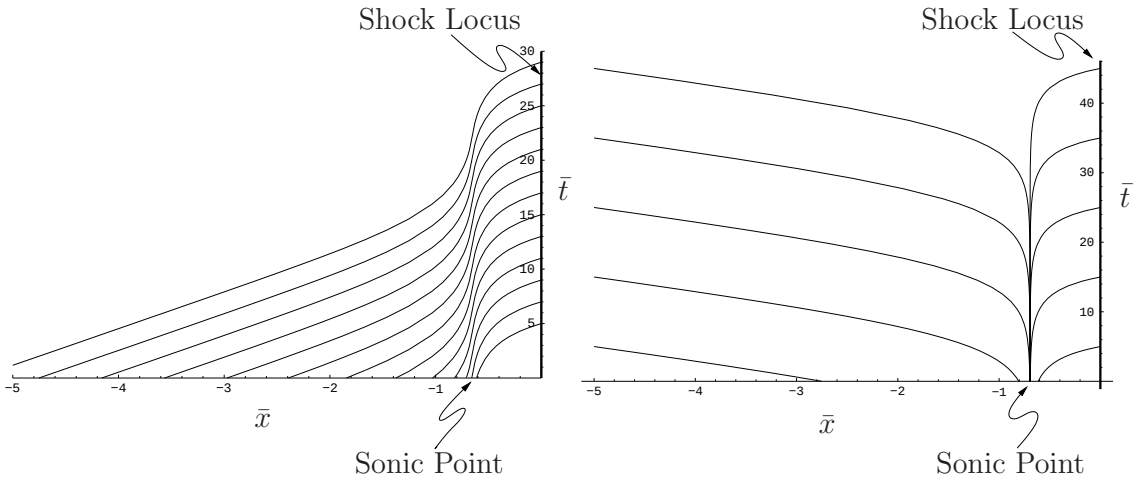

Figure H.9. Characteristics of a strong and weak eigen-detonation.

which agrees with the assumptions made in Appendices D and H.2.2. Thus, Eqs. (H.11d) reduce to simply

$$\frac{d}{d\bar{t}}\left(Y_B\right) = \frac{M\dot{\omega}_B}{\rho},$$

since Y_A is then determined by Eq. (H.28). In the literature, Y_B in normally denoted as λ and is termed the progress variable.

The reaction rate is given by

$$\frac{M\dot{\omega}_B}{\rho} = a(1 - Y_B)\exp\left(\frac{-E\rho}{p}\right) \tag{H.29}$$

where a is a collision frequency factor with dimensions of inverse time and E is the activation energy. Initially, the HE is assumed to be composed entirely of species A; thus, $Y_B = 0$ at $t = 0$. The reaction terminates at $Y_B = 1$ as seen by examining Eq. (H.29).

For this kinetics scheme, Eq. (H.15) becomes

$$Q = Y_B \left(h^0_{f,A} - h^0_{f,B} \right)$$

which states that the heat released is equal to the amount of energy left over as a mass fraction of A changes to B.

H.5 Results

Eqs. (H.11), may be non-dimensionalized by the scaling

$$\rho^* = \frac{\rho}{\rho_o}, \qquad p^* = \frac{p}{p_o},$$
$$\bar{t}^* = \frac{\bar{t}}{k}, \qquad \bar{x}^* = \frac{\bar{x}}{k\sqrt{p_o/\rho_o}},$$
$$\bar{u}^* = \frac{\bar{u}}{\sqrt{p_o/\rho_o}}, \qquad \text{and} \qquad e^* = \frac{e}{p_o/\rho_o}.$$

where k is an unspecified time constant, M is a molar mass, and $\dot{\omega}$ is the rate of species production.

The resulting non-dimensional governing equations are

$$\rho^* \bar{u}^* = -D^*, \tag{H.30a}$$
$$\rho^* (\bar{u}^*)^2 + p^* = (D^*)^2 + 1, \tag{H.30b}$$
$$e^* + \frac{\bar{u}^*}{2} + \frac{p^*}{\rho^*} = e^*_o + \frac{(D^*)^2}{2} + 1, \tag{H.30c}$$
$$e^* = \frac{1}{\gamma - 1}\frac{p^*}{\rho^*} - q^* Y_B, \tag{H.30d}$$
$$\frac{dY_B}{d\bar{t}^*} = ak(1 - Y_B) \exp\left(\frac{-E^* \rho^*}{p^*} \right), \tag{H.30e}$$

where superscript * quantities are dimensionless, $q^* = \frac{\rho_o}{p_o}\left(h^0_{f,A} - h^0_{f,B} \right)$ is the di-

TABLE H.1

NON-DIMENSIONAL CHAPMAN-JOUGUET PARAMETERS

E^*	q^*	γ	D^*_{cj}	ak
50	50	1.2	6.80947462966999	2568.68431787116

mensionless heat release per mass fraction of B, and ak is a dimensionless quantity chosen such that the half reaction time is equal to unity.

Solving Eq. (H.30a) through Eq. (H.30d) gives ρ^*, p^*, and $\bar{u}^*$ as algebraic functions of Y_B. Thus, solving Eq. (H.30e) for Y_B as a function of time gives the structured solution. This is seen in Figures H.10 through H.15. The parameters for classical ZND solution as given in Ref. [19] are reproduced in Table H.1.

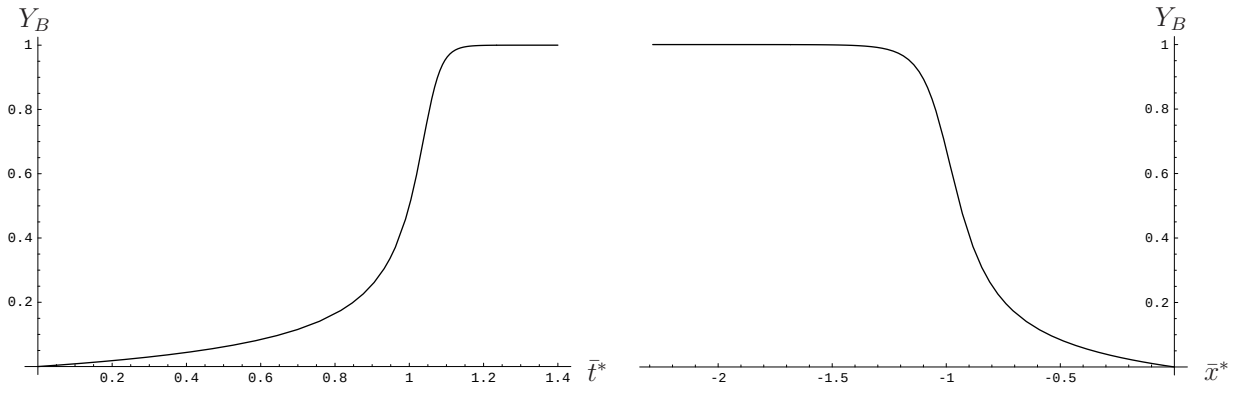

Figure H.10. Mass fraction of species B following a material particle as a function of time or space.

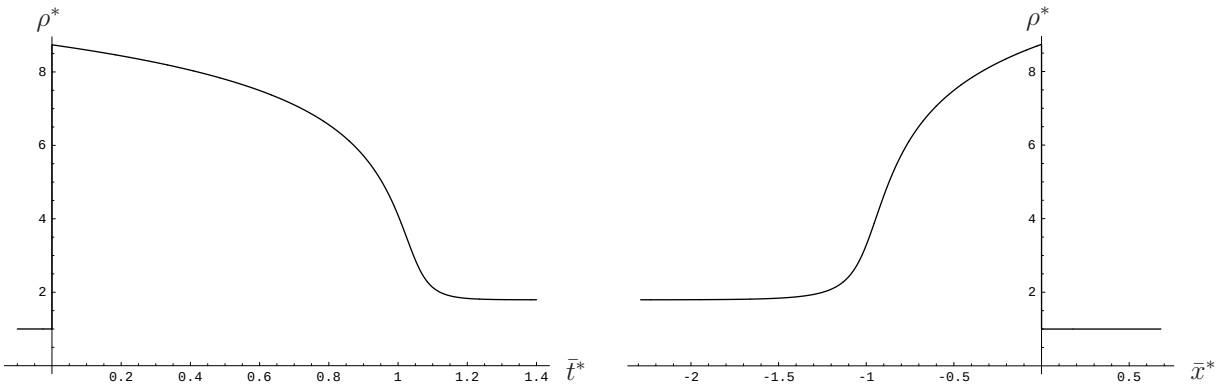

Figure H.11. Density of a material particle as a function of time or space.

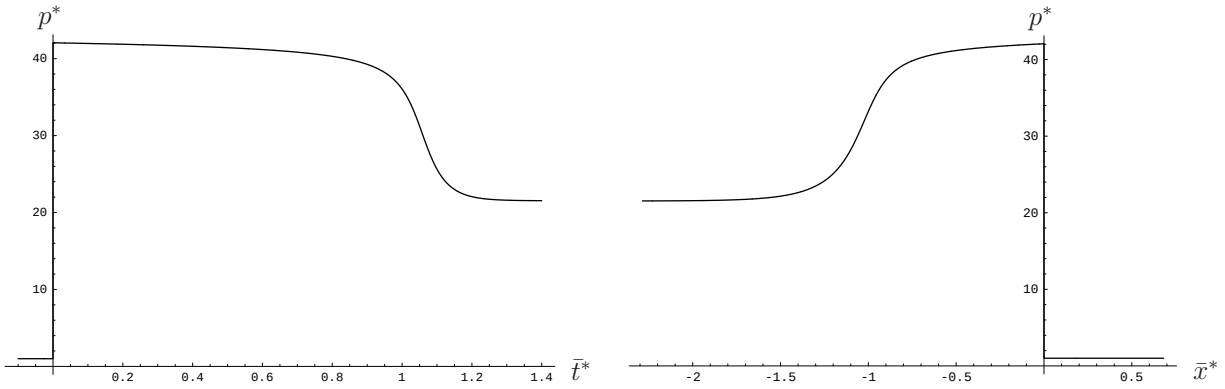

Figure H.12. Pressure of a material particle as a function of time or space.

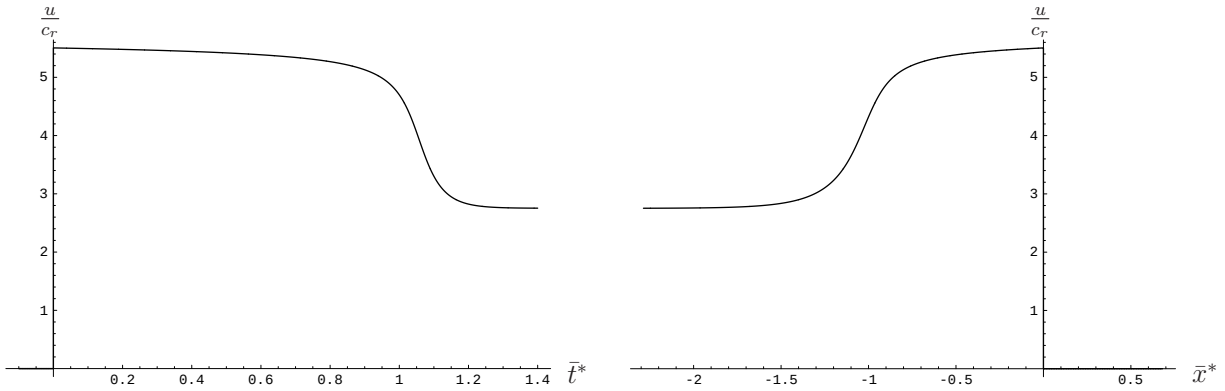

Figure H.13. Particle velocity over quiescent sound speed as a function of time or space.

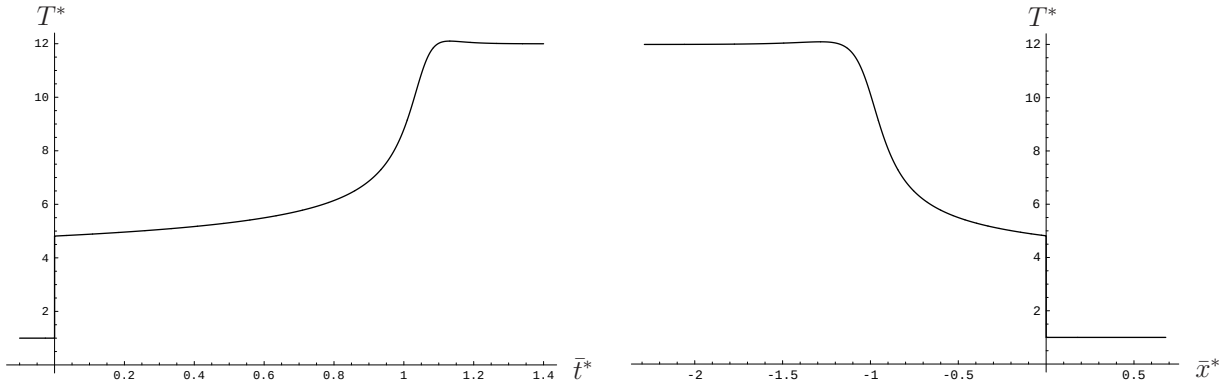

Figure H.14. Temperature of a material particle as a function of time or space.

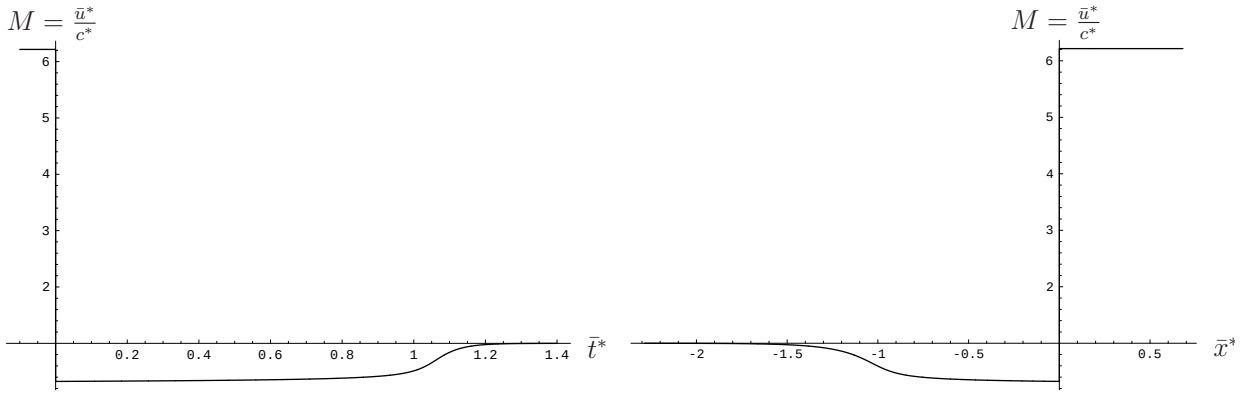

Figure H.15. Mach number of a material particle as a function of time or space.

APPENDIX I

POINT BLAST EXPLOSION

The problem of an intense explosion in a gas was solved independently by Taylor [77], Sedov [78], and von Neumann. Of particular interest is the closed form similarity solution discovered by Sedov which can be given to arbitrary accuracy. Such a solution is valuable in the verification of high order numerical codes. Here, the similarity solution is given in detail following the work of Refs. [71, 79].

I.1 Problem definition

The Sedov blast wave solution assumes axisymmetric flow in the strong shock limit of a calorically perfect ideal gas. Viscosity, heat conduction, and gravity are neglected. The gas is characterized by the ratio of specific heats, given by the constant γ, and is initially at rest with a density ρ_o and pressure $p_o \approx 0$. At time $t = 0$, an amount of energy E is released at the origin, generating a blast wave. This is illustrated in Fig. I.1 where the location of the shock is denoted $R(t)$.

The absence of viscosity and conduction results in an isentropic flow governed by the axisymmetric Euler equations. For an ideal gas, the entropy can be written

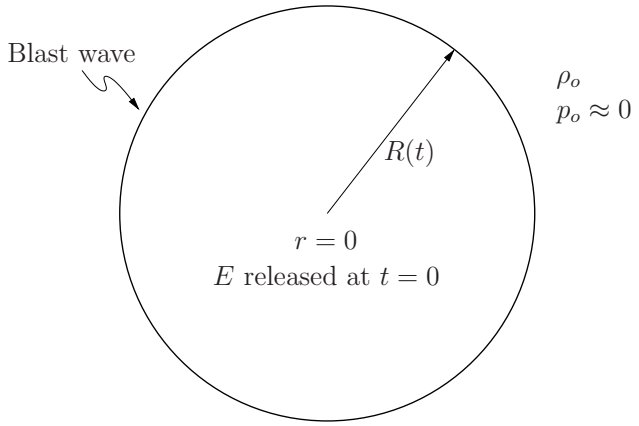

Figure I.1. Diagram of a point blast explosion.

as

$$\begin{aligned} s &= \ln \frac{p}{\rho^\gamma} + \text{constant} \\ &= \ln \left(\left(\gamma \frac{p}{\rho} \right) \left(\gamma^{-1} \right) \left(\rho^{-(\gamma-1)} \right) \right) + \text{constant} \\ &= \ln c^2 - \ln(\gamma) - (\gamma - 1) \ln \rho + \text{constant}. \end{aligned} \tag{I.1}$$

Thus, the isentropic nature of the flow field, $\frac{ds}{dt} = 0$, is given by

$$\frac{d}{dt} \left(\ln c^2 \right) - (\gamma - 1) \frac{d}{dt} \left(\ln \rho \right) = 0. \tag{I.2}$$

With Eq. (I.2), conservation of mass, momentum, and entropy are given by

$$\frac{\partial \rho}{\partial t} + u\frac{\partial \rho}{\partial r} + \rho\left(\frac{\partial u}{\partial r} + n\frac{u}{r}\right) = 0, \tag{I.3a}$$

$$\frac{\partial u}{\partial t} + u\frac{\partial u}{\partial r} + \frac{1}{\gamma}\left(\frac{\partial c^2}{\partial r} + c^2\frac{\partial}{\partial r}\left(\ln \rho\right)\right) = 0, \tag{I.3b}$$

$$\frac{\partial}{\partial t}\left(\ln c^2\right) + u\frac{\partial}{\partial r}\left(\ln c^2\right) - (\gamma - 1)\left(\frac{\partial}{\partial t}\left(\ln \rho\right) + u\frac{\partial}{\partial r}\left(\ln \rho\right)\right) = 0, \tag{I.3c}$$

where r is the spatial coordinate, t is the temporal coordinate, ρ is the density, u is the physical component of velocity in the r direction, and

$$c^2 = \gamma\frac{p}{\rho} \tag{I.4}$$

is the square of the sound speed. The parameter n in Eq. (I.3a) determines the type of axisymmetric flow:

$$n = \begin{cases} 0 & \text{for planar geometry} \\ 1 & \text{for cylindrical geometry} \\ 2 & \text{for spherical geometry.} \end{cases} \tag{I.5}$$

Lastly, for the Eulerian flow of an ideal gas in the strong shock limit, the Rankine-Hugoniot jump conditions reduce to

$$\rho(R(t), t) = \frac{\gamma + 1}{\gamma - 1}\rho_o, \tag{I.6a}$$

$$u(R(t), t) = \frac{2}{\gamma + 1}D_n, \tag{I.6b}$$

$$p(R(t), t) = \frac{2}{\gamma + 1}\rho_o D_n. \tag{I.6c}$$

Equations (I.3) and (I.6) form the governing equations and jump conditions for the point blast explosion.

I.2 Dimensional analysis

The only dimensional parameters in the problem are ρ_o and E. The dimensions of density are M/L^3 while the dimensions of energy are scaled according to the chosen geometry, ML^n/T^2. The only combination of these parameters which is independent of M is $E/\rho_o = L^{n+3}/T^2$. Thus the shock position $r = R(t)$ can only have the correct dimension of L if it is of the functional form

$$R(t) = k\left(\frac{E}{\rho_o}\right)^{1/m} t^{2/m}, \qquad \text{where} \qquad m = n+3 \tag{I.7}$$

and k is a dimensionless number.

The shock speed is found from differentiation of Eq. (I.7) to be

$$D_n = \frac{dR}{dt} = \frac{2k}{m}\left(\frac{E}{\rho_o}\right)^{1/m} t^{2/m-1} \tag{I.8a}$$

$$= \frac{2}{mt}R(t). \tag{I.8b}$$

Except for the undetermined constant k, the shock motion and state are known from Eqs. (I.6), (I.7), and (I.8) without solving the resulting flow field:

$$\rho(R(t),t) = \frac{\gamma+1}{\gamma-1}\rho_o, \tag{I.9a}$$

$$u(R(t),t) = \frac{4}{m(\gamma+1)}t^{-1}R(t), \tag{I.9b}$$

$$p(R(t),t) = \frac{8}{m^2(\gamma+1)}\rho_o t^{-2}R(t)^2. \tag{I.9c}$$

The square of the sound speed at the shock is given from Eqs. (I.4), (I.9a), and (I.9c) to give

$$c^2(R(t),t) = \gamma \frac{8(\gamma-1)}{m^2(\gamma+1)^2} t^{-2} R(t)^2. \tag{I.9d}$$

I.3 Similarity transformation

In order for a dimensionless function of r and t to exist, it must dependent only on a dimensionless combination of the parameters and independent variables. Having already discovered the functional form for the shock location in Eq. (I.7), it is expedient to define the dimensionless variable in terms of $R(t)$:

$$\xi = \frac{r}{R(t)}. \tag{I.10}$$

Then the structure between the origin and shock is sought as a similarity solution in the form of

$$G(\xi) = \frac{\rho}{\rho_o}, \tag{I.11a}$$

$$U(\xi) = \frac{1}{A}\frac{ut}{r}, \tag{I.11b}$$

$$Z(\xi) = \frac{1}{B}\frac{c^2 t^2}{r^2}, \tag{I.11c}$$

where A and B are dimensionless constants chosen to simplify the form of the resulting solutions. In Eqs. (I.11), $G(\xi)$, $U(\xi)$ and $Z(\xi)^{1/2}$ are the dimensionless density, velocity, and sound speed, respectively.

I.3.1 Governing equations

In order to substitute $G(\xi)$, $U(\xi)$, and $Z(\xi)$ into Eqs. (I.3), it is helpful to first compute the necessary derivatives in isolation. First, the partial derivatives of Eq. (I.10) are

$$\frac{\partial \xi}{\partial r} = \frac{1}{R(t)} = \frac{\xi}{r}, \tag{I.12a}$$

$$\frac{\partial \xi}{\partial t} = -\frac{r}{R(t)^2} D_n = -\frac{2}{m}\frac{\xi}{t}. \tag{I.12b}$$

The partial derivatives of density are found, using Eqs. (I.12), to be

$$\begin{aligned} \frac{\partial \rho}{\partial t} &= \frac{\partial}{\partial t}\left(\rho_o G(\xi)\right) \\ &= \rho_o G'(\xi)\frac{\partial \xi}{\partial t} \\ &= -\rho_o \frac{2}{m}\frac{\xi}{t} G'(\xi) \end{aligned} \tag{I.13}$$

and

$$\begin{aligned} \frac{\partial \rho}{\partial r} &= \frac{\partial}{\partial r}\left(\rho_o G(\xi)\right) \\ &= \rho_o G'(\xi)\frac{\partial \xi}{\partial r} \\ &= \rho_o \frac{\xi}{r} G'(\xi). \end{aligned} \tag{I.14}$$

Similarly, the derivatives of u and c^2 appearing Eq. (I.3) are found in terms of $U(\xi)$ and $Z(\xi)$ to be

$$\begin{aligned}\frac{\partial u}{\partial t} &= \frac{\partial}{\partial t}\left(A\frac{r}{t}U(\xi)\right)\\ &= -A\frac{r}{t^2}U(\xi) + A\frac{r}{t}U'(\xi)\frac{\partial \xi}{\partial t}\\ &= -A\frac{r}{t^2}\left(U(\xi) + \frac{2}{m}\xi U'(\xi)\right),\end{aligned} \tag{I.15}$$

$$\begin{aligned}\frac{\partial u}{\partial r} &= \frac{\partial}{\partial r}\left(A\frac{r}{t}U(\xi)\right)\\ &= \frac{A}{t}U(\xi) + A\frac{r}{t}U'(\xi)\frac{\partial \xi}{\partial r}\\ &= \frac{A}{t}\left(U(\xi) + \xi U'(\xi)\right),\end{aligned} \tag{I.16}$$

$$\begin{aligned}\frac{\partial c^2}{\partial t} &= \frac{\partial}{\partial t}\left(B\frac{r^2}{t^2}Z(\xi)\right)\\ &= -2B\frac{r^2}{t^3}Z(\xi) + B\frac{r^2}{t^2}Z'(\xi)\frac{\partial \xi}{\partial t}\\ &= -2B\frac{r^2}{t^3}\left(Z(\xi) + \frac{1}{m}\xi Z'(\xi)\right),\end{aligned} \tag{I.17}$$

and

$$\begin{aligned}\frac{\partial c^2}{\partial r} &= \frac{\partial}{\partial r}\left(B\frac{r^2}{t^2}Z(\xi)\right)\\ &= 2B\frac{r}{t^2}Z(\xi) + B\frac{r^2}{t^2}Z'(\xi)\frac{\partial \xi}{\partial r}\\ &= B\frac{r}{t^2}\left(2Z(\xi) + \xi Z'(\xi)\right).\end{aligned} \tag{I.18}$$

Lastly, it is convenient to couch the derivatives of the dependent quantities in terms of logarithms. Using Eqs. (I.13) through (I.18), in conjunction with the chain rule, the logarithmic derivatives are given by

$$\frac{\partial \ln \rho}{\partial t} = \frac{1}{\rho}\frac{\partial \rho}{\partial t} = -\frac{2}{m}\frac{\xi}{t}\frac{G'(\xi)}{G(\xi)}, \tag{I.19}$$

$$\frac{\partial \ln \rho}{\partial r} = \frac{1}{\rho}\frac{\partial \rho}{\partial r} = \frac{\xi}{r}\frac{G'(\xi)}{G(\xi)}, \tag{I.20}$$

$$\frac{\partial \ln c^2}{\partial t} = \frac{1}{c^2}\frac{\partial c^2}{\partial t} = -\frac{2}{t}\left(1 + \frac{\xi}{m}\frac{Z'(\xi)}{Z(\xi)}\right), \tag{I.21}$$

$$\frac{\partial \ln c^2}{\partial r} = \frac{1}{c^2}\frac{\partial c^2}{\partial r} = \frac{1}{r}\left(2 + \xi\frac{Z'(\xi)}{Z(\xi)}\right). \tag{I.22}$$

Such derivatives are common in similarity analysis where solutions can be written in a form independent of the dimensional units chosen.

Substituting Eqs. (I.11) through (I.18) into Eqs. (I.3), canceling, and rearrangement gives

$$\left(U(\xi) - \frac{1}{A}\frac{2}{m}\right)\xi\frac{G'(\xi)}{G(\xi)} + \xi U'(\xi) + (n+1)U(\xi) = 0, \tag{I.23a}$$

$$\begin{aligned}\left(U(\xi) - \frac{1}{A}\frac{2}{m}\right)\xi U'(\xi) + U(\xi)^2 - \frac{1}{A}U(\xi) \\ + \frac{1}{\gamma}\left(\frac{B}{A^2}\left(2Z(\xi) + \xi Z'(\xi)\right) + \frac{B}{A^2}Z(\xi)\xi\frac{G'(\xi)}{G(\xi)}\right) = 0,\end{aligned} \tag{I.23b}$$

$$\xi\frac{Z'(\xi)}{Z(\xi)} - (\gamma - 1)\xi\frac{G'(\xi)}{G(\xi)} + \frac{2(U(\xi) - \frac{1}{A})}{U(\xi) - \frac{1}{A}\frac{2}{m}} = 0. \tag{I.23c}$$

Note that neither r nor t appear explicitly in the transformed equations. Choosing

$$A = \frac{2}{m} \qquad \text{and} \qquad B = A^2 = \frac{4}{m^2} \tag{I.24}$$

simplifies Eqs. (I.23) to

$$(U(\xi)-1)\,\xi\frac{G'(\xi)}{G(\xi)}+\xi U'(\xi)+(n+1)U(\xi)=0, \tag{I.25a}$$

$$\begin{aligned} Z\,(U(\xi)-1)\,\xi U'(\xi)+\left(U(\xi)-\frac{m}{2}\right)U(\xi) \\ +\frac{1}{\gamma}\left(2Z(\xi)+\xi Z'(\xi)+Z(\xi)\xi\frac{G'(\xi)}{G(\xi)}\right)=0, \end{aligned} \tag{I.25b}$$

$$\xi\frac{Z'(\xi)}{Z(\xi)}-(\gamma-1)\xi\frac{G'(\xi)}{G(\xi)}+\frac{2(U(\xi)-\frac{m}{2})}{U(\xi)-1}=0, \tag{I.25c}$$

giving the final form of the governing equations.

I.3.2 Boundary conditions

Boundary conditions for Eqs. (I.25) are provided by the strong shock relations. At the shock, $r=R(t)$ and $\xi=1$ so that

$$G(1)=\frac{\rho(R(t),t)}{\rho_o}, \tag{I.26a}$$

$$U(1)=\frac{mt}{2R(t)}u(R(t),t), \tag{I.26b}$$

$$Z(1)=\frac{m^2t^2}{4R(t)^2}c^2(R(t),t), \tag{I.26c}$$

from Eqs. (I.11) evaluated at the shock. The shock state density, velocity, and sound speed are known from the shock jump conditions, Eqs. (I.9). Substituting Eqs. (I.9) into Eq. (I.26) gives

$$G(1)=\frac{\gamma+1}{\gamma-1}, \tag{I.27a}$$

$$U(1)=\frac{2}{\gamma+1}, \tag{I.27b}$$

$$Z(1)=\frac{2\gamma(\gamma-1)}{(\gamma+1)^2}. \tag{I.27c}$$

Equations (I.25) and (I.27) give a complete self-similar system of equations amenable to numerical integration as seen in Fig. I.2. While it is now possible to solve this system for $G(\xi)$, $U(\xi)$, $Z(\xi)$, the constant k in Eq. (I.7) has yet to be determined. Thus in order to transform the solution back into the (r, t) plane, it is necessary to reconsider the similarity structure of the solution.

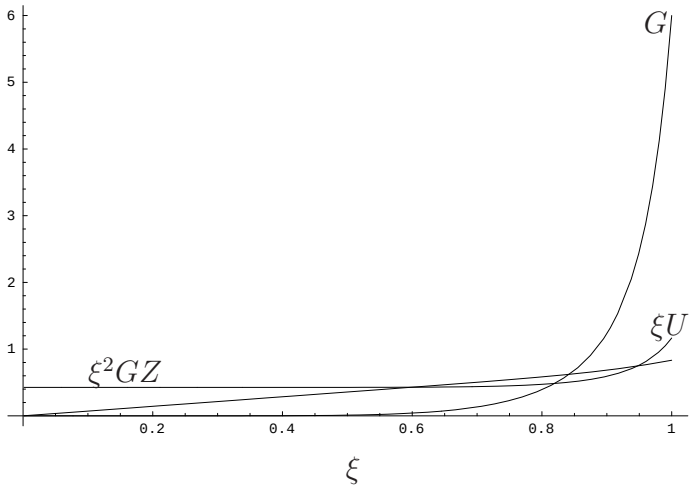

Figure I.2. Similarity solution for spherical geometry ($m = 5$) and $\gamma = 1.4$.

I.4 Similarity structure

In order to determine the parameter k, one begins with the observation that the total amount of energy in the blast wave is a fixed constant, E. This follows from the fact that the ambient state of the gas is at rest with zero internal energy

(*i.e.* $p_o \approx 0$); thus the flux of energy into the blast wave is identically zero. Indeed, this is absolutely necessary for a similarity solution; otherwise, further dimensional parameters are introduced which prevent self-similarity.

Knowing *a priori* the total energy of the blast wave, one now has a constraint on the total energy integral computed using the known (perhaps numerical) solutions for $G(\xi)$, $U(\xi)$, $Z(\xi)$ in the range $\xi \in [0,1]$. This constraint only involves one unknown: k. Furthermore, the fact that the energy integral evaluated with constant limits of integration is a constant indicates that the integrand is a function of ξ alone. In other words, the self similar nature of the solution requires the integral amount of $\mathcal{E} = \rho(e + \frac{1}{2}u^2)$ between any two values of ξ to be constant.

This may be verified by considering the energy integral

$$\mathcal{E}(r,t) = \int_o^r \rho\left(e + \frac{1}{2}u^2\right) dI, \qquad \text{where} \qquad dI = \begin{cases} d\hat{r} & \text{for planar} \\ 2\pi\hat{r}d\hat{r} & \text{for cylindrical} \\ 4\pi\hat{r}^2 d\hat{r} & \text{for spherical} \end{cases} \tag{I.28}$$

and a $\hat{}$ is used as needed to distinguish dummy integration variables. Since $e = \frac{c^2}{\gamma(\gamma-1)}$ for a calorically perfect ideal gas, Eq. (I.28) may be written generally as

$$\mathcal{E}(r,t) = \int_o^r \rho\left(\frac{c^2}{\gamma(\gamma-1)} + \frac{1}{2}u^2\right) \pi^l (2\hat{r})^n d\hat{r}, \qquad \text{where} \qquad l = \begin{cases} 0 & \text{for planar} \\ 1 & \text{for non-planar.} \end{cases} \tag{I.29}$$

In order to write Eq. (I.29) in terms of ξ, consider that by definition dr is a

differential keeping $dt = 0$. Thus, since $r = R(t)\xi$ from Eq. (I.10), $dr = R(t)d\xi$. Furthermore the limits of integration change from

$$\hat{r} = 0 \rightarrow \hat{\xi} = 0 \qquad \text{and} \qquad \hat{r} = r \rightarrow \hat{\xi} = \frac{r}{R(t)} = \xi. \tag{I.30}$$

Thus Eq. (I.29) becomes

$$\begin{aligned}\mathcal{E}(\xi) &= \frac{2^{n+2}\pi^l \rho_o}{m^2} \int_0^\xi G(\hat{\xi}) \left(\frac{1}{\gamma(\gamma-1)} Z(\hat{\xi}) + \frac{1}{2} U(\hat{\xi})^2 \right) \frac{r^2}{t^2} R(t)^{n+1} \hat{\xi}^n d\hat{\xi} \\ &= \frac{2^{n+2}\pi^l \rho_o}{m^2} \int_0^\xi G(\hat{\xi}) \left(\frac{1}{\gamma(\gamma-1)} Z(\hat{\xi}) + \frac{1}{2} U(\hat{\xi})^2 \right) \frac{r^2}{R(t)^2} \frac{1}{t^2} R(t)^{n+3} \hat{\xi}^n d\hat{\xi}, \end{aligned} \tag{I.31}$$

after substitution of Eq. (I.11) and rearrangement. Now, from the definition of $R(t)$

$$\left(\frac{R(t)}{t^2} \right)^m = k^m \frac{E}{\rho_o} = \left(\frac{R(t)}{t^2} \right)^{n+3}, \tag{I.32}$$

since $m = n + 3$. As $\frac{r^2}{R(t)^2} = \xi^2$, Eq. (I.31) becomes

$$\mathcal{E}(\xi) = \frac{2^{n+2}\pi^l k^m E}{m^2} \int_0^\xi G(\hat{\xi}) \left(\frac{1}{\gamma(\gamma-1)} Z(\hat{\xi}) + \frac{1}{2} U(\hat{\xi})^2 \right) \hat{\xi}^{n+2} d\hat{\xi}. \tag{I.33}$$

Note that Eq. (I.33) is a function of ξ alone, as expected, and the energy between any two values ξ_1 and ξ_2 is the constant $\mathcal{E}(\xi_2) - \mathcal{E}(\xi_1)$.

Now, the parameter E is the total amount of energy in the blast, the region

between $\xi \in [0,1]$. Thus

$$\mathcal{E}(1) = E = \frac{2^{n+2}\pi^l k^m E}{m^2} \int_0^1 G(\xi) \left(\frac{1}{\gamma(\gamma-1)} Z(\xi) + \frac{1}{2} U(\xi)^2 \right) \xi^{n+2} d\xi. \tag{I.34}$$

Everything in Eq. (I.34) is known except k. Solving for k gives

$$k = \left(\frac{2^{n+2}\pi^l}{m^2} \int_0^1 G(\xi) \left(\frac{1}{\gamma(\gamma-1)} Z(\xi) + \frac{1}{2} U(\xi)^2 \right) \xi^{n+2} d\xi \right)^{-1/m}. \tag{I.35}$$

Examples of this constant as determined by γ and the geometry are given in Table I.1. With Eq. (I.35), the entire solution to the point blast explosion in the original coordinates can be found, including the blast wave radius as seen in Fig. I.3; validation of this result by Taylor [80] illustrates the usefulness of this result in modeling actual nuclear explosions.

I.5 Analytic solution

I.5.1 The energy constraint

Equations (I.25) and (I.27) can, as before, be solved numerically; however, a closed form analytical solution is desired. Once again, use is made of the similarity structure to solve the energy integral exactly, giving a direct expression between the functions $G(\xi)$, $U(\xi)$, and $Z(\xi)$. The key observation before was that the total energy $\mathcal{E}$ for any fixed ξ is a constant value. Since $r = \xi R(t)$, this becomes

$$\mathcal{E}(r,t) = \int_0^{\xi R(t)} \rho \left(e + \frac{1}{2} u^2 \right) dI = \text{constant}; \qquad \xi \in [0,1], \tag{I.36}$$

TABLE I.1

APPROXIMATIONS OF THE PARAMETER k FOR DIATOMIC AND MONATOMIC IDEAL GASES IN LINEAR, CYLINDRICAL, AND SPHERICAL GEOMETRIES

		n		
		0	1	2
γ	7/5	1.229	1.004	1.033
	5/3	1.491	1.154	1.152

where the energy flux due to the motion of the boundary is balance by the change in ρ, u, and e with time. It is precisely this balance for arbitrary ξ which gives the desired relationship.

In general, for an arbitrary moving volume, Reynolds' transport theorem gives

$$\frac{d}{dt}\int_{AV} F dV = \int_{AV} \frac{\partial F}{\partial t} dV + \int_{AS} F w^i n_i dS, \tag{I.37}$$

where F is an general function and w^i is the velocity of the volume. If F is governed by a conservation law of the form

$$\frac{\partial F}{\partial t} + f^i_{,i} = 0, \tag{I.38}$$

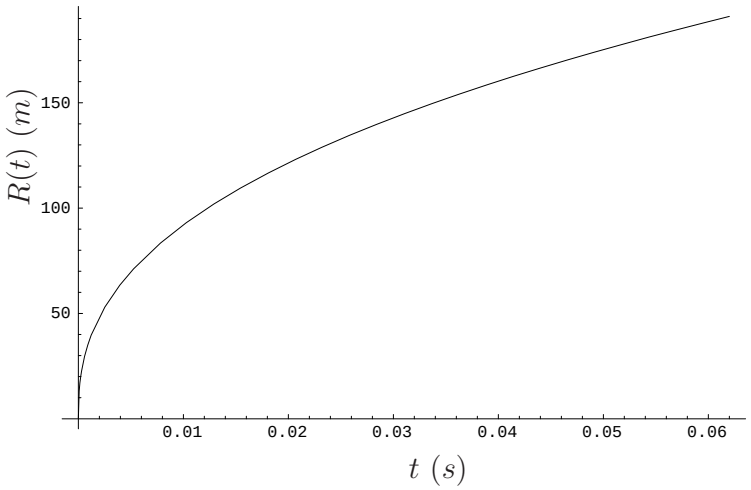

Figure I.3. Spherical blast radius for $\gamma = 1.4$, $\rho_o = 1.25\ kg/m^3$, and $E = 7.02912 \times 10^{13}\ J$. This is the approximate behavior of the 1945 Trinity explosion.

then Eq. (I.37) may be rewritten as

$$\begin{aligned} \frac{d}{dt}\int\limits_{AV} F dV &= \int\limits_{AV} -f^i_{,i} dV + \int\limits_{AS} F w^i n_i dS \\ &= \int\limits_{AS} \left(w^i F - f^i\right) n_i dS, \end{aligned} \tag{I.39}$$

using the divergence theorem.

Applying Eq. (I.39) to the energy contained within the moving axisymmetric volume defined by $r = \xi R(t)$, as given by Eq. (I.36), one has

$$F = \rho\left(\frac{c^2}{\gamma(\gamma-1)} + \frac{1}{2}u^2\right), \tag{I.40}$$

$$f^i n_i = \rho u\left(\frac{c^2}{\gamma-1} + \frac{1}{2}u^2\right), \tag{I.41}$$

from the Euler equations for a calorically perfect ideal gas. The volume is denoted

$V(\xi)$ where ξ is fixed; the corresponding surface is denoted $S(\xi)$. The left hand side of Eq. (I.39) is simply

$$\frac{d}{dt}\int\limits_{V(\xi)} F dV = \frac{d}{dt}\left(\mathcal{E}(\xi)\right) = 0, \tag{I.42}$$

since $\mathcal{E}(\xi)$ is constant for a fixed ξ. The velocity of $V(\xi)$ is given by

$$w^i n_i = \frac{\partial}{\partial t}\left(\xi R(t)\right) = \xi D_n = \frac{2}{m}\frac{r}{t}, \tag{I.43}$$

from Eqs. (I.8) and (I.10). Substitution of Eqs. (I.40), (I.41), and (I.42) into Eq. (I.39) gives

$$0 = \int\limits_{S(\xi)} \rho\left(\frac{2}{m}\frac{r}{t}\left(\frac{c^2}{\gamma(\gamma-1)} + \frac{1}{2}u^2\right) - \rho u\left(\frac{c^2}{\gamma-1} + \frac{1}{2}u^2\right)\right) dS. \tag{I.44}$$

The only way for this to be true for all $\xi \in [0,1]$ is for the integrand to be identically zero:

$$\rho\left(\frac{2}{m}\frac{r}{t}\left(\frac{c^2}{\gamma(\gamma-1)} + \frac{1}{2}u^2\right) = \rho u\left(\frac{c^2}{\gamma-1} + \frac{1}{2}u^2\right)\right). \tag{I.45}$$

This is the aforementioned balance. Note that this is an algebraic constraint; rather than a differential equation.

Substituting from Eqs. (I.11) in Eq. (I.45) gives, after simplification,

$$Z(\xi) = \frac{\gamma(\gamma-1)}{2}\frac{U(\xi)^2(U(\xi)-1)}{1-\gamma U(\xi)} \qquad \text{or} \tag{I.46a}$$

$$Z(U) = \frac{\gamma(\gamma-1)}{2}\frac{U^2(U-1)}{1-\gamma U}. \tag{I.46b}$$

It should be noted that this relationship satisfies the boundary conditions Eqs. (I.27b) and (I.27c) which is easily verified by substituting $U(1) = \frac{2}{\gamma+1}$ into Eq. (I.46b).

I.5.2 Differential-algebraic system

Have found an expression for $Z(U)$, it is expedient to replace the momentum equation, Eq. (I.25b), in Eqs. (I.25) yielding the following differential-algebraic system:

$$(U(\xi) - 1)\frac{d\ln G}{d\ln \xi} + \frac{dU}{d\ln \xi} + (n+1)U(\xi) = 0, \tag{I.47a}$$

$$\frac{d\ln Z}{d\ln \xi} - (\gamma - 1)\frac{d\ln G}{d\ln \xi} + \frac{2(U(\xi) - \frac{m}{2})}{U(\xi - 1)} = 0, \tag{I.47b}$$

$$Z(U) = \frac{\gamma(\gamma-1)}{2}\frac{U^2(U-1)}{1-\gamma U}, \tag{I.47c}$$

where logarithmic derivatives have been used to simplify the form of Eqs. (I.47a) and (I.47b).

Multiplying Eq. (I.47a) by $(\gamma - 1)$ and Eq. (I.47b) by $(U(\xi) - 1)$ and adding eliminates $\frac{d\ln G}{d\ln \xi}$ to give

$$\frac{dU}{d\ln \xi} + \frac{U(\xi) - 1}{\gamma - 1}\frac{d\ln Z}{d\ln \xi} + \frac{\chi U(\xi) - m}{\gamma - 1} = 0, \tag{I.48}$$

where

$$\chi = (n+1)(\gamma - 1) + 2. \tag{I.49}$$

Multiplying by $\frac{d\ln\xi}{dU}$ gives

$$1+\frac{U(\xi)-1}{\gamma-1}\frac{d\ln Z}{dU}+\frac{\chi U(\xi)-m}{\gamma-1}\frac{d\ln\xi}{dU}=0. \tag{I.50}$$

Equation (I.50) is a differential equation involving an unknown function $\ln\xi$ and a known function $Z(U)$ given by Eq. (I.47c).

Thus, taking the logarithm of Eq. (I.47c) and differentiating with respect to U gives

$$\frac{d\ln Z}{dU}=\frac{2}{U}+\frac{1}{U-1}+\frac{\gamma}{1-\gamma U}. \tag{I.51}$$

Substituting Eq. (I.51) into Eq. (I.50) gives

$$1+\frac{U-1}{\gamma-1}\left(\frac{2}{U}+\frac{1}{U-1}\right)+\frac{\chi U-m}{\gamma-1}\frac{d\ln\xi}{dU}=0. \tag{I.52}$$

Solving for $\frac{d\ln\xi}{dU}$ and rearrangement gives

$$\frac{d\ln\xi}{dU}=\frac{\gamma}{m-\chi U}+\frac{2(U-1)}{U(m-\chi U)}+\frac{\gamma(U-1)}{(m-\chi U)(1-\gamma U)}, \tag{I.53}$$

which can be integrated to give $\xi(U)$.

Having found an expression for $\frac{d\ln\xi}{dU}$ in Eq. (I.53), consider multiplying the mass equation, Eq. (I.47a) by $\frac{d\ln\xi}{dU}$ to give

$$(U(\xi)-1)\frac{d\ln G}{dU}+1+(n+1)U(\xi)\frac{d\ln\xi}{dU}=0. \tag{I.54}$$

Substitution of Eq. (I.53) and solving for $\frac{d\ln G}{dU}$ yields

$$\frac{d\ln G}{dU} = -\frac{1}{U-1} - (n+1)\left(\frac{\gamma U}{(m-\chi U)(U-1)} + \frac{2}{m-\chi U} + \frac{\gamma U}{(m-\chi U)(1-\gamma U)}\right), \quad \text{(I.55)}$$

which can be integrated to give $G(U)$.

Thus the final form of the differential-algebraic system is given by Eqs. (I.47c), (I.53), and (I.55):

$$Z(U) = \frac{\gamma(\gamma-1)}{2}\frac{U^2(U-1)}{1-\gamma U}, \quad \text{(I.47c)}$$

$$\frac{d\ln \xi}{dU} = \frac{\gamma}{m-\chi U} + \frac{2(U-1)}{U(m-\chi U)} + \frac{\gamma(U-1)}{(m-\chi U)(1-\gamma U)}, \quad \text{(I.53)}$$

$$\frac{d\ln G}{dU} = -\frac{1}{U-1} - (n+1)\left(\frac{\gamma U}{(m-\chi U)(U-1)} + \frac{2}{m-\chi U} + \frac{\gamma U}{(m-\chi U)(1-\gamma U)}\right). \quad \text{(I.55)}$$

I.5.3 Integration technique

Integration of Eqs. (I.53) and (I.55) is facilitated using the formula

$$\int \frac{c_1 U + c_2}{(m-\chi U)(c_3 U - c_4)} dU = \left(\frac{c_1 c_4 - c_2 c_3}{c_3(m c_3 + \chi c_4)} - \frac{c_1}{\chi c_3}\right)\ln|m-\chi U| + \frac{c_2 c_3 - c_1 c_4}{c_3(m c_3 + \chi c_4)}\ln|c_3 U + c_4| + \text{constant}, \quad \text{(I.56)}$$

which is easily derived using partial fractions. Begin by removing the term involving U from the numerator:

$$\begin{aligned}\frac{c_1U+c_2}{(m-\chi U)(c_3U-c_4)} &= \frac{c1}{c3}\frac{c_3U+c_4+\frac{c_2c_3}{c_1}-c_4}{(m-\chi U)(c_3U+c_4)} \\ &= \frac{c_1}{c_3}\frac{1}{m-\chi U}+\frac{c_2c_3-c_1c_4}{c_3}\frac{1}{(m-\chi U)(c_3U+c_4)}. \end{aligned} \quad \text{(I.57)}$$

The last term can now be divided into partial fractions to give

$$\begin{aligned}\frac{c_1U+c_2}{(m-\chi U)(c_3U-c_4)} &= \frac{c_1}{c_3}\frac{1}{m-\chi U} \\ &\quad + \frac{c_2c_3-c_1c_4}{c_3(mc_3+\chi c_4)}\left(\frac{\chi}{m-\chi U}+\frac{c_3}{c_3U+c_4}\right). \end{aligned} \quad \text{(I.58)}$$

Integration and regrouping now gives Eq. (I.56).

I.5.4 $\xi(U)$ and bounds on U

Integration of Eq. (I.53) is done using Eq. (I.56) on each term to give

$$\begin{aligned}\ln\xi = &-\frac{\gamma}{\chi}\ln|m-\chi U| \\ &+\frac{2\chi-2m}{\chi m}\ln|m-\chi U|-\frac{2}{m}\ln|U| \\ &+\left(\frac{1}{\chi}+\frac{\gamma-1}{\chi-\gamma m}\right)\ln|m-\chi U|+\frac{1-\gamma}{\chi-m\gamma}\ln|1-\gamma U|+\text{constant}. \end{aligned} \quad \text{(I.59)}$$

Regrouping and simplifying gives

$$\begin{aligned}\ln\xi &= \frac{1}{m}\left(\frac{\chi-\gamma m-m}{\chi}+\frac{\chi-m}{\chi-\gamma m}\right)\ln|m-\chi U|+\frac{1-\gamma}{\chi-m\gamma}\ln|1-\gamma U| \\ &\quad -\frac{2}{m}\ln|U|+\text{constant} \\ &= \beta_1\ln|m-\chi U|+\beta_2\ln|1-\gamma U|-\frac{2}{m}\ln|U|+\text{constant},\end{aligned} \tag{I.60}$$

where

$$\begin{aligned}\beta_1 &= \frac{1}{m}\left(\frac{\chi-\gamma m-m}{\chi}+\frac{\chi-m}{\chi-\gamma m}\right) \\ &= \frac{\chi-m}{m(1-\gamma)}\left(\frac{(1-\gamma)(\chi-\gamma m-m)}{\chi(\chi-m)}+\beta_2\right) \qquad \text{(I.61a)} \\ \beta_2 &= \frac{1-\gamma}{\chi-m\gamma}. \qquad \text{(I.61b)}\end{aligned}$$

The constant of integration is determined by applying the boundary condition Eq. (I.27b) so that Eq. (I.60) becomes

$$\ln\xi = \beta_1\ln\left|\frac{(\gamma+1)(m-\chi U)}{m(\gamma+1)-2\chi}\right|+\beta_2\ln\left|\frac{\gamma+1}{1-\gamma}(1-\gamma U)\right|-\frac{2}{m}\ln\left|\frac{\gamma+1}{2}U\right|. \tag{I.62}$$

Taking the exponential of Eq. (I.62) gives the final form for $\xi(U)$:

$$\xi = \left(\frac{(\gamma+1)(m-\chi U)}{m(\gamma+1)-2\chi}\right)^{\beta_1}\left(\frac{\gamma+1}{1-\gamma}(1-\gamma U)\right)^{\beta_2}\left(\frac{\gamma+1}{2}U\right)^{-\frac{2}{m}}. \tag{I.63}$$

Now at the shock, $U(\xi=1)$ is bounded by the jump condition Eq. (I.27b)

$$U(1) = \frac{2}{\gamma+1}. \tag{I.27b}$$

The lower bound is found from Eq. (I.63) evaluated at $\xi=0$. The only way for

Eq. (I.63) to be zero is for one of its terms to be zero:

$$U = 0, \tag{I.64a}$$

$$U = \frac{1}{\gamma}, \tag{I.64b}$$

$$U = \frac{m}{(m-2)\gamma + 4 - m}. \tag{I.64c}$$

The lower bound is given by the maximum of Eqs. (I.64) which is also less than the upper bound given by Eq. (I.27b).

If it is assumed that $\gamma > 1$, then Eq. (I.64b) is always less than the upper bound; since it is also greater than Eq. (I.64a), the case $U = 0$ can be discarded. Second, it is easy to show that Eq. (I.64c) is always greater than Eq. (I.64b); however, Eq. (I.64c) is also greater than the upper bound when $3m-8 > (m-4)\gamma$. This is always the case for either planar or cylindrical geometries. For spherical geometries this is only violated for $\gamma > 7$. Thus the bounds are U are

$$\frac{2}{\gamma+1} \geq U \geq \begin{cases} \frac{1}{\gamma} & \text{if } 3m - 8 > (m-4)\gamma \\ \frac{m}{(m-2)\gamma+4-m} & \text{if } m = 3 \text{ and } \gamma > 7. \end{cases} \tag{I.65}$$

I.5.5 $G(U)$

Again integration of Eq. (I.55) is performed using the formula Eq. (I.56) to give

$$\begin{aligned}\ln G = &-\ln|U-1| - (n+1)\\ &\left(\left(-\frac{\gamma}{m-\chi}-\frac{\gamma}{\chi}\right)\ln|m-\chi U| + \frac{\gamma}{m-\chi}\ln|U-1| - \frac{2}{\chi}\ln|m-\chi U|\right.\\ &\left.+\left(-\frac{1}{\chi-\gamma m}+\frac{1}{\chi}\right)\ln|m-\chi U| + \frac{1}{\chi-\gamma m}\ln|1-\gamma U|\right) + \text{constant}. \quad \text{(I.66)}\end{aligned}$$

Regrouping and simplifying gives

$$\begin{aligned}\ln G = &-\left(\frac{(n+1)\gamma}{m-\chi}+1\right)\ln|U-1|\\ &+(n+1)\left(\frac{\gamma+1}{\chi}+\frac{\gamma}{m-\chi}+\frac{1}{\chi-\gamma m}\right)\ln|m-\chi U|\\ &-\frac{n+1}{\chi-\gamma m}\ln|1-\gamma U| + \text{constant}\\ &= \beta_3\ln|U-1| + \beta_4\ln|m-\chi U| + \beta_5\ln|1-\gamma U| + \text{constant}, \quad \text{(I.67)}\end{aligned}$$

where

$$\beta_3 = -\left(\frac{(n+1)\gamma}{m-\chi}+1\right) \quad \text{(I.68a)}$$

$$\begin{aligned}\beta_4 &= \frac{n+1}{m-\chi}\left(\frac{(\gamma+1)(m-\chi)}{\chi}+\frac{\gamma\chi}{\chi}+\frac{m-\chi}{\chi-\gamma m}\right)\\ &= \frac{n+1}{m-\chi}\left(\frac{\gamma m+m+\chi}{\chi}+\frac{m-\chi}{\chi-\gamma m}\right)\\ &= \frac{n+1}{m-\chi}(-m\beta_1) \quad \text{(I.68b)}\end{aligned}$$

$$\beta_5 = -\frac{n+1}{\chi-\gamma m}. \quad \text{(I.68c)}$$

Substituting the boundary conditions Eqs. (I.27a) and (I.27b) into Eq. (I.67) and solving for the constant of integration gives

$$\text{constant} = \ln\left|\frac{\gamma+1}{\gamma-1}\right| - \beta_3 \ln\left|\frac{2}{\gamma+1} - 1\right| - \beta_4 \ln\left|m - \chi\frac{2}{\gamma+1}\right| - \beta_5 \ln\left|1 - \gamma\frac{2}{\gamma+1}\right|. \quad \text{(I.69)}$$

Substitution for the constant into Eq. (I.67) gives

$$\ln G = \ln\left|\frac{\gamma+1}{\gamma-1}\right| + \beta_3 \ln\left|\frac{\gamma+1}{\gamma-1}(1-U)\right| + \beta_4 \ln\left|\frac{\gamma+1}{m(\gamma+1)-2\chi}(m-\chi U)\right| + \beta_5 \ln\left|\frac{\gamma+1}{\gamma-1}(\gamma U - 1)\right|. \quad \text{(I.70)}$$

Finally, the exponentiation of Eq. (I.70) gives the final expression for $G(U)$ to be

$$G(U) = \frac{\gamma+1}{\gamma-1}\left(\frac{\gamma+1}{\gamma-1}(1-U)\right)^{\beta_3}\left(\frac{\gamma+1}{m(\gamma+1)-2\chi}(m-\chi U)\right)^{\beta_4}\left(\frac{\gamma+1}{\gamma-1}(\gamma U-1)\right)^{\beta_5}. \quad \text{(I.71)}$$

I.5.6 Summary of exact solution

In summary, the exact similarity solution to the point blast explosion problem is given by

$$G(U) = \frac{\gamma+1}{\gamma-1}\left(\frac{\gamma+1}{\gamma-1}(1-U)\right)^{\beta_3}\left(\frac{\gamma+1}{m(\gamma+1)-2\chi}(m-\chi U)\right)^{\beta_4} \left(\frac{\gamma+1}{\gamma-1}(\gamma U-1)\right)^{\beta_5}, \tag{I.71}$$

$$\xi(U) = \left(\frac{(\gamma+1)(m-\chi U)}{m(\gamma+1)-2\chi}\right)^{\beta_1}\left(\frac{\gamma+1}{1-\gamma}(1-\gamma U)\right)^{\beta_2}\left(\frac{\gamma+1}{2}U\right)^{-\frac{2}{m}}, \tag{I.63}$$

$$Z(U) = \frac{\gamma(\gamma-1)}{2}\frac{U^2(U-1)}{1-\gamma U}, \tag{I.47c}$$

where the β's are given by Eqs. (I.61) and (I.68)

$$\beta_1 = \frac{\chi-m}{m(1-\gamma)}\left(\frac{(1-\gamma)(\chi-\gamma m-m)}{\chi(\chi-m)}+\beta_2\right), \tag{((I.61a))}$$

$$\beta_2 = \frac{1-\gamma}{\chi-m\gamma}, \tag{((I.61b))}$$

$$\beta_3 = -\left(\frac{(n+1)\gamma}{m-\chi}+1\right),, \tag{((I.68a))}$$

$$\beta_4 = \frac{n+1}{m-\chi}(-m\beta_1), \tag{((I.68b))}$$

$$\beta_5 = -\frac{n+1}{\chi-\gamma m}, \tag{((I.68c))}$$

$\chi = (n+1)(\gamma-1)+2$ is given by Eq. (I.49) , n is given by Eq. (I.5), and $m = n+3$. In practice, one desires the answer at a given ξ and so an iterative process is used to find the corresponding root to Eq. (I.63). This root is always bracketed by Eq. (I.65).

Lastly, the dimensional solution is recovered from Eqs. (I.11) where the constants E and k are related through Eq. (I.34). It it worth noting that integral

relating E and k, Eq. (I.35), can be easily rewritten in terms of U as

$$E = \frac{2^{n+2}\pi^l k^m E}{m^2} \int G(U) \left(\frac{1}{\gamma(\gamma-1)} Z(U) + \frac{1}{2} U^2 \right) \xi(U)^m \frac{d\ln\xi}{dU} dU, \tag{I.72}$$

where $d\xi/\xi = d\ln\xi$, $\frac{d\ln\xi}{dU}$ is given by Eq. (I.53), and the bounds are given by Eq. (I.65). As an attractive alternative to specifying E and then calculating k, one may instead specify the composite $k^m E$. This allows for immediate computation of the dimensional solution using Eq. (I.7). In such a case, Eq. (I.72) provides a manner of calculating E in isolation. This is especially useful for generating consistent numerical test solutions at different times without ever requiring the calculation of E.

BIBLIOGRAPHY

[1] A. R. Kasimov and D. S. Stewart. On the dynamics of self-sustained one-dimensional detonations: A numerical study in the shock-attached frame. *Physics of Fluids*, 16(10):3566–3578, 2004.

[2] L. I. Rubinsteĭn. *The Stefan Problem*. Zvaigzne Publishers, Riga, Latvia, 1967. Translation available from the American Mathematical Society, 1971.

[3] V. Alexiades and A. D. Solomon. *Mathematical Modeling of Melting and Freezing Processes*. Hemisphere Publishing Corporation, Washington, D.C., 1993.

[4] E. F. Toro. *Riemann Solvers and Numerical Methods for Fluid Dynamics: A Practical Introduction*. Springer-Verlag, Berlin, second edition, 1999.

[5] R. J. LeVeque. *Numerical Methods for Conservation Laws*. Birkhäuser Verlag, Basel, Switzerland, 1992.

[6] R. J. LeVeque. *Finite Volume Methods for Hyperbolic Problems*. Cambridge University Press, Cambridge, UK, 2002.

[7] J. T. Lin. The numerical analysis of a phase field model in moving boundary problems. *SIAM Journal of Numerical Analysis*, 25(5), 1988.

[8] T. D. Aslam. A level–set algorithm for tracking discontinuities in hyperbolic conservation laws I. scalar equations. *Journal of Computational Physics*, 167: 413–438, 2001.

[9] T. D. Aslam. A level set algorithm for tracking discontinuities in hyperbolic conservation laws II: Systems of equations. *Journal of Scientific Computing*, 19:37–62, 2003.

[10] S. Osher and R. Fedkiw. *Level Set Methods and Dynamic Implicit Surfaces*. Springer-Verlag, New York, 2003.

[11] G. Moretti and G. Bleich. A time-dependent computational method for blunt-body flows. *AIAA Journal*, 4:2136–2141, 1966.

[12] G. Moretti. Computation of flows with strong shocks. *Annual Review of Fluid Mechanics*, 19:313–337, 1987.

[13] G. P. Brooks. A Karhunen-Loéve least-squares technique for optimization of geometry of a blunt body in supersonic flow. *Journal of Computational Physics*, 195:387–412, 2004.

[14] G. P. Brooks. Standardized pseudospectral formulation of the inviscid supsersonic blunt body problem. *Journal of Computational Physics*, 197:58–85, 2004.

[15] M. Akram and F. Ali. Shock fitting and numerical modeling of detonation waves. *International Journal of Modern Physics C*, 8:1193–1207, 1997.

[16] T. D. Aslam, J. B. Bdzil, and L. G. Hill. Analysis of the LANL detonation-confinement test. In *Shock Compression of Condensed Matter - 2003: Proceedings of the Conference of the American Physical Society Topical Group on Shock Compression of Condensed Matter*, volume 706 (1), pages 831–834. American Institute of Physics, 2004.

[17] J. A. Zukas and W. P. Walters, editors. *Explosive Effects and Applications*. Springer-Verlag, New York, 1997.

[18] J. M. Powers and S. Paolucci. Accurate spatial resolution estimates for reactive supersonic flow with detailed chemistry. *AIAA Journal*, 43:1088–1099, 2005.

[19] W. Fickett and W. C. Davis. *Detonation: Theory and Experiment*. Dover, Mineola, New York, 2000.

[20] J. B. Bdzil. Steady-state two-dimensional detonation. *Journal of Fluid Mechanics*, 108:195–226, 1981.

[21] W. C. Davis. Lecture notes: Introduction to explosives. Los Alamos National Laboratory, Los Alamos, New Mexico, Fall, 2003.

[22] A. W. Campbell and Engelke. The diameter effect in high-density heterogeneous explosives. In *Proceedings of the Sixth International Symposium on Detonation*, pages 642–652, Coronado, CA, 1976. Office of Naval Research.

[23] W. W. Wood and J. G. Kirkwood. Diameter effect in condensed explosives - the relation between velocity and radius of curvature of the detonation wave. *Journal of Chemical Physics*, 22:1920 – 1924, 1954.

[24] D. S. Stewart. Lectures on detonation physics: Introduction to the theory of detonation shock dynamics. TAM Report 721, University of Illinois at Urbana-Champaign, August 1993.

[25] T. D. Aslam and J. B. Bdzil. Numerical and theoretical investigations on detonation-inert confinement interactions. In *Proceedings of the Twelfth International Symposium on Detonation*, San Diego, CA, 2002.

[26] C. J. Chapman. *High Speed Flow*. Cambridge University Press, Cambridge, 2000.

[27] R. Aris. *Vectors, Tensors, and the Basic Equations of Fluid Mechanics*. Dover Publications, Inc., Mineola, NY, 1962.

[28] W. Kaplan. *Advanced Calculus*. Addison-Wesley Publishing Company, Inc., New York, 4th edition, 1991.

[29] H. Luo and T. R. Bewley. On the contravariant form of the Navier-Stokes equations in time-dependent curvilinear coordinate systems. *Journal of Computational Physics*, 199:355–375, 2004.

[30] A. C. Eringen. *Mechanics of Continua*. John Wiley & Sons, Inc., New York, 1967.

[31] A. Jeffrey. *Quasilinear Hyperbolic Systems and Waves*. Pitman Publishing, London, UK, 1976.

[32] H. Viviand. Formes conservatives des équations de la dynamique des gaz. *La Recherche Aérospatiale*, 1:65–66, 1974.

[33] M. Valorani, M. Onofri, B. Favini, and F. Sabetta. Nonequilibrium hypersonic inviscid steady flows. *AIAA Journal*, 30:89–93, 1992.

[34] D. S. Stewart and J. B. Bdzil. Examples of detonation shock dynamics for detonation wave spreading applications. In *Proceedings Ninth Symposium (International) on Detonation*, volume 1, pages 773–783, Portland, OR, 1989. Office of Naval Research.

[35] A. K. Henrick, T. D. Aslam, and J. M. Powers. Mapped weighted essentially non-oscillatory schemes: Achieving optimal order near critical points. *Journal of Computational Physics*, 207(2):542–467, 2005.

[36] R. J. LeVeque and H. C. Yee. A study of numerical methods for hyperbolic conservation laws with stiff source terms. *Journal of Computational Physics*, 86:187–210, 1990.

[37] B. Van Leer. Towards the ultimate conservative difference scheme II, monotonicity and conservation combined in a second order scheme. *Journal of Computational Physics*, 14:361–470, 1974.

[38] B. Van Leer. Towards the ultimate conservative difference scheme V, a second order sequel to Godunov's method. *Journal of Computational Physics*, 32: 101–136, 1979.

[39] A. Harten, B. Enquist, S. Osher, and S. Chakravarthy. Uniformly high order accurate essentially non-oscillatory schemes III. *Journal of Computational Physics*, 71:231–303, 1978.

[40] C-W. Shu and S. Osher. Efficient implementation of essentially non-oscillatory shock-capturing schemes. *Journal of Computational Physics*, 77: 439–471, 1988.

[41] C-W. Shu and S. Osher. Efficient implementation of essentially non-oscillatory shock-capturing schemes II. *Journal of Computational Physics*, 83:32–78, 1989.

[42] X-D. Liu, S. Osher, and T. Chan. Weighted essentially non-oscillatory schemes. *Journal of Computational Physics*, 115:200–212, 1994.

[43] G-S. Jiang and C-W. Shu. Efficient implementation of weighted ENO schemes. *Journal of Computational Physics*, 126:202–228, 1996.

[44] D. S. Balsara and C.-W. Shu. Monotonicity preserving weighted essentially non-oscillatory schemes with increasingly high order of accuracy. *Journal of Computational Physics*, 160:405–452, 2000.

[45] R. Fedkiw. Simplified discretization of systems of hyperbolic conservation laws containing advection equations. *Journal of Computational Physics*, 157: 302–326, 2000.

[46] C. W. Shu. Numerical methods for systems of conservation laws of mixes type using flux splitting. *NASA Contract Report*, 182084, 1990.

[47] C. A. Fletcher. *Computational Techniques for Fluid Dynamics 2*. Springer-Verlag, Berlin, 2nd edition edition, 1991.

[48] E. Katzer and S. Osher. Efficient implementation of essentially non-oscillatory schemes for systems of nonlinear hyperbolic differential equations. CAM Report 88-14, University of California, Los Angeles, May 1998.

[49] S. Osher and J. A. Sethian. Fronts propagating with curvature-dependent speed: Algorithms based on hamilton-jacobi formulations. *Journal of Computational Physics*, 79:12–49, 1988.

[50] S. Osher and C-W. Shu. High-order essentially nonoscillatory schemes for hamilton-jacobi equations. *SIAM Journal on Numerical Analysis*, 28:907–922, 1991.

[51] C. B. Macdonald. Constructing high-order runge-kutta methods with embedded strong-stability-preserving pairs. Master's thesis, Simon Fraser University, 2003.

[52] A. K. Henrick, T. D. Aslam, and J. M. Powers. Simulations of pulsating one-dimensional detonations with true fifth order accuracy. *Journal of Computational Physics*, 213(1):311–329, 2006.

[53] J. J. Erpenbeck. Stability of steady-state equilibrium detonations. *Physics of Fluids*, 5(5):604–614, 1962.

[54] W. Fickett and W. W. Wood. Flow calculations for pulsating one-dimensional detonations. *Physics of Fluids*, 9:903–916, 1966.

[55] H. I. Lee and D. S. Stewart. Calculation of linear detonation instability: One–dimensional instability of plane detonation. *Journal of Fluid Mechanics*, 212: 103–132, 1990.

[56] A. Bourlioux, A. J. Majda, and V. Roytburd. Theoretical and numerical structure for unstable one-dimensional detonations. *SIAM Journal on Applied Mathematics*, 51(2):303–343, 1991.

[57] L. He and J. H. S. Lee. The dynamical limit of one-dimensional detonations. *Physics of Fluids*, 7(5):1151–1158, 1995.

[58] J. Yao and D. S. Stewart. On the dynamics of multi-dimensional detonation. *Journal of Fluid Mechanics*, 309:225–275, 1996.

[59] M. Short. Multidimensional linear stability of a detonation wave at high activation energy. *SIAM Journal of Applied Mathematics*, 57(2):307–326, 1997.

[60] G. J. Sharpe. Linear stability of idealized detonations. *Proceedings of the Royal Society A*, 453(1967):2603–2625, 1997.

[61] P. Hwang, R. P. Fedkiw, B. Merriman, T. D. Aslam, A. R. Karagozian, and S. J. Osher. Numerical resolution of pulsating detonation waves. *Combustion Theory and Modelling*, 4(3):217–240, 2000.

[62] G. J. Sharpe and S. A. E. G. Falle. Numerical simulations of pulsating detonations: I. Nonlinear stability of steady detonations. *Combustion Theory and Modelling*, 4(4):557–574, 2000.

[63] H. D. Ng, A. J. Higgins, C. B. Kiyanda, M. I. Radulescu, J. H. S. Lee, K. R. Bates, and N. Nikiforakis. Nonlinear dynamics and chaos analysis of one-dimensional pulsating detonations. *Combustion Theory and Modelling*, 9(1): 159–170, 2005.

[64] A. Majda and S. Osher. Propagation of error into regions of smoothness for accurate difference approximations to hyperbolic equations. *Communications on Pure and Applied Mathematics*, 30(6):671–705, 1977.

[65] J. Casper and M. H. Carpenter. Computational consideration for the simulation of shock-induced sound. *SIAM Journal on Scientific Computing*, 19(3): 818–828, 1998.

[66] M. H. Carpenter and J. H. Casper. Accuracy of shock capturing in two spatial dimensions. *AIAA Journal*, 37(9):1072–1079, 1999.

[67] J. M. Powers and T. D Aslam. Exact solution for multidimensional compressible reactive flow for verifying numerical algorithms. *AIAA Journal*, 44 (2):337–344, 2006.

[68] M. J. Feigenbaum. Quantitative universality for a class of non-linear transformations. *Journal of Statistical Physics*, 19(1):25–52, 1978.

[69] M. J. Feigenbaum. The universal metric properties of nonlinear transformations. *Journal of Statistical Physics*, 21(6):669–706, 1979.

[70] D. A. Kopriva, T. A. Zang, and M. Y. Hussaini. Spectral methods for the Euler equations: the blunt body problem revisited. *AIAA Journal*, 29(9): 1458–1462, 1991.

[71] G. B. Whitham. *Linear and Nonlinear Waves*. John Wiley & Sons, Inc., New York, 1974.

[72] R. L. Burden and J. D. Faires. *Numerical Analysis*. Prindle, Weber and Schmidt, Boston, MA, 1985.

[73] E. A Jackson. *Perspectives on Nonlinear Dynamics*. Cambridge University Press, New York, 1991.

[74] P. G. Drazin. *Nonlinear Systems*. Cambridge University Press, New York, 1992.

[75] M. Short, I. I. Anguelova, T. D. Aslam, A. K. Henrick, and G. J Sharpe. Detonation stability for a pressure-sensitive reaction model with a variable reaction order. *Journal of Fluid Mechanics*, to appear.

[76] J. L. Steger. Implicit finite-difference simulation of flow about arbitrary two–dimensional geometries. *AIAA Journal*, 16:679–686, 1978.

[77] G. I. Taylor. The air wave surrounding an expanding sphere. *Royal Society of London Proceedings Series A*, 186:273–292, September 1946.

[78] L. I. Sedov. *Similarity and Dimensional Methods in Mechanics*. Hemisphere Publishing Corporation, New York, 1959.

[79] L. D. Landau and E. M. Lifshitz. *Fluid Mechanics*. Elsevier Science Ltd., New York, 2nd edition, 2004.

[80] G. I. Taylor. The formation of a blast wave by a very intense explosion II: The atomic explosion of 1945. *Royal Society of London Proceedings Series A*, 201:175–186, March 1950.

This document was prepared & typeset with pdfLaTeX, *and formatted with* NDdiss2$_\varepsilon$ *classfile (v3.0[2005/07/27]) provided by Sameer Vijay.*